Hydrodynamics in Millichannel-based Fixed-bed Device and Its Application in Transport Processes

Thesis Submitted for the Degree of

Doctor of Philosophy (Ph.D.)

in

Chemical Engineering

Submitted by

Mr. Somen Mondal

Department of Chemical Engineering

Indian Institute of Technology Guwahati

Guwahati, Assam, India

October 2020

"Confidence and hard-work is the best medicine to kill the disease called failure. It will make you a successful person."

- A.P.J. Abdul Kalam (1931 - 2015)

This thesis is dedicated to my parents and family.

INDIAN INSTITUTE OF TECHNOLOGY GUWAHATI
GUWAHATI - 781039, ASSAM, INDIA

DEPARTMENT OF CHEMICAL ENGINEERING

CERTIFICATE

This is to certify that the thesis entitled "***Hydrodynamics in Millichannel-based Fixed-bed Device and Its Application in Transport Processes***" submitted by **Somen Mondal** in fulfillment of the requirement of the *Degree of Doctor of Philosophy in Engineering*, is a record of bonafide research work carried out by him, in the Department of Chemical Engineering, Indian Institute of Technology, Guwahati, under my guidance and supervision. The work documented in this thesis has not been submitted to any other University or Institute for the award of any degree or diploma. In my opinion, the thesis has reached the standard fulfilling the requirements of the Ph. D. degree as prescribed in the regulations of this institute.

Date 22 / 10 / 2020

Prof. Subrata Kumar Majumder
(Thesis Supervisor)
Department of chemical Engineering,
Indian institute of Technology Guwahati,
Guwahati, Assam -781039, India.

Acknowledgment

Undertaking doctoral research provided me a truly life-changing experience, and it would not be possible to do without the support and guidance that I received from numerous peoples. Hence, it gives me immense pleasure to acknowledge all those who have guided, contributed, and supported me in carrying out my doctoral research entitled "**Hydrodynamics in Millichannel-based Fixed-bed Device and Its Application in Transport Processes**" at the Indian Institute of Technology, Guwahati, Assam, India.

I owe my deepest gratitude to my supervisor, **Dr. Subrata Kumar Majumder**, Professor, Department of Chemical Engineering, Indian Institute of Technology Guwahati, for his guidance and supervision, which enabled me to carry out my research ventures. I have learned every aspect of this research work from him. Without his active and continuous monitoring, this research work would not have been possible.

It is an honor for me to thank my doctoral committee, Dr. Pankaj Biswas (Professor, Department of Mechanical Engineering), Dr. Anugrah Singh (Professor and Head, Department of Chemical Engineering), Dr. Raghvendra Gupta (Associate Professor, Department of Chemical Engineering), Indian Institute of Technology Guwahati, for allowing me to perform the research under their evaluation and guidance.

I gratefully acknowledge the Ministry of Human Resource Development (MHRD, Government of India), for providing me the fellowship during this tenure; the University authority**, Science & Engineering Research Board** (SERB-DST, International Travel Support, File No.: ITS/2019/003911), and **Council of Scientific and Industrial Research** (CSIR - HRDG, Travel Grant, File No.: TG/11112/19-HRD), for granting me the necessary funds for participation in the national, and international conferences. I am also thankful to the Department of Science and Technology (Water Technology Initiative), Government of India, for the financial support to fulfill a part of my thesis work, through the Grant Number: DST/TM/WTI/2K16/20 (C)-A, dated March 3, 2017.

I am also grateful to the staff of the analytical laboratory (Department of Chemical Engineering), and the Central Instrument Facility (CIF, Indian Institute of Technology Guwahati), for their necessary support, without which it would not be possible to conduct this research.

I want to thank Prof. Pallab Ghosh, Dr. Prabu Vairakannu, Prof. Mihir Kumar Purkait, Prof. Vaibhav V. Goud, Prof. Bishnupada Mandal, Prof. Animes Kumar Golder, Dr. Nageswara Rao Peela, Dr. Senthilmurugan S, Prof. Tamal Banerjee, Prof. Prabir Kumar Saha, Dr. Pankaj Tiwari, for their advice, support, and blessings throughout my tenure.

I sincerely thank all the persons concerned in official, and administrative departments in Indian Institute of Technology Guwahati, including Mr. Deep Jyoti Sinha, Mr. Saiful Alam, Mr. Harsaraj Biswanath, Mr. Pankaj Kumar, Mr. Ariful Hoque, Dr. Kaustavmoni Deka, Mr. Sailen Das, Mr. Debajit Borah, Mr. Prasun Kumar Bhattacharjee, Mr. Jayanta Kumar Mout, Mr. Pankaj Sekhar Baruah, for their help, and co-operation during the tenure of my work. I am very grateful to all faculty members, staff, and research scholars of the Department of Chemical Engineering, Indian Institute of Technology Guwahati, for their valuable comments and suggestions throughout the work.

I am heartily thankful for my lab-mates Ms. Surabhi Patel, Mr. Ritesh Prakash, Mr. M. K. Fahad, Mr. Goshika Bharath Kumar, Ms. kumari Ruby, Mr. Babban Lal Maurya, Mr. Gourav Singh, and my friends Mr. Piyal Mondal, Mr. Surendra Singh Gaur, Mr. Kuldeep Roy, Mr. K Dharmalingam, Mr. Siddharth Thakur, Ms. Sushma Chakraborty, Ms. Barnali Bhui, Mr. Saptarshi Gupta, Mr. Mahboob Alam, Ms. Soumi Sarkar, Mr. Bitang Kwrung Tripura, Mr. Rupam Sinha, Mr. Bikashbindu Das, Mr. Pyarimohan Dehury, Ms. Aritra Das, Mr. Sayan Kumar Bhattacharjee, Mr. Palash Das, Mr. Abhijit Das, for their help, and support when necessary.

I am also thankful to my seniors at Indian Institute of Technology Guwahati, Mr. Supriyo Kumar Mondal, Mr. Atanu Kumar Paul, Mr. Narendren S, Mr. Pradip Das, Mr. Pallab Das, Mr. Rahul Saha, Mr. Suman Saha, Mr. Mood Mohan, Mr. Raj Kumar Das, Mr. Prince Kumar Baranwal, Mrs. Sadhana Kumari, Mr. Shailesh Ravi Varade, Mr. Shirsendu Mitra, and my juniors Ms. Sutapa Das,

Mr. Kaniska Murmu, Mr. Bharath Velaga, Mr. Anirban Chowdhury, Mr. Bhargav Baruah, Mr. Saikat Biswas, Mr. Jinesh Machale, Ms. Kajal Ingtipi, and Mr. Pradeep Sahu, for their help and support at the different stages of my research work.

I would like to thank Mr. Saptarshi Sengupta, Mr. Subhankar Bhattacharjee, Mr. Purusarth Prasannam, Mr. Sakil Mollah, and Mr. Swadhin Dey from Jadavpur University, for their support and sincerity in work during the summer internship period.

I want to thank the most important person in my life, my mother (Mrs. Sabita Mondal), for her unpredictable love, support, encouragement, and dedication. Her dedication level was like that; she said to me, "I would like to die after when you will complete your doctorate degree". I would also like to thank my late father (Lt. Girish Chandra Mondal) for his blessing and support behind my eyes, and I am pleased to fulfill his last will by becoming a complete Engineer. I want to thank my younger sister (Ms. Sima Mondal), elder sister (Mrs. Soma Mondal), for their mental support to nourish my mind, which helped me in the involvement in research. I want to thank my father in law (Lt. Mr. Sankar Chatterjee), mother in law (Mrs. Rama Chatterjee) for their support, and blessings. I would like to acknowledge the blessings of my paternal grandparents (Lt. Ram Chandra Mondal, and Lt. Binapani Mondal), maternal grandfather (Lt. Bhupendra Nath Mondal), and brother in law (Lt. Subhash Chandra Mondal) which, have always been with me even after their demise. I want to thank my maternal grandmother (Mrs. Sudha Rani Mondal), nephew (Mr. Suman Mondal), and all of my relatives, friends, and well-wishers for their blessings, support, wishes and everything they did for me so that I could carry out this research work successfully. I want to thank my good luck, Mr. Chunku Mondal. Last but not least, I would like to acknowledge my life partner (Mrs. Shrabani Chatterjee Mondal), for her enormous support, and encouragement throughout the whole research work.

Finally, yet importantly, I thank the universal supreme power, which provides me my inner strength in performing all the works that I do.

With regards,

(**SOMEN MONDAL**)

Contents

Abstract

The present study reports the feasible applications of the millichannel based packed bed geometries as the efficient transport devices. Before the application of any millimetric channel geometries as the transport devices, the hydrodynamics, mixing, and flow characteristics for the flow of fluids through them to be very well known. The pressure drop characteristics of single-phase as well as aqueous-organic liquid-liquid two-phase flow through the rectangular straight and serpentine millichannels, both in packed and unpacked conditions, using medium sand as the packing material were described in the present context. The experimental results are enunciated with the available models for both unpacked and packed channels. Empirical models are developed to predict the pressure drop and friction factor for both single and two-component liquid-liquid flows through the prescribed straight and serpentine geometries based on the operating variables. The variation of local entropy generation rate at a particular temperature gradient in the two-phase flows through the unpacked straight channel is enunciated.

From the previous literature, it was obvious that the millimetric devices with parallel multichannel are more efficient than their series. The incorporation of another inert phase may also enhance the transport efficiencies as the turbulence or mixing increases, proving more residence time to the contaminants inside the multichannel. The process intensification by using the millimetric multichannel packed bed devices providing the two-phase flows is the key focus for researchers for the enhancement of the mass transfer applications. Millimetric multichannel-based devices have elevated heat and mass transfer performance and thus have great prospects, particularly in exothermic or explosive reactions. Residence time distribution (RTD) is the most important parameter to characterize the flow distribution inside the device. The RTDs of a liquid tracer for the air-water two-phase concurrent flows through the millimetric packed multichannel devices (consist of 11 number of same dimensional parallel channels) with the variable heights were measured by the conductivity measurements and represented by the axial dispersion model (ADM). The axial dispersion coefficients, as well as the specific energy dissipation values, were estimated. The effects of the operating variables, pressure drop, and the geometries on the hydrodynamics and the mixing properties were well expressed. Based on the experimental data, new correlations were proposed and compared with the available literature.

Then the heat transport studies were executed based on the hydrodynamics and the local entropy generation rate for the water-toluene, water-benzene, and water-p-xylene (aqueous-organic) two-phase flow through the straight and serpentine rectangular narrow channels, packed with irregularly shaped sand particles of different diameters. The widely used Ergun equation for the calculation of pressure drop in packed bed is modified for the application in randomly packed straight and serpentine narrow rectangular channels in a horizontal orientation. New correlations for the convective heat transfer coefficient are proposed. The flow dynamics other than the temperature gradient, on the local entropy generations for the liquid-liquid flows in the packed straight and serpentine channels, are enunciated. The influence of the changing diameter of the packing material and the fluid mixture on the local entropy generation were demonstrated. The packed straight channel acquires a lower-pressure drop in the absence of Dean flow. The packed serpentine channel of the same dimension, having less entropy generation rate for the same temperature driving force, establishes its efficiency for the more beneficial application to design the heat transport equipment at the higher mass flow rate, provided the same diameter of the packing material and the fluid mixture at the expense of higher pressure drop.

The mass transfer (extraction) studies were also performed to investigate the effect of copper ion concentration in the solution, extractant concentration in the solvent, solution pH, mixture velocity of the phases, and the temperature on the copper extraction from a copper-laden solution. Copper is separated from a mixture of copper, nickel, and cadmium solution as hydroxide precipitate by changing the pH of the solution. Copper is then extracted from the aqueous phase to the organic phase using a commercially available extractant D2EHPA [Bis - (2-ethylhexyl) phosphoric acid] dissolved in the organic phase (benzene). The effect of pH and the other parameters on the stripping process of copper from the organic phase to the acidic aqueous phase has also been studied, introducing a rectangular serpentine packed millichannel as a novel extracting device.

From the previous studies, it was clear that the inert packing materials should be replaced by the adsorbent material to fabricate the millichannel based packed bed adsorption device. Hence, the synthesis of the cost-effective, potentially efficient adsorbents became the target. Though the activated carbon-based materials are widely used by the industries due to their low cost, they are not usable in millimetric packed-channel devices due to their slow adsorption kinetics. The

retention time inside the millimetric packed channels is very low, which makes the activated carbons are inefficient in these small dimensional channels. Then the only option remains to go for the graphene-based composite materials, which may provide faster kinetics having the high surface area and the higher surface functionality. Due to the presence of a huge number of functional groups on the adsorbent surface, it may facilitate the ionic interactions, proving the faster kinetics to the process. The Ag-RGO nanocomposite film was prepared by following the in-situ green synthesis using turnip leaves-extract as a reducing as well as a capping agent. The synthesized material was utilized as an efficient naproxen adsorbent from the contaminated aqueous solutions, which showed a multilayered ion-exchange type of adsorption process on the heterogeneous adsorbent surfaces. The process parameters were optimized to get the maximum adsorption capacity and were validated using response surface methodology (RSM).

It was evident from the previous studies that the graphene-based materials can be used as the packing material for the fabrication of millimetric packed channel adsorption devices for their higher capacity and faster kinetics. Lastly, the hydrodynamics and the mixing characteristics for the single-phase flow through a millimetric multichannel packed bed device was studied to meet the specific requirements of the small-scale transport systems. Residence Time Distribution (RTD) studies were performed to characterize the velocity distribution for the internal flow inside that packed bed. The effects of the operating variables and the geometries on the hydrodynamics and mixing properties were enunciated. Copper adsorption with the parametric effects was studied in the same packed multichannel geometry with the amine-functionalized reduced graphene oxide (RGO-NH_2) coated glass beads. The Thomas and Yoon-Nelson adsorption models analyzed the experimental results. The adsorptive mass transfer rates were correlated to the hydrodynamic parameters of the said packed bed device, and the regeneration studies were performed.

This study will be helpful in designing millichannel-based packed bed transport devices, along with the synthesis and characterization of the various kind of adsorbent materials.

List of Figures

List of Tables

List of Abbreviations

Abbreviation	Expanded form
3D	Three dimensional
AAS	Atomic absorption spectroscopy
AC	Activated carbon
ADM	Axial dispersion model
AFM	Atomic force microscopy
ANOVA	Analysis of variance
BET	Brunauer–Emmett–Teller
CCD	Central Composite Design
CTAB	N-cetyl-N, N, N-trimethyl ammonium bromide
D2EHPA	Di-(2-ethylhexyl) phosphoric acid
DMG	Dimethylglyoxime
DMF	Dimethylformamide
EDTA	Ethylenediaminetetraacetic acid
EV	experimental value
FESEM	Field emission scanning electron microscopy
FTIR	Fourier transform infrared spectroscopy
GO	Graphene oxide
LMTD	Log mean temperature difference
LPSA	Laser particle size analyzer
MAPE	Mean average percentage error
MD	Mean deviation
NPX	Naproxen
PPM	Parts per million
PT	Pressure transducer
PV	Predicted value
PZC	Point of zero charge
RMSD	Root mean squared deviation
RSM	Response surface methodology
RTD	Residence time distribution
SD	Standard deviation
SDS	Sodium dodecyl sulfate
SX	Solvent extraction
SEM	Scanning electron microscopy
TBP	Tributyl phosphate
TEM	Transmission electron microscopy
TKN	Total Kjeldahl nitrogen
TT	Temperature transducer
UV-VIS	Ultraviolet-visible
WHO	World Health Organization
XRD	X-ray powder diffraction

List of Symbols

Symbols	Indicates (Unit)
A	cross-sectional area of the channel (m^2)
A/O	ratio of aqueous to organic volumetric flow rate (-)
A_c	channel aspect ratio ($=\frac{w}{h}$) (-)
A_i	cross-sectional area of the individual channel (m^2)
A_p	single-particle surface area (m^2)
A_S	effective surface area of the channel (m^2)
a,b,c	rational number (-)
a_e	initial adsorption rate of Elovich equation (mg g^{-1} min^{-1})
b	Langmuir's equilibrium constant (dm^3 mg^{-1})
b'	Temkin isotherm constant (kJ mol^{-1})
B	Temkin isotherm constant (related to the heat of adsorption, -)
B'	Dubinine-Radushkevich (D-R) model constant (mol^2 kJ^{-2})
b_e	the extent of surface coverage in Elovich equation (g mg^{-1})
Be	Bejan number ($=\frac{ds_{m,p\ (\text{heat transfer})}}{ds'_{m,p}}$) (-)
Bo	Bond number ($=\frac{\Delta\rho g d_H^2}{\sigma_m}$) (-)
C	Chisholm constant (-)
C_1	intercept of the intraparticle diffusion model (-)
C_A	solid-phase equilibrium concentration (mg dm^{-3})
Ca	Capillary number ($=\frac{\mu U}{\sigma}$) (-)
C_{ad}	quantity adsorbed at time t_t (mg dm^{-3})
C_a^{in}	solute concentration in the aqueous phase at the inlet (mol L^{-1})
C_a^{out}	solute concentration in the aqueous phase at the outlet (mol L^{-1})

C_o^{out}	solute concentration in the organic phase at the outlet (mol L^{-1})
$C_{a,Eqb}^{in}$	solute concentration in the aqueous phase in equilibrium with the solute concentration of the organic phase at the inlet (mol L^{-1})
$C_{a,Eqb}^{out}$	solute concentration in the aqueous phase in equilibrium with the solute concentration of the organic phase at the outlet (mol L^{-1})
Ca_p	Capillary number (-)
C_E	Extractant concentration in the solvent (mol L^{-1})
C_e	solution concentration at equilibrium (mg dm^{-3})
C_m	Copper concentration in the solution (mol L^{-1})
C_0	initial or inlet solute concentration (mg dm^{-3})
C_P	specific heat capacity of the fluid (J kg^{-1} K^{-1})
C_t	concentration in the solution at time t (mg dm^{-3})
$c(t)$	concentration profile of the tracer at the outlet (molar, M)
d	diameter of the channel (m)
Da	Damköhler number (-)
D_{ax}	axial dispersion coefficient (m^2 min^{-1})
De	Dean number ($=\frac{d_H U\rho}{\mu}\sqrt{\frac{d_H}{2r_c}}$) (-)
d_H	hydraulic diameter (m)
D_m	molecular diffusion coefficient (m^2 min^{-1})
d_p or $d_{p,eff}$	effective or average particle diameter of the packing material (m)
ds'	entropy generation rate per unit length (W K^{-1} m^{-1})
E	mean free energy of adsorption (kJ mol^{-1})
E'	modified Ergun equation 1st constant (-)
E''	modified Ergun equation 2nd constant (N m^{-3})
E_d	specific energy dissipation (W kg^{-1})
$E(t)$	density distribution function (min^{-1})
Eu	Euler number (-)
Eu'	modified Euler number (-)
f'	Fanning friction factor (-)

Fr	Froude number ($=\frac{U}{\sqrt{gd_H}}$) (-)
G	mass flux (kg m^{-2} s^{-1})
g	gravity of acceleration (m s^{-2})
ΔG^0	Gibbs free energy change (kJ mol^{-1})
h	height of the individual channel (m)
h'	heat transfer coefficient (W m^{-2} K^{-1})
ΔH^0	standard enthalpy change (kJ mol^{-1})
j	volumetric flux (m^3 s^{-1} m^{-2})
K'	contraction or expansion coefficient (-)
k	conductive heat transfer coefficient (W m^{-1} K^{-1})
k_1	pseudo-first-order rate constant (min^{-1})
k_2	pseudo-second-order rate constant (g mg^{-1} min^{-1})
K_C	equilibrium constant of adsorption (-)
K_D	distribution coefficient (-)
K_e	equilibrium constant (-)
K_r	kinetic mass transfer rate (min^{-1})
K_T	Thomas rate constant (dm^3 min^{-1} mg^{-1})
K_{YN}	Yoon-Nelson model-constant (min^{-1})
k_f	Freundlich's constant (related to adsorption capacity (mg g^{-1})
k_p	rate constant of the intra-particle diffusion model (mg g^{-1} $min^{-1/2}$)
k_t	Temkin adsorption isotherm constant (dm^3 mg^{-1})
K_La	overall volumetric mass transfer coefficient (s^{-1})
L	length of the channel (m)
l	total length of the multichannel (m)
l_i	length of the individual channel (m)
Lo^*	Laplace constant ($=\left(\frac{\sigma_m}{g(\rho_w-\rho_o)}\right)^{0.5}/d_H$) (-)
M	molarity of the solution (mol L^{-1})
M_w	molecular weight of the liquid (g mol^{-1})

M_a	total mass of the adsorbent (g)
M_f	mass of the fluid into which the specific energy is dissipated (kg)
m	adsorbent dosage (g)
M'	mass flow rate (kg s^{-1})
M_b	mass of the bed (kg)
MD	mean deviation (%)
m_t	total quantity of copper (II) fed to the packed bed (mg)
Nu	Nusselt number ($=\left(\frac{h' d_H}{k}\right)$) (-)
N *or* n	total number of variables or data points (-)
n	Freundlich's constant (related to adsorption intensity (-)
N'	total number of particles (-)
n_w	total number of moles of water (mol)
n_0	total number of moles of organic (mol)
n_L	number of moles of water in the liquid phase (mol)
n_s	number of moles of water at the surface (mol)
n_v	number of moles of water in the vapor phase (mol)
P	perimeter (m)
Pe_a	axial Peclet number (-)
Pe_m	Peclet number for the molecular diffusion (-)
Pr	Prandtl number ($=\frac{\mu C_P}{k}$) (-)
ΔP_a	accelerating pressure drop (N m^{-2})
ΔP_f	frictional pressure drop (N m^{-2})
ΔP_g	pressure loss due to gravity (N m^{-2})
ΔP_i	pressure loss of the i^{th} channel (N m^{-2})
ΔP_{inlet}	sum of inlet pressure losses (N m^{-2})
ΔP_T	total pressure drop (N m^{-2})
Q	total volumetric flow rate of the liquid (m^3 s^{-1})
Q_i	volumetric flow rate through each channel (m^3)
q	heat transfer rate (J s^{-1} or Watt)

q_{cal}	equilibrium values obtained from the isotherm model (mg g^{-1})
q_e	adsorption capacity at equilibrium (mg g^{-1} or mol g^{-1})
q_{exp}	equilibrium values obtained from the experiment (mg g^{-1})
q_o	maximum adsorption capacity of the adsorbent (mg g^{-1})
q_s	Dubinine-Radushkevich (D-H) model constant (mol g^{-1})
q_t	adsorption capacity at time t (mg g^{-1})
$q_t^{'}$	quantity of the total contaminant adsorbed (mg)
R	universal gas constant (kJ mol^{-1} K^{-1})
R_c	radius of curvature for the channel geometry (m)
r_c	diameter of the smallest drawn circle surrounding the particle, m
r_p	diameter of the largest drawn circle possible inside the particle, m
Re	Reynolds number ($=\frac{d_H U \rho}{\mu}$) (-)
R_U	relative uncertainties (-)
$\%R$	removal percentage (%)
SD	standard deviation (-)
St	Stanton number ($=\frac{Nu}{\mathrm{Re\ Pr}}$ or $\frac{Nu}{De\ \mathrm{Pr}}$) (-)
S_U	standard uncertainties (-)
ΔS^0	standard entropy change (kJ mol^{-1} K^{-1})
T	temperature (K or °C)
t	sampling time (min)
t'	required time for 50% adsorbate breakthrough (min)
t_b	breakthrough time (min)
T_{inlet}	inlet temperature (K)
t_m	mean residence time (min)
T_{outlet}	outlet temperature (K)
ΔT_{inlet}	inlet temperature difference (K)
ΔT_{outlet}	outlet temperature difference (K)
ΔT_{lm}	log mean temperature gradient (-)
t_t	total time of flow (min)

U	actual velocity (m s^{-1})
V	volume of contaminated solution taken for each batch (dm^3)
$V_{Channel}$	total volume of the channel (m^3)
V_B	total volume of the bed (m^3)
V_{eff}	total treated volume of the fluid (ml)
V_p	volume of the pores (m^3)
v_p	volume of the single-particle (m^3)
V_{tot}	total volume of the liquid-liquid mixture (m^3)
V_T	total volume of the packed bed (m^3)
V_t	volume of fluid passed at time t (ml)
V_{void}	total void volume of the packed bed (m^3)
v_s	superficial velocity (m s^{-1})
w	individual channel width (m)
We	Weber number ($= \mathrm{Re}Ca = \frac{d_H \rho U^2}{\sigma}$) (-)
We'	modified Weber number ($= DeCa = \frac{d_H \rho U^2}{\sigma}\sqrt{\frac{d_H}{2r_c}}$) (-)
x	two-phase mass quality (-)
x_w	liquid phase mole fraction of water (-)
x_o	liquid phase mole fraction of organic (-)
x_i	i^{th} component of variables (-)
$\bar{x}$	mean value of the components (-)
X	Martinelli parameter (-)
y	overall mole fraction (-)
y_w	overall mole fraction of water (-)
y_o	overall mole fraction of organic (-)
z_w	vapor-phase mole fraction of water (-)
z_o	vapor-phase mole fraction of organic (-)
$[\,]$	the concentration of each species (mol L^{-1})

Greek symbols

ρ	density (kg m^{-3})
ρ_b	the density of the packed bed (kg m^{-3})
β	phase volumetric fraction (-)
μ	viscosity (N-s m^{-2})
σ	surface tension (N m^{-1})
ζ	entrance loss coefficient (-)
θ	dimensionless time (-)
θ_r	residence time inside the packed bed (s)
τ	tortuosity of the packed bed (-)
ε	Polanyi potential in case of the adsorption (-)
ε_{eff}	effective porosity (-)
ε_{total}	total porosity (-)
α	holdup (-)
ϕ	two-phase friction multiplier (-)
ϕ_s or ϕ_p	sphericity of the packing material (-)
λ	the correlation coefficient (-)
$\%E$	percentage extraction (-)
$\%S$	percentage stripping (-)
$\%\eta$	percentage efficiency (-)
χ	volumetric flow fraction or holdup (-)
σ_v	variance (min)
σ_θ	dimensionless form of the variance (-)
Δ_{LMC}	log mean concentration difference (mol L^{-1})

Subscripts

a or w	water or aqueous phase
b	fixed bed properties
C	curved channel

m	multiphase flow or mixture flow through the unpacked channel
m,p	multiphase flow through the packed channel
o	organic phase
p	particle or packed channel
S	straight channel
s	single phase
s,o	single-phase organic
s,p	single-phase flow through the packed channel
s,w	single-phase water
g	gas or air or vapor phase

Chapter 1

Background and Formulation of the Research

The scarcity of pure water is a universal problem and a threat to all living creatures and human beings. With the increasing population, the era of industrialization started to fulfill the rising demand. The effluent released from the industries pollutes the natural sources of the water bodies continuously. Therefore, proper treatment of the effluent is necessary before their release to the environment. There are various kinds of separation processes like physical separation, evaporation, distillation, extraction, adsorption, crystallization, and membrane separation. According to their difficulty level, those are arranged in Fig. 1.1. The physical separation processes are easy enough; however, these techniques decrease resource utilization, increasing the time of operation. The main disadvantages of the evaporation processes are the excessive capital, energy, and maintenance costs, the massive size of apparatus, enhanced temperatures requirement, corrosion problems, and scaling or foaming problems. Another disadvantage of the evaporation process is that it is harder to scale up; having an advantage of solar power employment is easier with the evaporation. The distillation process is one of the most effective and efficient separation process, which is easy to implement and produce highly pure fractions of the mixtures. The disadvantages associated with these processes are the higher cost of operation along with the operational hazards as the high heat energy is required to operate the distillation columns. It can also come up with the pollution of rivers, streams, and other bodies of water, by improper handling of the wastewater from the refineries.

The distillation processes are applicable to the mixtures when the boiling points of the components of the mixtures are quite different from one another (at least 30 $^{\circ}$C). Solvent extraction is the second most important separation technique used in the industries for purification of some materials or removal of some unwanted materials from the others present in a solution. Solvent extraction is an attractive separation technique in the separation of non-volatile solutes from aqueous solutions,

separation of heat-sensitive materials such as antibiotics (e.g., penicillin that is recovered from fermentation broth by using the solvent butyl acetate), separation of the close boiling component mixtures.

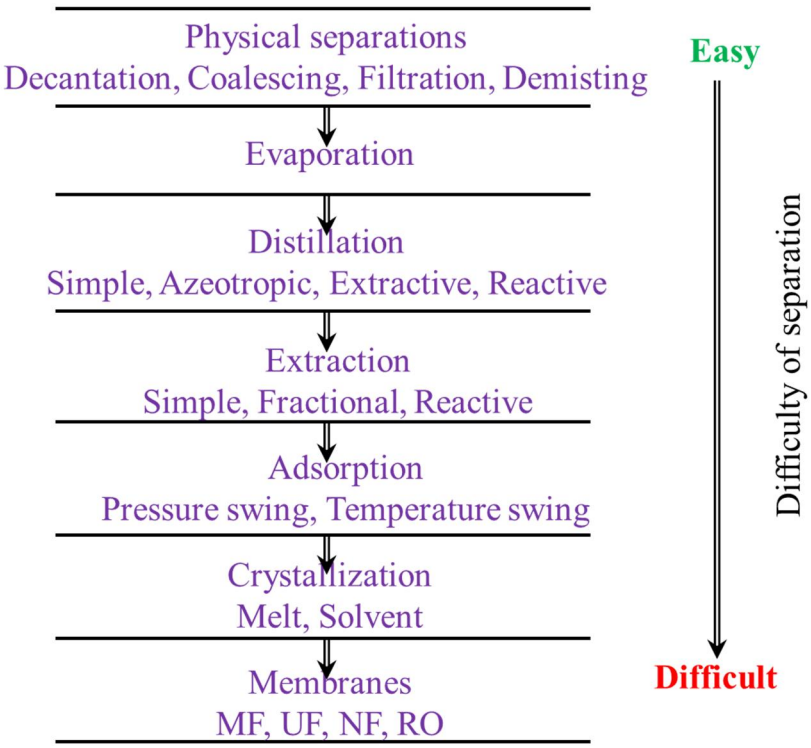

Fig.1.1. Different types of separation processes.

The other most important use of solvent extraction for most of the chemicals, petrochemicals, refineries, and other industries is the removal of organics from their waste effluent. Solvent extraction is a simple process, and no complex equipment is required. It is a time-saving process with higher screening and higher throughput, which eliminates environmental hazards. Controlled recovery can be achieved with large selectivity and flexibility.

The disadvantages associated with the extraction processes are the emulsion formation, loss of compounds, laborious, pre-concentration steps required in some cases. Hence, the selection of proper solvent and the extractant are very much essential to achieve fruitful utilization of that process. The next separation process is the adsorption, which is widely used by the industries. In that process, the atoms, ions, or molecules from a gas, liquid, or dissolved solid adhere to a surface,

creating a film of the adsorbate on the adsorbent. Adsorption is purely a surface phenomenon and maybe faster or slower depending on the physical and chemical characteristics of the adsorbent materials. The main advantages of the adsorption process are easy operation, low cost, high performance, and operated under the high pH range. The effectiveness of the adsorption process depends on the type of substance to be eliminated. The substances, which acquired a high molecular weight, and the low water solubility, are adsorbed, preferably with the active carbon. The disadvantages associated with that process are the weak selectivity during separation, and it may create a waste product when the adsorbates are not separable, or the regeneration of the adsorbent materials is not possible in a simple way after the adsorption. In the crystallization process, the pure crystals of the wanted materials are formed from a super-saturated solution upon cooling from a higher temperature. The heat-sensitive materials can be safely purified by this method, but some impurities may intact inside the agglomerated crystals, and the liquid requires being refined for further use. An accurate control system is required for controlling the heating and cooling rate to obtain the wanted product increases the process cost. Membrane processes can be used in the separation and purification of a huge variety of materials across a wide range of industries. These processes can function effectively at low temperatures with no phase changes involved. Microfiltration and ultrafiltration processes are efficient for the fractionating of the particle species according to their sizes. However, the processes are liable to the membrane fouling, decreasing the permeate flux, which may require expensive cleaning and regeneration. The membranes made by the shear sensitive materials may be damaged at the high flow rates, generally used in the cross-flow operations. Moreover, if the manufacturing process of the membrane is not controlled precisely, the membrane with the wide pore size distribution may results, which gives the poor separation performance. Keeping in mind, the previously stated advantages and disadvantages of the separation processes, in the present context, the attentions are provided on the modification and intensification of the extraction and adsorption processes, which are utilizing extensively by the industries.

In recent years, micro- and milli-channel technologies have attracted considerable attention for the process intensification in the transport devices. Millichannel has the potential to overcome the shortcomings associated with large-scale equipment through the reduction of analyte and reagent volumes. Millichannels are also amenable to gentle and high throughput cell handling. Miniature

channels are used by various industries for their process application or making products. There is a significant pressure loss for the flow through the miniature channels due to the wall shear, and the boundary layer flow. Therefore, the amount of energy consumption is high enough for supplying sufficient pressure by the pumps or other devices to maintain the flow through the miniature channels. Appropriate channel design with lower energy consumption is a challenge to researchers and engineers.

Various designs of the miniature channels are available for heat transfer and pressure drop study, but they are mainly designed and investigated for the single-phase liquid flow. Therefore, the extensive study is required for the liquid-liquid two-phase flow, which is used in the microchannel-based extraction process. The researchers are targeting to make appropriate microchannel devices for liquid-liquid extraction in rectangular geometry, instead of a cylindrical channel (Priest et al., 2011).

1.1. Advantages of the mini-channels for the separation processes

(i) Higher separation efficiency due to higher surface to volume ratio with small process volume and holdup
(ii) Extremely short response times considerably simplifying process control
(iii) Can handle a large heat and mass fluxes
(iv) Safe environment for hazardous or toxic chemicals during the process
(v) The same % of separation occurred with the use of very less space
(vi) No strict limit in size reduction or expansion of plant components since any production capacity is achievable by means of parallel operation
(vii) Vast improvements in energy efficiency, mechanical agitators or rotors are not required
(viii) Safety, reliability, and scalability are the other advantages

Therefore, the researchers and engineers are struggling to make a design of such mini-channel geometry so that it can be used industrially with the consumption of less power having higher separation efficiency.

1.2. Applications of the mini-channels in industries

The advantages of the use of mini-channel devices made them indispensable for their applications in the following industries for a variety of purposes.

(i) Pharmaceutical and fine chemicals producing industries (Sun Pharmaceutical Industries Ltd., Mumbai; Lupin Ltd., Pune; etc.)

(ii) Sensors and actuators producing industries (Mettler Toledo India Pvt. Ltd., Mumbai; Bosch, Karnataka; etc.)

(iii) Micro mixer and microreactor producing industries (Amar Equipments Pvt. Ltd., Mumbai; Chemito Technologies Pvt. Ltd., Maharashtra; etc.)

(iv) Micro-heat exchangers or heat sinks producing industries (Pranav Bikas (India) Pvt. Ltd., Pune; Sapa Extrusion India Pvt. Ltd., Karnataka; etc.)

(v) Gas processing industries (Oil and Natural Gas Corporation Ltd., Gujarat; Gas Authority India Ltd., Madhya Pradesh; etc.)

(vi) Drinks processing industries (Hindustan Coca-Cola Beverages Pvt. Ltd., Haryana; PepsiCo India, Haryana; etc.)

(vii) Pesticides and toxic chemicals producing industries (Insecticides (India) Pvt. Ltd., Jammu & Kashmir; Bayer Crop Science, Maharashtra; etc.)

(viii) Microchips and electrical equipment producing industries (Advanced Micro Devices, California; Maxim Integrated, California, etc.)

The efficiencies of the separation or transport processes in mini-channel geometries depend on the hydrodynamic characteristics of the flow inside the channels, which also depend on the pressure drop and other operating variables. Therefore, the pressure drop is one of the most important design parameters for designing heat and mass transfer equipment, especially in channel-based equipment for the process intensification. Hence, a comprehensive understanding of pressure drop and the flow hydrodynamics during the liquid-liquid flow through the mini-channel is of considerable practical importance. In the current context, the rectangular milli-channel geometries are used for the hydrodynamics and transport (mass and heat) studies for the single-phase as well as the two-phase flows (Fig. 1.2).

It is known to all that any kind of transport process between the two immiscible phases (like the extraction process) depends on the extent of mixing of the phases inside the devices. The packed bed provides a higher surface area to interact (catalyst packing), along with the higher interfacial mixing between the phases at the detrimental of the higher-pressure drop. Hence, the millichannel devices were packed with an inert material (medium size red sand), and the mass and heat transport studies were performed along with their relative hydrodynamic characteristics.

The corresponding packed channels used in this study are shown in Fig. 1.3. The experimental results revealed the fact that the packed channel geometries are more efficient to mass transport (extraction) as the mass transfer resistance is negligible than the unpacked channels (Mondal and Majumder, 2018c). Whereas, the serpentine packed channels are more efficient to heat transport than the packed straight channels (Mondal and Majumder, 2020).

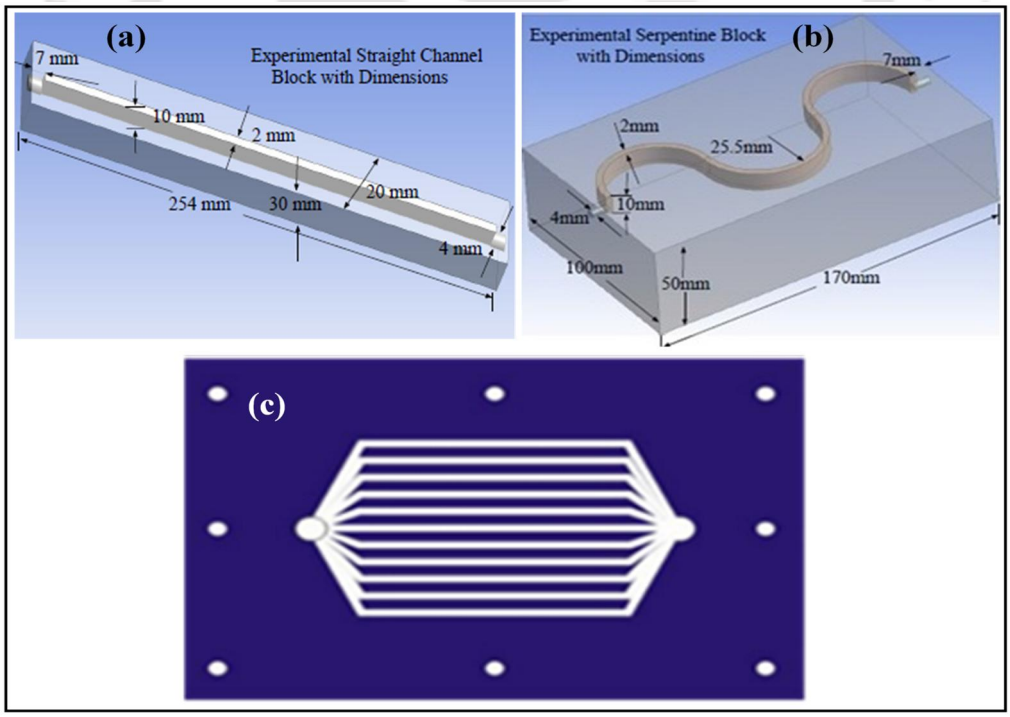

Fig. 1.2. Unpacked channel geometries (a) straight channel, (b) serpentine channel, and (c) parallel straight multichannel.

However, miniature devices found to be lacking in industrial applications by means of large production and high throughput, which required a numbering-up approach in terms of

multichannel devices (Saber et al., 2010; Yue et al., 2010). The parallelized milli- or micro-multichannel geometries are more effective than their series (Kockmann, 2007). The multi-millimetric channels can be used for the heat and mass transfer applications for their intense mixing and intensified transport properties (Guo et al., 2018).

In the case of the fabrication of the millichannel based adsorption devices, the inert packing materials should be replaced by an active one. In that concern, it was difficult to select an efficient active material amongst so many. Activated carbons are universally used by the industries and also experimented by the researchers for the adsorptive separation processes due to its high surface area and low cost. Adsorption is a surface phenomenon, mainly depends on the surface area and active sites present on the surface of the adsorbent. The generation of higher surface area and the active sites depend on the selection of the precursor materials, and the activating agent, the activation process, and the process parameters employed.

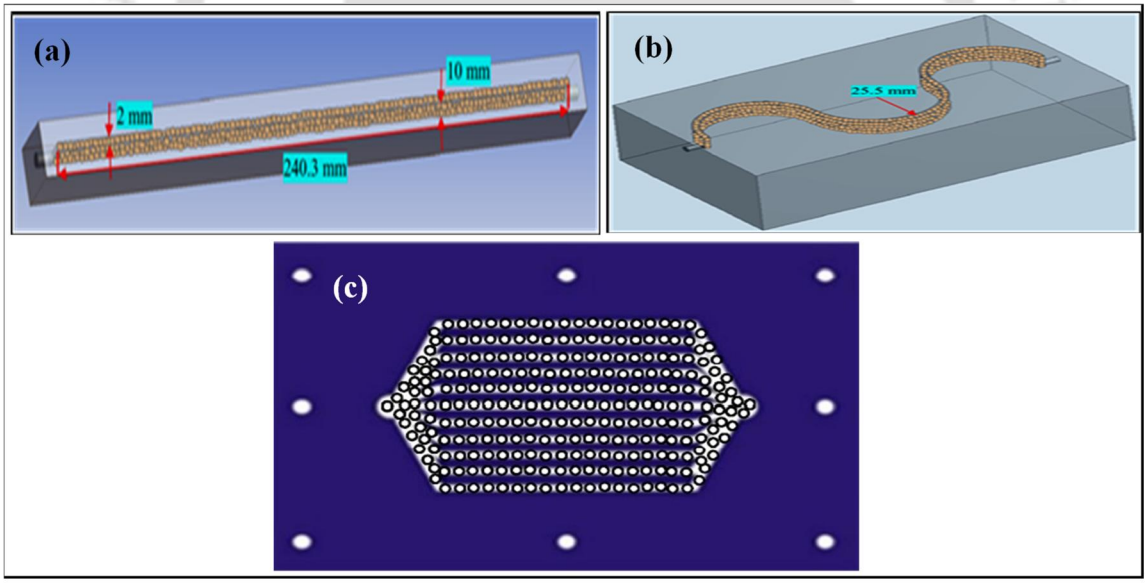

Fig. 1.3. Packed channel geometries (a) straight channel, (b) serpentine channel, and (c) parallel straight multichannel.

Most of the researchers performed the experiments in batch mode. However, to fulfill the increasing demand of the society, a continuous mode of operation was necessary beyond the batch process. The adsorption process mainly being a physical phenomenon. It requires a longer time to

reach the adsorption equilibrium, which made it improper to use as the adsorbent inside a millichannel based packed bed device, as the residence time of the adsorbate molecules or ions inside the small bed was very low. So, the surface modification or the changes of adsorbent materials were may be the solutions. The surface modification by the surfactant may change the point of zero charge (PZC) values and the surface charge of the adsorbent, preferring the higher adsorption of particular adsorbate molecules depending on their charges, as shown in Fig. 1.4 (Ntakirutimana et al., 2018).

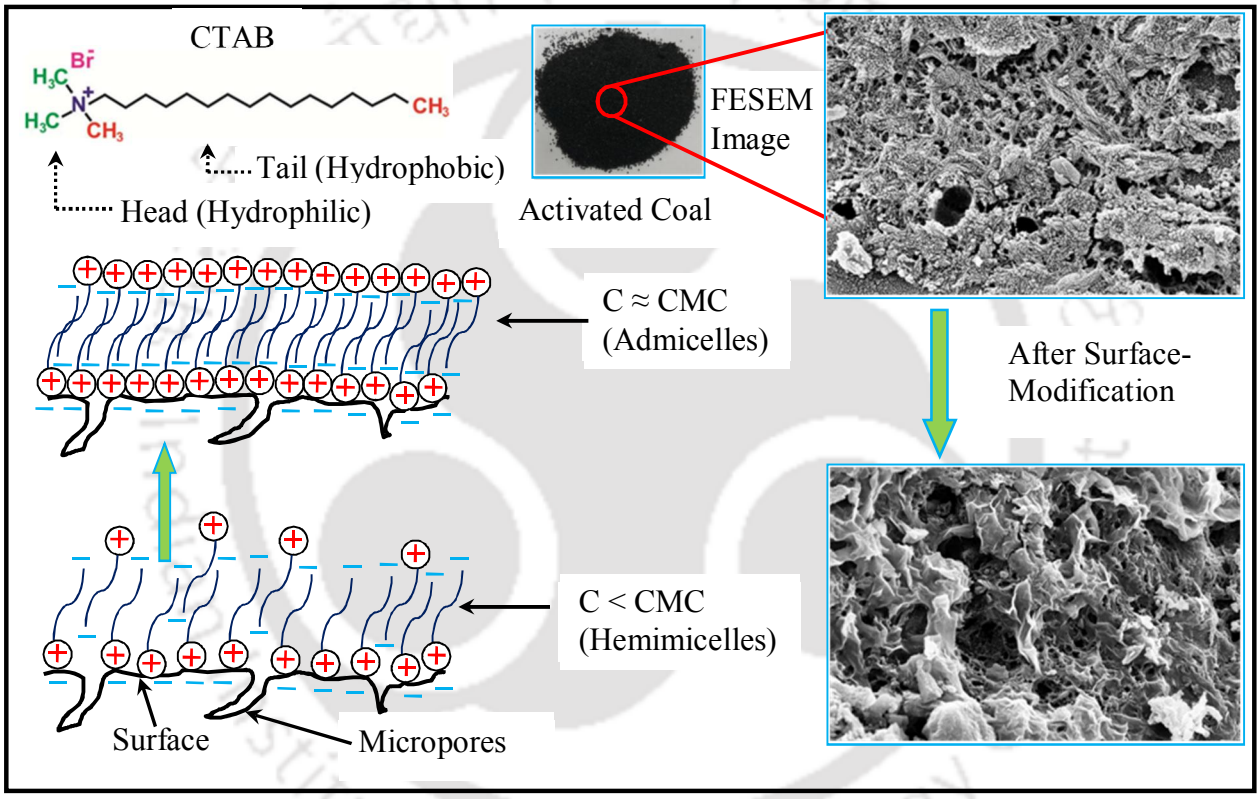

Fig. 1.4. Surface modification of the activated carbon by the use of surfactant (Ntakirutimana et al., 2018).

However, the surface modification increases the adsorption capacity of the activated carbon; it is not sufficient to be used as the adsorbing material in a millichannel-based adsorption device with respect to its equilibrium time. Then the only way was left to achieve the goal was to go for the graphene-based composite materials forgetting about the cost. According to Sang et al. (2017), the silver nanoparticle deposited reduced graphene oxide (RGO) high catalytic activity.

The graphene-based materials provide high surface area for the adsorption along with the high surface functionality susceptible to the better adsorption by ionic interactions. It can also take part in π-π interactions providing higher efficiency and capacity to the process. The composite material responded well enough with respect to the adsorption capacity and equilibrium time (the equilibrium reached within 3.0 min). Therefore, the adsorption studies were performed in a rectangular millimetric multichannel-based packed bed device (packing material: functionalized reduced graphene oxide coated glass beads), and the hydrodynamics of flow and the residence time distribution (RTD) studies. The fabricated devices were efficient in the continuous separation processes, which were demonstrated in the subsequent chapters.

Now, from the above discussion, it is not clear that what type of contaminants are focused on separating from the mainstream using the extraction or adsorption techniques. According to the world health organization (WHO), the heavy metals are the water pollutants after a certain limit. The contamination of these metal ions is increasing day by day due to the improper handling of the effluents from their respective industries like metal polishing, leather, fertilizer, and battery making industries. In the present study, the attention was given mainly on the one major heavy metal pollutant copper (Cu^{2+}). Moreover, some attention was given on the adsorptive separation of an organic pollutant like naproxen ($C_{14}H_{14}O_3$, a nonsteroidal anti-inflammatory drug). The literature reviews for the overall studies have been shown in the subsequent chapters.

1.3. The objectives of the overall study

Based on the present status of the research, the experimental investigations and analysis were done on the following objectives:

(i) Hydrodynamics (Flow pattern, holdup of the organic phase, pressure drop) of liquid-liquid flow through the millichannels in packed and unpacked conditions

(ii) Mixing characteristics of fluids in millichannels and its analysis, and development of the models

(iii) Heat transport and entropy analysis in the rectangular millimetric channels in packed and unpacked conditions

(iv) Efficacy of the packed and unpacked millichannels as the metal ions extraction and stripping devices

(v) Synthesis and characterization of the efficient graphene-based nanocomposite material, and its utilization for the adsorptive transport

(vi) Adsorptive separation of water contaminant in millichannel based packed bed device

1.4. Significance of the work

Liquid-liquid flows through rectangular straight and serpentine channels in both packed and unpacked conditions have potential application in the mass and heat transfer in micro and millichannel based extraction or heat exchanger devices for process intensifications. In addition, the single-phase, as well as the two-phase gas-liquid flows through the millimetric multichannel devices packed with the interacting material, have potential applications in the mass transfer like adsorption, extraction, and any other reactive or exothermic processes for the process intensifications. The study of the hydrodynamics and the mixing characteristics inside the device are essential, for designing an efficient transport device since the mixing efficiency highly affects the parameters like transport rate, product yield, and selectivity. The parallel multichannel devices are more efficient than the series of channels of the same dimension. The multi-millimetric channels provide the fast mixing effect and the compact transport properties.

The local entropy generation is one of the determining factors for the performances of the thermal devices. Hence, the effect of flow properties and the pressure drop on the local entropy generation rate for the same driving force (temperature difference) is required to study in straight and serpentine channel-based packed thermal devices. The effect of the variations of the particle diameter and the fluid mixtures on the entropy generation are also essential to study.

The heavy metal, having some toxic nature, and also water pollutants after a specific limit are inimical in living creatures. So, maximum recovery of heavy metal (e.g., copper) from industrial waste effluent by a process intensification would be economically and environmentally beneficial. Solvent extraction is the second most important and attractive separation technique used in the industries for purification of some materials and the separation of some non-volatile solutes from the others present in a solution. Researchers and engineers are interested in miniaturization for the

chemical process intensifications. The development of micro and millichannel based liquid-liquid extraction device is gaining importance. Hence, the extraction parameters are required to optimize for the separation of metal from an aqueous phase using suitable extractant diluted in benzene through a rectangular serpentine packed and unpacked millichannel.

In recent years, reduced graphene oxide (RGO) has been attracted to the researchers for its excellent electrical, thermal, mechanical, and optical properties. Moreover, RGO and its nanocomposites are broadly used as excellent adsorbents and applied in water purification processes. Adsorption being a surface phenomenon not only depends on the surface area and micropores present, but it also depends on the surface characteristics of the adsorbing materials. The 2D planes of RGO with the attachment of fewer amounts of functional groups provide high surface area and bonding sites susceptible to adsorption. The delocalized π-electrons present in RGO have energetic binding efficiency towards the harmful pollutants, which makes it a rapid adsorbent for the removal of contaminants. The effects of operating variables on adsorption kinetics and equilibrium isotherms are required to investigate and analyze appropriately in the current context.

For designing an efficient adsorption device, the study of the hydrodynamics and the mixing characteristics inside the device are essential since the mixing efficiency highly affects the parameters like transport rate, product yield, and selectivity.

Hence, the present study may be valuable to the researchers, designers, and industries for further research, design, and the process execution of the multichannel-based millimetric transport devices, based on the present studies.

1.5. Thesis outline

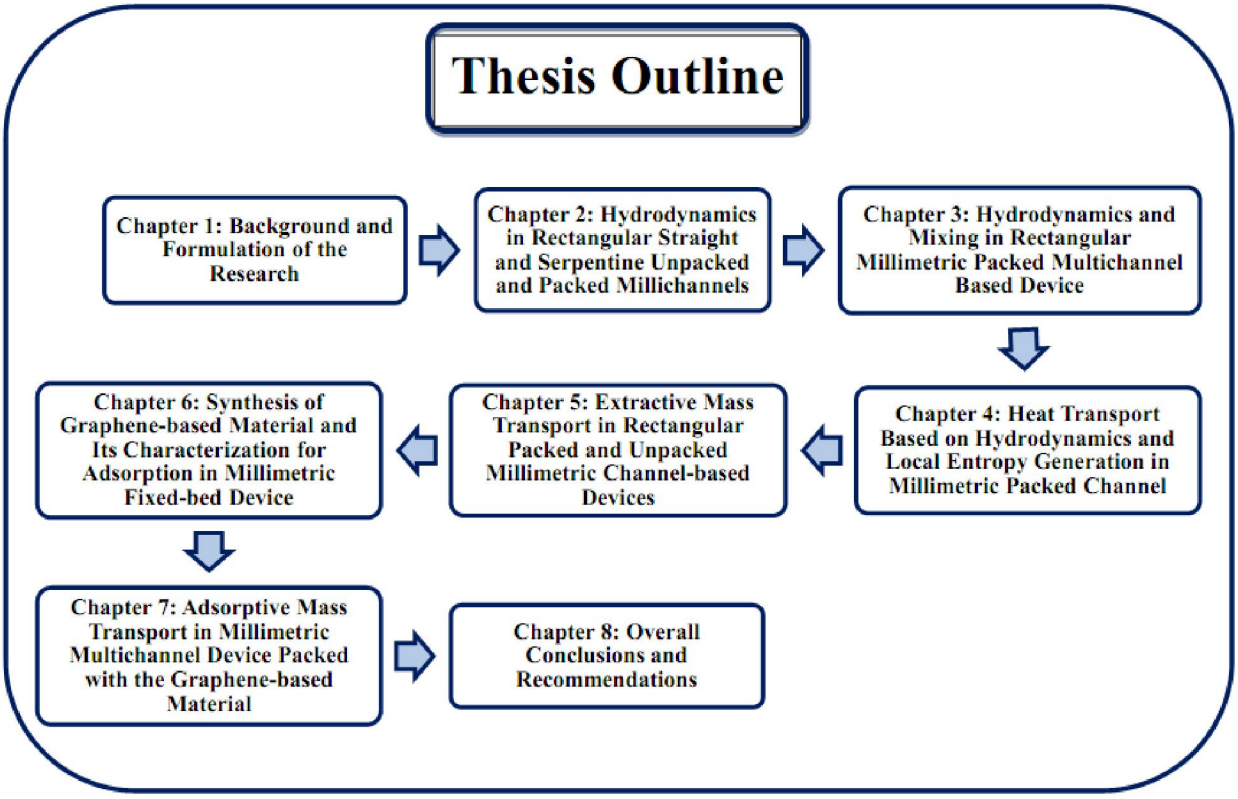

Chapter 2

Hydrodynamics in Rectangular Straight and Serpentine Unpacked and Packed Millichannels

Hydrodynamics and pressure drop studies are essential to understand the flow statistics in designing any kind of heat and mass transfer devices. The transport characteristics can be enhanced by changing the flow behavior or initiating the turbulence inside the device at the expense of higher-pressure drop. The turbulence may be generated by either increasing the volumetric flow rate/velocity of the fluid or by incorporating the packing material or by introducing curvature in the flow geometry. In the present context, the single and two-phase flow hydrodynamics and pressure drop in rectangular millimetric (a) straight channel and (b) serpentine channel geometries were studied.

2.1. Introduction

Millichannel technologies with the liquid-liquid flow have attracted considerable attention in compact heat exchangers and mass transfer devices in chemical industries. Liquid-liquid extraction is an important mass transfer operation in the chemical, food processing, and pharmaceutical industries. The essential oil from the natural sources dissolved in alcoholic water can be extracted by an organic phase by continuously passing the two-phases through the packed channel. The packed channel facilitates high retention time of phases and intense mixing, which benefits the higher extraction rate. Mary et al. (2008) studied the liquid-liquid extraction through a microfluidic device using water and butanol. Seibert and Fair (1988) studied the influences of phase flow rates, the direction of solute transfer, and phase dispersion in spray and packed liquid-liquid extraction column. They developed a fundamental model to account dispersed phase holdup, and mass-transfer efficiency with two widely different chemical systems: toluene/acetone/water and 1-butanol/succinic acid/water. Esmaeilzadeh et al. (2014) studied the spearmint oil extraction in a packed bed using SC-CO_2 and its analysis by mathematical modeling. Sahu et al. (2016), studied

the overall extraction performance characterizing as a function of the residence time of the phases and the hydrodynamics. They reported that the micro-channel gives a superior extraction performance in the slug flow regime as compared to the well-mixed batch system, although both have comparable sizes of the dispersed phase. They stated that "This is attributed to the strong internal circulations induced by shear in the slug flow regime". Priest et al. (2011) demonstrated microfluidic solvent extraction (SX) of metal ions from particle-laden aqueous solutions as an alternative to conventional solvent extraction for the extraction of Cu^{2+} using 2-hydroxy-5-nonylacetophenone. They reported that the microfluidic method is also able to access extraction kinetics for particle-laden systems. As the microchannels are closed systems, there is greater potential for recycling of volatile liquids and reduced human exposure to potentially hazardous chemicals. Darekar et al. (2016), studied single-stage solvent extraction of HNO_3 using TBP in dodecane in microbore tubes. The experiments showed that the configuration of the microbore tube is efficient in the extraction of the solute. Kriel et al. (2015), studied the extraction of integrating scrubbing, and stripping process in the channel based microfluidic solvent extraction (micro SX) chips using a secondary amine as the extractant. They reported the real time-efficiency of the phase disengagement. Tsaoulidis and Angeli (2015) studied the effect of channel size on the mass transfer characteristics of liquid-liquid plug flow for capillaries with an internal diameter ranging from 0.5 to 2 mm. The extraction of $\{UO_2\}^{2+}$ ions from nitric acid solutions into TBP/IL mixtures, relevant to spent nuclear fuel reprocessing, was studied for different residence times, dispersed phase fractions, and mixture velocities. They reported that extraction efficiencies dependent on channel size. The packed column is widely used in oil purification and recovery in oil industries, as well as a small sand-packed column is also used in the laboratories (Gudina et al., 2013; Bigui et al., 2018). Varteressian and Fenske (1936) studied liquid-liquid extraction performance in a packed column. Later on, Moorhead and Himmelblau (1962), optimized the operating condition of a packed liquid-liquid extraction column.

Hence, these attracted considerable attention to both academics and the process industries for the chemical process intensification. Moreover, the rectangular channel geometries have extensive applications in nuclear engineering. Through the reduction of reagent volume utilization, the millichannel based equipment minimizes the imperfections incorporated with the large-scale equipment. High heat and mass transport rate and easy controlling are other advantages of

millichannel. The introduction of packing materials into the rectangular channel again enhances the transport processes increasing the chaos inside the system. Pressure drop calculations are necessary to design the millichannel based transport apparatus, for the process escalation. The benefits of the rectangular channel over the conventional circular channels are higher pressure drop increasing higher ease of molecular transport processes (especially for specific reactive mass transport or heat transport processes) with low fabrication cost (Mondal and Majumder, 2018b). The miniatured rectangular channels attracted great attention to the researchers (Ide and Matsumura, 1990; Warrier et al., 2002; Cavallini et al., 2005; Zhao et al., 2006; Santoso et al., 2006; Hwang and Kim, 2006; Ide et al., 2007; Field and Hrnjak, 2007; Fries et al., 2008; Kim et al., 2011; Wang et al., 2013; Xing et al., 2013; Choi and Kim, 2014; Mansour et al., 2015; Li and Hibiki, 2017a). They performed various kinds of experiments to understand the geometric effects on the hydrodynamics of mainly air-water or refrigerant systems.

Incorporation of curvature into the rectangular channel specifies the importance of Dean flow inside the noncircular ducts (Norouzi and Biglari, 2013), causing the high efficiency of mixing, resulting in higher mass transfer. Another way to enhance the transport processes is the incorporation of packing materials inside the rectangular curved ducts.

The information on pressure drop is significant to understand the energy dissipation, modeling the system, and the assessment of the performance of the heat and mass transport equipment. The estimation of pressure drop is necessary to control the flow rates of the fluids to avail the required quantity of heat and mass transport. Pressure drop calculation for the fluid flows through the channel is required to install an appropriate pump for pumping the fluids. Inside the flow systems, the mixing of two-phase is mostly dependent on the pressure drop of the system, on which mass and heat flux depend. Therefore the comprehensive understanding of pressure drop during liquid-liquid flows through millichannel is of considerable practical importance.

Several models interpret the two-phase flow systems in channels of different geometry for a long time. The separated flow model was proposed by Lockhart and Martinelli (1949) for the gas-liquid systems through pipes in a horizontal orientation in the form of friction multipliers. Chisholm

(1967), gives the correlation for the friction multipliers. There are several models available to interpret the two-phase flow systems in unpacked pipes and channels, as summarized in Table 2.1.

Blasius (1913) proposed a friction factor relation with Reynolds number for fully developed turbulent flow through the circular tubes as well as rectangular channels. Shah and London (1978), Harnett and Kostic (1989), Abdelall et al. (2005), Hrnjak and Tu (2007) used the same relation to determine the friction factors for laminar flow through rectangular channels. Leon and Roman (1984), Bhatti and Shah (1987) also proposed the friction factor correlations depending mainly on the Reynolds number along with the aspect ratio of the channel. Bhatti and Shah (1987) introduced the effect of viscosity of the fluids on the friction factor. Phillips (1990) categorized the friction factor for both developing and developed flow regimes through rectangular microchannel. Churchill (1977) developed a friction factor correlation for flow through the rectangular channel. Li and Hibiki (2017b) used the same correlation developed by Churchill (1977) for both laminar and turbulent flow through a rectangular channel. Flows through curved microchannel were investigated by Hua and Yang (1985), Wang and Liu (2007). They (Hua and Yang, 1985; Wang and Liu, 2007) developed the pressure drop and friction factor relationship as a function of Reynolds number and Dean number.

The inclusion of packing into the rectangular channel enhances the transport phenomena at the cost of increasing pressure. In the year 1952, Ergun, (Ergun, 1952; McCabe et al., 2005) proposed the first pressure drop model applicable for the packed bed, which is the combination of Kozeny–Carman equation and Burke-Plummer equation (McCabe et al., 2005). The proposed equation by Ergun is applicable for the laminar and turbulent flow due to the applicability of the above two prescribed equations (McCabe et al., 2005) in the specified fields. Many researchers (Feng, 1989; Foumeny et al., 1993; Eisfeld and Schitzlein, 2001; Montillet et al., 2007) attempted to modify the Ergun equation depending on various kinds of geometries and applications of their packed units. In a packed unit, friction factor relations for the spherical particles are given by Rose (1945), Rose and Rizk (1949), Kürten et al. (1966), Hicks (1970), Tallmadge (1970), Lee and Ogawa (1974), Watanabe (1989), Montillet et al. (2007), and Ozahi et al. (2008). Though the equations are developed for the spherical particles with sphericity 1.0, these are compared to our experimental data, and a new correlation is generated for packed bed using packing of sand of sphericity 0.85.

Table 2.1. Summary of the previous work on the frictional pressure drop for the flow through the unpacked channel.

Authors	Fluids in consideration	Geometry and Orientation of the channel	Correlations
Lockhart and Martinelli, 1949	water, oils, hydrocarbons	Circular pipes, Horizontal	$\left(\frac{dP}{dz}\right)_m = \left(\frac{dP}{dz}\right)_w \phi_w^2$ where $\phi_w^2 = 1 + \frac{C_w}{X} + \frac{1}{X^2}$; $X = \sqrt{\left(\frac{dP}{dz}\right)_w / \left(\frac{dP}{dz}\right)_o}$, $\left(\frac{dP}{dz}\right)_w = f_w' \frac{2G^2}{d_H \rho_W}(1-x_O)^2$ and $\left(\frac{dP}{dz}\right)_O = f_o' \frac{2G^2}{d_H \rho_o} x_o^2$
Chisholm, 1967	Gas-liquid and Vapor-liquid	Circular pipes, Horizontal	$\left(\frac{dP}{dz}\right)_m = \left(\frac{dP}{dz}\right)_w \phi_w^2$, $\phi_w^2 = 1 + \left(X^2 - 1\right)\left[Bx_o^{\frac{2-n}{2}}(1-x_o)^{\frac{2-n}{2}} + x_o^{2-n}\right]$ where n = 0.2, $X^2 = \left(\frac{dP}{dz}\right)_W / \left(\frac{dP}{dz}\right)_O$
Moriyama et al., 1992	R113-N_2	Rectangular channel, d_H = 0.014 –0.195 mm, Horizontal	$C = 21\left[1 - \exp\left(-0.358/Lo^*\right)\right]$ where $Lo^* = \left(\frac{\sigma_m}{g(\rho_w - \rho_o)}\right)^{0.5} / d_H$ $0.014 \le d_H \le 6.25$ mm; $\mathrm{Re}_w \le 2000$ and $\mathrm{Re}_o \le 2000$
Mishima and Hibiki, 1996	Water-air	Mainly vertical and horizontal round tube,	$C = 21\left[1 - \exp\left(-0.319 d_H\right)\right]$

		also applicable in a horizontal rectangular duct. d_H = 1.0 – 4.0 mm.	
Mishima et al., 1993	Water-air	Rectangular channel, d_H = 2.08 – 8.89 mm, Vertical upward	$C = 21\left(1 - e^{-319 d_H}\right)$ using the Lockhart-Martinelli model
Yang and Webb, 1996	Refrigerants, R-12	Rectangular channel, d_H = 1.56 – 2.64 mm.	$\left(\frac{dp}{dz}\right)_m = -0.87\,\mathrm{Re}_{eq}^{0.12} f_w'\left(\frac{G_{eq}^2 \rho_w}{d_H}\right)$ where $\mathrm{Re}_{eq} = \frac{G_{eq} d_H}{\mu_w}$, $\mathrm{Re}_{eq} > 2500$; $G_{eq} = G\left[(1-x_o) + x_o\left(\frac{\rho_w}{\rho_o}\right)^{0.5}\right]$
Tran et al., 2000	R- 134a, R-12, and R-1 13	Rectangular channel, d_H = 2.397 mm, Horizontal	$\left(\frac{dP}{dz}\right)_m = \left(\frac{dP}{dz}\right)_w \phi_w^2$ with $\phi_w^2 = 1 + \left(4.3X^2 - 1\right)\left[Lo^* x_o^{0.875}(1-x_o)^{0.875} + x_o^{1.75}\right]$ $Lo^* = \left(\frac{\sigma_m}{d_H^2 g(\rho_w - \rho_o)}\right)^{0.5}$ and $X^2 = \frac{\left(dP/dz\right)_w}{\left(dP/dz\right)_o}$
Lee and Lee, 2001	Water-air	Rectangular channel, d_H = 0.78 – 6.67 mm, Horizontal	$C = A\lambda^p \psi^q \mathrm{Re}_{eq}^r$ using the Lockhart-Martinelli model

			$\lambda = \frac{\mu_w^2}{\rho_w \sigma_m d_H}$ and $\psi = \frac{\mu_w j}{\sigma_m}$; $\mathrm{Re}_{eq} = Lo^*$ $A = 6.833\times10^{-8}$, $p = -1.317$, $q = 0.719$ and $r = 0.557$
Lee and Mudawar, 2005	Water-R134a	Rectangular channel, d_H = 0.349 mm, Horizontal	For laminar liquid and laminar vapor: $C_w = 2.16\mathrm{Re}_w^{0.047} We_w^{0.6}$ For laminar liquid and turbulent vapor: $C_w = 1.45\mathrm{Re}_w^{0.25} We_w^{0.23}$ and $We_w = \frac{G_w^2 d_H}{\rho_w \sigma_w}$ using the Lockhart-Martinelli model
Qu et al., 2003	Water-air	Rectangular channel, d_H = 0.23 mm, Horizontal	$C = 21(1-e^{-319 d_H})(0.00418G + 0.0613)$
Yue et al., 2004	Nitrogen-water	Rectangular microchannel, d_H = 0.33 mm and 0.53 mm, Horizontal	$C_w = 0.185 X^{-0.0942} \mathrm{Re}_w^{0.711}$
Chen et al., 2007	Air-water	Rectangular channel, d_H = 3 – 4.5 mm, Horizontal	For laminar flow region: $\phi_w = 0.2485\, A_c^{-0.355} \left\{ U_w / (g d_H)^{0.5} \right\}^{-0.233} \mathrm{Re}_w^{(3/8)}$

			For turbulent flow region: $\phi_w = 0.848 A_c^{-0.145} \left\{ \left(U_w + U_o\right) / U_w \right\}^{0.425} \mathrm{Re}_w^{(3/8)}$
Yue et al., 2008	CO_2-water	Rectangular microchannel, d_H = 0.68 mm, 0.40 mm and 0.20 mm, Horizontal	$\phi_w^2 = 0.217 \beta^{-\frac{1}{2}} \mathrm{Re}_w^{0.3}$ $^{*}\phi_w^2 = 0.217 \beta^{-\frac{1}{2}} \mathrm{Re}_w^{0.3}$; applicable for the high aspect ratio.
Kawahara et al., 2009	Nitrogen-water	Rectangular microchannel, d_H = 0.25 mm, Horizontal	$C_w = 3.87 Bo^{0.19} \mathrm{Re}_w^{-0.01} We_w^{0.01}$ where $Bo = \frac{\Delta \rho g d_H^2}{\sigma_m}$
Sun and Mishima, 2009	R123, R134a, R22, R236ea, R245fa, R404a, R407C, R410a, R507, CO_2, water, and air.	Rectangular Channel & tube, d_H = 0.506 – 12 mm, Horizontal	For Re_w<2000 and Re_o<2000: $\left(\frac{dp}{dz}\right)_m = \phi_w^2 \left(\frac{dp}{dz}\right)_w$; $\phi_w^2 = 1 + \frac{C_w}{X} + \frac{C_w}{X^2}$; $C_w = 26\left(1 + \frac{\mathrm{Re}_w}{1000}\right)\left[1 - e^{\left(\frac{-0.153}{0.8+0.27 Lo^*}\right)}\right]$ For $\mathrm{Re}_w \geq$ 2000 and $\mathrm{Re}_o \geq$ 2000: $\left(\frac{dp}{dz}\right)_m = \phi_w^2 \left(\frac{dp}{dz}\right)_w$; $\phi_w^2 = 1 + \frac{C_w}{X^{1.19}} + \frac{1}{X^2}$

Li et al., 2010	12 fluids	Circular and rectangular channel, d_H = 0.148-3.25 mm, Horizontal	$Bo \le 1.5$; $C = 11.9 Bo^{0.45}$ $1.5 < Bo \le 11$; $C = 109.4(Bo\mathrm{Re}^{0.5})^{-0.56}$
Qin et al., 2012	Water-steam	Rectangular channel, d_H = 3.81 mm, Vertical	$C = 209.5\mathrm{Re}_m^{-0.29}(1-x_o)^{1.38}$
Zhang et al., 2010a	Liquid-gas and liquid-vapor flow	Modified the correlation given by Moriyama et al., 1992	For adiabatic liquid-gas flow: $C_w = 21\left[1-e^{\frac{-0.674}{Lo^*}}\right]$ For adiabatic liquid-vapor flow: $C_w = 21\left[1-e^{\frac{-0.142}{Lo^*}}\right]$
Present work	Liquid-liquid (water-toluene)	Rectangular straight channel, d_H = 3.33 mm, Horizontal	$\left(\frac{dp}{dz}\right)_m = \phi_w^2\left(\frac{dp}{dz}\right)_w$; $\phi_w^2 = 1.7796(\mathrm{Re}_w Ca_w)^{0.3638} = 1.7796(We_w)^{0.3638}$ and $C_w = 1.2375\left(\mathrm{Re}_w Ca_w\right)^{0.4854} = 1.2375\,(We_w)^{0.4854}$
Present work	Liquid-liquid (water-toluene)	The rectangular serpentine channel, d_H = 3.33 mm, Horizontal	$\left(\frac{dp}{dz}\right)_m = \phi_w^2\left(\frac{dp}{dz}\right)_w$; $\phi_w^2 = 7.594(De_w Ca_w)^{0.0398} = 7.594(We_w')^{0.0398}$ and $C_w = 4.92(De_w Ca_w)^{0.07912}$

From the literature, it is observed that very little attention has been given to the rectangular straight and serpentine channels in both the micro and macro domains. It is noticed that in the case of the circular channel as well as the rectangular channel, the investigations are performed using mostly the air-water or gas-liquid systems (Kreutzer et al., 2005; Warnier et al., 2010). Most of the experiments have been carried out using air-water systems even though they used the rectangular curved channel. According to our knowledge, very few experiments have been performed to scrutinize the pressure drop of liquid-liquid flow through the packed and unpacked rectangular millichannels in both straight and serpentine geometries. The liquid-liquid two-phase flows have advantageous applications in the mass and heat transfer operations like micro and millichannel based extraction and heat exchanger devices. The present study aims to investigate the effect of operating variables on the pressure drop and friction factor for the liquid-liquid flow through the rectangular straight and serpentine millichannel with and without packing, and the development of general empirical models to interpret the results based on experimental results. The present work also aims to generate the empirical correlations to elucidate the experimental results and the local entropy generation rate in straight channel geometry. In industries, it would be the new beginning of the introduction of the rectangular packed bed for the process intensification for physical and reactive mass transfer.

2.2. Theoretical background

Frictional pressure drop for two-phase liquid flow can be expressed as

$$\Delta P_f = \Delta P_T - \Delta P_a - \Delta P_g - \Delta P_{inlet} \tag{2.1}$$

where ΔP_f is the two-phase frictional pressure drop, ΔP_T is the total pressure drop, ΔP_a is the pressure drop due to the acceleration of fluid velocity, ΔP_g is the gravitational pressure drop. In the present study, the ΔP_a term of Eq. (2.1) is nullified as the inlet and outlet velocities are considered to be the same. ΔP_{inlet} is the sum of contraction or expansion and entrance loss at the inlet which can be expressed as

$$\Delta P_{inlet} = (K + \zeta)\frac{\rho U^2}{2} \tag{2.2}$$

where ρ is the density of the fluid, U is the actual velocity of the fluid at the contraction or expansion zone, K is the contraction or expansion coefficient which is assumed to be equal to 0.5

and ζ is entrance loss coefficient and holds the value nearly equal to 1.31 (Martin, 1974). Gravitational effect on the pressure drop is expressed as Froude number

$$Fr = \frac{U}{\sqrt{gd_H}} \tag{2.3}$$

where g is the gravitational acceleration, and d_H is the hydraulic diameter. Though the horizontal flow is encountered in the following context, the density ratio of the two fluids greater than one results in the slip between the phases which incorporated the effect of Froude number or gravity or hydraulic jump (Sun et al., 1992; Woods and Hanratty, 1999; Kuntoro et al., 2015; Pressure Loss Calculations, http://fekete.com.). In that case, when the velocity of the phases increases, a wave is generated at the interphase of the two fluids, and at high velocity, the waves break down and form bubbles or slugs inside the flow field. Surface waves can form under the influence of gravity even in the absence of air and in the horizontal flow condition when the densities of the fluids are different. If there is stratified flow due to density difference is considered the film inversion (Estimation of Flow Patterns, http://14.139.172.204/nptel.) at the bends is also influencing the mixing or formation of bubble and slug in the experimental channel. At that condition, there is a density difference present along the vertical line through the channel that demands the effect of gravity or Froude number. In the present study, the density ratio is 1.154, and the Froude number for the mixture ranges from 0.99 – 5.18 makes the incorporation of Froude number in case of mixed-phase flow significantly. The Froude number ranges for the hydraulic jumps mainly for air-water flows are Weak jump ($1 < Fr < 2.5$), Oscillating jump ($2.5 < Fr < 4.5$), Steady Jump ($4.5 < Fr < 9$) and Strong jump ($Fr > 9$) (Rautenbach and Katz, 2010). The liquid densimetric Froude number is given by the Eq. (2.4) (Crowe, 2005).

$$Fr_d = \left(\frac{\rho_S}{\Delta\rho g d_H} \right)^{0.5} U_s \tag{2.4}$$

The hydraulic jump is also observed in single-phase flow in laboratory channels (Crowe, 2005; Gas pockets and hydraulic jumps in pressurized pipelines, https://www.google.co.in/url.). In the present study, the Froude number for the single-phase flow ranges from 0.39 – 3.02, which also implies some effect on the fluids flow. In oil and gas stations, they keep Froude number always less than 0.30 using submerged outlets to avoid air entrainment and ensure undistributed flow without pulsations. The present study handles taking an air open outlet, so some entrainment might

be there, causing hydraulic jump and accounting higher Froude numbers. Moreover, there might be the release of some dissolved gas or vapor of its own or some air pocket at the joining of the pressure sensors. As a result, the Froude number is significant in both single and mixed-phase flows in the present study. Depending on the above effects, various types of flow patterns are observed in the liquid-liquid two-phase flows through the rectangular channels (Zhao et al., 2006; Cherlo et al., 2010; Tsaoulidis et al., 2013). The hydraulic diameter of the rectangular channel was calculated as

$$d_H = \frac{2wh}{(w+h)} \tag{2.5}$$

where w and h are the width and height of the rectangular channel, respectively. The calculations were done based on the actual velocities of the phases, depending on the flow distribution inside the channel. Actual velocities are calculated from the volume fraction of each phase inside the channel by measuring the volumetric flow rate of each phase. The friction factor is a dimensionless representation of the viscous pressure drop due to the effect of the viscosity of the fluid near the surface of the channel. As per the Fanning equation, the Fanning friction factor can be represented by

$$f' = \frac{d_H \Delta P_f}{2\rho U^2 L} \tag{2.6}$$

In the case of the packed bed, U is replaced by U/ε_{eff}. ε_{eff} is the porosity of the packed channel. From the experimental results, it was observed that with changing velocities of the phases, the pressure drop changes. Therefore, the pressure drop mainly depends on the Reynolds number (*Re*). In the case of a rectangular curved channel, the radius of curvature affects the flow creating the Dean effect. As a result, the Dean number (*De*) replaces the Reynolds number (*Re*) for the flow through the rectangular curved channel. Friction factor depends on another two significant dimensionless numbers, such as a capillary number (*Ca*) for milli and micro-channel and Froude number (*Fr*) for mainly the fluids of different densities (Dimensionless numbers in fluid mechanics, https://en.wikipedia.org/wiki/.). According to the viscous-capillary paradox, which is an apparent contradiction, the structure of Darcy's law is that of a viscous law, but typical capillary numbers of 10^{-6} - 10^{-3} indicate a capillary dominated behavior (Cense and Berg, 2009). In the viscous-inertia regime, the capillary number is higher than 10^{-3}. When one studies a two-phase

flow system, the calculation of the capillary number is very much important to understand the factors that are affecting the flow behavior. The critical value of the capillary number depends on the geometry of the packing material and other fluid properties. The internal circulation within the slugs may arise depending on the physical properties of the fluids and the prevalent operating conditions (Kashid et al., 2005; Chaoqun et al., 2013). In fluid dynamics, capillary pressure is the pressure between two immiscible fluids in a thin tube or channel resulting from the interactions of forces between the fluids and solid walls of the tube. The capillary pressure can serve as both an opposing and driving force for fluid transport. In the present study, both phase water and toluene are also the wetting phase with the channel wall and the sand particles. So, there must be some capillary pressure due to the wetting characteristics. The Dean number, capillary number, Froude number, and friction factor for single and two-phase flows through the unpacked channel are represented as follows:

Dean number for the single-phase is defined as

$$De_s = \mathrm{Re}_s \sqrt{\frac{d_H}{2R_c}} \tag{2.7}$$

where

$$\mathrm{Re}_s = \frac{d_H \rho_s U_s}{\mu_s} \tag{2.8}$$

$$Ca_s = \frac{\mu_s U_s}{\sigma_s} \tag{2.9}$$

$$Fr_s = \frac{U_s}{\sqrt{g d_H}} \tag{2.10}$$

and

$$f_s' = \frac{d_H}{2\rho_s U_s^2} \frac{\Delta P_f}{L} \tag{2.11}$$

Dean number for the mixture phase is defined as

$$De_m = \mathrm{Re}_m \sqrt{\frac{d_H}{2R_c}} \tag{2.12}$$

where

$$\mathrm{Re}_m = \frac{d_H \rho_m U_m}{\mu_m} \tag{2.13}$$

$$Ca_m = \frac{\mu_m U_m}{\sigma_m} \tag{2.14}$$

$$Fr_m = \frac{U_m}{\sqrt{g d_H}} \tag{2.15}$$

$$U_m = U_{s,o}/\alpha_o + U_{s,w}/\alpha_w \tag{2.16}$$

and

$$f_m^{'} = \frac{d_H}{2\rho_m U_m^2}\frac{\Delta P_f}{L} \tag{2.17}$$

where the subscripts '*s*' and 'm' represent the single- and the two-phase mixture flow. Hydraulic diameter (d_H) is represented by the Eq. (2.5). Similarly, the three dimensionless numbers and the friction factor for the packed channel are calculated using the following relations:

Dean number for the single-phase flow through the packed channel is defined as

$$De_{s,p} = \mathrm{Re}_{s,p}\sqrt{\frac{d_H}{2R_c}} \tag{2.18}$$

where

$$\mathrm{Re}_{s,p} = \frac{d_p \rho_s (U_s/\varepsilon_{eff})}{\mu_s} \tag{2.19}$$

$$Ca_{s,p} = \frac{\mu_s (U_s/\varepsilon_{eff})}{\sigma_s} \tag{2.20}$$

$$Fr_{s,P} = \frac{(U_s/\varepsilon_{eff})}{\sqrt{g d_p}} \tag{2.21}$$

and

$$(f_s^{'})_p = \frac{d_p}{2\rho_s (U_s/\varepsilon_{eff})^2}\frac{(\Delta P_f)_p}{L} \tag{2.22}$$

Dean number for mixture flow through the packed channel is defined as

$$De_{m,p} = \mathrm{Re}_{m,p}\sqrt{\frac{d_H}{2R_c}} \tag{2.23}$$

where

$$\mathrm{Re}_{m,p} = \frac{d_p \rho_m (U_m/\varepsilon_{eff})}{\mu_m} \tag{2.24}$$

$$Ca_{m,p} = \frac{\mu_m (U_m / \varepsilon_{eff})}{\sigma_m} \tag{2.25}$$

$$Fr_{m,p} = \frac{(U_m / \varepsilon_{eff})}{\sqrt{g d_p}} \tag{2.26}$$

$$U_{m,p} = (U_{s,o} / \varepsilon_{eff} \alpha_o + U_{s,w} / \varepsilon_{eff} \alpha_w) \tag{2.27}$$

and

$$(f_m^{'})_p = \frac{d_p}{2\rho_m (U_m / \varepsilon_{eff})^2} \frac{(\Delta P_f)_p}{L} \tag{2.28}$$

where the subscripts *'s,p'* represents the single-phase flow, and *'m,p'* represents the two-phase flow through the packed channel.

The mixture properties of the fluids are calculated from the following equations

$$\rho_m = \rho_w \alpha_w + \rho_o \alpha_o \tag{2.29}$$

where ρ_m, ρ_w and ρ_o are densities of the mixture, aqueous phase (water), and the organic phase (toluene), respectively. The symbols α_w and α_o denote the volume fractions of the aqueous phase and organic phase, respectively. According to Olimans (1976), the viscosity of the mixture is calculated by

$$\mu_m = \mu_w \alpha_w + \mu_o \alpha_o \tag{2.30}$$

where μ_m, μ_w and μ_o are viscosities of the mixture, aqueous phase, and an organic phase, respectively.

***The surface tension of the liquid-liquid mixture*:** The liquid mixture of two components, water and organic liquid (Toluene), is assumed to be in equilibrium with its own vapor. The liquid-vapor interface is treated here in the manner of Bakker (Bakker, 1928), Verschaffelt (Verschaffelt, 1936) and Guggenheim (Guggenheim, 1957) as a thin phase, separated from the bulk liquid and vapor by two dividing surfaces which enclose the region of property variation normal to the interface (Eberhart, 1966). The bulk liquid phase is assumed to have mole fractions x_w for water and x_o for organic liquid (Toluene), while the bulk vapor phase has mole fractions z_w and z_o for water and organic liquid, respectively. Although the interfacial or surface phase has a composition that varies in a direction normal to the dividing surfaces, it is assigned overall mole fractions y_w and y_o for

water and organic liquid, respectively, which satisfy the material balance conditions for the system. For component water in the mixture, for example, this condition is $n_w = n_L x_w + n_s y_w + n_v z_w$ where n_w is the total number of moles of water in the three "phases," of the mixture and n_L, n_s, and n_v are the number of moles of water and toluene in the liquid, surface, and vapor phases, respectively. Since, in general, n_s and n_v are very much smaller than n_L, it will be assumed that x_w is essentially equal to the overall mole fraction of water, $n_w/(n_w+n_0)$. The surface tension of liquid mixture, σ_m, is then assumed to be a linear function of the surface layer mole fraction, which is expressed as Eberhart (1966). In the present study, we are considering the liquid-liquid surface tension separately with its individual liquid-vapor. Based on the individual surface tension of the liquid with its vapor, the surface tension of the liquid-liquid mixture is calculated according to Eq. (2.31).

$$\sigma_m = y_w\sigma_w + y_o\sigma_o = \frac{(\alpha_w V_{tot}\rho_w)/M_{w,w}}{(\alpha_w V_{tot}\rho_w)/M_{w,w} + (\alpha_o V_{tot}\rho_o)/M_{w,o}}\sigma_w + \frac{(\alpha_o V_{tot}\rho_o)/M_{w,o}}{(\alpha_w V_{tot}\rho_w)/M_{w,w} + (\alpha_o V_{tot}\rho_o)/M_{w,o}}\sigma_o \quad (2.31)$$

where σ_m, σ_w and σ_o are surface tensions of the mixture, aqueous phase, and the organic phase, respectively. V_{tot} is the total volume of the liquid-liquid mixture, M_w is the molecular weight of the liquid (g mol^{-1}).

The average particle diameter ($d_{p,eff}$), effective porosity of the packed bed (ε_{eff}), and sphericity of the packing material (ϕ_p) are the three important parameters to govern the hydrodynamics in the packed bed. The average particle diameter is determined by the sieving method. In this method, a series of sieve sets have been used, and the particles are screened by the sieve of sizes ASTM No. 35 and 40 (U.S. Standard). Based on the average particle diameter according to the literature (USGS Wentworth Grain Size Chart, https://www.scribd.com/.), the sand is classified as medium sand. The average particle size, as per the present experiment is 462 µm. The effective porosity is calculated by using the Eq. (2.32) (Total Porosity and Effective Porosity, http://www.informit.com/.)

$$\varepsilon_{eff} = \frac{V_p}{V_B} \quad (2.32)$$

where V_p is the volume of the pores, and V_B is the total volume of the bed. According to Zou and Yu (1995) for $d_H/d_p > 3.95$, the effective porosity ε_{eff} is defined as

$$\varepsilon_{eff} = 0.372 + 0.002\left(e^{15.306 d_p/d_H} - 1\right) \quad (2.33)$$

The effective porosity (ε_{eff}) of a packed bed can also be calculated by the correlation (Eq. (2.34)) developed by Klerk (2003), which is valid in the range of $2 \leq d_H/d_p \leq 19$. The correlation can be expressed as

$$\varepsilon_{eff} = 0.373 + 0.917 \exp\left(-0.824 \frac{d_H}{d_p}\right) \tag{2.34}$$

The effective porosity estimated experimentally in the present work is 0.36, which is within 6% error based on the predicted value calculated by the Eqs. (2.33) and (2.34). The effective porosity is estimated by dividing the pore volume with the total volume of the channel. From the literature, it is seen that the porosity range of the medium sand is 0.22 to 0.49 (Morris and Johnson, 1967; Ribeiro et al., 2010; USGS Wentworth Grain Size Chart, https://www.scribd.com/.). Therefore, the present experimental data of porosity is justified for the sand particle taken for the experiment. The third and another important parameter for the packed bed is the sphericity of the packing materials. The sphericity is calculated by using the modified procedure of Krumbein and Sloss (1963). It is defined as the ratio of the diameter of the largest drawn circle possible inside the particle (r_p) to the diameter of the smallest drawn circle surrounding the particle (r_c) as shown in Fig. 2.1(a). A typical snapshot of the sand particle taken by Sony DSC-H400 Point and Shoot Camera is shown in Fig. 2.1(b).

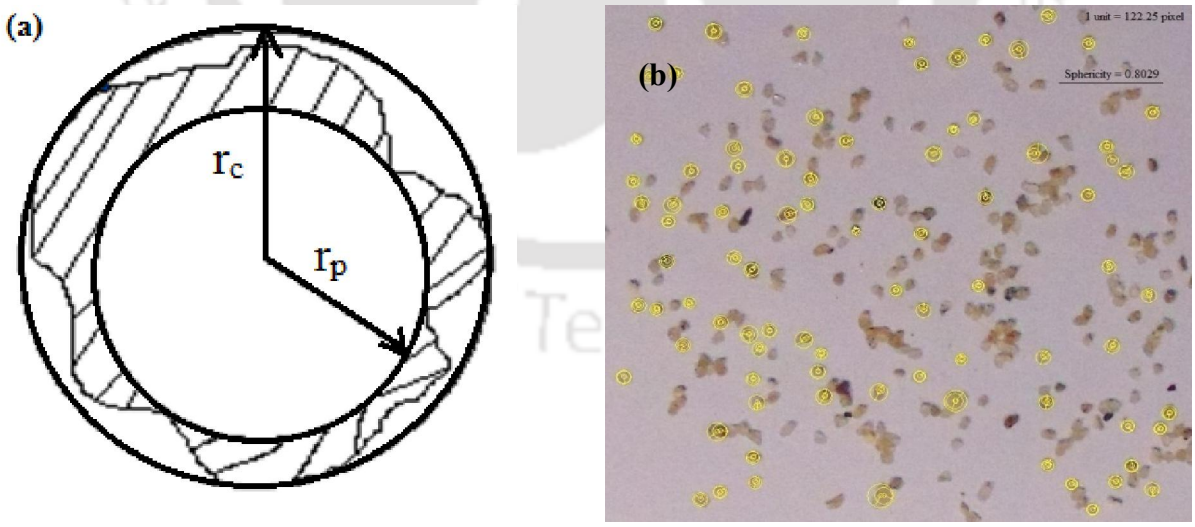

Fig. 2.1. Measurement of sphericity of packing materials: (a) schematic representation of sphericity, (b) typical pictorial analysis of particle by the image analysis software.

It is analyzed by Digimizer® 4 software. The mathematical form of sphericity of particle is expressed as

$$\phi_p = \frac{r_c}{r_p} \tag{2.35}$$

From the analysis, it is found that the sphericity of the particle is 0.80, which is within the range of 0.50 to 0.90 for natural sands reported by Cho et al. (2006). The volume fraction of each phase inside the channel was measured by the volumetric flow rate measurement process using a measuring cylinder (Borosil, 100 ml, Tolerance ±0.5 ml) and a stopwatch (Seiko digital stopwatch Cal. S056, Accuracy ±0.0012%).

The percentage error of the experimental and calculated values are determined by

$$\%\text{Error} = \left(\frac{\text{Experimental} - \text{Calculated}}{\text{Experimental}}\right) \times 100\% \tag{2.36}$$

Finally, the deviation of experimental results from the available correlations and newly generated correlations are analyzed by the root mean square deviation (RMSD) and mean deviation (MD) which are defined respectively as

$$RMSD = \left(\frac{1}{N}\sum\left[\left(\left|\frac{(\text{Experimental} - \text{Calculated})}{\text{Experimental}}\right|\right)^2\right]\right)^{0.5} \times 100\% \tag{2.37}$$

$$MD = \left(\frac{1}{N}\sum\left|\frac{(\text{Experimental} - \text{Calculated})}{\text{Experimental}}\right|\right) \times 100\% \tag{2.38}$$

2.3. Experimental methods and materials

A simplified experimental setup diagram of the straight channel geometry is represented in Fig. 2.2. A schematic layout of the experimental setup of the serpentine geometry is shown in Fig. 2.3. Both the setup consist of two centrifugal pumps which provide the flows of aqueous and organic phases, transforming into one mixed-flow passing through a 'Y' connector before entering the test section. Inlet zone contains two rotameters, two control valves, two bypass lines along with another two control valves and two sets of the pressure sensor (PS100-2BAR and PS100-5BAR from Lutron Electronics, accuracy: 1% full-scale) connected with two pressure meters (Fisher Scientific Traceable™, accuracy: 1% full-scale +1 digit) just before the inlet point. The outlet zone contains one pressure sensor and a pressure meter of the above-specified model. Two pressure meters are

finally connected to the computers for data logging. The test section contains the rectangular straight and serpentine channel blocks, respectively, and a temperature sensor (Fisher Scientific TraceableLIVE^{TM}, accuracy: ±0.1 ℃) dipped in a constant temperature bath. The channels were 240 ± 0.3 mm long (L), 2 mm width (w), and 10 mm height (h) in case of the straight and serpentine channels. The radius of curvature (R_c) was 25.5 mm, for the serpentine channel geometry.

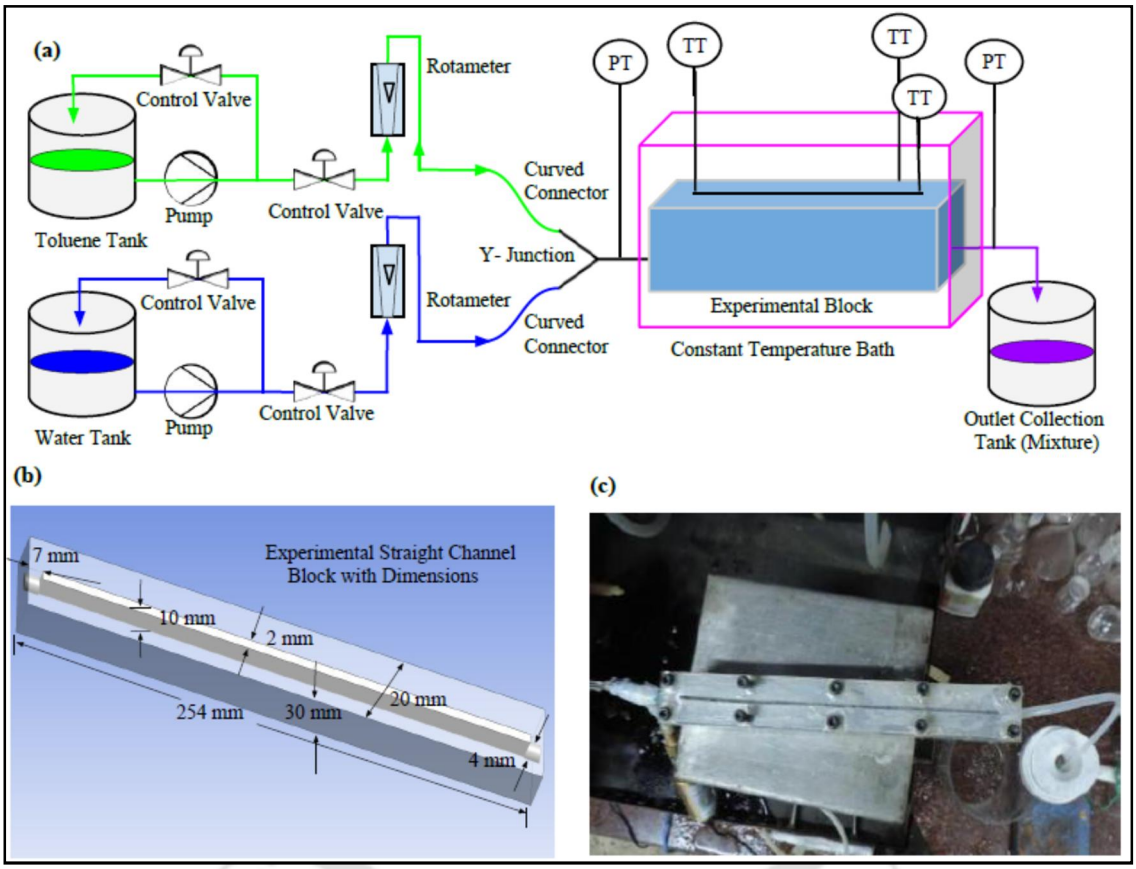

Fig. 2.2. Experimental setup details: (a) simplified diagram, (b) 3D perspective of the rectangular channel block, and (c) the illustrated view of the experimental channel (PT = Pressure transmitter, and TT = Temperature transmitter).

The whole experiment is conducted at a temperature of 25 ± 1 ℃ temperature. Medium red sand packing was used to fill the rectangular straight and serpentine channel blocks for making the packed beds. The physical properties of the systems measured at 25 ± 1 ℃ are shown in Table 2.2.

Table 2.2. The physical properties of the fluids, measured at 25±1 ºC.

Phases	Density (kg m^{-3})	Viscosity (Ns m^{-2})	Surface tension (N m^{-1})
Water	997.05	8.9×10^{-4}	7.2×10^{-2}
Toluene	864.00	5.6×10^{-4}	2.77×10^{-2}

The dimensions of the channel blocks are shown in the schematic diagram (Fig. 2.2 and Fig. 2.3). The pressure sensors and the temperature sensor are calibrated before the main experiment. The pressure sensors are calibrated with the help of a mercury manometer in which one side of the manometer was kept open to the air. A graduated cylindrical column of height 1.5 m is connected to the pressure sensor and the manometer at the same height from the datum level. The column is filled with water at a certain level and sets the pressure sensor reading as zero as per the initial manometer reading. After that, the water height of the column is increased, and the change in the manometer mercury level is noted down along with the pressure sensor reading.

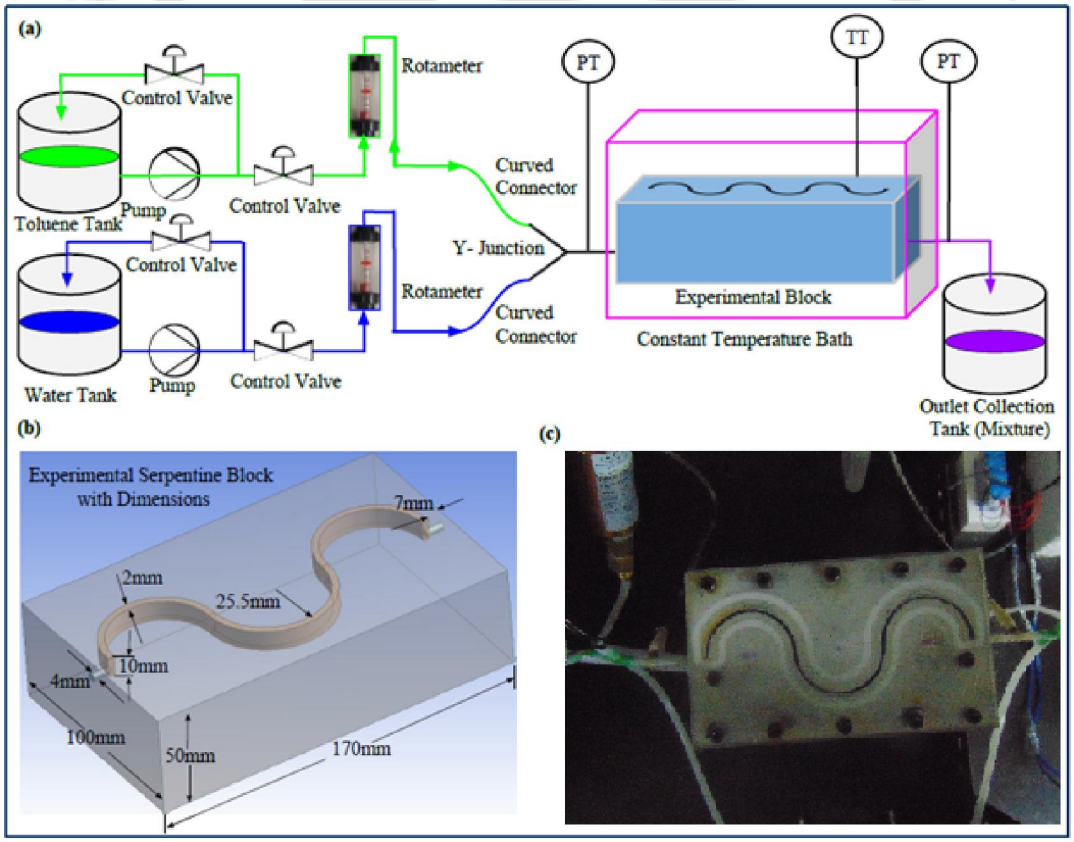

Fig. 2.3. Details of the experimental setup: (a) schematic diagram, (b) 3D view of serpentine channel block, and (c) pictorial view of the channel.

The temperature sensor is calibrated with the help of a TTI-10 high accuracy handheld thermometer by Isotech company (accuracy = ± 0.01 ℃), which is already calibrated by the primary standard platinum resistance thermometer. Both the temperature sensor (Accuracy = ± 0.1 ℃) and the thermometer are dipped in a constant temperature water bath. The densities, viscosities and surface tensions are measured by specific gravity bottle (ATICO Medical Pvt. Ltd., AM-90024, 100 ml), rheometer (Anton Paar, Physica MCR-301) and tensiometer (Kyowa Interface Science, DY-300) respectively.

Finally, the volumetric flow rate of the two-fluid mixtures is measured by collecting the sample for a particular time by measuring cylinder and a stopwatch. The volumetric flow rates are controlled and measured by the valves and the rotameters by changing one keeping the other fixed and vice versa. Average pressure drop for a particular mixture flow rate is noted by averaging 200 data points measured using pressure sensors at each flow rate. The volume fraction of each phase in the channel is calculated from the total mixed-phase volumetric flow rate and the volumetric flow rate of a single-phase for a particular set of flow conditions. At first, the total volume of mixtures was collected at the outlet at a particular flow condition for a time interval of 1 minute. As the two-phases are immiscible and their densities are different, they are separated out by gravity. The total volume of the two-phases and the volume of each phase were measured separately.

Then the volumes of the phases are divided by the time of collection to get the volumetric flow rate. The holdup of the particular phase was calculated separately as the ratio of the volumetric flow rate of the particular phase to the total volumetric flow rate of the mixture of the phases collected. Variation of the organic phase holdup with the aqueous phase volumetric flow rate for the straight channel is shown in Fig. 2.4. The organic phase holdup decreases with the increase of aqueous phase volumetric flow rate following a nonlinear relationship for both the channels, and the effect is higher in case of the packed channel (Fig. 2.4). Average pressure drops are recorded by averaging 200 sensor data for a single flow rate. The single-phase volumetric flow rate is used to measure the holdup of each phase in the channel for a specific set of flow conditions.
The uncertainty analysis for all experimental results are calculated based on the theory as given in **Appendix - I**.

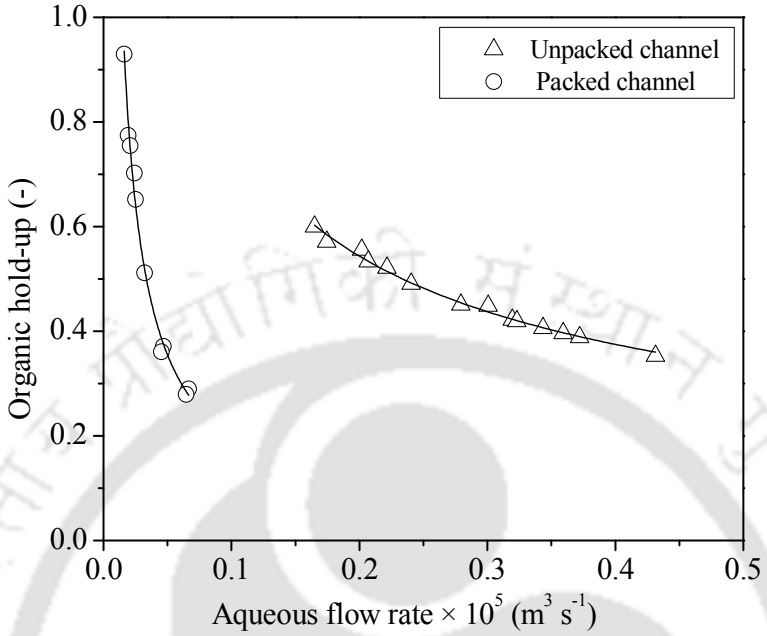

Fig. 2.4. Variation of the organic phase holdup with the aqueous phase volumetric flow rate.

2.4. Results and discussions

2.4.1. Variations of the frictional pressure drop and friction factor with the operating variables

2.4.1.1. Straight channel geometry

Frictional pressure drop is influenced by the flow rates of the phases. In the case of milli- or micro-channel Capillary number has an important impact, whereas gravity in terms of Froude number affects the water-toluene flow due to their differences in densities. The pressure drop varies with the variation of the above specified dimensionless parameters, as shown in Figs. 2.5(a) and 2.5(b) for single and two-phase flows, respectively. As shown in the Figs. 2.5(a) and 2.5(b), a sharp increase is observed in the case of the Reynolds number variation, which confirms the higher impact of Reynolds number on frictional pressure drop than the other parameters with the increasing phase velocities. The effect of the Froude number is insignificant for the single-phase flow. There always remains a slip velocity due to the density differences between the two-phases.

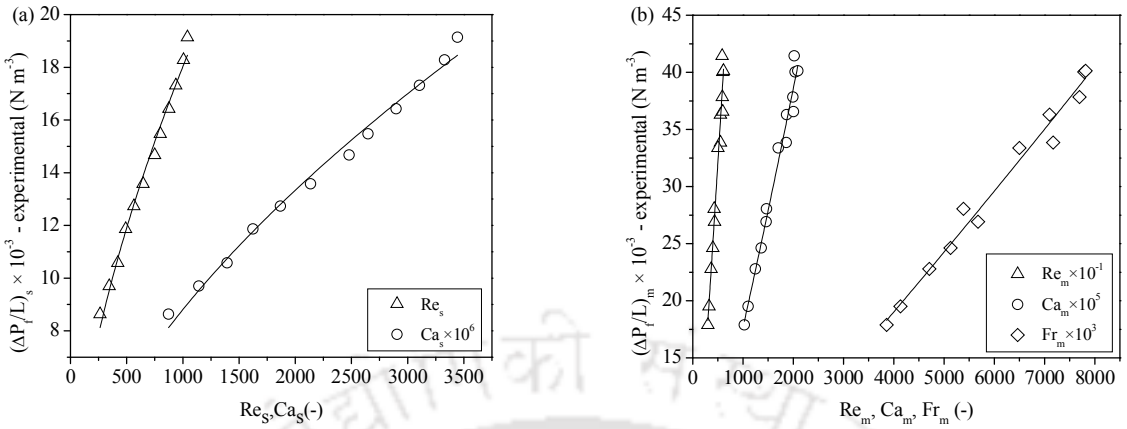

Fig. 2.5. Variation of frictional pressure drop with the dimensionless parameters for the flow through the straight unpacked channel: (a) single-phase flow and (b) two-phase flow.

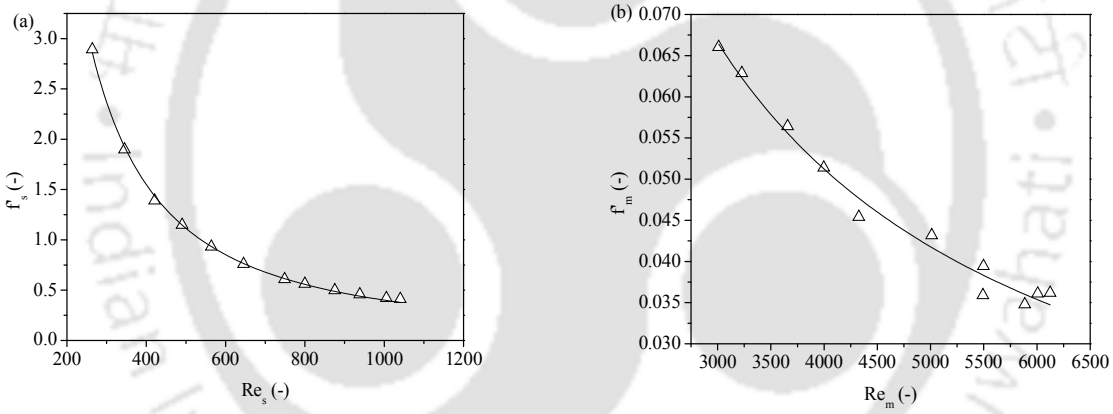

Fig. 2.6. Variation of friction factor with Reynolds number for the flow through the straight unpacked channel: (a) single-phase flow and (b) two-phase flow.

As a consequence, when the velocities of the fluids are increased, the fluid interphase becomes wavy. Very high velocities form bubbles or slugs with the breaking of the waves. At this condition, a density difference always persists along the vertical axis, which satisfies the effect of the Froude number significantly. The friction factor variation with the Reynolds number for the straight unpacked channel is shown in Figs. 2.6(a) and 2.6(b). The friction factor decreases with increasing Reynolds number (Figs. 2.6(a) and 2.6(b)). Higher Reynolds number for the water-toluene flow promotes the lower friction factor value than the single-phase flow. Reynolds' number has a

notable impact on the pressure drop and friction factor in the case of the packed millichannel. The frictional pressure drop inside the packed millichannel is also influenced by the Froude number as like the Reynolds number and the capillary number.

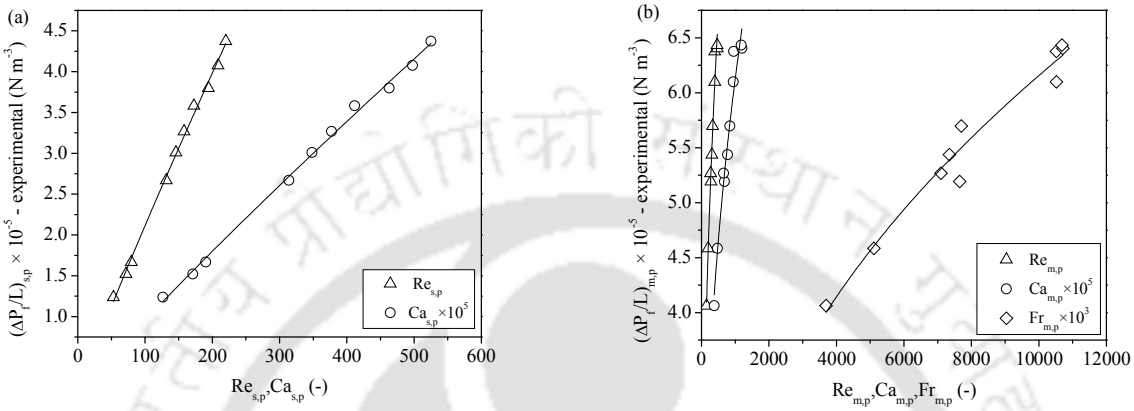

Fig. 2.7. Variation of the frictional pressure drop with the dimensionless parameters for the flow through the packed straight channel: (a) single-phase flow and (b) two-phase flow.

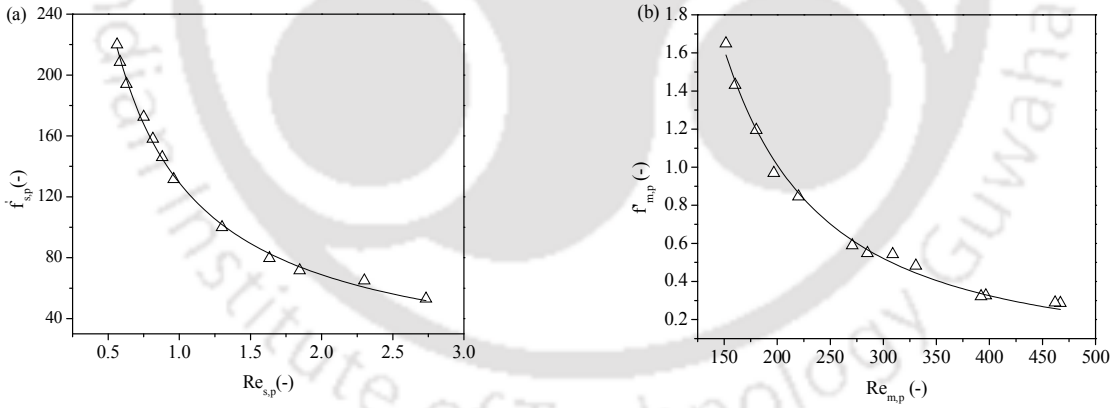

Fig. 2.8. Variation of the friction factor with the Reynolds number for the flow through the packed straightchannel: (a) single-phase flow and (b) two-phase flow.

The effect of the dimensionless parameters on the frictional pressure drop in the packed rectangular straight channel is shown in Figs. 2.7(a) and 2.7(b). The Reynolds number has a precious effect on the friction factor. The effect of the Reynolds number on the friction factor in the packed channel is shown in Figs. 2.8(a) and 2.8(b). Higher pressure drop and friction factor values are

observed in the packed millichannel (Fig. 2.7 and Fig. 2.8) than in the unpacked millichannel (Fig. 2.5 and Fig. 2.6).

2.4.1.2. Serpentine channel geometry

Frictional pressure drop depends on flow velocity. Flow velocity is directly influenced by the Reynolds number. Reynolds number increases with the increasing flow velocity. Dean number is considered to interpret the hydrodynamics in case of flow through the serpentine channel as the curvature effects generate secondary flow (Norouzi and Biglari, 2013). The capillary number influences the flow when the channel becomes milli- or micro. In the case of two-phase flow, when the densities of the two-phases are different, the gravity also affects the flow. The variations of pressure drop per unit length of the channel with the above three dimensionless numbers are shown in Fig. 2.9(a) and Fig. 2.9(b) for single and two-phase flows, respectively.

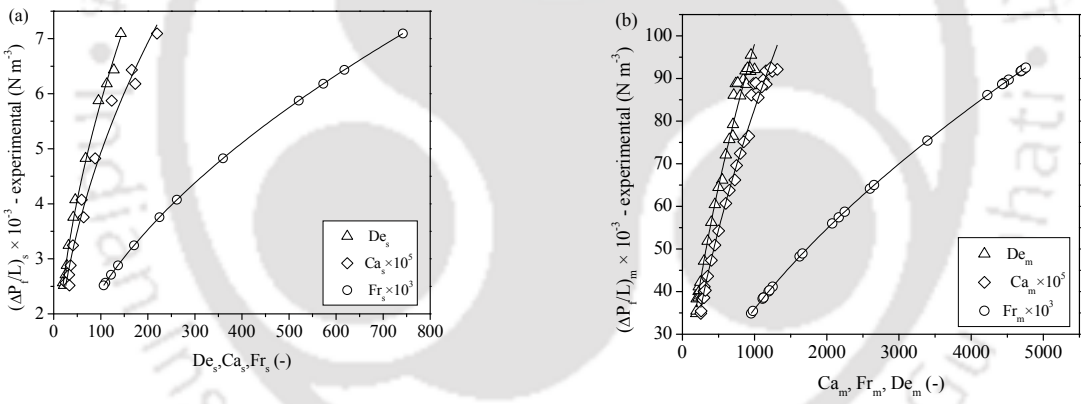

Fig. 2.9. Variation of frictional pressure drop with the dimensionless numbers for the unpacked serpentine channel: (a) single-phase flow and (b) two-phase flow.

Frictional pressure drop per unit length increases with increasing Dean number, capillary number as well as Froude number for both single and two-phase flow (Fig. 2.9(a), Fig. 2.9(b)). In both the figures, the Dean number curve is steeper than the others, which confirms the higher effect on frictional pressure drop with increasing the velocity of the phases. According to the experimental result, the Froude number effect is more pronounced in the case of two-phase flow than single-phase flow due to the density difference between the two fluids. As the Dean number has a higher

contribution to frictional pressure drop, its influence on the friction factor prevails accordingly, as shown in Fig. 2.10(a) and Fig. 2.10(b).

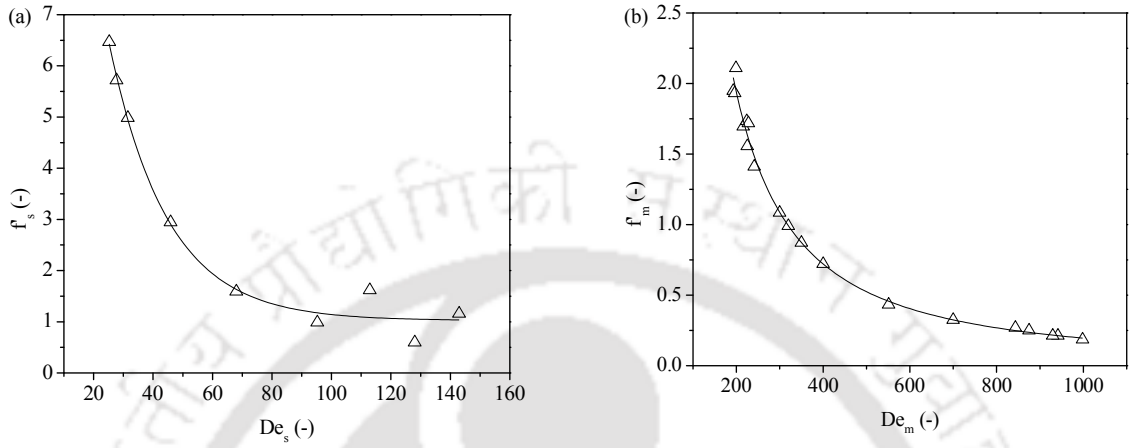

Fig. 2.10. Variation of friction factor with Dean number for the unpacked serpentine channel: (a) single-phase flow and (b) two-phase flow.

The friction factor decreases exponentially with increasing Dean number (Fig. 2.10(a) and Fig. 2.10(b)). The friction factor value for the two-phase flow is lower than the single-phase flow as the Dean number is higher for the two-phase system.

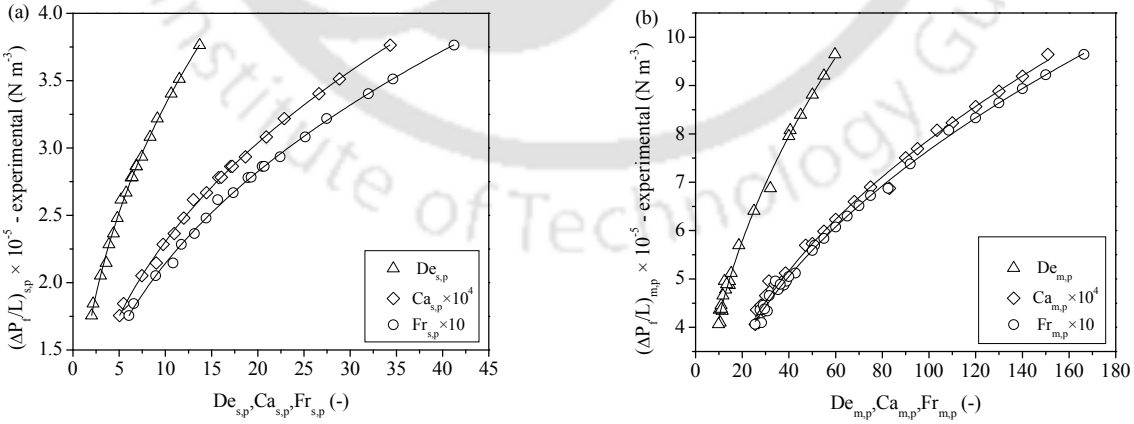

Fig. 2.11. Variation of frictional pressure drop with dimensionless numbers for the packed serpentine channel: (a) single-phase flow and (b) two-phase flow.

In the case of the packed channel, also the Dean number has a significant effect on pressure drop as well as friction factor. Along with the Dean number, capillary number and Froude number effects are significant on the frictional pressure drop for the flow through the packed channel, as shown in Fig. 2.11(a) and Fig. 2.11(b). As the Dean number has a higher impact on the pressure drop, it demands a valuable impression on friction factor. The friction factor variation with the Dean number for the flow through the packed channel is shown in Fig. 2.12(a) and Fig. 2.12(b).

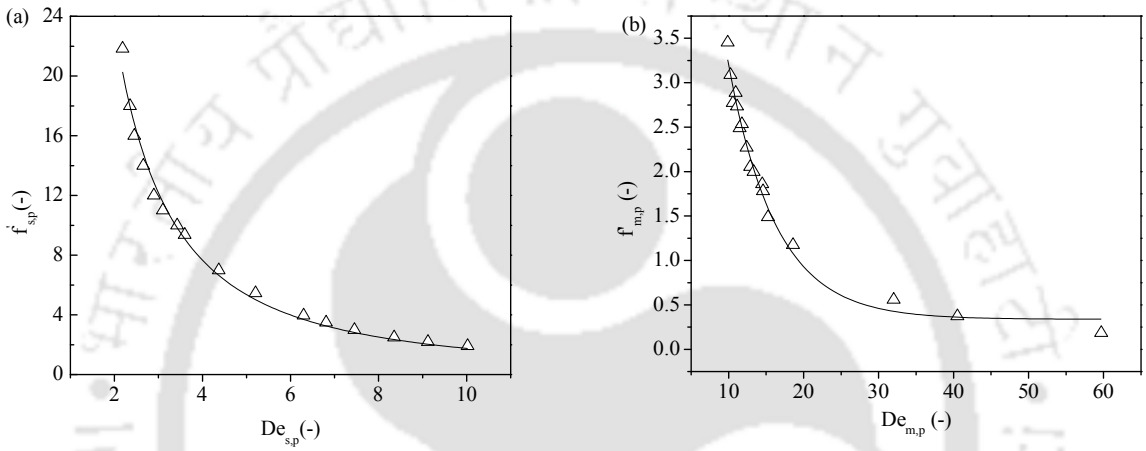

Fig. 2.12. Variation of friction factor with Dean number for the packed serpentine channel: (a) single-phase flow and (b) two-phase flow.

Fig. 2.11, and Fig. 2.12 shows the higher values of the pressure drop and friction factor for the packed channel than those in the unpacked channel (Fig. 2.9 and Fig. 2.10).

2.4.2. Analysis by model

There is no reliable theoretical model available to predict the pressure drop as well as friction factor for the water or organic single-phase and water-toluene two-phase flow through the rectangular packed and unpacked straight and serpentine horizontal channels. In the present study, an attempt has been made to predict the pressure drop and friction factor by developing empirical correlations.

2.4.2.1. Analysis of pressure drop in the unpacked straight and serpentine millichannels

2.4.2.1.1. Unpacked straight channel geometry

The hydraulic diameter, actual velocity, density, viscosity, and surface tension of the liquids are the main controlling parameters for the pressure drop for the single-phase flow. In addition to the above variables, the effect of the gravity of acceleration is significant for the water-toluene flow. The empirical correlations are generated to estimate the pressure drop in packed and unpacked channels in terms of operating variables, as shown in Eq. (2.39).

$$\left(\frac{\Delta P_f}{L}\right) = f\left(d_H, U, \rho, \mu, \sigma, g\right) \tag{2.39}$$

The pressure drop models are generated for the unpacked millichannel by dimensional analysis as the function of dimensionless parameters and are expressed in the form of Eqs. (2.40) and (2.41). The correlations for the single-phase (Eq. (2.40)) and for the water-toluene phase (Eq. (2.41)) in the unpacked channel are represented as

$$\left(\frac{d_H}{\rho_s U_s^2}\frac{\Delta P_f}{L}\right)_s = 2f_s^{'} = 1.9544\left(\mathrm{Re}_s\, Ca_s\right)^{-0.7126} = 1.9544\left(We_s\right)^{-0.7126} \tag{2.40}$$

In Eq. (2.40), $\mathrm{Re}_s = \frac{d_H \rho_s U_s}{\mu_s}$; $Ca_s = \frac{\mu_s U_s}{\sigma_s}$ and $f_s^{'} = \frac{d_H}{2\rho_s U_s^2}\frac{\Delta P_f}{L}$. The Eq. (2.40) is valid within a range of variables: $8636.78 < \left(\frac{\Delta P_f}{L}\right)_s < 19142.69$ N m^{-3}; $263.83 < \mathrm{Re}_s < 1040.39$; $0.00087 < Ca_s < 0.0034$.

$$\left(\frac{d_H}{\rho_m U_m^2}\frac{\Delta P_f}{L}\right)_m = 2f_m^{'} = 0.1507\left(\mathrm{Re}_m\, Ca_m\right)^{1.3960}\left(Fr_m\right)^{-3.6356} = 0.1507\left(We_m\right)^{1.3960}\left(Fr_m\right)^{-3.6356} \tag{2.41}$$

In Eq. (2.41), $\mathrm{Re}_m = \frac{d_H \rho_m U_m}{\mu_m}$; $Ca_m = \frac{\mu_m U_m}{\sigma_m}$; $Fr_m = \frac{U_m}{\sqrt{g d_H}}$ and $f_m^{'} = \frac{d_H}{2\rho_m U_m^2}\frac{\Delta P_f}{L}$. The U_m values are calculated by using the relation, $U_m = U_{s,o}/\alpha_o + U_{s,w}/(1-\alpha_o)$. The Eq. (2.41) is valid within a range of variables: $17882.64 < \left(\frac{\Delta P_f}{L}\right) < 41442.92$ N m^{-3}; $3009.63 < \mathrm{Re}_m < 6124.44$ $0.0103 < Ca_m < 0.0209$ and $3.86 < Fr_m < 8.07$.

The correlation coefficients and the standard errors are evaluated for the above expressions. These are seen to be equal to 0.9985 and 0.026 for Eq. (2.40), 0.9922 and 0.023 for Eq. (2.41) (The theory for the calculation of the correlation coefficient and standard error with ANOVA is given in **Appendix – I**). Eqs. (2.40-2.41) are able to satisfy the experimental data with a maximum error of 4.52% and 4.24%, respectively. The pressure drops for both the single as well as the two-phase flow through the millichannel is controlled by the two important dimensionless parameters like Reynolds number and capillary number as per Eqs. (2.40-2.41). Froude number or the gravity effect is consolidated due to the slip between the two-phases as a consequence of density difference, though the liquid-liquid flow through the horizontal millichannel is experienced.

2.4.2.1.2. Unpacked serpentine channel geometry

As like the unpacked straight channel, the pressure drop in unpacked serpentine channel generally depends on different operating variables: hydraulic diameter, the radius of curvature, liquid superficial or actual velocity (U), the density of the liquid, the viscosity of the liquid, the surface tension of the liquid. The experimental data have been analyzed to develop the correlation for pressure drop as a function of the operating variables as:

for single-phase flow

$$\left(\frac{\Delta P_f}{L}\right)_s = f\left(d_H, R_c, U_s, \rho_s, \mu_s, \sigma_s, g\right) \tag{2.42}$$

for mixture flow

$$\left(\frac{\Delta P_f}{L}\right)_m = f\left(d_H, R_c, U_m, \rho_m, \mu_m, \sigma_m, g\right) \tag{2.43}$$

The subscripts ‘s’ denotes single-phase flow whereas *‘m’* denotes the mixture flow of phases. The functionality of pressure drop obtained by dimensional analysis (Buckingham Pi theorem) in terms of various significant dimensionless groups which can be expressed as

$$Eu' = Eu\frac{d_H}{L} = \frac{\Delta P_f}{\rho U^2}\frac{d_H}{L} = \lambda De^a Ca^b Fr^c \tag{2.44}$$

where Eu' is the modified Euler number. The Euler number (Eu) is signified by the ratio of pressure forces to inertial forces. The parameter λ is a coefficient and ‘a’, ‘b’, and ‘c’ is the rational

numbers. The correlations for flows through horizontal serpentine rectangular millichannel without packing are represented as follows:

for single-phase flow through the unpacked channel:

$$\left(\frac{d_H}{\rho_s U_s^2}\frac{\Delta P_f}{L}\right)_s = 2f_s' = 1.15\left(De_s Ca_s\right)^{0.3730}\left(Fr_s\right)^{-2.2135} \quad (2.45)$$

The ranges of validity of the correlation (Eq. 2.45) are as follows:

$2518 < \left(\frac{\Delta P_f}{L}\right)_s < 7094$ N m^{-3}; $19.69 < De_s < 142.96$; $0.00026 < Ca_s < 0.0022$ and $0.092 < Fr_s < 0.742$.

The correlation for aqueous-organic two-phase flow through the unpacked channel is

$$\left(\frac{d_H}{\rho_m U_m^2}\frac{\Delta P_f}{L}\right)_m = 2f_m' = 9.47\left(De_m Ca_m\right)^{1.2953}\left(Fr_m\right)^{-3.9670} \quad (2.46)$$

within a range of variables:

$34892 < \left(\frac{\Delta P_f}{L}\right) < 92530$ N m^{-3}; $192.67 < De_m < 998.13$; $0.0025 < Ca_m < 0.0132$ and $0.987 < Fr_m < 5.178$.

The correlation coefficients and the standard errors are found to be 0.999 and 0.035 for Eq. (2.45), 0.999 and 0.024 for Eq. (2.46) (The theory for the calculation of the correlation coefficient and standard error with ANOVA is given in **Appendix – I**). The Eq. (2.45) and Eq. (2.46) fit the experimental data with maximum 4.6% (Fig. 2.19(a)) and 5.0% (Fig. 2.19(b)) error respectively. From Eq. (2.45) and Eq. (2.46), it is obvious that the pressure drop for single and two-phase flow depends on three significant dimensionless numbers, such as Dean number (De), capillary number (Ca), and Froude number (Fr).

2.4.2.2. Analysis of the pressure drop by the Lockhart-Martinelli model

2.4.2.2.1. Model analysis for the unpacked straight channel

The first pressure drop model in pipes was proposed by Lockhart-Martinelli (1949). The frictional pressure drop was expressed by them as the Eq. (2.47).

$$\left(\Delta P_f / L\right)_m = \phi_w^2 \left(\Delta P_f / L\right)_w \tag{2.47}$$

In Eq. (2.1.8), ϕ_w^2 is the pressure drop multiplier, and the relationships between the pressure drop multiplier and the Lockhart-Martinelli's parameter are demonstrated by the Eqs. (2.48a-2.48b)

$$\phi_w^2 = 1 + \frac{C}{X} + \frac{1}{X^2} \tag{2.48a}$$

$$\phi_o^2 = 1 + CX + X^2 \tag{2.48b}$$

In Eq. (2.48a & b), C is the Chisholm's constant (1967). Lockhart-Martinelli's parameter for the two-phase flow represented as X and is expressed as the Eq. (2.49).

$$X = \left[\frac{(\Delta P_f / L)_w}{(\Delta P_f / L)_o}\right]^{0.5} \tag{2.49}$$

The correlations of 'ϕ_w^2' and C are generated considering the combined effect of the dependent variables, as shown in Eq. (2.50) and Eq. (2.52).

$$\phi_w^2 = 1.7796\left(\mathrm{Re}_w\, Ca_w\right)^{0.3638} = 1.7796\left(We_w\right)^{0.3638} \tag{2.50}$$

In Eq. (2.50), We is the Weber number, expressed as shown in Eq. (2.51).

$$We = \mathrm{Re}\, Ca = \frac{d_H \rho U^2}{\sigma} \tag{2.51}$$

$$C_w = 1.2375\left(\mathrm{Re}_w\, Ca_w\right)^{0.4854} = 1.2375\left(We_w\right)^{0.4854} \tag{2.52}$$

In Eq. (2.50) and Eq. (2.52), the operating variables vary within the ranges of $1370.35 < \mathrm{Re}_w < 3017.22$ and $0.0045 < Ca_w < 0.0099$. The maximum error and the standard deviation of the Eqs. (2.50) and (2.52) are found to be 4.46% and 0.027, respectively.

The variations of the parameters (ϕ_w^2 and C) are shown in Figs. 2.13(a) and 2.13(b). The experimental and predicted values are compared and shown in Figs. 2.14(a) and 2.14(b).

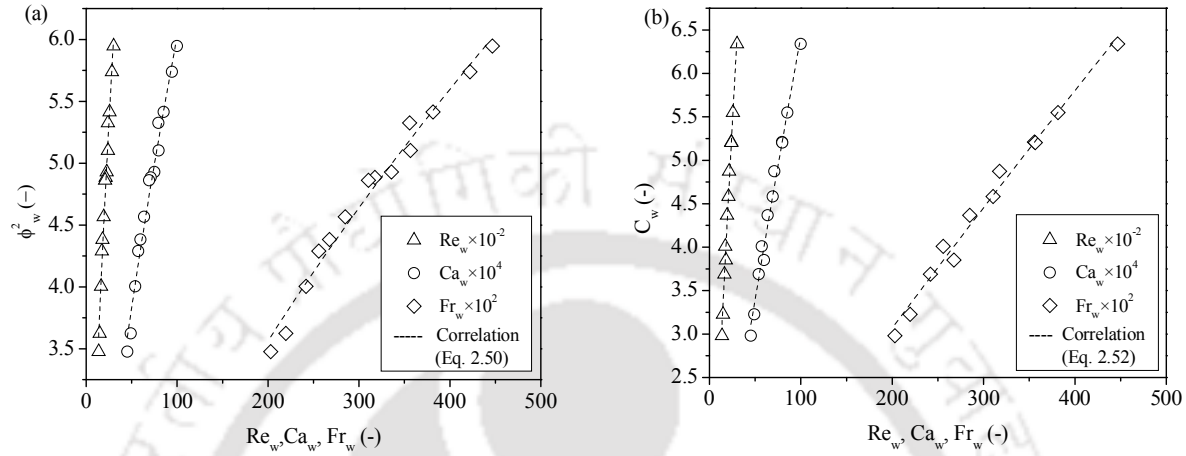

Fig. 2.13. Variation of the pressure drop with the dimensionless parameters for the straight channel: (a) pressure drop multiplier and (b) Chisholm's constant.

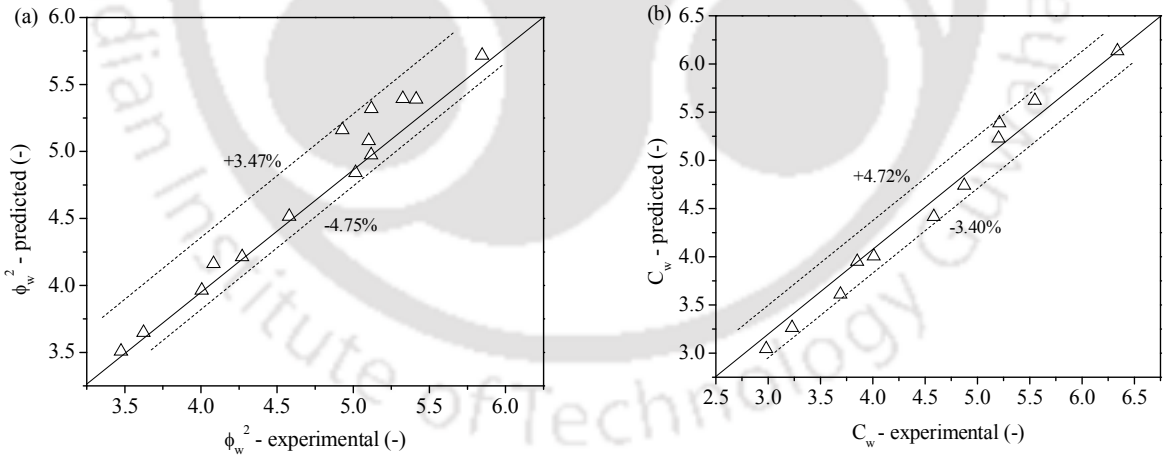

Fig. 2.14. Comparison between the experimental and predicted values for the straight channel: (a) Lockhart-Martinelli parameter and (b) Chisholm constant.

In the present context, the experimental data are differentiated from the models available in the literature, and the mean deviation values are tabulated in Table 2.3.

Table 2.3. Comparison of ϕ_w^2 and C values obtained from the experiments for the straight channel and the available models.

Comparison of ϕ_w^2 values		**Comparison of *C* values**	
Authors	**Mean deviation (MD) (%)**	**Authors**	**Mean deviation (MD) (%)**
Chisholm, 1967	26.24	Moriyama et al., 1992	21.54
Tran et al., 1999	70.58	Mishima et al., 1993	67.01
Chen et al., 2007	33.35	Lee and Lee, 2001	98.71
Yue et al., 2008	13.28	Qu et al., 2003	79.84
Sun and Mishima, 2009	5.26	Yue et al., 2004	76.00
Present correlation	2.04	Lee and Mudawar, 2005	74.65
		Kawahara et al., 2009	32.25
		Sun and Mishima, 2009	48.82
		Li et al., 2010	57.96
		Zhang et al., 2010a	48.05
		Present correlation	1.10

Comparison of the experimental values of the pressure drop parameters (ϕ_w^2 and C) with the available models are also shown in Figs. 2.15(a) and 2.15(b). There is a remarkable deviation between the experimental and predicted values for the pressure drop parameters (ϕ_w^2 and C) in rectangular millichannel. The present study consists of the geometry of different dimensions along with the different fluids. Hence, the moderation of the available models is required, which is performed in this present context. From Table 2.3, it is seen that, for the ϕ_w^2 value, Sun and Mishima (2009) correlation is best fitted with the experimental data having only 5.26% error, whereas, for the *C* values, Moriyama et al. (1992) model is more appropriate having 21.54% error.

Our newly proposed correlation in the present work is satisfactory with the experimental data according to the error percentage, as represented in Figs. 2.15(a) and 2.15(b). The single and two-phase friction factor ($f_s^{'}$ and $f_m^{'}$) in the rectangular millichannel are calculated from the Eqs. (2.40-2.41).

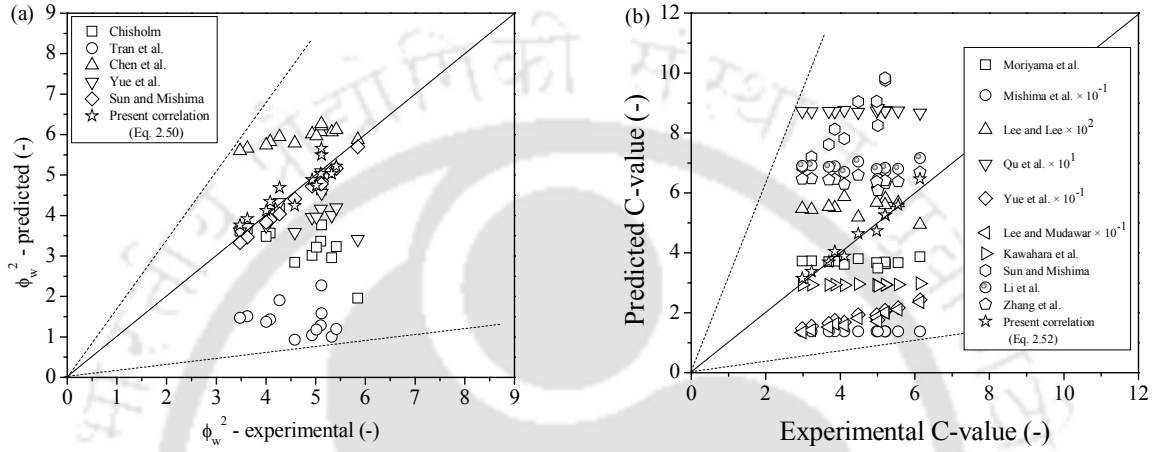

Fig. 2.15. Comparison of the experimental values for the straight channel with the available models: (a) ϕ_w^2 value comparison and (b) C value comparison.

Available friction factor models in packed and unpacked straight channels are compared with the experimental data, and their deviations are shown in Table 2.4.

Table 2.4. The friction factor correlations and their deviations from the calculated values for the unpacked rectangular straight channel.

Authors	**Friction factor correlations**	**Mean deviation (MD) (%)**	
		Singl-phase	**Two-phase**
Blasius, 1913	$f^{'} = 0.0791\,\mathrm{Re}^{-0.25}$ where $2000 < \mathrm{Re} < 10^5$	97.83	78.08

Shah and London, 1978	$f' = 24/\mathrm{Re}\left[(1+A_c)^2(1-0.6274A_c)\right]$ for A_c<0.2	96.19	90.89
Leon and Roman, 1984	$f' = 0.0791\left[\mathrm{Re}/(2A_c)^{0.16}\right]^{-0.25}$	96.90	78.87
Bhatti and Shah, 1987	$f' = \left(0.0054 + 2.3\times10^{-8}\,\mathrm{Re}^{1.5}\right)(\mu_m/\mu_w)^{0.11}$ where 2300<*Re*<4000	99.15	68.39
Harnett and Kostic, 1989; Abdelall et al., 2005; Hrnjak and Tu, 2007	$f' = (96/\mathrm{Re})(1-1.3553A_c+1.9467A_c^2-1.701$ $+0.9564A_c^4-0.2537$	84.76	63.52
Li and Hibiki, 2017a; Churchill, 1977	$f' = 8\left[\left(\frac{8}{\mathrm{Re}}\right)^{12}+\frac{1}{(A+B)^{3/2}}\right]^{1/12}$ where $A=\left\{2.457\ln\left[\frac{1}{\left(\frac{7}{\mathrm{Re}}\right)^{0.9}+0.27\frac{k}{d_H}}\right]\right\}^{16}$ and $B=\left(\frac{37530}{\mathrm{Re}}\right)^{16}$ when $\mathrm{Re}\geq3000$; k = 0.03 mm	87.22	96.92
Present work	Single-phase flow: $f_s' = 9.77\times10^{-1}\left(\mathrm{Re}_s\,Ca_s\right)^{-0.7126}$ Two-phase flow: $f_m' = 7.53\times10^{-2}\left(\mathrm{Re}_m\,Ca_m\right)^{1.3960}\left(Fr_m\right)^{-3.6356}$	1.86	1.66

In Table 2.4, the data developed from the present experiment are analogized with the available models. Harnett and Kostic (1989), showed better fit with the experimental friction factor data having 84.76% and 63.52% error for the single and two-phase flows, respectively (Table 2.4). But, our derived correlation closely resembles the experimental data within the maximum deviation of 1.86%.

2.4.2.2.2. Model analysis for the unpacked serpentine channel

Based on the present experimental results, the correlations for 'ϕ_w^2' and C are developed incorporating the different operating variables which are represented as follows:

$$\phi_w^2 = 7.594\left(De_w Ca_w\right)^{0.0398} = 7.594\left(We'_w\right)^{0.0398} \tag{2.53}$$

where We'_w is the modified Weber number which is defined as

$$We'_w = \left(De_w Ca_w\right) = \left(\mathrm{Re}_w \sqrt{\frac{d_H}{2r_c}} Ca_w\right) \tag{2.54}$$

and

$$C_w = 4.92\left(De_w Ca_w\right)^{0.07912} \tag{2.55}$$

The ranges of operating variables for the correlations (Eq. (2.53) and Eq. (2.55)) are $77.77 < De_w < 441.21$ and $1.01\times10^{-3} < Ca_w < 5.713\times10^{-3}$. The correlation satisfies the experimental data within the maximum 4.7% error within the mean deviation of 2.51. The variations of ϕ_w^2 and C with the dimensionless numbers are shown in Fig. 2.16(a) and Fig. 2.16(b).

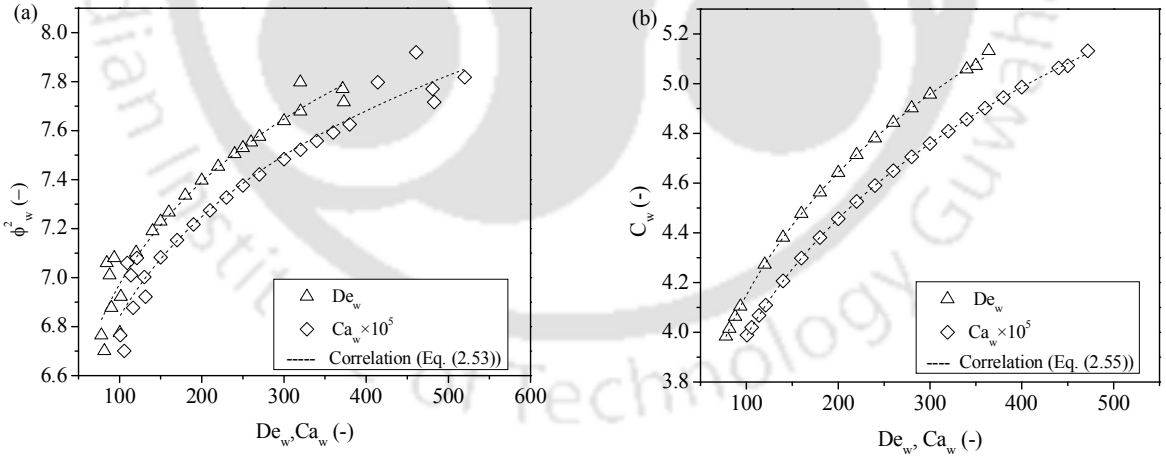

Fig. 2.16. Variation of pressure drop parameters with dimensionless numbers for the serpentine channel: (a) pressure drop multiplier and (b) Chisholm's constant.

The predicted values from the correlations are close enough to the experimental values. Predicted values from the present correlation are plotted against the experimental values and represented in Figs. 2.17(a) and 2.17(b) and Figs. 2.18(a) and 2.18(b).

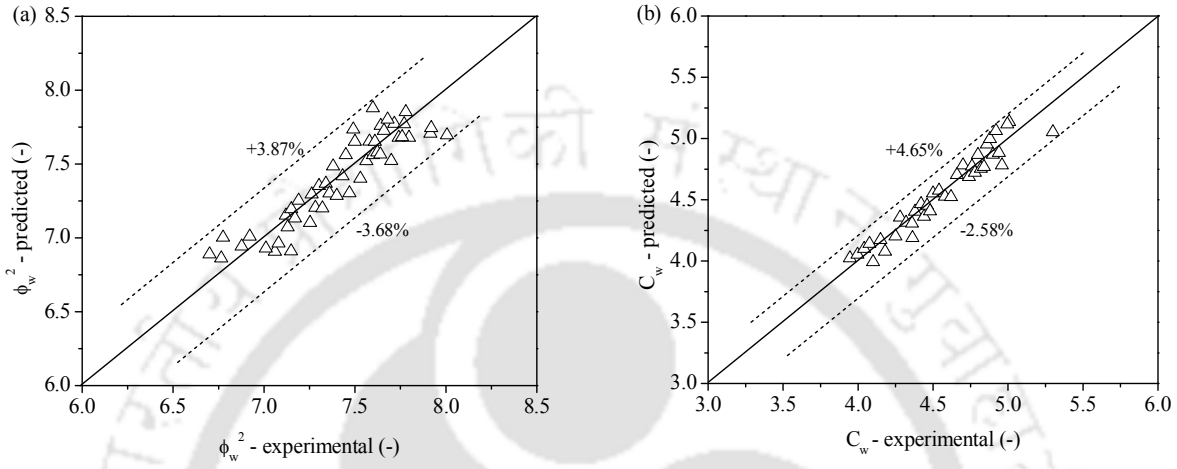

Fig. 2.17. Experimental and predicted value comparison for the serpentine channel: (a) Lockhart-Martinelli parameter and (b) Chisholm constant.

The pressure drop data obtained from the present study were also compared with the previous models, as shown in Table 2.1. The mean and root mean square deviation of the experimental values with predicted values from the available models are tabulated (Table 2.5 and Table 2.6). Percentage errors of the models with the experimental values are also plotted, as shown in Fig. 2.18(a) and Fig. 2.18(b).

Table 2.5. Comparison of the ϕ_w^2 values with the other models.

Authors	**Mean deviation (MD) (%)**	**Root mean square deviation (RMSD) (%)**
Chisholm, 1967	81.01	81.07
Tran et al., 1999	37.32	38.63
Chen et al., 2007	707.09	708.25
Present correlation	2.09	2.36

Fig. 2.18(a) and Fig. 2.18(b) represents the fact that there is a wide difference between the experimental data for ϕ_w^2 and C with the other available pressure drop equations for flow through the rectangular channel, which is either straight rectangular channel or two-phase flow having one gaseous in most of the cases.

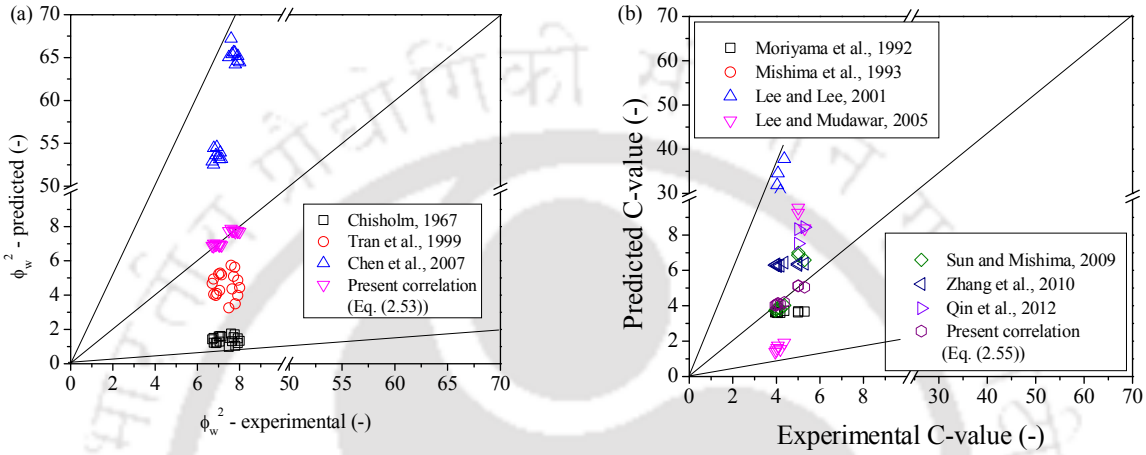

Fig. 2.18. Comparison of the experimental values with the models for the serpentine channel: (a) ϕ_w^2 value comparison and (b) C value comparison.

Table 2.6. *C* –value comparison.

Authors	**Mean deviation (MD) (%)**	**Root mean square deviation (RMSD) (%)**
Moriyama et al., 1992	16.99	18.89
Mishima et al., 1993	213.71	216.19
Lee and Lee, 2001	493.29	558.86
Lee and Mudawar, 2005	66.45	67.49
Sun and Mishima, 2009	15.28	20.51
Zhang et al., 2010a	44.24	46.51
Qin et al., 2012	136.48	148.20
Present correlation	2.51	2.72

The present study consists of very different geometries as well as different fluids like water and toluene. In this context, the modification of the previous model was done. The calculated 'ϕ_w^2' and 'C' values of experimental data are compared with the available correlations (Table 2.5 and Table 2.6). From Table 2.5 and Fig. 2.18(a), it is seen that Tran et al. (1999) model is the best fit with present experimental value for ϕ_w^2 whereas Sun and Mishima (2009), Zhang et al. (2010a) models show better fit for coefficient C as shown in Table 2.6 and Fig. 2.18(b). As per the newly developed correlation in this work, the present experimental data is shown better fit with respective errors, as shown in Fig. 2.17(a) and Fig. 2.17(b). The single-phase friction factor (f_s') for the flow through the unpacked channel can be obtained by the Eq. (2.45). Similarly, the two-phase friction factor (f_m') for the flow through the unpacked channel can be obtained from Eq. (2.46). Models available for the calculation of friction factor for both unpacked and packed channels and their deviation from the present values are tabulated in Tables 2.7-2.8, and Tables 2.11-2.12.

Table 2.7. Correlations for friction factor as per different investigators for unpacked serpentine channel.

Authors & Years	**Friction factor correlations**	**Channel geometry**	**Flow types**
Fanning, 1896	$f = \frac{d_H \Delta P_f}{2\rho_m U_m^2 L}$ For rectangular serpentine channel, this equation takes the form $f = \frac{180}{\Pi r_c \theta_c} \frac{w^3 h^3 \Delta P_f}{\rho_m Q_m^2 (h+w)}$	Rectangular serpentine channel	Fully developed flow
Blasius, 1913	$f = 0.0791\,\mathrm{Re}^{-0.25}$ where $2000 < \mathrm{Re} < 10^5$	The circular tube as well as Rectangular channel	Fully developed turbulent flow
Shah and London, 1978; Harnett and	$f = 24\lambda / \mathrm{Re}$ Where	Rectangular channel	Laminar flow

Kostic, 1989; Abdelall et al., 2005; Hrnjak and Tu, 2007	$\lambda = \begin{pmatrix} 1-1.3553A_c+1.9467A_c^2 \\ -1.7012A_c^3+0.9564A_c^4-0.2537A_c^5 \end{pmatrix}$		
Hua and Yang, 1985	$f = \frac{5}{\mathrm{Re}^{0.65}}\left(\frac{w}{2r_c}\right)^{0.175}$ where $\mathrm{Re} < 600$	Curved Microchannel	Laminar flow regimes
Phillips, 1990	$f = A\,\mathrm{Re}^{*B}$ Where $A = 0.09290 + \frac{1.01612}{x/d_H}$ and $B = -0.26800 - \frac{0.32930}{x/d_H}$; For rectangular microchannels laminar-equivalent Reynolds number $\mathrm{Re}^* = \frac{\rho_m U_m d_H}{\mu_m} = \frac{\rho_m U_m [(2/3)+(11/24)(1/A_c)(2-1/A_c)]d_H}{\mu_m}$	Rectangular microchannel	Both developing and developed flow regimes
Wang and Liu, 2007	$f\,\mathrm{Re}_c / f\,\mathrm{Re}_s = 0.96194 + 0.01035\,De^{0.78715}$ where $0 < De \le 450$	Curved microchannel	Laminar flow regimes
Li and Hibiki, 2017b; Churchill, 1977	$f_m' = 8\left[\left(\frac{8}{\mathrm{Re}_m}\right)^{12} + \frac{1}{(A+B)^{3/2}}\right]^{1/12}$ where $A = \left\{2.457\ln\left[\frac{1}{\left(\frac{7}{\mathrm{Re}_m}\right)^{0.9}+0.27\frac{k}{d_H}}\right]\right\}^{16}$ and	Rectangular Channel	For both laminar and turbulent regimes

	$B = \left(\frac{37530}{\mathrm{Re}_m}\right)^{16}$ when $\mathrm{Re} \geq 3000$		
Present work	For the single-phase: $f_s' = 57.7 \times 10^{-2} \left(De_s Ca_s\right)^{0.3743} \left(Fr_s\right)^{-2.2106}$ For the mixture phase: $f_m' = 4.7252 \left(De_m Ca_m\right)^{1.292} \left(Fr_m\right)^{-3.971}$	Rectangular serpentine millichannel	For both laminar and turbulent flow regimes

Calculated friction factor values from the present experiment are compared with the available correlations, which are shown in Table 2.7. Churchill (1977), Li and Hibiki (2017b) correlations are the better fit with our present experimental data, but the error percentage is high enough 91.06 (Table 2.8).

Table 2.8. Deviation of calculated friction factor values from different correlations with the present experimental data for the unpacked serpentine channel.

Authors	**Mean deviation (MD) (%)**		**Root mean square deviation (RMSD) (%)**	
	Single-phase	**Two-phase**	**Single-Phase**	**Two-phase**
Blasius, 1913	98.85	97.69	98.85	97.70
Shah and London, 1978	95.18	97.81	95.19	97.81
Hua and Yang, 1985	95.89	96.29	95.92	96.31
Phillips, 1990	-	97.52	-	97.53
Li and Hibiki, 2017b; Churchill, 1977	-	90.85	-	91.06
Present correlation	2.48	1.47	2.94	1.73

2.4.2.3. Analysis of pressure drop in the packed straight and serpentine millichannels

2.4.2.3.1. Packed straight channel geometry

The pressure drop correlation models are derived for the water, and water-toluene flows through the rectangular millichannel in packed condition by utilizing the same procedure as the unpacked channel. The developed models for the single and two-phase flows are represented by the Eqs. (2.56) and (2.57).

$$\left(\frac{d_p}{\rho_s U_s^2 / \varepsilon_{eff}^2}\right)\left(\frac{\Delta P_f}{L}\right)_{s,p} = 2\left(f_s^{'}\right)_p = 1.2063\left(\mathrm{Re}_{s,p}\, Ca_{s,p}\right)^{-0.5451} = 1.2063\left(We_{s,p}\right)^{-0.5451} \quad (2.56)$$

In Eq. (2.56), $\mathrm{Re}_{s,p} = \frac{d_p \rho_s (U_s/\varepsilon_{eff})}{\mu_s}$; $Ca_{s,p} = \frac{\mu_s (U_s/\varepsilon_{eff})}{\sigma_s}$ and $(f_s^{'})_p = \frac{d_p}{2\rho_s (U_s/\varepsilon_{eff})^2}\frac{(\Delta P_f)_p}{L}$.

$$\left(\frac{d_p}{\rho_m U_m^2 / \varepsilon_{eff}^2}\right)\left(\frac{\Delta P_f}{L}\right)_{m,p} = 2\left(f_m^{'}\right)_p = 6.93\times10^{01}\left(\mathrm{Re}_{m,p}\, Ca_{m,p}\right)^{0.3089}\left(Fr_{m,p}\right)^{-2.1987} \quad (2.57)$$
$$= 6.93\times10^{01}\left(We_{m,p}\right)^{0.3089}\left(Fr_{m,p}\right)^{-2.1987}$$

In Eq. (2.57), $\mathrm{Re}_{m,p} = \frac{d_p \rho_m (U_m/\varepsilon_{eff})}{\mu_m}$; $Ca_{m,p} = \frac{\mu_m (U_m/\varepsilon_{eff})}{\sigma_m}$; $Fr_{m,p} = \frac{(U_m/\varepsilon_{eff})}{\sqrt{g d_p}}$ and $(f_m^{'})_p = \frac{d_p}{2\rho_m (U_m/\varepsilon_{eff})^2}\frac{(\Delta P_f)_p}{L}$. The $U_{m,p}$ values are calculated by using the relation, $U_{m,p} = [U_{s,o}/\varepsilon_{eff}\alpha_o + U_{s,w}/\varepsilon_{eff}(1-\alpha_o)]$.The subscript '$s,p$' and '$m,p$' represent the single-phase and two-phase packed condition, respectively. Eqs. (2.56) and (2.57) satisfies the experimental data with the correlation coefficients and the standard errors of 0.9979, 0.026, and 0.9989 and 0.021, respectively. The Eqs. (2.56) and (2.57) are valid within a range of variables:

$1.237\times10^5 < \left(\frac{\Delta P_f}{L}\right)_{s,p} < 4.374\times10^5$ N m^{-3}; $53.08 < \mathrm{Re}_{s,p} < 220.08$; $0.0013 < Ca_{s,p} < 0.0053$

and $4.06\times10^5 < \left(\frac{\Delta P_f}{L}\right)_{m,p} < 5.86\times10^5$ N m^{-3}; $151.71 < \mathrm{Re}_{m,p} < 466.83$;

$0.0038 < Ca_{m,p} < 0.012$; $3.69 < Fr_{m,p} < 10.71$. Eqs. (2.56) and (2.57) closely resemble the experimental data by the maximum error of 3.87% and 3.54%. Figs. 2.19(a) and 2.19(b), shows the comparison between the experimental and the predicted pressure drop values.

The earlier experiments for the pressure drop were performed by the researchers either in the cylindrical geometry or in the structured column. Our experience says, a very small number of researchers accomplished their experiments in rectangular packed millichannels to date. The values generated from the available models deviated to a great extent as the geometry, and the working fluids are not similar in the present case. But our newly generated Ergun equation satisfies the present experimental data very closely for the packed channel geometry having a maximum error of 3.87% in the case of both single and two-phase flows (Figs. 2.20(a) and 2.20(b)).

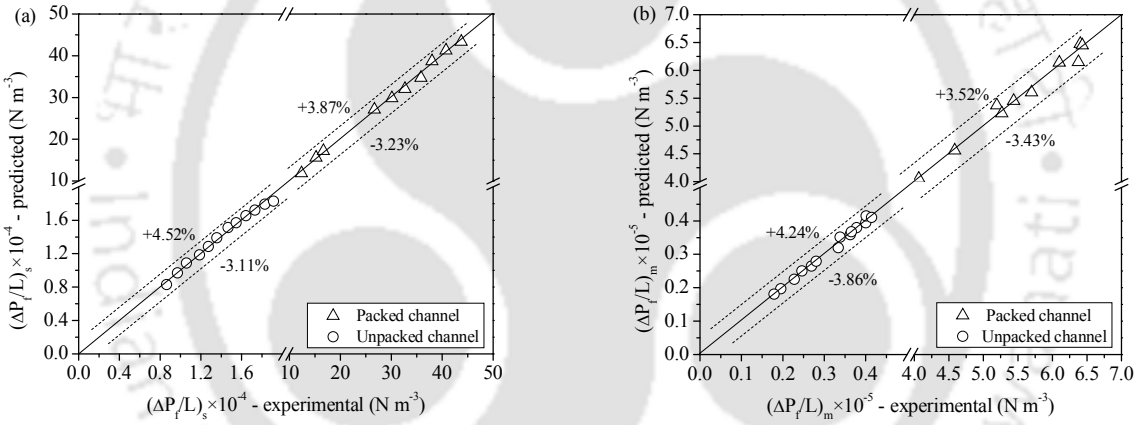

Fig. 2.19. Comparison between the experimental and the predicted pressure drop values for (a) single-phase flow, and (b) two-phase flow, through the packed and unpacked straight channel.

The modified Ergun equations are represented by the Eqs. (2.58) and (2.59).

$$\left(\frac{\Delta P_f}{L}\right)_{s,p} = 7.57\times10^2\left[\frac{\mu U_s\left(1-\varepsilon_{eff}\right)^2}{\phi_p^2 d_p^2 \varepsilon_{eff}^3} + \frac{\rho U_s^2\left(1-\varepsilon_{eff}\right)}{\phi_p d_p \varepsilon_{eff}^3}\right]^{0.460} \tag{2.58}$$

$$\left(\frac{\Delta P_f}{L}\right)_{m,p} = 2.96\times10^4\left[\frac{\mu U_m\left(1-\varepsilon_{eff}\right)^2}{\phi_p^2 d_p^2 \varepsilon_{eff}^3} + \frac{\rho U_m^2\left(1-\varepsilon_{eff}\right)}{\phi_p d_p \varepsilon_{eff}^3}\right]^{0.213} \tag{2.59}$$

The friction factor $(f_s^{'})_p$ and $(f_m^{'})_p$ is calculated from the Eqs. (2.56-2.57). The presently developed correlations are differentiated with the available correlations, which are shown in Table 2.9.

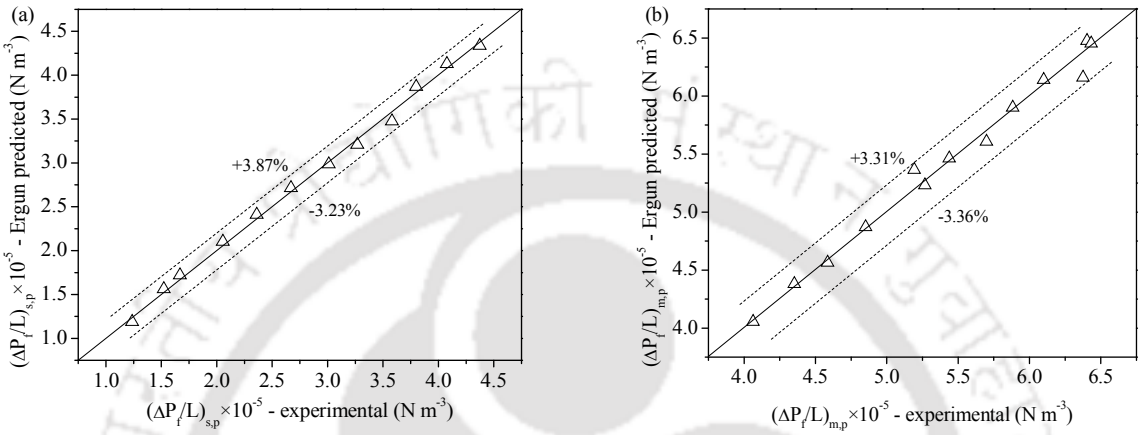

Fig. 2.20. Comparison of the pressure drop values obtained from the experiment and the modified Ergun equation for (a) single-phase flow, and (b) two-phase flow, through the packed straight channel.

Table 2.9. Important pressure drop correlations for the flow-through packed straight channel.

Authors & years	**Equations**	**Mean deviation (MD)%**	
		Single-phase	**Two-phase**
Ergun, 1952; McCbe et al., 2005	$\Delta P = 150\mu\frac{(1-\varepsilon)^2 L}{\phi_p^2\varepsilon^3 d_p^2}v_s + 1.75\frac{(1-\varepsilon)L\rho}{\phi_p d_p\varepsilon^3}v_s^2$	82.99	85.36
Feng, 1989	$\frac{\Delta P}{L} = \frac{0.106}{2g}\frac{\rho}{D}\mathrm{Re}_p^{-0.25}\left(\frac{u}{\varepsilon}\right)^2$ kPa m^{-1}; $D = d_p\frac{\phi^2}{6}\sqrt{\frac{2}{3(1-\varepsilon)}}$	99.27	98.84

Foumeny et al., 1993	$\Delta P = 130\mu\frac{(1-\varepsilon)^2 L}{\phi_p^2\varepsilon^3 d_p^2}v_s + \frac{d_H/d_p}{0.335\left(d_H/d_p\right)+2.28}\frac{(1-\varepsilon)L\rho}{\phi_p d_p\varepsilon^3}$	68.30	99.43
Eisfeld and Schitzlein, 2001	$\frac{\Delta P d_p}{\rho v_s^2 L} = \frac{154A_w^2}{\mathrm{Re}_p}\frac{(1-\varepsilon)^2}{\phi_p^2\varepsilon^3} + \frac{A_w}{B_w}\frac{1-\varepsilon}{\phi_p\varepsilon^3}$ where $A_w = 1+\frac{2}{3\left(d_H/d_p\right)(1-\varepsilon)}$ and $B_w = \left[1.15\left(\frac{d_p}{d_H}\right)^2 + 0.87\right]^2$	79.39	91.70
Montillet et al., 2007	$\frac{\Delta P d_p}{L\rho v_s^2} = 0.061\left(\frac{1-\varepsilon}{\varepsilon^3}\right)\left(\frac{d_H}{d_p}\right)^{0.20}\left(\frac{1000\mathrm{Re}_p^{-1}}{\phi_p^2} + \frac{60\mathrm{Re}_p^{-0.5}}{\phi_p} + 1\right.$	63.74	71.94
Newly deveoped modiied Ergun equaton (presnt work)	$\left(\frac{\Delta P_f}{L}\right)_{s,p} = 7.57\times10^2\left[\frac{\mu v_s(1-\varepsilon)^2}{\phi_p^2 d_p^2\varepsilon^3} + \frac{\rho v_s(1-\varepsilon)}{\phi_p d_p\varepsilon^3}\right]^{0.460}$ and $\left(\frac{\Delta P_f}{L}\right)_{m,p} = 2.96\times10^4\left[\frac{\mu v_s(1-\varepsilon)^2}{\phi_p^2 d_p^2\varepsilon^3} + \frac{\rho v_s(1-\varepsilon)}{\phi_p d_p\varepsilon^3}\right]^{0.213}$	2.04	2.95

The present experimental data for the pressure drop are compared with the available models in the packed channel and represented in Fig. 2.21. The data obtained from the experiments are varied to a great extent from the available models having the Maximum deviation of 99.27% and 99.43% for the single and two-phase flows, respectively (Table 2.9 and Fig. 2.21). Montillet et al. (2007), correlation predicts better results than the others both in the case of single and two-phase flows, 63.74% and 71.94%, respectively. The available models on the friction factor for the spherical particles in the packed bed are shown in Table 2.10. According to the correlations, the friction factor of the packed bed mainly depends on the Reynolds number of particles and the effective porosity of the bed when the particles are spherical ones. In our case, the particles are medium red sand with the sphericity 0.85, which makes the deviation of the friction factor values much from

the available models. Lee and Ogawa (1974) model satisfies our experimental data closely for the two-phase packed channel flow within the minimum deviation of 35.58%. Hence, the new fiction factor correlation is generated following the Eqs. (2.56-2.57) the incorporation of the sphericity values in the calculations satisfies our experimental data with a maximum 2.11% deviation (Table 2.10).

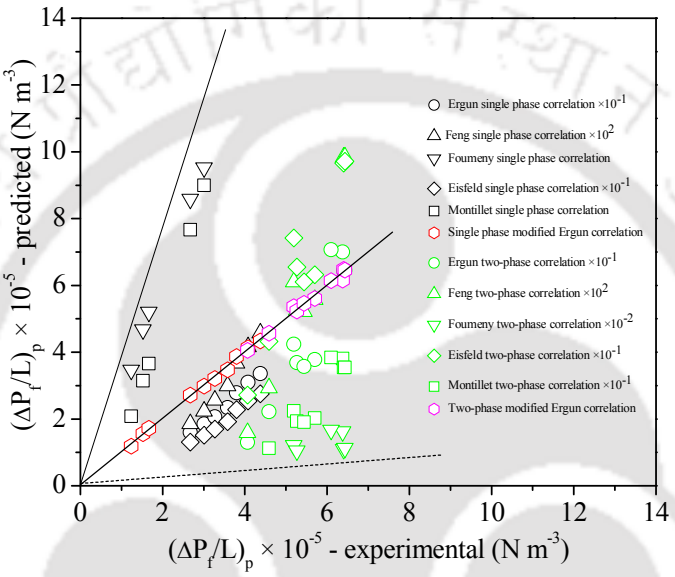

Fig. 2.21. Variation of the experimental pressure drop values with the available models for the flow through the packed straight channel (Montillet et al., 2007).

Table 2.10. Friction factor correlations for the packed bed (Montillet et al., 2007).

Authors	Correlations	Range of validity	Mean deviation (MD)%	
			Singl-phase	Two-phase
Rose, 1945	$f_p' = 1000\,\mathrm{Re}_p^{-1} + 60\,\mathrm{Re}_p^{-0.5} + 12$	-	95.93	97.00
Rose and Rizk, 1949	$f_p' = 1000\,\mathrm{Re}_p^{-1} + 125\,\mathrm{Re}_p^{-0.5} + 14$	-	96.87	97.71

Kürten et al., 1966	$f_p^{'} = \left[\frac{25}{4\varepsilon_{eff}}(1-\varepsilon_{eff})^2\right]\left[21\mathrm{Re}_p^{-1} + 6\mathrm{Re}_p^{-0.5} + 0.28\right]$	$0.1 \le \mathrm{Re}_p \le 4000$	99.99	95.65
Hicks, 1970	$f_p^{'} = 6.8 \times \frac{(1-\varepsilon_{eff})^{1.2}}{\varepsilon_{eff}^3}\mathrm{Re}_p^{-0.2}$	$500 \le \mathrm{Re}_p \le 6\times10^4$	97.80	98.62
Tallmadg, 1970	$f_p^{'} = \left[\frac{150}{\mathrm{Re}_p}\frac{(1-\varepsilon_{eff})^2}{\varepsilon_{eff}^3}\right] + \left[\frac{4.2(1-\varepsilon_{eff})^{1.166}}{\varepsilon_{eff}^3}\mathrm{Re}_p^{-1/6}\right]$	$0.1 \le \mathrm{Re}_p \le 10^5$	99.43	98.55
Lee and Ogawa, 1974	$f_p^{'} = \frac{1}{2}\left[\frac{12.5}{\mathrm{Re}_p}(1-\varepsilon_{eff})^2\right]\left[29.32\mathrm{Re}_p^{-1} + 1.56\mathrm{Re}_p^{-n} + 0.\right.$ with $n = 0.352 + 0.1\varepsilon_{eff} + 0.275\varepsilon_{eff}^2$	$1 \le \mathrm{Re}_p \le 10^5$	72.44	35.58
Watanabe, 1989	$f_p^{'} = \left[\frac{25}{4\varepsilon_{eff}^3}(1-\varepsilon_{eff}^2)\right]\left[21\mathrm{Re}_p^{-1} + 6\mathrm{Re}_p^{-0.5} + 0.28\right.$	$0.1 \le \mathrm{Re}_p \le 4\times10^3$	99.38	99.53
Montillet et al., 2007	$f_p^{'} = a\left(\frac{1-\varepsilon_{eff}}{\varepsilon_{eff}^3}\right)\left[\frac{d_H}{d_p}\right]^{0.2}\left[1000\mathrm{Re}_p^{-1} + 60\mathrm{Re}_p^{-0.5} + 12\right.$	$10 \le \mathrm{Re}_p \le 2500$	97.36	99.90
Ozahi et al., 2008	$f_p^{'} = \frac{160}{\mathrm{Re}_p} + 1.61\phi_p$	$708.2 \le \mathrm{Re}_p \le 7772.73$	98.29	99.56
Present correlation	$f_{s,p}^{'} = 0.6032(\mathrm{Re}_{s,p}\,Ca_{s,p})^{-0.5451}$ and $f_{m,p}^{'} = 22.09(\mathrm{Re}_{m,p}\,Ca_{m,p})^{0.0732}(Fr_{m,p})^{-1.6941}$	$53 \le \mathrm{Re}_p \le 220$ and $152 \le \mathrm{Re}_p \le 467$	2.11	1.25

2.4.2.3.2. Packed serpentine channel geometry

Following the similar way of the unpacked channel, the correlations were generated for the pressure drop for both single and two-phase flows through the packed rectangular serpentine millichannel. Medium sand was used as the packing material. The generated correlations are as follows:

For single-phase:

$$\left(\frac{d_p}{\rho_s U_s^2 / \varepsilon_{eff}^2}\right)\left(\frac{\Delta P_f}{L}\right)_{s,p} = 2\left(f_s^{'}\right)_p = 1.94\times10^2\left(De_{s,p}Ca_{s,p}\right)^{0.368}\left(Fr_{s,p}\right)^{-2.351} \quad (2.60)$$

The subscript 's, p' represents the single-phase flow through the packed bed. The correlation coefficient and the standard error of the Eq. (2.60) are 0.999 and 0.023, respectively. Various parameters for the correlation are $1.845\times10^{5} < \left(\frac{\Delta P_f}{L}\right)_{s,p} < 3.764\times10^{5}$ N m^{-3}; $1.77 < De_{s,p} < 11.84$; $0.00053 < Ca_{s,p} < 0.0035$ and $0.387 < Fr_{s,p} < 3.016$. Eq. (2.60) shows the similarity with the experimental data by the maximum error of 5.1% (Fig. 2.22(a)).

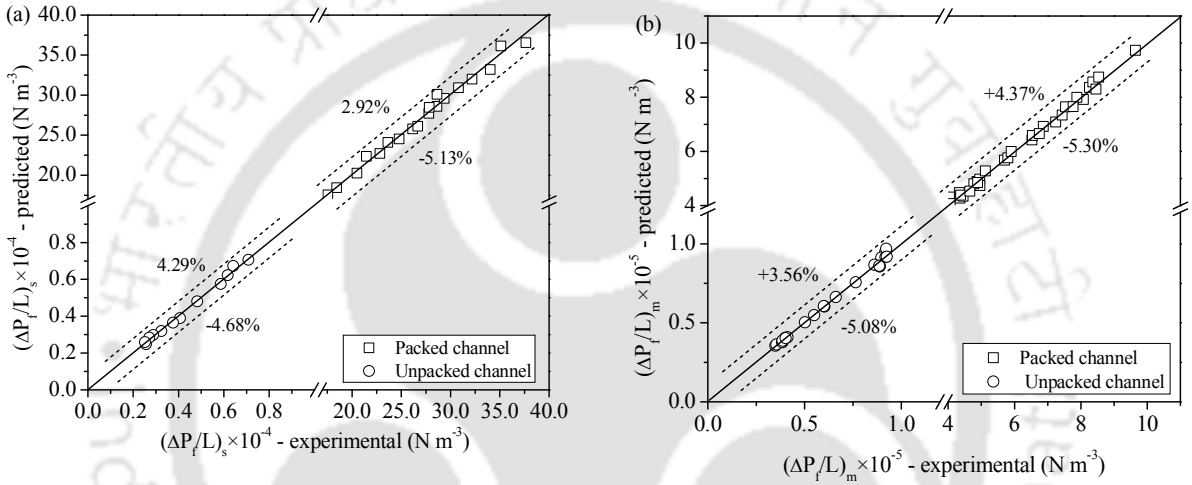

Fig. 2.22. Comparison of experimental and predicted pressure drop values for (a) single-phase flow, and (b) two-phase flow, through the packed and unpacked serpentine channel.

For a mixture of two-phases:

$$\left(\frac{d_p}{\rho_m U_m^2 / \varepsilon_{eff}^2}\right)\left(\frac{\Delta P_f}{L}\right)_{m,p} = 2\left(f_m'\right)_p = 4.419\times10^{1}\left(De_{m,p}Ca_{m,p}\right)^{0.073}\left(Fr_{m,p}\right)^{-1.694} \qquad (2.61)$$

The subscript 'm, p' represents the two-phase flow through the packed bed. The correlation coefficient and the standard error of the Eq. (2.61) are 0.999 and 0.025, respectively. The ranges of operating variables for the correlation are $4.063\times10^{5} < \left(\frac{\Delta P_f}{L}\right)_{m,p} < 9.644\times10^{5}$ N m^{-3}; $9.866 < De_{m,p} < 59.697$; $0.0026 < Ca_{m,p} < 0.0151$ and $2.548 < Fr_{m,p} < 16.640$. Eq. (2.61) shows

the similarity with the experimental data by the maximum error of 5.3% (Fig. 2.22(b)). The comparison of the experimental pressure drop values with the values calculated from the present correlation are shown in Fig. 2.23. The previously specified correlations for the pressure drop in packed bed were for the generally cylindrical geometry and for a structured column. According to our knowledge, no study has been performed until date using rectangular serpentine packed channels.

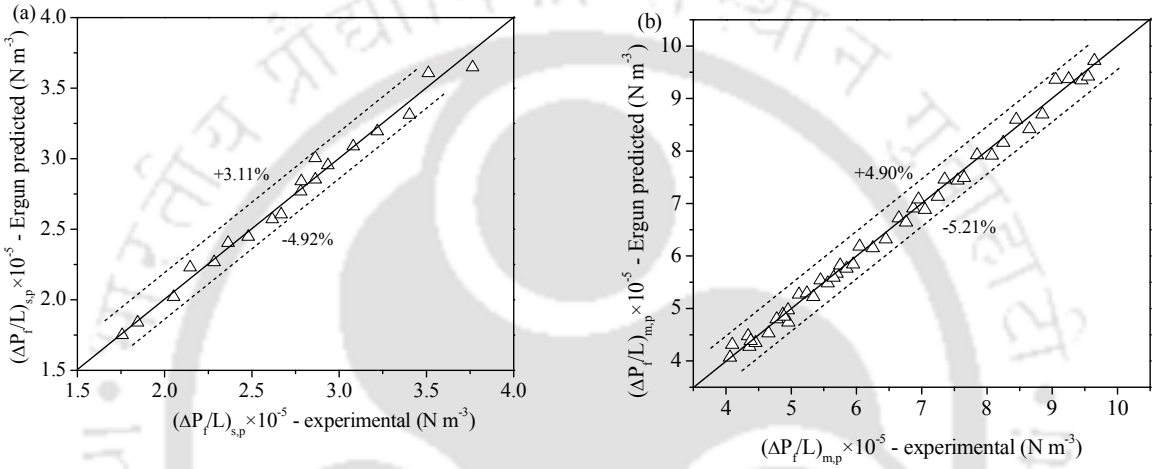

Fig. 2.23. Comparison of experimental and modified Ergun pressure drop values: (a) single-phase flow, and (b) two-phase flow, through the packed serpentine channel.

Due to the variation in the system geometry from the present study, the pressure drop calculated using the above available correlations indicates a higher deviation from the experimental values. However, the newly generated modified Ergun equation shows a maximum 5.21% error for both single and two-phase flow through rectangular serpentine packed channel (Fig. 2.23(a), Fig. 2.23(b)).

The single-phase friction factor $(f_s^{'})_p$ and two-phase friction factor $(f_m^{'})_p$ for the flow through the packed channel can be obtained by the Eq. (2.60) and Eq. (2.61) respectively. Different correlations for the flow through the packed channel are represented in Table 2.11.

Table 2.11. Important correlations for pressure drop in the packed channels (Ribeiro et al., 2010).

Authors & years	Equations
Ergun, 1952	$\Delta P = 150\mu \frac{(1-\varepsilon)^2 L}{\phi_p^2 \varepsilon^3 d_p^2} v_s + 1.75 \frac{(1-\varepsilon) L \rho}{\phi_p d_p \varepsilon^3} v_s^2$
Feng, 1989	$\frac{\Delta P}{L} = \frac{0.106}{2g} \frac{\rho}{D} \mathrm{Re}^{-0.25} \left(\frac{u}{\varepsilon}\right)^2$ kPa m^{-1} ; $D = d_p \frac{\phi^2}{6} \sqrt{\frac{2}{3(1-\varepsilon)}}$
Foumeny et al., 1993	$\Delta P = 130\mu \frac{(1-\varepsilon)^2 L}{\phi_p^2 \varepsilon^3 d_p^2} v_s + \frac{d_H / d_p}{0.335 \left(d_H / d_p\right) + 2.28} \frac{(1-\varepsilon) L \rho}{\phi_p d_p \varepsilon^3} v_s^2$
Eisfeld and Schitzlein, 2001	$\frac{\Delta P d_p}{\rho v_s^2 L} = \frac{154 A_w^2}{\mathrm{Re}_p} \frac{(1-\varepsilon)^2}{\phi_p^2 \varepsilon^3} + \frac{A_w}{B_w} \frac{1-\varepsilon}{\phi_p \varepsilon^3}$ where $A_w = 1 + \frac{2}{3\left(d_H / d_p\right)(1-\varepsilon)}$ and $B_w = \left[1.15 \left(\frac{d_p}{d_H}\right)^2 + 0.87\right]^2$
Montillet et al., 2007	$\frac{\Delta P d_p}{L \rho v_s^2} = 0.061 \left(\frac{1-\varepsilon}{\varepsilon^3}\right) \left(\frac{d_H}{d_p}\right)^{0.20} \left(\frac{1000 \mathrm{Re}_p^{-1}}{\phi_p^2} + \frac{60 \mathrm{Re}_p^{-0.5}}{\phi_p} + 12\right)$
Newly developed modified Ergun equation (present work)	$\left(\frac{\Delta P_f}{L}\right)_{s,p} = 9.51 \times 10^4 \left[\frac{\mu v_s (1-\varepsilon)^2}{\phi_p^2 d_p^2 \varepsilon^3}\right]^{-0.468} \left[\frac{\rho v_s (1-\varepsilon)}{\phi_p d_p \varepsilon^3}\right]^{0.427}$ and $\left(\frac{\Delta P_f}{L}\right)_{m,p} = 1.895 \times 10^4 \left[\frac{\mu v_s (1-\varepsilon)^2}{\phi_p^2 d_p^2 \varepsilon^3}\right]^{0.155} \left[\frac{\rho v_s (1-\varepsilon)}{\phi_p d_p \varepsilon^3}\right]^{0.149}$

The model proposed by Montillet et al. (2007) satisfies the experimental results better with root means square deviation error of 15.14% for the two-phase flow (Table 2.12).

Table 2.12. Deviations of the calculated data for pressure drop from correlation with the present experimental data for the packed channel.

Authors	Mean deviation (MD) (%)		Root mean square deviation (RMSD) (%)	
	Single-Phase	Two-phase	Single-Phase	Two-phase
Ergun, 1952	67.07	171.26	83.68	174.41
Feng, 1989	50.01	93.95	55.38	99.54
Foumeny et al., 1993	63.54	136.12	79.14	139.14
Eisfeld and Schitzlein, 2001	39.04	53.02	46.85	57.25
Montillet et al., 2007	49.39	12.94	56.53	15.14
Newly developed modified Ergun equation (present work)	1.77	1.90	2.08	2.51

The experimental pressure drop in the packed channel is plotted against predicted values from available correlations, which is shown in Fig. 2.24.

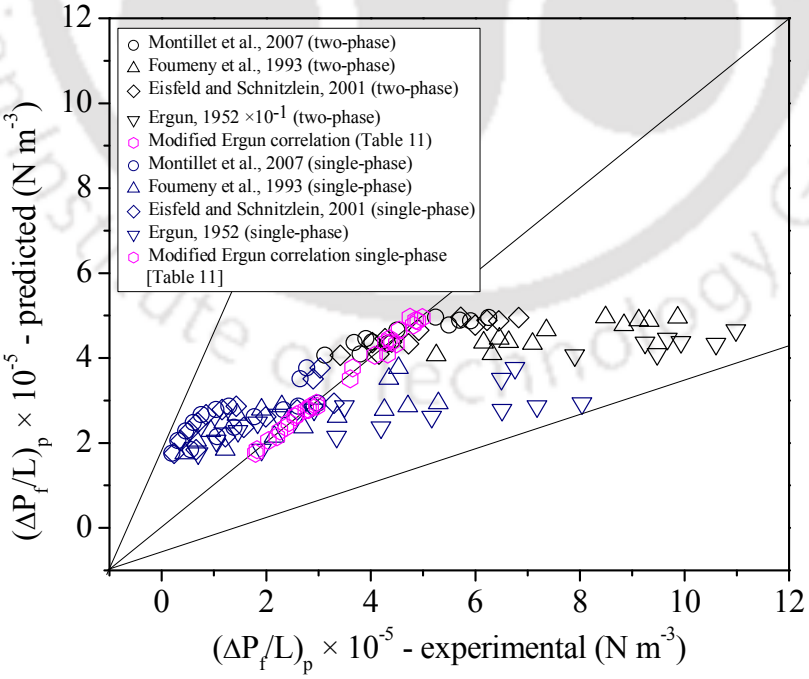

Fig. 2.24. Variation of the experimental values with the models in the packed serpentine channel.

From Table 2.12 and Fig. 2.24, it is seen that most of the correlation shows a high deviation from the experimental data. The maximum deviation is 174.02% for single-phase and 224.74% for two-phase flow. Among them, Montillet et al. (2007) correlation predicts closer results with the experimental values, maximum mean 49.39% for single-phase, and 12.94% for two-phase flow. On the other hand, the best fitting expression for the single-phase flow is given by Eisfeld and Shnitzlein (2001), having a maximum 39.04% error.

2.4.3. Local entropy generation rate for the two-phase flow through the unpacked channel according to the separated flow model

Local entropy generation plays a vital role in non-equilibrium thermodynamics. The local entropy generation rate is minimum for the stationary phases. According to Bejan (2001), entropy is a principle thermodynamic parameter for the design of the heat transfer equipment. At the diabatic flow condition, the entropy generation rate per unit length is expressed as Eq. (2.62), (Revellin et al., 2009)

$$ds' = \frac{q_m^2 P}{h_m' \Delta T_{lm}^2} + \frac{M_m' U_m}{\Delta T_{lm}} \left(- \frac{\Delta P_f}{L} \right) \tag{2.62}$$

where, q_m is the two-phase heat transfer rate and M_m' is the mass flow rate of the two-phase mixture, P is the perimeter of the channel, ΔT_{lm} is the log mean temperature difference, and L is the total length of the channel. In case of heating, the wall temperature of the channel is maintained at 30 ℃ by submerging the channel into a constant temperature water bath, and the inlet temperature of the two fluids is 25℃. h_m' is the heat transfer coefficient or specific enthalpy of the two-phase mixture. The heat transfer coefficient h_m' can be calculated for the forced convection by using the equations shown in Table 2.13, depending on their validity range of parameters (Gnielinski, 1975; Incropera et al., 2007).

Table 2.13. Available correlations for forced convection in turbulent flow through the unpacked straight channel.

Authors	Correlation	Validity
Geielinski (Geielinski, 1975; Incropera et al., 2007)	$Nu_m = \frac{h_m' d_H}{k_m} = \frac{(f_D/8)(\mathrm{Re}_m - 1000)\,\mathrm{Pr}_m}{1 + 12.7(f_D/8)^{1/2}(\mathrm{Pr}_m^{2/3} - 1)}$ where f_D is the Darcy friction factor, obtained either from Moody chart or from the correlation developed by Petukhov: $f_D = (0.79\ln(\mathrm{Re}_m) - 1.64)^{-2}$	$0.5 \le \mathrm{Pr}_m \le 2000$; $3000 \le \mathrm{Re}_m \le 5\times10^6$
Dittus-Boelter (Incropera et al., 2007)	$Nu_m = \frac{h_m' d_H}{k_m} = 0.023\,\mathrm{Re}_m^{0.8}\,\mathrm{Pr}_m$ $m = 0.3$ for cooling and 0.4 for heating.	$0.6 \le \mathrm{Pr}_m \le 160$; $\mathrm{Re}_m \ge 10000$ and $L/d_H \ge 10$
Seider-Tate (Incropera et al., 2007)	$Nu_m = \frac{h_m' d_H}{k_m} = 0.027\,\mathrm{Re}_m^{0.8}\,\mathrm{Pr}_m^{0.33}\left(\frac{\mu_m}{\mu_{m,wall}}\right)^{0.14}$	$0.7 \le \mathrm{Pr}_m \le 16700$; $\mathrm{Re}_m \ge 10000$ and $L/d_H \ge 10$

From Table 2.13, it is seen that the most suitable correlation is given by Geielinski for our experimental conditions: $6.29 \le \mathrm{Pr}_m \le 7.14$; $3010 \le \mathrm{Re}_m \le 6124$. The Geielinski correlation represents the Nusselt number (Nu_m) as a function of Reynolds number (Re_m), Prandtl number (Pr_m), and the friction factor (f_m'). The Prandtl number for the two-phase mixture can be represented as

$$\mathrm{Pr}_m = \frac{C_{P,m}\mu_m}{k_m} \tag{2.63}$$

In the Eq. (2.63), $C_{P,m}$, μ_m and k_m are the specific heat capacity, viscosity, and the conductive heat transfer coefficient of the two-phase mixture. $C_{P,m}$ and k_m are calculated by Eqs. (2.64) and (2.65) respectively

$$C_{P,m} = (M_w'/M_m')C_{P,w} + (M_o'/M_m')C_{P,o} \tag{2.64}$$

$$k_m = \alpha_w k_w + \alpha_o k_o \tag{2.65}$$

The average C_p and k values between the temperature 25°C – 30°C for water and toluene are 4179.0 J kg^{-1} K^{-1}, 0.6104 W m^{-1} K^{-1}, and 1752.18 J kg^{-1} K^{-1}, 0.1398 W m^{-1} K^{-1} respectively. In Eq. (2.64), M' is the mass flow rate of the fluids. The two-phase heat transfer rate (q_m) is calculated by using the Eq. (2.66).

$$q_m = h_m^{'} A_S \Delta T_{lm} = h_m^{'} (P \times L) \Delta T_{lm} \tag{2.66}$$

It is clear that the local entropy generation rate does not only depend on the temperature gradient. It depends on the flow condition and the physical properties of the fluid mixtures. The variation of the local entropy generation rate for a constant temperature gradient with the change of flow properties like Nusselt number and mass flow rate of the water-toluene mixture is shown in Figs. 2.25(a) and 2.25(b).

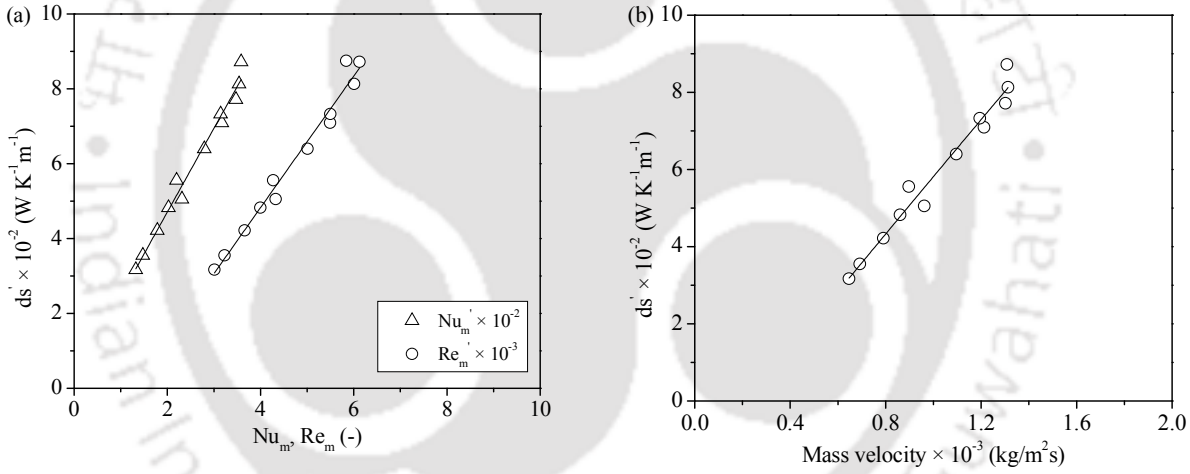

Fig. 2.25. Variation of local entropy generation rate with the flow properties: (a) Nusselt number and Reynolds number and (b) Mass velocity.

From Fig. 2.25, it is seen that with the increase of the Nusselt number or mass flow rate of the two-phases, the local entropy generation rate increased due to the increase of turbulence within the flow channel. Similarly, the entropy generation rate becomes greater with the increase of the Reynolds number and decrease of the friction factor as the Reynolds number and friction factor are inversely proportional to each other. The pressure drop contribution to the entropy generation rate also shows a similar trend in the case of the two-phase flows (Fig. 2.26).

Generally, with the increase of pressure on a stationary system, the entropy of the system decreases. But, in the present experiment, the increased pressure drop is obtained as a result of the increased mass flow rate or Reynolds number. Hence, increased turbulence within the channel increases the local entropy generation rate as the consequence of higher-pressure loss. Nusselt number is the most important dimensionless number in the convective heat transfer calculations, which attracts the attention of the researchers for the generation of the correlations.

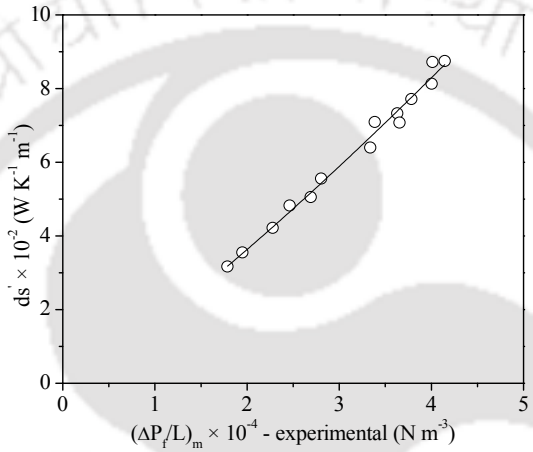

Fig. 2.26. Variation of local entropy generation rate with the pressure drop.

The experimental Nusselt number values are calculated by using the Eq. (2.67).

$$Nu_m = \frac{h_m' d_H}{k_m} \tag{2.67}$$

The h_m' (heat transfer coefficients) values are calculated by using the Eq. (2.68)

$$M_m' C_{p,m}(T_{outlet} - T_{inlet}) = h_m' A_S \Delta T_{lm} \tag{2.68}$$

where T_{outlet} and T_{inlet} are the outlet and inlet temperatures of the fluids, respectively. A_S is the total heat transfer surface area of the rectangular channel. The regression analysis is done to form the Nusselt number correlation for the water-toluene two-phase flow through the rectangular channel, as shown in Eq. (2.69).

$$Nu_m = 6.38 \times 10^{-4} \left(\mathrm{Re}\,\mathrm{Pr}\right)^{0.9629} \tag{2.69}$$

The Eq. (2.69) satisfies the experimental data with the correlation coefficients and the standard errors of 0.9988 and 0.009, respectively. It shows a maximum 62.37% error with the Geielinski correlation, which is valid for single-phase and vertical columns but shows only a maximum 1.74% error with the experimental data. The deviation of the experimentally calculated Nusselt number values from the values estimated from our newly generated correlations is shown in Fig. 2.27.

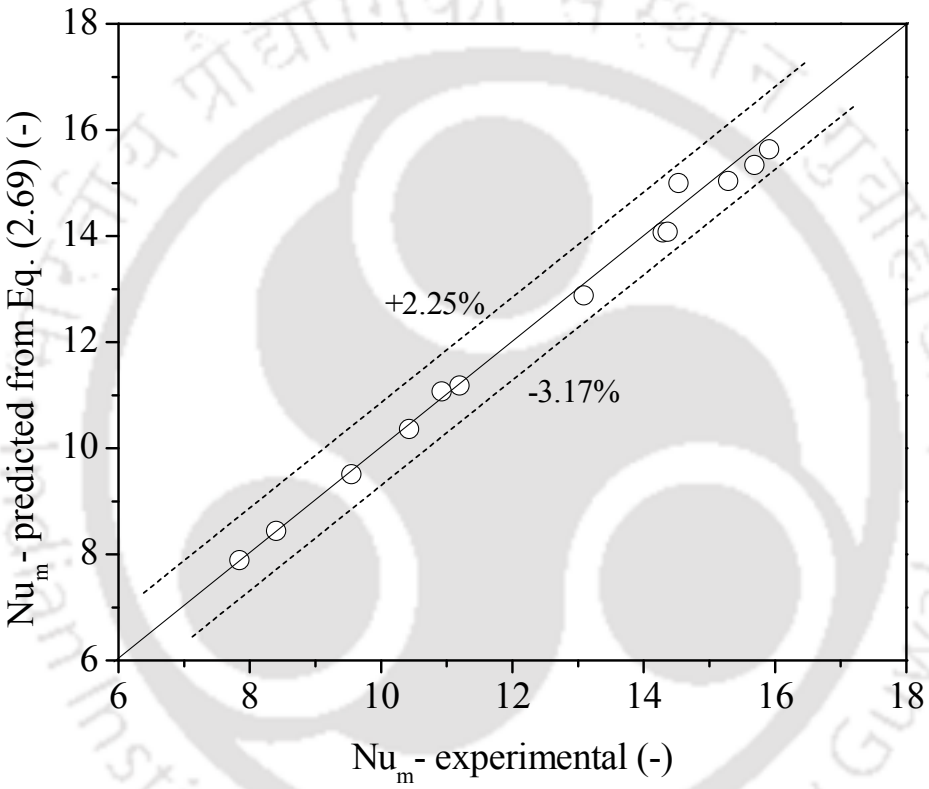

Fig. 2.27. Comparison of Nusselt number values obtained from the experiment and our newly generated correlation.

2.5. Conclusions

The frictional pressure drops in the packed and unpacked rectangular straight and serpentine channels in horizontal orientation are enunciated in the present context. The results obtained in the present study are not predicted well with the available correlation as the geometry, and the flowing fluids are different. Therefore, the new correlation is developed for the present geometry and fluids

systems based on the concept of different models. Depending on the results of the present research, the conclusions are assembled as follows:

a. The fluids flow rate is significant for the calculations of pressure drop and friction factor in the packed and unpacked rectangular straight and serpentine millichannels. The effect of gravity is absent in the case of the single-phase flow.
b. The present work modifies the Ergun equation applicable to the flow in the packed straight and serpentine channels. The modified Ergun equation shows excellent performance to predict the frictional pressure drop.
c. The local entropy generation rate increases with the increase of pressure drop in the case of the water-toluene flow through the unpacked straight channel.

The geometry of the rectangular straight and serpentine channels used in the present study can be scaled up by a numbering up approach. Our proposed correlations, based on the present experiment, may be used for the design of millichannel based two-phase unit. The present study may be useful for further understanding of two-phase flow through milli or microchannel based devices applied for process intensification. The rectangular serpentine channel provided a higher mixing efficiency due to the existence of the Dean flow at the expense of higher pressure loss, which can make it more feasible in transport applications. With the incorporation of packing material, the mixing efficiency was again increased. The rectangular serpentine channel in the packed condition is highly recommended for intense mixing efficiency for the higher mass transport applications at the cost of higher frictional loss.

Chapter 3

Hydrodynamics and Mixing in Rectangular Millimetric Packed Multichannel Based Device

In the present chapter, the hydrodynamics and mixing characteristics for the single aqueous as well as the two-phase air-water flows through the rectangular millimetric packed channels having the variable cross-sections are studied with the help of residence time distribution (RTD) method. RTD studies are essential to determine the operating parameters for the design or scaling up the non-ideal reactors. The present study includes the mixing and mass transfer characteristics, which were explained with the help of the axial dispersion model (ADM) for the water, and air-water two-phase flows through the millimetric packed multichannel systems with different cross-sections.

3.1. Introduction

Gas-liquid flow through the fixed bed reactors are extensively used in the chemical industries, as in the operations of trickle bed reactors (gas-liquid concurrent downflow) (Stegeman et al., 1996; Iliuta et al., 1996a), packed bubble column reactors (concurrent upflow) (Iliuta et al., 1996b), and absorption or catalytic distillation columns (countercurrent flow) (Yuan et al., 2004). However, the gas phase may flow, in the concurrent or countercurrent direction, the concurrent flow is highly suggested for high loading, as there is a possibility of flooding in countercurrent flow (Wammes et al., 1991). The liquid-liquid mass transfer can also be intensified by the gas agitation (Su et al., 2009). The packed bed provides a higher surface area to interact (catalyst packing), along with the higher interfacial mixing between the phases at the detrimental of the higher-pressure drop. The characteristic features of the packed bed made it preferable for the heat and mass transport applications. In recent decades, the milli- and micro-channels captivated the attraction of the researchers due to its high surface to volume ratio, which is beneficial for the amelioration of the transport applications. The mixing efficiency inside the packed columns profoundly affects the

other parameters like transport rate, product yield, and selectivity in any process. Hence, the residence time distribution (RTD) analysis is an important tool for the design of a transport device, which provides the essential information to interpret the mixing efficiency of the single- or two-phase flows inside the packed columns. Significant advancement in process intensification has been achieved by the implementation of miniature packed reactors with their enhanced fluids mixing and transport performances. However, the miniature devices are found to be lacking in industrial applications through large production and high throughput, which is required a numbering-up approach in terms of multichannel devices (Tonomuraet al., 2007; Saberet al., 2010; Yue et al., 2010). In a multichannel device, the conformity in the fluid distribution is regarded as the crucial issue to attain high-level performance and industrial-level production, which prompted to the parallelization of a large number of flow paths or packed multichannel. The parallelized milli- or micro-multichannel geometries are more effective than their series (Kockmann, 2007). The multi-millimetric channels can be used for the heat and mass transfer applications for their intense mixing and intensified transport properties (Guo et al., 2018). The literature showed that only a few studies are available for the flow-through millimetric single channel with packing (Serres et al., 2018), and without packing (Kulkarni and Kalyani, 2009; Zhang et al., 2011b), and the millimetric multichannel without packing (Guo et al., 2018). There is a lack of studies in the millimetric packed multichannel geometries for the single as well as gas-liquid two-phase flows.

In the present study, the hydrodynamics and mixing characteristics for the single-phase (water), and the air-water two-phase flows through the packed multichannel geometries (millimetric dimensions) were studied by pulse tracer input method. Depending on the flow rates and the other geometrical parameters, the characteristic features of the fluid distribution uniformity in the multichannel devices change, which can be demonstrated by the axial dispersion RTD representation. The mixing characteristics depending on the operating parameters were interpreted with the help of the RTD curves and were compared with the available correlations. The effect of the multichannel dimensions on the flow distribution was also illustrated adequately by varying the heights of the channels for the two multichannel blocks in the present context.

3.2. Experimentation

3.2.1. Reagents and instrumentation

Deionized water from the Milli-Q water purification system (Millipore, MA, USA) was used in the experiment. The other two required materials, potassium chloride (KCl, 99.5.0%, M.W. = 74.55 g mol^{-1}, ACS reagent grade) and glass beads (average diameter (d_p) of 350 µm) were supplied by the Merck Life Science Private Limited and Amazon.in, respectively.

The main experimental section consists of two different rectangular multichannel blocks (11 channels each) of variant heights packed with the glass beads. The width (w) of the individual channels were 2×10^{-3} m with the heights (h) of 0.6×10^{-3} (Block-1), and 1.2×10^{-3} m (Block-2), respectively, for the two multichannel blocks. The total length (l) of all the channels was 9.7×10^{-1} m, and the average of the total length was considered as the length (l_i) of each channel (8.82×10^{-2}) in the multichannel block. The particle diameter (d_p) is considered as the characteristic length in the case of the packed bed. It was assumed that the flow was equally divided through the channels. A schematic diagram of the experimental setup, as shown in Fig. 3.1.

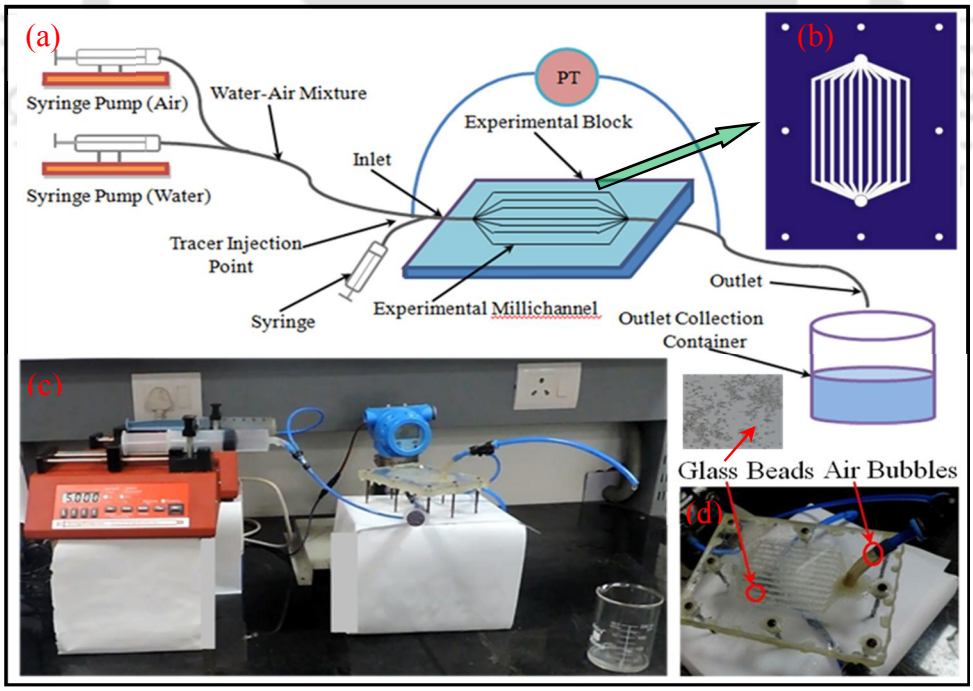

Fig. 3.1. (a) Schematic diagram of the experimental setup, (b) Top view of the experimental multichannel block, (c) Snapshot of the experimental setup, and (d) Snapshot of the multichannel block in operating condition.

Two syringe pumps (supplied by Amar Equipments Pvt. Ltd.) were used to regulate the volumetric flow rates of the gaseous phase (air), and the aqueous phase (water) respectively, through the channels, and the tracer solution was inserted (pulse input) into the system just before the inlet point through the injection port. A pre-calibrated differential pressure transmitter (Make: Electronet Equipments Pvt. Ltd., Model: ELPRT100SDP, Accuracy: ± 0.075% of URL for turndown ratio ≤ 10:1) was connected at the inlet and outlet points to measure the pressure drop for the volumetric flow rates of the fluids. An electrical conductivity meter (Model: VSI-04 ATC Deluxe, VSI Electronics Pvt. Ltd., India) was used to measure the conductivity of the collected samples. All the experiments were performed at room temperature (298 K).

3.2.2. Procedure to perform the mixing studies (Residence Time Distribution, RTD)

The millimetric multichannel block packed with the glass beads was filled with the fresh milli-Q water so that the air inside the channel removed. Then the syringe pumps (for air and water supply) were started simultaneously, and the 0.5 ml of 1 M KCl solution as the tracer was injected just before the inlet of the packed bed column by pulse input method. The stopwatch was started immediately with the pulse input, and the samples were collected at the outlet with the same time intervals. The conductivities (S m^{-1}) of the collected samples were measured to estimate the concentrations of the tracer solution at the outlet point with respect to time. At the same time, the differential pressure values (minimum 20 values) were noted down, and the average of the values was considered as the actual pressure difference between the inlet and outlet points. The same processes were repeated by changing the flow rates of the fluids pair. In the case of the single-phase flow operations, both the syringes were filled with the water (aqueous phase) only.

3.3. Theoretical background

3.3.1. Pressure drop analysis

The viscosity, surface tension, density, velocity of the flowing fluids and their mixtures, the diameter of the packed materials, and the dimensions of the channel affects the pressure drop in the rectangular packed milli-channel blocks for the single-phase and multiphase flows. The

physical properties of the multichannel columns, packing materials, packed bed, and the flowing fluid are tabulated in Table 3.1. The pressure drop value for the flow through the channel can be correlated using the following dimensionless numbers, as shown in (Eqs. (3.1-3.4)).

$$\mathrm{Re}_{p,m} = \frac{\rho_m (U_m / \varepsilon_{eff}) d_p}{\mu_m} \tag{3.1}$$

$$Ca_{p,m} = \frac{\mu_m (U_m / \varepsilon_{eff})}{\sigma_m} \tag{3.2}$$

$$We_{p,m} = \mathrm{Re}_{p,m}\, Ca_{p,m} = \frac{\rho_m (U_m / \varepsilon_{eff})^2 d_p}{\sigma_m} \tag{3.3}$$

$$Fr_{p,m} = \frac{U_m / \varepsilon_{eff}}{\sqrt{(9.81 \times d_p)}} \tag{3.4}$$

where $Re_{p,m}$ (-), $Ca_{p,m}$ (-), $We_{p,m}$ (-), and $Fr_{p,m}$ (-) are the particle Reynolds number, Capillary number, Weber number, and Froude number for the flow through the individual packed channel. Whereas, ρ_m (kg m^{-3}), μ_m (N-s m^{-2}), and σ_m (N m^{-1}), are the fluid density, dynamic viscosity, and surface tension of the two-phase mixture, respectively. The mixture properties of the two-phases were calculated as per the method of Mondal and Majumder, 2018. The actual velocity of the fluid mixture through each channel and the effective porosity of the packed bed are represented by U_m (m min^{-1}), and ε_{eff} (-). d_p is the particle diameter (m) of the packing material. The hydraulic diameter of a rectangular channel can be calculated by Eq. (3.5).

$$d_H = \frac{2wh}{w+h} \tag{3.5}$$

where w and h are the width and height of the rectangular cross-section. In the present study, the experimental multichannel block consist of eleven channels of an identical cross-section. It was considered that each channel experienced the same pressure loss as the total pressure loss ($\Delta P_1 = \Delta P_2 = ... = \Delta P_i = \Delta P_f$; where ΔP_i is the pressure loss of the i^{th} channel, and ΔP_f is the total frictional pressure loss), and the total volumetric flow rate (Q) is equally subdivided into each channel ($Q_i = 11Q$). The gas holdup values at the different flow rates were determined by the ratio of the volumetric flow rates of the gas phase to the total volumetric flow rates of the two-phases.

Table 3.1. Properties of the multichannel columns, packing materials, packed bed, and the flowing fluid.

Channel geometry		**Packing material**		**Packed bed**		**Fluid properties**	
Multichannel block-1		**Multichannel block-1**		**Multichannel block-1**		**Water**	
Width of the individual channel, w (m)	2.0 $\times 10^{-3}$	Sphericity, ϕ (-)	1.0	Effective porosity, ε_{eff} (-)	0.34	Density, ρ_w (kg m^{-3})	9.97 $\times 10^{2}$
Height of individual channel, h (m)	0.6 $\times 10^{-3}$	Average diameter, d_p (m)	3.50 $\times 10^{-4}$	The total volume of the bed, V_T (m^3)	1.164 $\times 10^{-6}$	Viscosity, μ_w (N-s m^{-2})	8.97 $\times 10^{-4}$
The total length of the multichannel, l (m)	9.70 $\times 10^{-1}$	**Multichannel block-2**		Total void volume, V_{void} (m^3)	0.396 $\times 10^{-6}$	Surface tension, γ_w (N m^{-1})	7.18 $\times 10^{-2}$
Length of an individual channel, l_i (m)	8.82 $\times 10^{-2}$	Sphericity, ϕ (-)	1.0	Tortuosity, τ (-)	2.08	**Air**	
The cross-sectional area of an individual channel, A_i (m^2)	1.20 $\times 10^{-6}$	Average diameter, d_p (m)	3.50 $\times 10^{-4}$	**Multichannel block-2**		Density, ρ_a (kg m^{-3})	1.18
Multichannel block-2				Effective porosity, ε_{eff} (-)	0.34	Viscosity, μ_a (N-s m^{-2})	1.84 $\times 10^{-5}$
Width of the individual channel, w (m)	2.0 $\times 10^{-3}$			The total volume of the bed, V_T (m^3)	2.328 $\times 10^{-6}$	Surface tension,	N.A.

					γ_a (N m^{-1})	
Height of individual channel, h (m)	1.2 $\times 10^{-3}$		Total void volume, V_{void} (m^3)	0.792 $\times$ 10^{-6}		
The total length of the multichannel, l (m)	9.70 $\times 10^{-1}$		Tortuosity, τ (-)	2.08		
Length of an individual channel, l_i (m)	8.82 $\times 10^{-2}$					
The cross-sectional area of an individual channel, A_i (m^2)	2.40 $\times 10^{-6}$					

3.3.2. Residence Time Distribution (RTD) analysis

3.3.2.1. Moment analysis and the axial dispersion model

The density distribution function *E(t)* of an RTD for the pulse injection of the tracer can be obtained from the relation (Eq. (3.6)) given by Levenspiel (1999).

$$E(t) = \frac{c(t)}{\int_0^{\alpha} c(t)dt} \tag{3.6}$$

where *c(t)*, is the concentration profile of the tracer at the outlet. *E(t)* is generally characterized by the first and second moments of the distribution. The mean residence time (t_m), is described by the first moment of distribution (Eq. (3.7)). In the second moment of the distribution, the variance (σ_v) of RTD is defined as the square deviation from the mean and is represented by Eq. (3.8). Lower the value of variance corresponds to the narrower distribution.

$$t_m = \frac{\int_0^{\alpha} tE(t)dt}{\int_0^{\alpha} E(t)dt} = \int_0^{\alpha} tE(t)dt \tag{3.7}$$

$$\sigma_v^2 = \int_0^{\alpha} (t - t_m^2)E(t)dt = \int_0^{\alpha} t^2 E(t)dt - t_m^2 \tag{3.8}$$

The dimensionless form of the variance (σ_θ^2), can be calculated by the Eq. (3.9).

$$\sigma_\theta^2 = \frac{\sigma_v^2}{t_m^2} \tag{3.9}$$

where θ is the dimensionless time ($\theta = t / t_m$). In the context of the axial dispersion model (ADM), the analytical solution of the normalized *E(t)* curves for the open-open boundary conditions, and the large deviation from the plug flow (i.e., $Pe_a < 100$), was proposed by the Levenspiel (1999), which can be represented by the Eq. (3.10).

$$E_\theta(t) = \frac{1}{2\sqrt{\pi\theta / Pe_a}} \exp\left(-\frac{(1-\theta)^2 Pe_a}{4\theta} \right) \tag{3.10}$$

where Pe_a is the axial Peclet number, which is the ratio of convective to the diffusive transport. The reciprocal of the Peclet number is called the dispersion number, which is used for the measurement of the axial dispersion coefficient. Higher the axial Peclet number corresponds to the plug flow. The Peclet number for the axial dispersion is expressed by the Eq. (3.11).

$$Pe_a = \frac{(U_m / \varepsilon_{eff})d_p}{D_{ax}} \tag{3.11}$$

where D_{ax} is the axial dispersion coefficient ($m^2\ s^{-1}$) of the tracer in each channel. D_{ax} contains all the effects that are responsible for the deviation from plug flow. Based on the moment method, the Peclet number can be correlated to the variance of the RTD (experimental), as shown in Eq. (3.12).

$$\sigma_\theta^2 = \frac{\sigma^2}{t_m^2} = \frac{8}{Pe_a^2} + \frac{2}{Pe_a} \tag{3.12}$$

According to Guo et al. (2018), the global RTD curve obtained for the multichannel systems in case of a particular volumetric flow rate is the combination of all the individual RTD curves considering each channel flow rate as the weighting factor (Eq. (3.13)).

$$E(t) = \frac{1}{Q}\sum_{i=1}^{n} Q_i E_i(t) \tag{3.13}$$

where *i* stands for the i[th] number of channels, and *n* is the number of channels. Therefore, in the case of the multichannel flow devices, the Peclet number obtained from the global RTD curves is the combination of the Peclet numbers of each individual channel. According to Taylor (1953), and Aris (1956), the axial dispersion model is applicable when

$$4l_i / (d_H / 2) \gg 6.9 \tag{3.14}$$

In the present case, the value was found to be 764.24 (block-1), and 470.4 (block-2), which satisfied the applicability of the axial dispersion model in the present experimental system.

3.3.2.2. Velocity distribution model

The actual dispersion coefficient depends on the combined effect of axial dispersion and molecular dispersion coefficients. In the present experimental condition, due to the low residence time inside the packed bed and the continuous flow disturbance due to the presence of particles, the effect of molecular diffusion on the characteristics of the RTDs is negligible (Atmakidis and Kenig, 2015). Molecular diffusion is insignificant compared with the axial dispersion in the case of multichannel tubular columns (Guo et al., 2018). In the present experimentation, the geometry of the multichannel columns are different from that has been reported by Guo et al. (2018). Hence, the molecular diffusion coefficients, along with the axial dispersion coefficients, have been studied in the present context. The axial dispersion coefficient (D_{ax}), for the laminar flow of fluids through a packed bed, can be calculated based on the concept of Taylor (1953), and Aris (1956) (proposed the relation for the laminar flow in tubular columns), which can be expressed as

$$D_{ax} = \frac{d_p^2 (U_m / \varepsilon_{eff})^2}{48 D_m} + D_m \tag{3.15}$$

Squires and Quake (2005), and Ajdari et al. (2006) proposed the similar types of correlations for the non-circular tubes, which can be written in terms of the packed bed parameters as

$$D_{ax} = \frac{d_p^2 (U_m / \varepsilon_{eff})^2}{192 D_m} + D_m \tag{3.16}$$

where D_m is calculated from the molecular diffusive Peclet number, expressed as

$$D_m = \frac{\left(U_m / \varepsilon_{eff}\right) d_p}{Pe_m} \tag{3.17}$$

The Peclet number for the molecular diffusion (Pe_m) can be obtained from the Eq. (3.18) (Delgado, 2006).

$$\frac{1}{Pe_a} = \frac{1}{\tau}\frac{1}{Pe_m} + \frac{1}{2} \tag{3.18}$$

where τ is the tortuosity (-). The tortuosity for the flow through a randomly packed bed of symmetrical particles can be calculated by the Eq. (3.19) (Lanfrey et al., 2010).

$$\tau = 1.23\frac{\left(1-\varepsilon_{eff}\right)^{4/3}}{\varepsilon_{eff}\phi_s^2} \tag{3.19}$$

where ϕ_s is the sphericity (-, holds the value one for the spherical glass beads). The tortuosity value was found 2.08 (-) in the present multichannel packed bed. Depending on the simulation results, Zeiser et al. (2001) suggested a correlation for the determination of the dispersion coefficients inside a packed bed column, which is represented by the Eq. (3.20).

$$\frac{D_{ax}}{D_m} = 0.758 + \frac{Pe_m^{1.83}}{39} \tag{3.20}$$

3.3.3. Specific energy dissipation and the mixing performance in the multichannel packed bed columns

The specific energy dissipation (E_d) in a channel based column increases with the increase of pressure drop, as shown in the Eq. (3.21).

$$E_d = \frac{Q\Delta P}{M_f} \tag{3.21}$$

where,

$$M_f = \rho V_{void} \tag{3.22}$$

where M_f is the mass (kg) of the fluid into which the specific energy is dissipated, and V_{void} is the void volume of the multichannel packed bed, calculated by subtracting the volume of the packing material from the total volume of the bed. The higher value of specific energy dissipation (W kg^{-1}) indicates the higher mixing performance of the columns, and its value is higher in the case of

multichannel continuous flow columns than the series of batch columns (Kockmann, 2007). According to Su et al. (2015), depending on the volumetric flow rate and pressure drop, the specific energy dissipation holds the values of magnitude between 10^{-2} – 10^{3} W kg^{-1}. When the value is < 10^{2} W kg^{-1}, the mixing process is generally effected by molecular diffusion, which is a long way from ideal mixing. The value > 10^{2} W kg^{-1}, corresponds to the ideal or complete mixing controlled by the convection. In the packed bed multichannel columns, the performance of higher mixing may attain at the cost of higher dissipation of specific energy.

The error percentages ($\%E$) between the experimental (q_{exp}) and the calculated (q_{cal}) values are determined by following the Eq. (3.23).

$$\%E = \frac{\left|q_{\exp} - q_{cal}\right|}{q_{\exp}} \times 100 \tag{3.23}$$

where q_{exp}, and q_{cal} are the adsorption capacities obtained from the experiment, and the calculations, respectively.

3.4. Results and discussion

3.4.1. Mixing characteristics

3.4.1.1. Effect of volumetric flow rate on RTD curves and axial dispersion model (ADM)

The RTD curves become sharper at a higher flow rate, which corresponds to the lower mean residence time (t_m) for the single-phase flow (Fig. 3.2(a)). In the case of two-phase flow, when the flow rate of one phase is increased, leaving the other unaltered, the residence time decreased, and the RTD curves become sharper due to the increment of the velocity of the phases for the same volumetric flow rate (Fig. 3.2(b-c)). When the height of the packed channels (uniform packing materials and the bed porosity) decrease, for a particular flow rate of the fluids, the velocities and the mixing properties of the phases increased lowering the residence time and making the RTD sharper (Fig. 3.2(b), and Fig. 3.2(c)). The Peclet number, the ratio of advection to diffusion, is an important axial dispersion parameter, which reflects the degree of mixing, increases with the increase of flow rate or Reynolds number (Fig. 3.4(a)). The advection-dominated distribution is desired when the Peclet number is higher, whereas the smaller Peclet number is responsible for a diffusive flow. In the cases of the packed bed, the Peclet number increases with the increase of the

flow rate of fluid for the single-phase flow (Yoon and Nelson, 1984; Lanfrey et al., 2010; Zhang et al., 2016; Rastegar and Gu, 2017). However, in the case of water-air two-phase flow, with the increase of airflow, the Peclet number decreases due to the increasing gas holdup (Fig. 3.4(b)). The increasing gas holdups with the increasing gas flow rates are shown in Fig. 3.3. The gas holdup attains the higher value at the higher gas flow rate and the lower liquid flow rate. At the low liquid and high gas velocities, the Peclet number holds the lower value, which indicates the presence of a diffusive process. In that case, the dispersion coefficient is proportional to the ratio of the diffusion coefficient to the tortuosity (τ). At the high liquid and low gas velocities, when the Peclet number is higher ($Pe_a > 10$), the dispersion is controlled by the advection (Yoon and Nelson, 1984). A similar trend in the case of molecular Peclet number was obtained in the case of the single-phase, as well as the two-phase flows due to the reason as mentioned above (Fig. 3.4(c) and Fig. 3.4(d)). The channel dispersion number is the inversion of the Peclet number. When the channel dispersion number increases, the RTD curves become broader, as shown in Fig. 3.2(a) (Sharma et al., 2017). As per the present experiment, the lowest flow rate (1.0 ml min^{-1}) corresponds to the highest dispersion number (0.09 (-)) for the single-phase flow through the channels block-1. However, in the case of multiphase flow, the above-specified trends altered for the gas flow. At the lowest water flow rate (5.0 ml min^{-1}) and highest air flow rate (23.0 ml min^{-1}), the dispersion number values were largest, which were 1.86 for the channels block-1, and 1.90 for the channels block-2. The axial dispersion coefficients, estimated from the RTD curves, hold a higher value at the higher flow rate of fluid in the case of single-phase, as shown in Fig. 3.5(a). However, in the case of two-phase flow, though the Peclet number decreases with the increase of gas flow, axial dispersion coefficient increases in both of the cases, either with the increase of liquid flow or gas flow, as the turbulence increases in both of the cases (Fig. 3.5(b)).

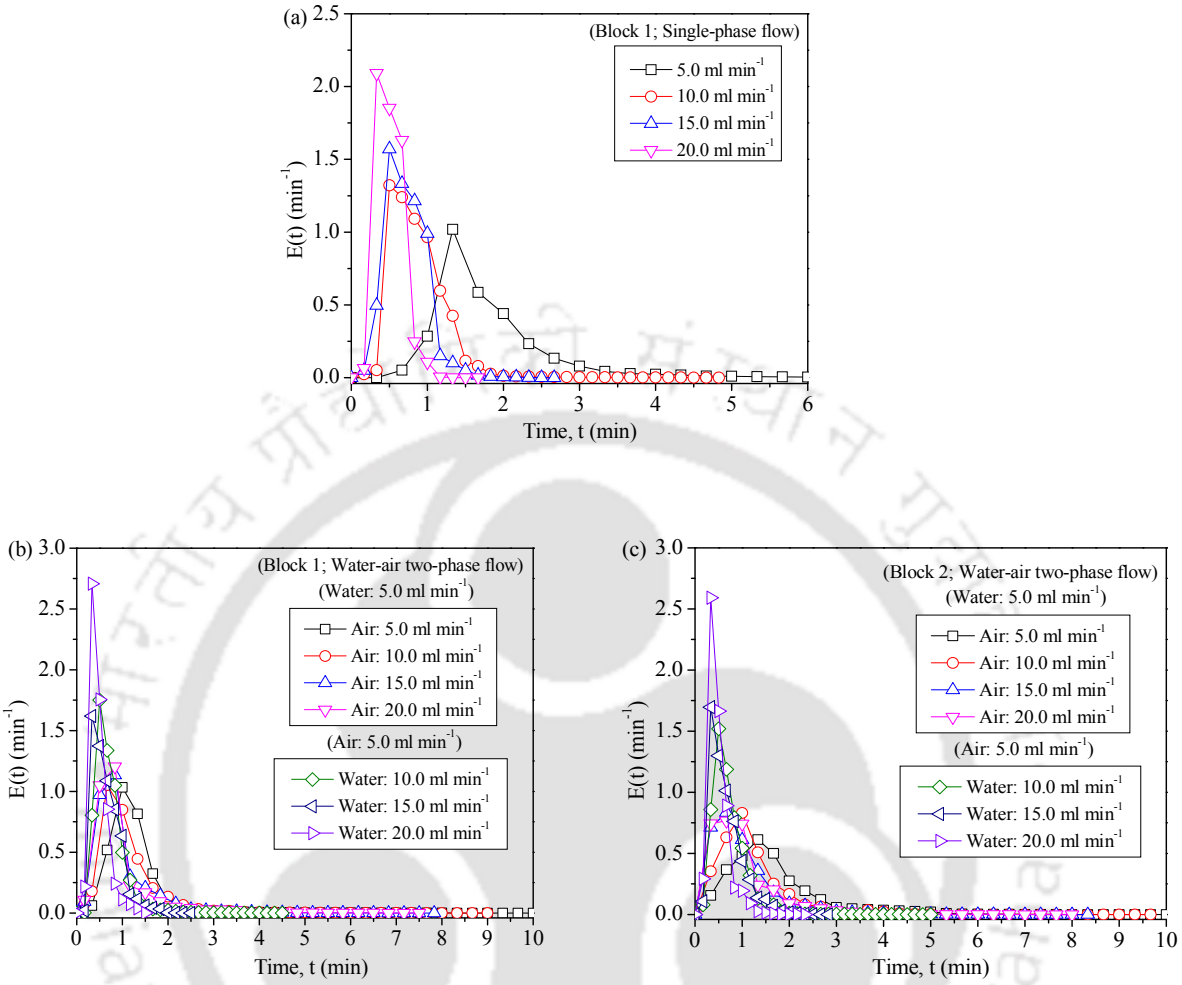

Fig. 3.2. The RTD curves at (a) different flow rates of water, (b) air-water two-phase flows (block – 1), and (c) air-water two-phase flows (block – 2).

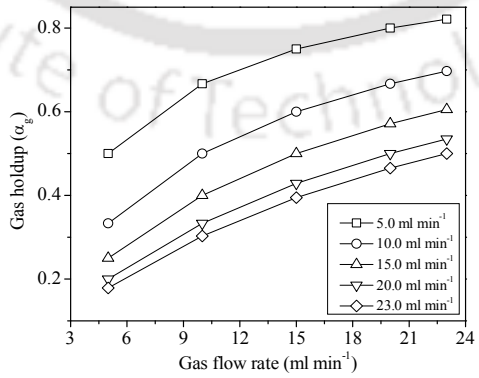

Fig. 3.3. Gas holdup with the variation of the gas flow rate.

With the increasing volumetric flow rate, the Reynolds number, and the rate of specific energy dissipation increases, which results in higher axial dispersion, as shown in Fig. 3.5(c), and Fig. 3.5(d).

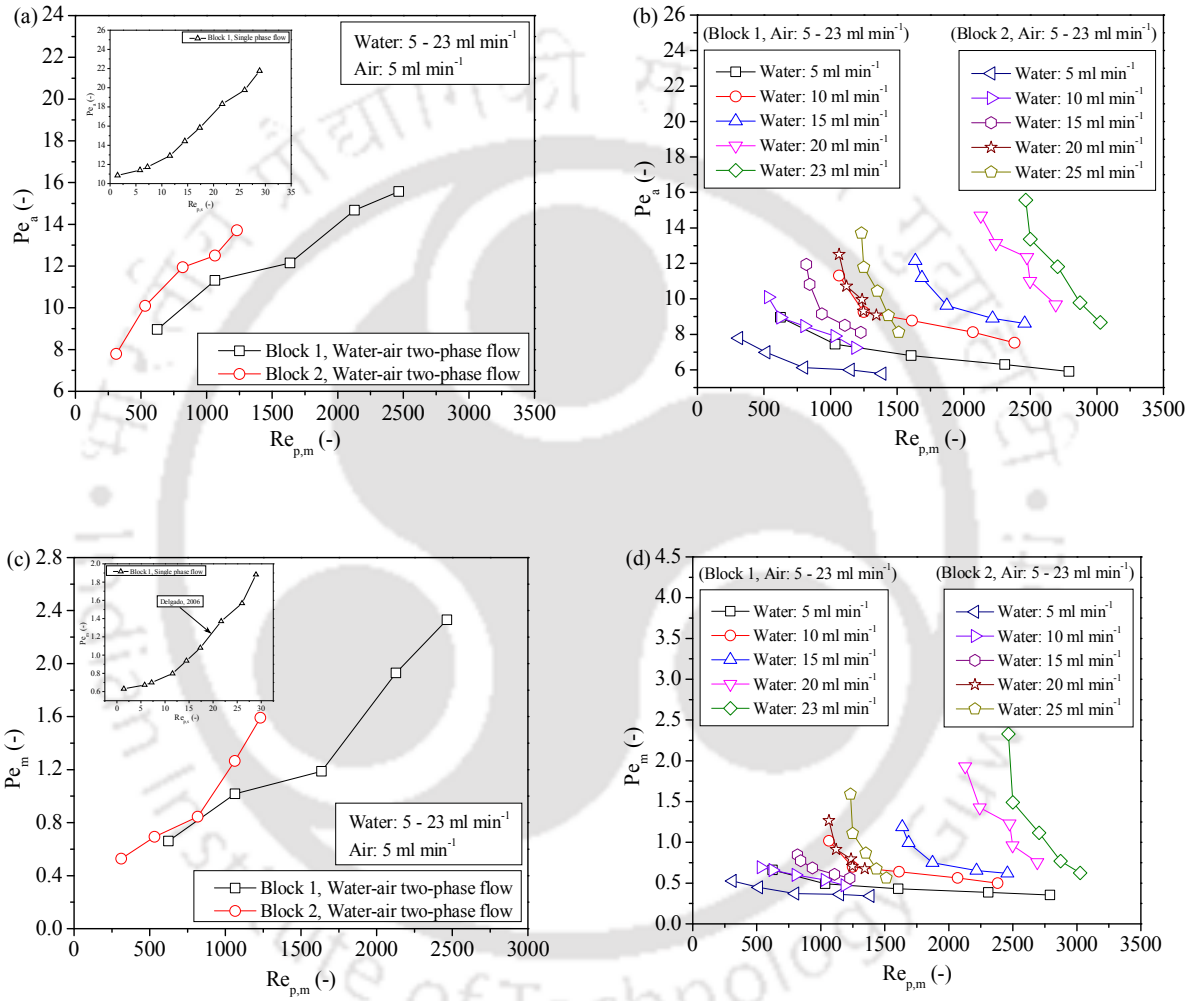

Fig. 3.4. Variation of the axial Peclet number, (a) with the variation of single-phase flow, (b) with the variation of two-phase flow, and the variation of the molecular Peclet number (c) with the variation of single-phase flow, (d) with the variation of two-phase flow.

In the present context, the specific energy dissipation (E_d) values were < 10^2 W kg^{-1} for both the blocks within the flow range. Therefore, according to Zeiser et al. (2001), the mixing processes were affected by molecular diffusion. The specific energy dissipation (Ed) values for the single

and two-phase flows for both the channel blocks were shown in Fig. 3.5(c) and Fig. 3.5(d), respectively. Though, the increment of D_{ax}/D_m ratio, with the increase of Reynolds number, indicates that the axial dispersion coefficient dominates over the diffusion coefficient at higher velocities (Fig. 3.8).

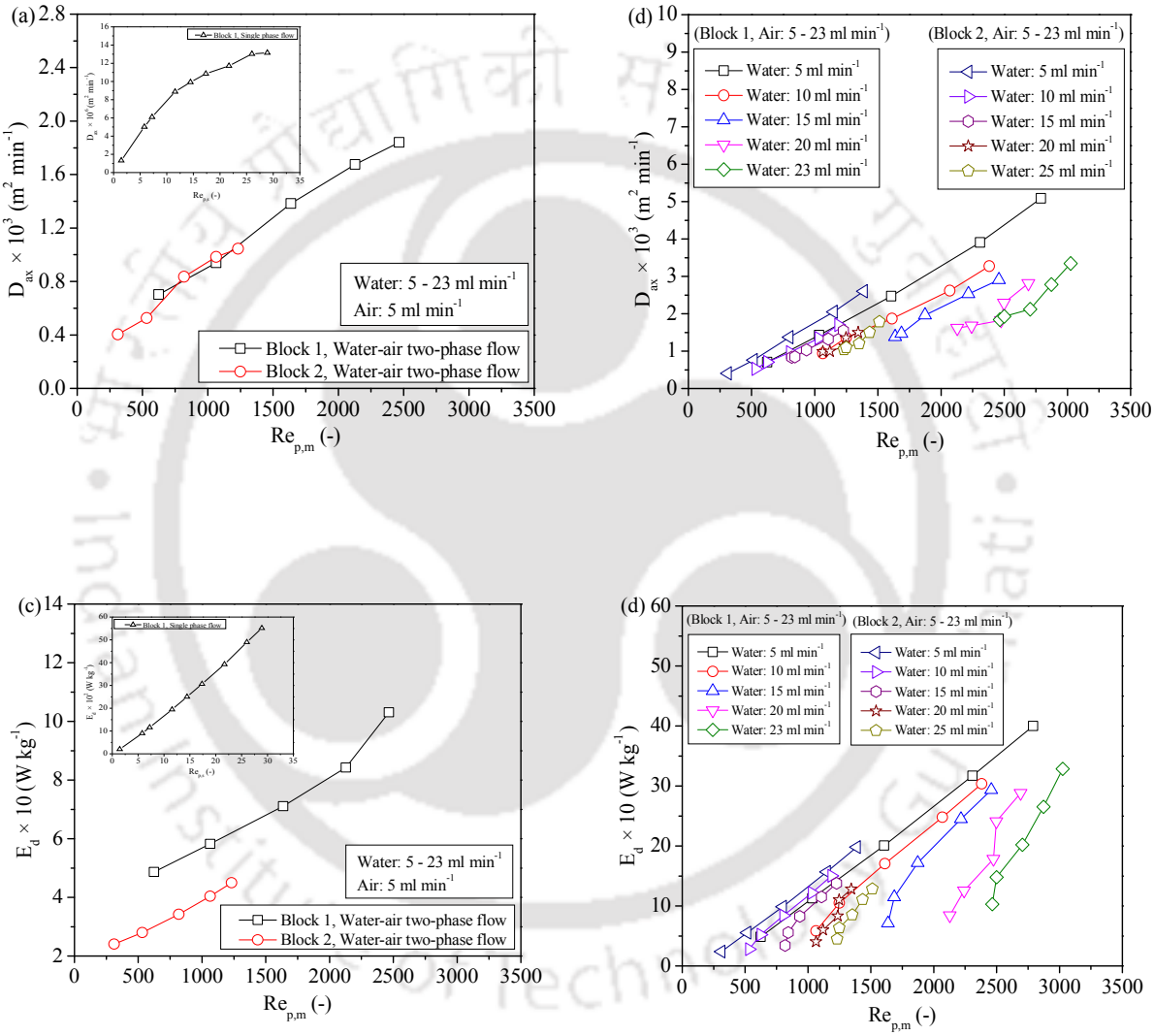

Fig. 3.5. Variation of the axial dispersion coefficient, (a) with the variation of single-phase flow, (b) with the variation of two-phase flow, and the variation of the specific energy dissipation (c) with the variation of single-phase flow, (d) with the variation of two-phase flow.

When the flow rate increases, the Reynolds number increases, giving the tracer molecules less time to pass through the device (Fig. 3.6). The Reynolds number value is greater in the case of block-1, over the block-2, for the same volumetric flow rate, as it experienced a higher velocity due to the lower cross-sectional area. Therefore, the residence time is lower for block-1 than block-2 at the same volumetric flow rate (Fig. 3.6(b)). With the increasing liquid flow rate or gas flow rate at a particular liquid flow rate, the axial dispersion coefficient increases, increasing the mass transport rate. Still, due to the decrease of the retention time inside the device, the overall mass transport decreases for the physical transport processes like adsorption, where higher residence time is beneficial (Fig. 3.6(a)).

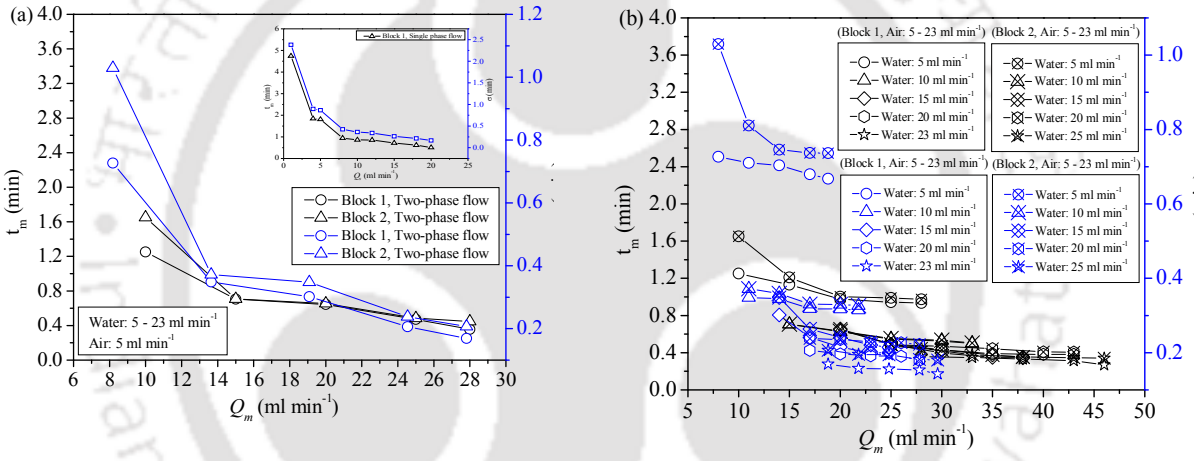

Fig. 3.6. Variation of the mean residence time (t_m), and the variance (σ) of RTD with respect to the volumetric flow rate for the (a) single-phase flow, and (b) two-phase flow.

The RTD parameters, Reynolds number, pressure drop, and the specific energy dissipation for the individual channel for the single-phase flow through block-1 are shown in Table 3.2. The two-phase flow parameters for the block-1 and block-2 are shown in Table 3.3, and Table 3.4, respectively.

3.4.1.2. Effect of pressure drop on mixing characteristics

Pressure drop is another most important factor to characterize the performance of a millichannel based packed bed device. Pressure drop is the source of the energy input required for the process

of mixing. Pressure drop for the continuous flows through the packed systems depends on the particle Reynolds number (Re_p) and increases with the increase of it. The Reynolds number increases with the increasing flow velocity and the decrease of the Fanning friction factor (f'). The variation of the friction factor values depending on the Reynolds number of the two-phase flow is shown in Fig. 3.7. In that way, the pressure drop is dependent on the Reynolds number, which increases with the increase of the volumetric flow rate, which is shown in Fig. 3.8.

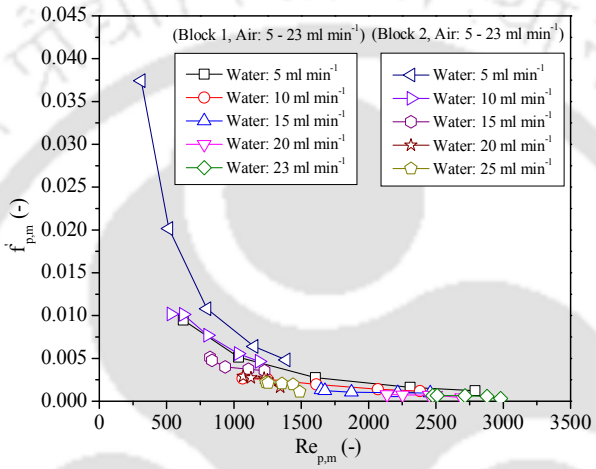

Fig. 3.7. The variation of the Fanning friction factor with respect to the Reynolds number.

In the present context, the pressure drop values are correlated with the dimensionless parameters by doing multiple regression analysis. It was observed that for the single-phase flow, the pressure drop values are dependent on the Reynolds and Capillary numbers, whereas for the two-phase flow Froude number effects the flow along with the other two dimensionless numbers (Mondal and Majumder, 2018a, and 2018b)). The pressure drop correlations for the two-phase flows are represented as follows.

$$\left(\frac{d_p}{\rho_m U_m^2 / \varepsilon_{eff}^2}\right)\left(\frac{\Delta P_f}{l_i}\right)_{p,m} = 2\left(f_p'\right)_m = 2.32\times10^{-10}\left(Re_{p,m}\right)^{4.79}\left(Ca_{p,m}\right)^{-1.17}\left(Fr_{p,m}\right)^{-5.42} \text{ (Block-1)} \qquad (3.24)$$

$$\left(\frac{d_p}{\rho_m U_m^2 / \varepsilon_{eff}^2}\right)\left(\frac{\Delta P_f}{l_i}\right)_{p,m} = 2\left(f_p^{'}\right)_m = 9.85\times10^{-11}\left(Re_{p,m}\right)^{4.89}\left(Ca_{p,m}\right)^{-1.30}\left(Fr_{p,m}\right)^{-5.49} \text{ (Block-2)} \quad (3.25)$$

The Eq. (3.24), and Eq. (3.25) satisfied the experimental data well with the correlation coefficients of 0.99 (The theory for the calculation of the correlation coefficient and standard error with ANOVA is given in Appendix – I). The maximum error percentages were 4.87 and 3.21, respectively. The Eq. (3.24) is valid within the range of operating variables: $624 \le \mathrm{Re}_{m,p} \le 2980$; $0.01 \le Ca_{m,p} \le 0.07$ and $27 \le Fr_{m,p} \le 133$, whereas, the Eq. (3.25) is valid within the operating ranges of $311 \le \mathrm{Re}_{m,p} \le 1488$; $0.01 \le Ca_{m,p} \le 0.03$ and $13 \le Fr_{m,p} \le 67$.

Higher-pressure drop incorporates higher turbulence, which increases the efficiencies of mixing and dispersions, resulting in higher mass transfer coefficients (Su et al., 2009). As a result, the block-1, having the less cross-sectional area, it may provide the higher mass transfer coefficients, generating the higher-pressure drop for the two-phase flow. However, due to the decrement of residence time, despite having a higher mass transport coefficient, block-1 at the higher flow rate may not be preferable over the block-2 for the slow mass transfer processes. Therefore, for the reactive mass transport processes, block-1, with a higher flow rate, may be preferable.

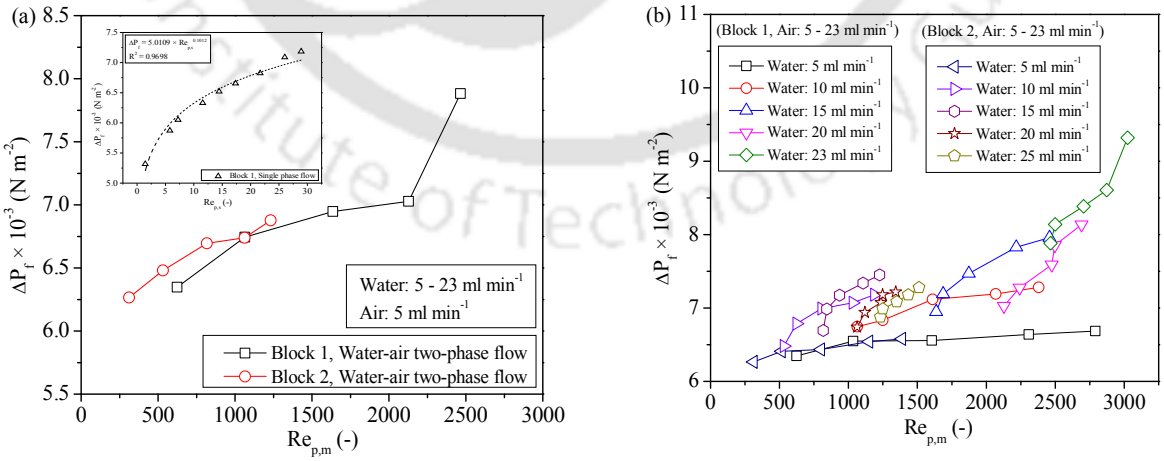

Fig. 3.8. Pressure drop variation with respect to the Reynolds number for the (a) single-phase flow, and (b) two-phase flow.

Table 3.2. Mean residence time, Particle Reynolds number, and the coefficient of axial dispersion D_{ax} in the multichannel based packed bed device (block-1) for different flow rates of single-phase fluid with a KCl of 1 mole dm^{-3} solution (T = 298 K).

Single-phase flow (block-1)								
Total volumetric flow rate, Q (ml min^{-1})	**Velocity through an individual channel, U_i (m min^{-1})**	**Mean residence time, t_m (min)**	**Total pressure drop, ΔP_f (N m^{-2})**	**Particle Reynolds number for an individual channel, Re_p (-)**	**σ_θ^2 (-)**	**Axial Peclet number of the multichannel packed bed, Pe_a (-)**	**Axial dispersion coefficient for an individual channel, D_{ax} (m^2 min^{-1})**	**Specific energy dissipation for the individual channel, E_d (W kg^{-1})**
1.0	1.26×10^{-3}	4.74	5.32×10^{3}	1.45	2.52×10^{-1}	10.86	1.32×10^{-6}	2.04×10^{-2}
4.0	5.05×10^{-3}	1.84	5.87×10^{3}	5.78	2.37×10^{-1}	11.41	5.01×10^{-6}	9.01×10^{-2}
5.0	6.31×10^{-3}	1.81	6.05×10^{3}	7.23	2.29×10^{-1}	11.73	6.10×10^{-6}	1.16×10^{-1}
8.0	1.01×10^{-2}	0.94	6.33×10^{3}	11.56	2.03×10^{-1}	12.90	8.87×10^{-6}	1.94×10^{-1}
10.0	1.26×10^{-2}	0.86	6.52×10^{3}	14.45	1.77×10^{-1}	14.42	9.92×10^{-6}	2.50×10^{-1}
12.0	1.52×10^{-2}	0.84	6.66×10^{3}	17.34	1.58×10^{-1}	15.82	1.09×10^{-5}	3.06×10^{-1}
15.0	1.89×10^{-2}	0.72	6.82×10^{3}	21.68	1.33×10^{-1}	18.31	1.17×10^{-5}	3.93×10^{-1}
18.0	2.27×10^{-2}	0.62	7.09×10^{3}	26.02	1.22×10^{-1}	19.76	1.30×10^{-5}	4.90×10^{-1}
20.0	2.53×10^{-2}	0.51	7.19×10^{3}	28.91	1.09×10^{-1}	21.76	1.31×10^{-4}	5.51×10^{-1}

Table 3.3. Mean residence time, Particle Reynolds number, and the coefficient of axial dispersion D_{ax} in the multichannel based packed bed device (block-1) for different flow rates of two-phase fluid (water-air) with a KCl of 1 mole dm^{-3} solution (T = 298 K).

Two-phase flow (block-1)										
Water volumetric flow rate, Q_{water} (ml min^{-1})	**Air volumetric flow rate, Q_{air} (ml min^{-1})**	**Total volumetric flow rate, Q (ml min^{-1})**	**Velocity through an individual channel, U_i (m min^{-1})**	**Mean residence time, t_m (min)**	**Total pressure drop, ΔP_f (N m^{-2})**	**Particle Reynolds number for an individual channel, $Re_{p,m}$ (-)**	**σ_θ^2 (-)**	**Axial Peclet number of the multichannel packed bed, Pe_a (-)**	**Axial dispersion coefficient for an individual channel, D_{ax} (m^2 min^{-1})**	**Specific energy dissipation for the individual channel, E_d (W kg^{-1})**
5.0	5.0	10.0	0.56	1.25	6.35×10^3	624.46	0.32	8.96	7.03×10^{-4}	0.49
5.0	10.0	15.0	0.94	1.13	6.55×10^3	1034.24	0.41	7.45	1.43×10^{-3}	1.13
5.0	15.0	20.0	1.48	0.98	6.56×10^3	1604.66	0.47	6.80	2.47×10^{-3}	2.01
5.0	20.0	25.0	2.17	0.94	6.64×10^3	2308.74	0.52	6.30	3.91×10^{-3}	3.17
5.0	23.0	28.0	2.65	0.93	6.69×10^3	2790.78	0.57	5.91	5.09×10^{-3}	4.00
10.0	5.0	15.0	0.94	0.71	6.75×10^3	1063.85	0.24	11.31	9.40×10^{-4}	0.58
10.0	10.0	20.0	1.11	0.63	6.83×10^3	1248.93	0.31	9.26	1.36×10^{-3}	1.05
10.0	15.0	25.0	1.45	0.55	7.12×10^3	1610.98	0.33	8.78	1.87×10^{-3}	1.70
10.0	20.0	30.0	1.88	0.53	7.19×10^3	2068.48	0.37	8.12	2.62×10^{-3}	2.48
10.0	23.0	33.0	2.17	0.50	7.28×10^3	2380.81	0.41	7.52	3.27×10^{-3}	3.03
15.0	5.0	20.0	1.45	0.65	6.95×10^3	1636.53	0.22	12.15	1.38×10^{-3}	0.71

15.0	10.0	25.0	1.48	0.49	7.19×10^3	1686.52	0.24	11.18	1.47×10^{-3}	1.15
15.0	15.0	30.0	1.67	0.40	7.47×10^3	1873.39	0.29	9.63	1.96×10^{-3}	1.72
15.0	20.0	35.0	1.98	0.35	7.83×10^3	2217.18	0.33	8.90	2.53×10^{-3}	2.45
15.0	23.0	38.0	2.21	0.34	7.96×10^3	2458.22	0.34	8.62	2.91×10^{-3}	2.94
20.0	5.0	25.0	1.88	0.47	7.03×10^3	2127.70	0.17	14.68	1.62×10^{-3}	0.84
20.0	10.0	30.0	1.98	0.43	7.28×10^3	2241.76	0.19	13.14	1.68×10^{-3}	1.26
20.0	15.0	35.0	2.17	0.39	7.59×10^3	2474.45	0.22	12.34	1.82×10^{-3}	1.78
20.0	20.0	40.0	2.22	0.38	7.86×10^3	2497.85	0.25	11.00	2.29×10^{-3}	2.41
20.0	23.0	43.0	2.40	0.38	8.14×10^3	2690.69	0.29	9.68	2.81×10^{-3}	2.88
23.0	5.0	28.0	2.17	0.36	7.88×10^3	2465.66	0.16	15.57	1.84×10^{-3}	1.03
23.0	10.0	33.0	2.21	0.35	8.14×10^3	2499.47	0.19	13.37	1.93×10^{-3}	1.48
23.0	15.0	38.0	2.40	0.33	8.39×10^3	2705.00	0.23	11.82	2.12×10^{-3}	2.02
23.0	20.0	43.0	2.56	0.32	8.61×10^3	2872.53	0.29	9.78	2.78×10^{-3}	2.65
23.0	23.0	46.0	2.65	0.27	9.32×10^3	3024.87	0.34	8.67	3.34×10^{-3}	3.29

Table 3.4. Mean residence time, Particle Reynolds number, and the coefficient of axial dispersion D_{ax} in the multichannel based packed bed device (block-2) for different flow rates of two-phase fluid (water-air) with a KCl of 1 mole dm^{-3} solution (T = 298 K).

Two-phase flow (block-2)										
Water volumetric flow rate, Q_{water} (ml min^{-1})	**Air volumetric flow rate, Q_{air} (ml min^{-1})**	**Total volumetric flow rate, Q (ml min^{-1})**	**Velocity through an individual channel, U_i (m min^{-1})**	**Mean residence time, t_m (min)**	**Total pressure drop, ΔP_f (N m^{-2})**	**Particle Reynolds number for an individual channel, $Re_{p,m}$ (-)**	**σ_θ^2 (-)**	**Axial Peclet number of the multichannel packed bed, Pe_a (-)**	**Axial dispersion coefficient for an individual channel, D_{ax} (m^2 min^{-1})**	**Specific energy dissipation for the individual channel, E_d (W kg^{-1})**
5.0	5.0	10.0	0.28	1.65	6.27×10^3	311.88	0.39	7.79	4.04×10^{-4}	0.24
5.0	10.0	15.0	0.47	1.21	6.41×10^3	515.96	0.45	6.99	7.60×10^{-4}	0.55
5.0	15.0	20.0	0.74	1.00	6.43×10^3	799.66	0.54	6.12	1.37×10^{-3}	0.99
5.0	20.0	25.0	1.09	0.99	6.54×10^3	1149.27	0.56	6.00	2.05×10^{-3}	1.57
5.0	23.0	28.0	1.33	0.97	6.58×10^3	1388.31	0.59	5.78	2.60×10^{-3}	1.98
10.0	5.0	15.0	0.47	0.71	6.48×10^3	531.62	0.28	10.09	5.27×10^{-4}	0.28
10.0	10.0	20.0	0.56	0.63	6.79×10^3	623.75	0.32	8.95	7.04×10^{-4}	0.52
10.0	15.0	25.0	0.72	0.55	6.99×10^3	804.13	0.35	8.46	9.70×10^{-4}	0.84
10.0	20.0	30.0	0.94	0.53	7.07×10^3	1031.92	0.38	7.90	1.35×10^{-3}	1.22
10.0	23.0	33.0	1.09	0.50	7.18×10^3	1187.35	0.43	7.24	1.70×10^{-3}	1.50
15.0	5.0	20.0	0.72	0.66	6.70×10^3	842.94	0.28	9.94	8.35×10^{-4}	0.34
15.0	10.0	25.0	0.74	0.49	6.99×10^3	817.64	0.29	9.82	8.45×10^{-4}	0.56
15.0	15.0	30.0	0.83	0.43	7.18×10^3	935.63	0.31	9.15	1.03×10^{-3}	0.83
15.0	20.0	35.0	0.99	0.38	7.34×10^3	1106.92	0.35	8.51	1.32×10^{-3}	1.15

15.0	23.0	38.0	1.10	0.35	7.45×10^3	1226.99	0.37	8.11	1.54×10^{-3}	1.38
20.0	5.0	25.0	0.94	0.48	6.74×10^3	1236.87	0.21	12.50	9.84×10^{-4}	0.40
20.0	10.0	30.0	0.99	0.47	6.94×10^3	1063.24	0.26	10.71	9.93×10^{-4}	0.60
20.0	15.0	35.0	1.09	0.44	7.07×10^3	1119.92	0.28	9.96	1.13×10^{-3}	0.83
20.0	20.0	40.0	1.11	0.41	7.18×10^3	1247.51	0.31	9.30	1.35×10^{-3}	1.10
20.0	23.0	43.0	1.20	0.41	7.22×10^3	1343.60	0.32	9.08	1.50×10^{-3}	1.28
23.0	5.0	28.0	1.09	0.45	6.88×10^3	1512.05	0.19	13.71	1.04×10^{-3}	0.45
23.0	10.0	33.0	1.10	0.38	6.99×10^3	1232.21	0.23	11.78	1.10×10^{-3}	0.64
23.0	15.0	38.0	1.20	0.35	7.09×10^3	1248.80	0.27	10.44	1.20×10^{-3}	0.85
23.0	20.0	43.0	1.28	0.35	7.18×10^3	1351.16	0.32	9.06	1.50×10^{-3}	1.11
23.0	23.0	46.0	1.33	0.34	7.28×10^3	1434.63	0.37	8.12	1.78×10^{-3}	1.29

3.4.1.3. Generation of correlation between the axial dispersion coefficient and the molecular diffusion coefficient

The axial dispersion coefficient is a function of different operating variables such as the actual velocity (U_m), density (ρ_m), viscosity (μ_m) of the fluid mixture, the hydraulic diameter (d_H) of the individual channel, and the particle diameter (d_p) of the packing material, etc. The dimensional analysis yields the following relation

$$\frac{D_{ax}}{d_p\left(U_m/\varepsilon_{eff}\right)} = f\left(\frac{d_H}{d_p}, \frac{1}{\mathrm{Re}_p}, \frac{1}{We_p}, \frac{D_m}{d_p\left(U_m/\varepsilon_{eff}\right)}\right) \tag{3.26}$$

In the case of the two-phase flows, the empirical correlations for the ratios of the diffusion coefficients were generated by doing the multiple regression analysis and can be represented as

$$D_{ax}/D_m = 1.04(\mathrm{Re}_p\, Ca_p)^{0.062} = 1.04We_p^{0.062} \quad \text{(Single-phase flow, block-1)} \tag{3.27}$$

$$D_{ax}/D_m = 5.61(\mathrm{Re}_p\, Ca_p)^{0.51}(\mathrm{Fr}_p)^{-0.88} = 5.61We_p^{0.51}Fr_p^{-0.88} \quad \text{(Two-phase flow, block-1)} \tag{3.28}$$

$$D_{ax}/D_m = 2.97(\mathrm{Re}_p\, Ca_p)^{0.35}(Fr_p)^{-0.59} = 2.97We_p^{0.35}Fr_p^{-0.59} \quad \text{(Two-phase flow, block-2)} \tag{3.29}$$

The proposed correlation for the single-phase flow is valid within the range of operating variables: $1.45 < Re_p < 28.91$, $4.64 \times 10^{-5} < Ca_p < 9.28 \times 10^{-4}$. The ranges of the operating variables for the Eqs. (3.28-3.29) were indicated previously.

The D_{ax}/D_m values obtained in the present experiment were compared with the various correlations like Taylor (1953) and Aris (1956) (Eq. (3.15)); Squires and Quake (2005), and Ajdari et al. (2006) (Eq. (3.16)); and Zeiser et al. 2001 (Eq. (3.20)), as shown in Fig. 3.9.

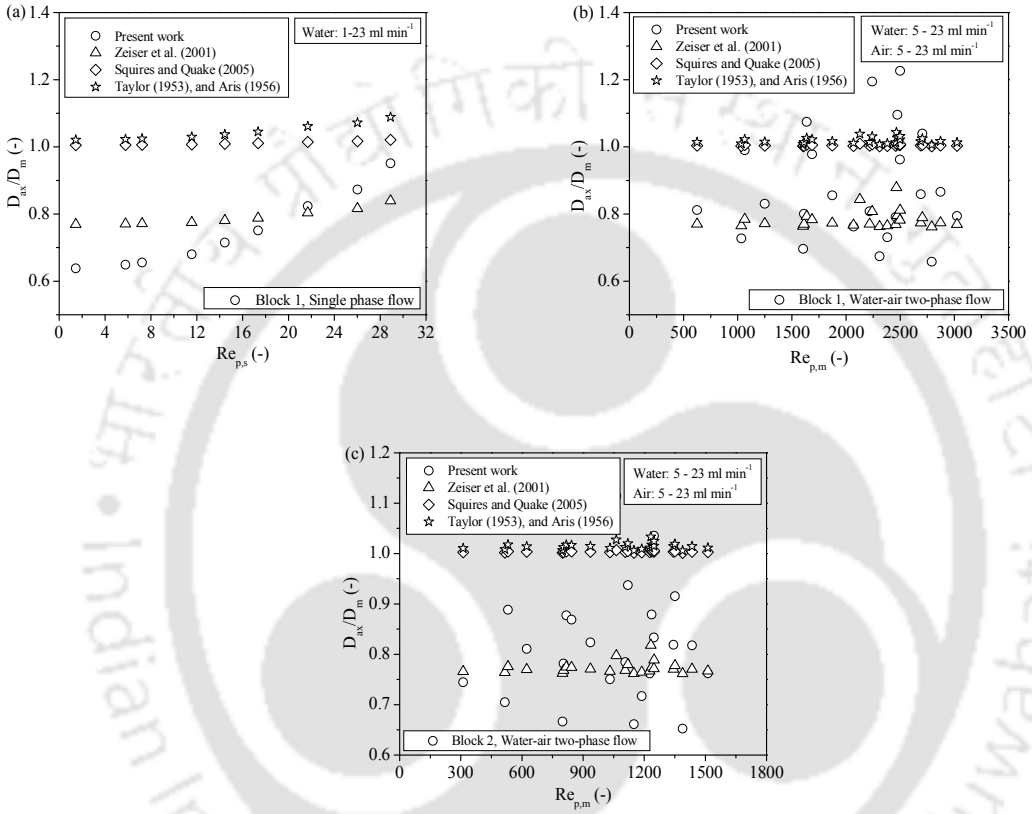

Fig. 3.9. Variation of the (D_{ax}/D_m) ratios with respect to the Reynolds number (a) single-phase flow (block – 1), (b) two-phase flow (block -1), and (c) two-phase flow (block -2).

The present proposed correlation satisfied the experimental data with a maximum error of 15.0%. When the experimental results were compared with the available correlations, the correlation suggested by Zeiser et al. (2001), closely resembled the experimental data with the maximum error of 8% (Fig. 3.9(a)). However, for the two-phase flows, all the available correlations did not satisfy the experimental data properly (maximum errors up to 50%), either for the geometrical difference or the proposed correlations were for the single-phase flow through the unpacked channels only.

3.5. Conclusion

In this chapter, the hydrodynamics and mixing characteristics for the single-phase (water), and the air-water two-phase flows through the packed multichannel geometries (millimetric dimensions) were enunciated based on the experimental observations. The characteristic features of the fluid distribution uniformity in the multichannel devices were analyzed by the axial dispersion model. The Peclet number values increase with the increase of volumetric flow rates for the single-phase flow. In the case of the two-phase flow, thought the Peclet number increases with the increase of liquid flow rates; it decreases with the increase of gas flow rate for a particular liquid flow rate. The axial dispersion coefficient, as well as the specific energy dissipation, increases with the increase of flow rates for both the phases. This increment is higher for the block-1 than block-2 of higher height, as for the same volumetric flow rate, the channel of lower cross-section produce the higher Reynolds number and pressure drop. With the increase of Reynolds number, the Dax/Dm ratio increases, which specifies that at the higher velocity, the axial dispersion coefficient dominates the diffusion coefficient. From the overall observations, it can be concluded that block-1, at the higher flow rates of the two-phases, provides higher energy dissipation and a higher mass transfer coefficient at the expense of higher pressure drop. Moreover, at that condition, the use of block-1 is not preferable for the slow transport process like adsorption, as the higher flow rate reduces the total mass transport capacity reducing the residence time inside the packed bed. Therefore, for fast transport processes like catalytic reaction, the operation of block-1 at the very high flow rate with the incorporation of air is preferable, and for the other slow processes block-2 with the lower flow rate of fluid is preferable.

Chapter 4

Heat Transport Based on Hydrodynamics and Local Entropy Generation in Millimetric Packed Channel

4.1. Introduction

The packed beds, which can improve the contact between the two phases, have essential applications in the chemical and biochemical industries. These are used in the separation processes like absorption, stripping, separation processes, catalytic reactions, and distillation. It can also be used for the development of heat and mass transport equipment. Recently, miniaturization is the main target of the researchers and engineers for process intensification. Depending on the specific demands, the application of new packing materials and the developments of the new packed beds are continuing since the last decades. In general, when the flow of fluids through the packed bed is considered, the pressure gradient is determined by the Ergun equation (Ergun, 1952; McCabe et al., 2005). It consists of the combination of the laminar flow term (Kozeny–Carman equation, viscous term), and the turbulent flow term (Burke-Plummer equation, inertia term) (McCabe et al., 2005). It simplified to Darcy's law if the body force of the fluids is neglected in the laminar flow regime. Many researchers have attempted to modify the Ergun equation for their specific application depending on the flow properties, bed geometries, and the characteristics of the packing materials (Metha and Hawley, 1969; Reichelt, 1972; Macdonald et al., 1979; Feng, 1989; Foumeny et al., 1993; Lee and Ogawa, 1994; Dolejš and Machač, 1995; Liu and Masliyah, 1996; Raichura et al., 1999; Gibilaro, 2001; Eisfeld and Schnitzlein, 2001; Nemec and Levec, 2005; Vafai et al., 2006; Singh et al., 2006; Montillet et al., 2007; Çarpinlioğlu and Özahi, 2008; Cheng, 2011; Allen et al., 2013; Chen et al., 2017a; Tian et al., 2018). The researchers have given the correlations for the pressure drops as well as the friction factors considering the same concept followed by Ergun, which are shown in Table 4.1, and Table 4.2.

The previous literature revealed the fact that most of the conduits were the columns with a circular cross-section. They were larger in-size, packed with large spherical or other regular shaped materials and, used mainly for the single-phase flow. Hence, the previous correlations would not be sufficient to demonstrate the present situation of the two-phase flow through narrow channels packed with the irregular shaped small size sand particles of different diameters. The present packed straight and serpentine channels are regular in size and do not involve the microscale effect. However, the present experimental channels are defined as narrow, based on the aspect ratio of the channels. According to the concept of Chow (1959), and Dey (2014), channels can be classified as wide and narrow, based on the aspect ratio w/h (w = width of the channel, and h = height of the channel). The ratio, $w/h < 5$, refers to the narrow channel, whereas it is regarded as a wide channel if the ratio is greater than 10. Based on the same concept of the aspect ratio, Kouidri et al. (2015) also stated their experimental channel of dimensions 5×10^{-3} m (w), and 25×10^{-3} m (h), with the aspect ratio of 0.2, as the narrow channel (Kouidri et al., 2015). In the present case, the ratio is 0.2 ($w = 2 \times 10^{-3}$ m, and $h = 10 \times 10^{-3}$ m), based on which the channels are considered as narrow channels. On the other hand, according to Bejan (2001), entropy is one of the most important thermodynamic parameters used in the design of heat transfer equipment. Entropy generation plays an essential role in the case of non-equilibrium thermodynamics. In the case of stationary phases, with increasing pressure and decreasing temperature gradient, the entropy of the systems decreases. In continuous flow, entropy generation depends on the fluid flow properties (Vafai and Sofen, 1990; Vollmari et al., 2015).

Nusselt number (represented by the convective to conductive heat transfer across the boundary), is considered the main dimensionless parameter in the convective heat transfer study. The Nusselt number is the function of the Reynolds number and the Prandtl number. The pressure drop in the two-phase flows is proportional to the Reynolds number. Hence, the Nusselt number and pressure drop both depend on the Reynolds number, and they are related to each other.

Table 4.1. Pressure drop correlations available for the packed channels.

Authors (years)	**Pressure drop equations in the packed bed (In each equation $\mathrm{Re}_{m,p}$ is replaced by $De_{m,p}$ in case of the serpentine channel).**	**Particle shape**
Ergun, 1952; McCabe et al., 2005	$\left(\frac{\Delta P_f}{L}\right)_{m,p} = 150\mu_m \frac{(1-\varepsilon_{eff})^2}{\phi_p^2 \varepsilon_{eff}^3 d_p^2} U_m + 1.75 \frac{(1-\varepsilon_{eff})\rho_m}{\phi_p d_p \varepsilon_{eff}^3} U_m^2$; $\frac{d_H}{d_p} >> 10$	Spherical and non-spherical
Metha and Hawley, 1969	$\frac{\Delta P_f}{L} = 150 \frac{(1-\varepsilon_{eff})^2}{\varepsilon_{eff}^3} \frac{\mu_m U_m}{d_p^2} M^2 + 1.75 \frac{(1-\varepsilon_{eff})}{\varepsilon_{eff}^3} \frac{\rho_m U_m^2}{d_p} M$; where $M = 1 + \frac{4 d_p}{6 d_H (1-\varepsilon_{eff})}$ and $7 < \frac{d_H}{d_p} < 91$	Spherical
Reichelt, 1972	$\left(\frac{\Delta P}{L}\right)_{m,p} = 150\mu_m \frac{(1-\varepsilon_{eff})^2}{\varepsilon_{eff}^3 d_p^2} U_m M^2 + \frac{(1-\varepsilon_{eff})\rho_m}{d_p \varepsilon_{eff}^3} U_m^2 \frac{M}{B_w}$; where $B_w = \left[c_1 (d_p / d_H)^2 + C_2\right]^2$; $c_1 = 1.5$ and $c_2 = 0.88$ for $1.73 < d_H / d_p < 91$.	Spherical
Macdonald et al., 1979	$\left(\frac{\Delta P_f}{L}\right)_{m,p} = 180\mu_m \frac{(1-\varepsilon_{eff})^2}{\varepsilon_{eff}^3 d_p^2} U_m + 1.8 \frac{(1-\varepsilon_{eff})\rho_m}{d_p \varepsilon_{eff}^3} U_m^2$	Spherical
Feng, 1989	$\left(\frac{\Delta P_f}{L}\right)_{m,p} = \frac{0.106}{2g} \frac{\rho_m}{D} \mathrm{Re}_{m,p}^{-0.25} \left(\frac{U_m}{\varepsilon_{eff}}\right)^2$ kPa m^{-1} ; $D = d_p \frac{\phi_p^2}{6} \sqrt{\frac{2}{3(1-\varepsilon_{eff})}}$	Spherical

Foumeny et al., 1993	$\left(\frac{\Delta P_f}{L}\right)_{m,p} = 130\mu_m \frac{(1-\varepsilon_{eff})^2}{\phi_p^2 \varepsilon_{eff}^3 d_p^2} U_m + \frac{d_H/d_p}{0.335\left(d_H/d_p\right)+2.28} \frac{(1-\varepsilon_{eff})\rho_m}{\phi_p d_p \varepsilon_{eff}^3} U_m^2$	Spherical
Lee and Ogawa, 1994	$\left(\frac{\Delta P_f}{L}\right)_{m,p} = \left[12.5 \frac{(1-\varepsilon_{eff})^2 \rho_m U_m^2}{2\varepsilon_{eff}^3 d_p}\right]\left[29.32\,\mathrm{Re}_{m,p}^{-1} + 1.56\,\mathrm{Re}_{m,p}^{-n} + 0.1\right]$ with $n = 0.352 + 0.1\varepsilon_{eff} + 0.275\varepsilon_{eff}^2$	Spherical
Liu and Masliyah, 1996	$\left(\frac{\Delta P}{L}\right)_{m,p} = 150\mu_m \frac{(1-\varepsilon_{eff})^2}{\varepsilon_{eff}^3 d_p^2} U_m C_{w1}^2 + 1.75 \frac{(1-\varepsilon_{eff})\rho_m}{d_p \varepsilon_{eff}^3} U_m^2 C_{w2}$; where $C_{w1}^2 = 1 + \frac{\pi d_p}{6 d_H (1-\varepsilon)}$ and $C_{w2} = 1 - \frac{\pi^2 d_p}{24 d_H}\left(1 - \frac{d_p}{2d_H}\right)$	Spherical
Raichura et al., 1999	$\left(\frac{\Delta P}{L}\right)_{m,p} = P_1 \mu_m \frac{(1-\varepsilon_{eff})^2}{\varepsilon_{eff}^3 d_p^2} U_m + P_2 \frac{(1-\varepsilon_{eff})\rho_m}{d_p \varepsilon_{eff}^3} U_m^2$; where $P_1 = 103\left(\frac{\varepsilon}{1-\varepsilon}\right)^2\left[6(1-\varepsilon) + \frac{80 d_p}{d_H}\right]$; $P_2 = 2.8 \frac{\varepsilon}{1-\varepsilon}\left(1 - \frac{1.82 d_p}{d_H}\right)$ and $5 < d_H/d_p < 50$.	Spherical
Gibilaro, 2001	$\left(\frac{\Delta P}{L}\right)_{m,p} = \left(18\frac{\mu_m}{\rho_m U_m d_p} + 0.33\right)\frac{\rho_m U_m^2}{d_p}(1-\varepsilon_{eff})\varepsilon_{eff}^{-4.8}$	Spherical
Eisfeld and Schitzlein, 2001	$\frac{d_p}{\rho_m U_m^2}\left(\frac{\Delta P_f}{L}\right)_{m,p} = \frac{154 A_w^2}{\mathrm{Re}_{m,p}} \frac{(1-\varepsilon_{eff})^2}{\phi_p^2 \varepsilon_{eff}^3} + \frac{A_w}{B_w} \frac{1-\varepsilon_{eff}}{\phi_p \varepsilon_{eff}^3}$ where	Spherical, cylindrical and cuboids

$$A_w = 1 + \frac{2}{3\left(d_H / d_p\right)\left(1-\varepsilon_{eff}\right)} \text{ and } B_w = \left[1.15\left(\frac{d_p}{d_H}\right)^2 + 0.87\right]^2$$

Nemec and Levec, 2005	$\left(\frac{\Delta P}{L}\right)_{m,p} = \left(\frac{150}{\phi_p^{3/2}\,\mathrm{Re}_{m,p}} + \frac{1.75}{\phi_p^{4/3}}\right)\frac{\rho_m (v_m)^2 (1-\varepsilon_{eff})}{d_p \varepsilon_{eff}^3}$; $Re_p < 400$ where v_m is the superficial velocity of the mixture.	Uniform spherical and non-spherical particles (cylinders, rings, trilobes, and quadralobes)
Dolejš and Machač, 2005	$\left(\frac{\Delta P_f}{L}\right)_{m,p} = \left[\frac{72\left[(1+\phi_p)M_D\right]^2}{\mathrm{Re}_{m,p}}\right]\frac{\rho_m v_m^2}{d_p}\left(\frac{1-\varepsilon_{eff}}{\varepsilon_{eff}^3}\right)$; where the particle Reynolds number $\mathrm{Re}_{m,p} = \frac{\rho_m v_m d_p}{\mu_m (1-\varepsilon_{eff})}$ and the correction coefficient $M_D = 1 + \frac{2d_p}{3(1-\varepsilon_{eff})(1+\phi_p)d_H}$; the resistance number $\phi_p = \left[0.5^4 - \left(\frac{\mathrm{Re}_{\mathrm{mod}}}{150}\right)^3 + \left(0.113(\mathrm{Re}_{\mathrm{mod}})^{0.507}\right)^3\right]^{1/3}$	spherical
Vafai et al., 2006	$\left(\frac{\Delta P_f}{L}\right)_{m,p} = 120\mu_m \frac{\left(1-\varepsilon_{eff}\right)^2 \varepsilon_{eff}}{\varepsilon_{eff}^3 d_p^2} U_m + 2.3\frac{\left(1-\varepsilon_{eff}\right)\rho_m \varepsilon_{eff}^2}{d_p \varepsilon_{eff}^3} U_m^2$	Porous media
Singh et al., 2006	$\left(\frac{\Delta P}{L}\right)_{m,p} = 4.466\left(\frac{\rho_m U_m d_p}{\mu_m}\right)^{-0.2} \varepsilon_{eff}^{-2.945} \frac{\rho_m U_m^2}{d_p}$; where $1000 < \mathrm{Re}_{m,p} < 2700$	Spherical, applicable for non-spherical particles also

Montillet et al., 2007	$\frac{d_p}{\rho_m U_m^2}\left(\frac{\Delta P_f}{L}\right)_{m,p} = 0.061\left(\frac{1-\varepsilon_{eff}}{\varepsilon_{eff}^3}\right)\left(\frac{d_H}{d_p}\right)^{0.20}\left(\frac{1000\mathrm{Re}_{m,p}^{-1}}{\phi_p^2}+\frac{60\mathrm{Re}_{m,p}^{-0.5}}{\phi_p}+12\right)$	Spherical
Çarpinlioğlu et al., 2008	$\left(\Delta P_f\right)_{m,p} = 139.57\left[\mathrm{Re}_{m,p}\left(d_p/L\right)\varepsilon_{eff}^7\right]^{-0.4733}$	Non-spherical
Cheng, 2011	$\left(\frac{\Delta P_f}{L}\right)_{m,p} = \left[\left(185+17\frac{\varepsilon_{eff}}{1-\varepsilon_{eff}}\left(\frac{d_H}{d_H-d_p}\right)^2\right)\frac{(1-\varepsilon_{eff})^2}{\varepsilon_{eff}^3}\frac{\mu_m U_m}{d_p^2}+\left(1.3\left(\frac{1-\varepsilon_{eff}}{\varepsilon_{eff}}\right)^{\frac{1}{3}}+0.03\left(\frac{d_H}{d_H-d_p}\right)^2\right)\right]\frac{\rho_m U_m^2}{d_p}\left(\frac{1-\varepsilon_{eff}}{\varepsilon_{eff}^3}\right)$	Spherical
Allen et al., 2013	$\left(\frac{\Delta P_f}{L}\right)_{m,p} = \left(\frac{A}{\mathrm{Re}_{m,p}}+\frac{B}{\mathrm{Re}_{m,p}C}\right)\rho_m\frac{v_m}{2}\frac{\sum A_p}{\sum V_p}\left(\frac{1-\varepsilon_{eff}}{\varepsilon_{eff}^3}\right)$	Rough spheres, smooth cylinders, cubes and crushed rock
Chen et al., 2017a	$\left(\frac{\Delta P_f}{L}\right)_{m,p} = 150\mu_m\frac{(1-\varepsilon_{eff})^2}{\varepsilon_{eff}^3 d_p^2}U_m + 2.5\frac{(1-\varepsilon_{eff})\rho_m}{d_p\varepsilon_{eff}^3}U_m^2$	Cubical pebbles
Tian et al., 2018	$\left(\frac{\Delta P_f}{L}\right)_{m,p} = 1.65M^2\frac{(1-\varepsilon_{eff})^2\mu_m U_m}{\phi_p^2\varepsilon_{eff}^3 d_p^2}+\left[\frac{1}{0.7/(d_H/d_p)^2+2.1}\right]M\frac{(1-\varepsilon_{eff})\rho_m U_m^2}{\phi_p d_p\varepsilon_{eff}^3}$	Non-spherical grains
Present work	Serpentine channel: $\left(\frac{\Delta P_f}{L}\right)_{m,p} = \left[\frac{135.6\mu_m U_m(1-\varepsilon_{eff})^2}{\phi_p^2 d_p^2\varepsilon_{eff}^3}+\frac{0.12\rho_m U_m^2(1-\varepsilon_{eff})}{\phi_p d_p\varepsilon_{eff}^3}\right]$ Straight channel: $\left(\frac{\Delta P_f}{L}\right)_{m,p} = \left[\frac{56.3\mu_m U_m(1-\varepsilon_{eff})^2}{\phi_p^2 d_p^2\varepsilon_{eff}^3}+\frac{0.1\rho_m U_m^2(1-\varepsilon_{eff})}{\phi_p d_p\varepsilon_{eff}^3}\right]$	Non-uniform sand particles

Table 4.2. Important correlations for the friction factor in the packed bed.

Authors (years)	**Available correlations (In each correlation $\mathrm{Re}_{m,p}$ is replaced by $De_{m,p}$ in case of the serpentine channel)**	**Particle shape and size**
Carman, 1937	$\left(f_m^{'}\right)_p = \frac{\Delta P_f d_p}{L\rho_m U_m^2}\frac{\varepsilon_{eff}^3}{(1-\varepsilon_{eff})} = \frac{180}{\mathrm{Re}_{m,p}} + \frac{2.87}{\mathrm{Re}_{m,p}^{0.1}}$; where $0.1 < \mathrm{Re}_{m,p} < 6\times10^4$	Spherical
Ergun, 1952); McCabe et al.,2005	$\left(f_m^{'}\right)_p = \frac{\Delta P_f d_p}{L\rho_m U_m^2}\frac{\varepsilon_{eff}^3}{(1-\varepsilon_{eff})} = \frac{150}{\mathrm{Re}_{m,p}} + 1.75$; where $d_H / d_p > 10$; $1 < \mathrm{Re}_{m,p} < 2000$	Spherical
Rose, 1945	$\left(f_m^{'}\right)_p = 1000\mathrm{Re}_{m,p}^{-1} + 60\mathrm{Re}_{m,p}^{-0.5} + 12$	Spherical
Rose and Rizk, 1949	$\left(f_m^{'}\right)_p = 1000\mathrm{Re}_{m,p}^{-1} + 125\mathrm{Re}_{m,p}^{-0.5} + 14$	Spherical
Hicks, 1970	$\left(f_m^{'}\right)_p = 6.8\times\frac{(1-\varepsilon_{eff})^{1.2}}{\varepsilon_{eff}^3}\mathrm{Re}_{m,p}^{-0.2}$; where $300 \le \mathrm{Re}_{m,p} \le 6\times10^4$	Spherical
Tallmadge, 1970	$\left(f_m^{'}\right) = \left[\frac{150}{\mathrm{Re}_{m,p}}\frac{(1-\varepsilon_{eff})^2}{\varepsilon_{eff}^3}\right] + \left[\frac{4.2(1-\varepsilon_{eff})^{1.166}}{\varepsilon_{eff}^3}\mathrm{Re}_{m,p}^{-1/6}\right]$; where $d_H / d_p > 11.4$; $0.1 \le \mathrm{Re}_{m,p} \le 10^5$; $0.33 < \varepsilon_{eff} < 0.88$	-
Brauer, 1971	$\left(f_m^{'}\right)_p = \frac{\Delta P_f d_p}{L\rho_m U_m^2}\frac{\varepsilon_{eff}^3}{(1-\varepsilon_{eff})} = \frac{160}{\mathrm{Re}_{m,p}} + \frac{3.1}{\mathrm{Re}_{m,p}^{0.1}}$; where $0.01 < \mathrm{Re}_{m,p} < 4\times10^4$	Spherical

Lee and Ogawa, 1974	$\left(f_m^{'}\right)_p = \frac{1}{2}\left[\frac{12.5}{\mathrm{Re}_{m,p}}(1-\varepsilon_{eff})^2\right]\left[29.32\,\mathrm{Re}_{m,p}^{-1} + 1.56\,\mathrm{Re}_{m,p}^{-n} + 0.1\right]$ with $n = 0.352 + 0.1\varepsilon_{eff} + 0.275\varepsilon_{eff}^2$ and $1 \le \mathrm{Re}_{m,p} \le 10^5$	-
Jones and Krier, 1983	$\left(f_m^{'}\right)_p = \frac{\Delta P_f d_p}{L\rho_m U_m^2}\frac{\varepsilon_{eff}^3}{(1-\varepsilon_{eff})} = \frac{150}{\mathrm{Re}_{m,p}} + \frac{3.89}{\mathrm{Re}_{m,p}^{0.13}}$; where $1\times10^3 < \mathrm{Re}_{m,p} < 1\times10^5$; $8 < d_H/d_p < 52$	Spherical
Watanabe, 1989	$\left(f_m^{'}\right)_p = \left[\frac{25}{4\varepsilon_{eff}^3}(1-\varepsilon_{eff}^2)\right]\left[21\mathrm{Re}_{m,p}^{-1} + 6\mathrm{Re}_{m,p}^{-0.5} + 0.28\right]$; where $0.1 \le \mathrm{Re}_{m,p} \le 4\times10^3$	Granular
Idelchik, 1989	$\left(f_m^{'}\right)_p = \frac{\Delta P_f d_p}{L\rho_m U_m^2}\frac{\varepsilon_{eff}^3}{(1-\varepsilon_{eff})} = \frac{\varepsilon_{eff}^3}{(1-\varepsilon_{eff})}\frac{0.765}{\varepsilon_{eff}^{4.2}}\left[\frac{30}{\mathrm{Re}_{m,p}} + \frac{3}{\mathrm{Re}_{m,p}^{0.7}} + 0.3\right]$; where $0.001 < \mathrm{Re}_{m,p} < 1000$; $0.3 \le \varepsilon_{eff} < 0.8$	Spherical
Wu and Pruess, 1996	$\left(f_m^{'}\right)_p = \frac{\varepsilon_{eff}^3 d_p}{3(1-\varepsilon_{eff})L}\frac{\Delta P_f}{\rho_m U_m^2}$	Porous media
Nemec and Levec, 2005	$\left(f_m^{'}\right)_p = \frac{\Delta P_f d_p}{L\rho_m U_m^2}\frac{\varepsilon_{eff}^3}{(1-\varepsilon_{eff})} = \frac{150}{\phi_p^{3/2}\mathrm{Re}_{m,p}} + \frac{1.75}{\phi_p^{4/3}}$; where $\mathrm{Re}_{m,p} < 400$	Uniform spherical and non-spherical particles (cylinders, rings, trilobes, and quadralobes)
Singh et al., 2006	$\left(f_m^{'}\right)_p = \frac{\varepsilon_{eff}^3}{(1-\varepsilon_{eff})}4.466\mathrm{Re}_{m,p}^{-0.2}\phi_p^{0.696}\varepsilon_{eff}^{-2.945}e^{11.85(\log\phi_p)^2}$; where $1500 < \mathrm{Re}_{m,p} < 5000$	Spherical, cubical and cuboids

Montillet et al., 2007	$\left(f_m^{'}\right)_p = a\left(\frac{1-\varepsilon_{eff}}{\varepsilon_{eff}^3}\right)\left[\frac{d_H}{d_p}\right]^{0.2}\left[1000\,\mathrm{Re}_{m,p}^{-1}+60\,\mathrm{Re}_{m,p}^{-0.5}+12\right]$ where $a = 0.061$ for dense packing or $a = 0.050$ for loose packing, $3.8 \le d_H/d_p \le 40-50$ and $10 \le \mathrm{Re}_{m,p} \le 2500$	Spherical
Ozahi et al., 2008	$\left(f_m^{'}\right)_p = 160+1.61\mathrm{Re}_{m,p}$; where $6.4 < d_H/d_p < 17.2$; $708 < \mathrm{Re}_{m,p} < 7773$; $0.36 < \varepsilon_{eff} < 0.56$	Spherical and non-spherical
Yang et al., 2012	$\left(f_m^{'}\right)_p = 145.3+0.99\mathrm{Re}_{m,p}$; where $d_H/d_p = 2.73$; $\varepsilon_{eff} = 0.476$	uniform sphere and ellipsoid, non-uniform sphere
Harrison et al., 2013	$\left(f_m^{'}\right)_p = 119.8\left(1+\frac{\pi d_p}{6(1-\varepsilon_{eff})d_H}\right)^2 + 4.63\left[1-\frac{\pi^2 d_p}{24 d_H}\left(1-\frac{0.5d_p}{d_H}\right)\right]\mathrm{Re}_{m,p}^{5/6}$; where $8.3 < d_H/d_p < 50$; $0.32 < \mathrm{Re}_{m,p} < 7700$; $0.33 < \varepsilon_{eff} < 0.88$	-
Chen et al., 2017a	$\left(f_m^{'}\right)_p = \frac{150}{\mathrm{Re}_{m,p}} + 2.5$	Cubical
Guo et al., 2017	$\left(f_m^{'}\right)_p = 180+\left(9.5374\frac{d_p}{d_H}-2.8054\right)\mathrm{Re}_{m,p}^{0.97}$; where $2 < d_H/d_p < 3$	Spherical
Present work	Serpentine channel: $\left(f_m^{'}\right)_p = 23.29\left(De_{m,p}Ca_{m,p}\right)^{0.0732}Fr^{-1.6939}$; $d_H/d_p = 7.21$ Straight channel: $\left(f_m^{'}\right)_p = 16.74\left(\mathrm{Re}_{m,p}Ca_{m,p}\right)^{0.1182}Fr^{-1.7022}$; $d_H/d_p = 7.21$	Non-uniform shape (sand particle)

The local entropy generation rate depends on the Nusselt number, which related to the pressure drop through the Reynolds number. Thus, the local entropy generation rate and pressure drop are inter-related (Revellin et al., 2009). Several attempts have been made to develop the correlation for the Nusselt number based on the operating variables, as shown in Table 4.3.

Table 4.3. Correlations proposed by various investigators for the forced convection (Nusselt number) in case of the turbulent flow.

Authors (years)	Nusselt number ($Nu_{m,p} = \frac{h'_{m,p} d_p}{k_{m,p}}$) correlations in turbulent flow condition (In each correlation $\mathrm{Re}_{m,p}$ is replaced by $De_{m,p}$ in case of the serpentine channel).
Dittus-Bolter, 1942	$Nu_{m,p} = 0.023\,\mathrm{Re}_{m,p}^{0.8}\,\mathrm{Pr}_{m,p}^{0.4}$; where $0.6 \le \mathrm{Pr}_{m,p} \le 160$; $\mathrm{Re}_{m,p} \ge 10000$
Ranz and Marshall, 1952	$Nu_{m,p} = 2 + 0.6\,\mathrm{Re}_{m,p}^{0.50}\,\mathrm{Pr}_{m,p}^{1/3}$; where $\mathrm{Pr}_{m,p} \ge 0.7$; $\mathrm{Re}_{m,p} \le 2\times10^5$
Bird et al., 1960	$Nu_{m,p} = 0.534\,\mathrm{Re}_{m,p}^{0.59}\,\mathrm{Pr}_{m,p}^{1/3}$
Beek, 1962	$Nu_{m,p} = 3.22\,\mathrm{Re}_{m,p}^{1/3}\,\mathrm{Pr}_{m,p}^{1/3} + 0.117\,\mathrm{Re}_{m,p}^{0.8}\,\mathrm{Pr}_{m,p}^{0.4}$
Hsu, 1965	$Nu_{m,p} = 0.921\,\mathrm{Re}_{m,p}^{0.5}\,\mathrm{Pr}_{m,p}^{0.5}$; where $Pr_{m,p}<1$; $\mathrm{Re}_{m,p} \le 2\times10^5$
Siderman, 1966	$Nu_{m,p} = 1.13\,\mathrm{Re}_{m,p}^{0.5}\,\mathrm{Pr}_{m,p}^{0.5}$; where $Pr_{m,p}<1$; $\mathrm{Re}_{m,p} \le 2\times10^5$
Kunii and Levenspiel, 1969	$Nu_{m,p} = 2 + 1.8\,\mathrm{Re}_{m,p}^{0.50}\,\mathrm{Pr}_{m,p}^{1/3}$
Galloway and Sage, 1970	$Nu_{m,p} = 2 + 2.03\,\mathrm{Re}_{m,p}^{0.5}\,\mathrm{Pr}_{m,p}^{0.33} + 0.049\,\mathrm{Re}_{m,p}\,\mathrm{Pr}_{m,p}^{0.5}$
Whitaker, 1972	$Nu_{m,p} = \left[0.5\,\mathrm{Re}_{m,p}^{-0.1}\left(\frac{(1-\varepsilon_{eff})^{0.5}}{\varepsilon_{eff}}\right) + 0.2\,\mathrm{Re}_{m,p}^{1/15}\left(\frac{(1-\varepsilon_{eff})^{1/3}}{\varepsilon_{eff}}\right)\right]\mathrm{Re}_{m,p}^{0.6}\,\mathrm{Pr}_{m,p}^{1/3}$ and $Nu_{m,p} = 2 + \left(0.4\,\mathrm{Re}_{m,p}^{0.5} + 0.06\,\mathrm{Re}_{m,p}^{0.67}\right)\mathrm{Pr}_{m,p}^{0.4}$ where $Pr_{m,p} = 0.7$; $\mathrm{Re}_{m,p} \le 8\times10^4$
Gnielinski, 1976	$Nu_{m,p} = \frac{\mathrm{Re}_{m,p}(f'_{m,p}/8)\,\mathrm{Pr}_{m,p}}{1+12.7(\mathrm{Pr}_{m,p}^{2/3}-1)(f'_{m,p}/8)^{0.5}}$;

where $f'_{m,p} = \left(0.79\ln(\mathrm{Re}_{m,p}) - 1.64\right)^{-2}$; $10^4 < \mathrm{Re}_{m,p} < 5\times10^6$

$0.5 < \mathrm{Pr}_{m,p} < 2000$

Wakao et al., 1979 $Nu_{m,p} = 2 + 1.1\left[6(1-\varepsilon_{eff})\right]^{0.6}\mathrm{Re}_{m,p}^{0.6}\,\mathrm{Pr}_{m,p}^{1/3}$; where $15 < \mathrm{Re}_{m,p} < 8500$

KTA, 1983 $Nu_{m,p} = 3.776\,\mathrm{Re}_{m,p}^{0.36}\,\mathrm{Pr}_{m,p}^{1/3} + 0.0825\,\mathrm{Re}_{m,p}^{0.86}\,\mathrm{Pr}_{m,p}^{0.5}$ where $Pr_{m,p} = 0.7$;

$100 < \mathrm{Re}_{m,p} < 10^5$ and $Nu_{m,p} = 1.27\dfrac{\mathrm{Pr}_{m,p}^{1/3}}{\varepsilon_{eff}^{1.18}}\mathrm{Re}_{m,p}^{0.36} + 0.033\dfrac{\mathrm{Pr}_{m,p}^{1/2}}{\varepsilon_{eff}^{1.07}}\mathrm{Re}_{m,p}^{0.86}$;

where $100 < \mathrm{Re}_{m,p} < 10^5$; $0.36 < \varepsilon_{eff} < 0.46$

Kays and London, 1984 $Nu_{m,p} = 0.26\dfrac{(1-\varepsilon_{eff})^{0.3}}{\varepsilon_{eff}}\mathrm{Re}_{m,p}^{0.7}\,\mathrm{Pr}_{m,p}^{1/3}$

Incropera and DeWitt, 1990 $Nu_{m,p} = \dfrac{0.79}{\varepsilon_{eff}}\mathrm{Re}_{m,p}^{0.425}\,\mathrm{Pr}_{m,p}^{1/3}$

Macias – Mechin et al., 1991 $Nu_{m,p} = 1.27 + 2.66\,\mathrm{Re}_{m,p}^{0.56}\,\mathrm{Pr}_{m,p}^{-0.41}\left(\dfrac{1-\varepsilon_{eff}}{\varepsilon_{eff}}\right)^{0.29}$

Kemp et al., 1994 $Nu_{m,p} = 2 + 0.5\,\mathrm{Re}_{m,p}^{0.5}\,\mathrm{Pr}_{m,p}^{1/3} + 0.02\,\mathrm{Re}_{m,p}^{0.8}\,\mathrm{Pr}_{m,p}^{1/3}$

Kuwahara et al., 2001 $Nu_{m,p} = \left[1 + \dfrac{4(1-\varepsilon_{eff})}{\varepsilon_{eff}}\right] + \dfrac{1}{2}(1-\varepsilon_{eff})^{1/2}\,\mathrm{Re}_{m,p}^{0.6}\,\mathrm{Pr}_{m,p}^{1/3}$

Nsofor and Adebiyi, 2001 $Nu_{m,p} = 8.74 + 9.34\,\mathrm{Re}_{m,p}^{0.2}\,\mathrm{Pr}_{m,p}^{1/3}$

Kreith et al., 2001 $Nu_{m,p} = 2.58\,\mathrm{Re}_{m,p}^{1/3}\,\mathrm{Pr}_{m,p}^{1/3} + 0.094\,\mathrm{Re}_{m,p}^{0.8}\,\mathrm{Pr}_{m,p}^{0.4}$

Kamiuto and Yee, 2005 $Nu_{m,p} = 0.124\left(\mathrm{Re}_{m,p}\,\mathrm{Pr}_{m,p}\right)^{0.791}$

Melissari and Argyropoulos, 2005 $Nu_{m,p} = 2 + 0.47\,\mathrm{Re}_{m,p}^{0.5}\,\mathrm{Pr}_{m,p}^{0.36}$; where $0.003 \le \mathrm{Pr}_{m,p} \le 10$;

$100 \le \mathrm{Re}_{m,p} \le 5\times10^4$

Benmansour et al., 2006 $Nu_{m,p} = 2 + 2.03\,\mathrm{Re}_{m,p}^{0.5}\,\mathrm{Pr}_{m,p}^{0.33} + 0.049\,\mathrm{Re}_{m,p}\,\mathrm{Pr}_{m,p}^{0.5}$; used the same correlation proposed by Galloway and Sage (1970).

Saidi et al., 2006 $Nu_{m,p} = 0.015 + 0.11\left(\mathrm{Re}_{m,p}\,\mathrm{Pr}_{m,p}\right)^{0.73}$

Frischmann et al., 2008	$Nu_{m,p} = 0.70\,\mathrm{Re}_{m,p}^{0.60}\,\mathrm{Pr}_{m,p}^{0.23}$
Nakayama et al., 2009	$Nu_{m,p} = 0.07\left(\frac{\phi_p}{1-\phi_p}\right)^{2/3}\mathrm{Re}_{m,p}\,\mathrm{Pr}_{m,p}$
Zhou et al., 2010	$Nu_{m,p} = 2 + 1.2\,\mathrm{Re}_{m,p}^{0.5}\,\mathrm{Pr}_{m,p}^{1/3}$
Nie et al., 2011	$Nu_{m,p} = 0.052\frac{\left(1-\varepsilon_{eff}\right)^{0.14}}{\varepsilon_{eff}}\mathrm{Re}_{m,p}^{0.86}\,\mathrm{Pr}_{m,p}^{1/3}$
Yang et al., 2012	$Nu_{m,p} = 1.73 + 0.16\left(\frac{d_p}{d_H}\varepsilon_{eff}\right)^{1/3}\mathrm{Re}_{m,p}^{0.7}\,\mathrm{Pr}_{m,p}^{1/3}$
Incropera et al., 2013	$Nu_{m,p} = \left(2.06/\varepsilon_{eff}\right)\mathrm{Re}_{m,p}^{0.425}\,\mathrm{Pr}_{m,p}^{1/3}$; where $\mathrm{Pr}_{m,p} = 0.7$; $90 < \mathrm{Re}_{m,p} < 4\times10^3$
Roshan et al., 2014	$Nu_{m,p} = \left(2.4\times10^{-5}\right) + 285.6\left(\mathrm{Re}_{m,p}^{2.7}\,\mathrm{Pr}_{m,p}^{1/3}\right)$
Feng et al., 2016	$Nu_{m,p} = 0.198\phi_p^{0.07}\,\mathrm{Re}_{m,p}^{0.66}\,\mathrm{Pr}_{m,p}^{1/3}$
Zanoni et al., 2017	$Nu_{m,p} = 0.001\mathrm{Re}_{m,p}^{1.97}\,\mathrm{Pr}_{m,p}^{1/3}$
Chen et al., 2017a	$Nu_{m,p} = 0.194\,\mathrm{Re}_{m,p}^{0.8}\,\mathrm{Pr}_{m,p}^{0.4}$; where $\mathrm{Pr}_{m,p} = 0.712$; $\mathrm{Re}_{m,p} \le 4\times10^4$
Tian et al., 2018	$Nu_{m,p} = 1.73 + \left[0.16\left\{\left(\frac{d_p}{d_H}\right)\varepsilon_{eff}\right\}^{1/3}\right]\left[\mathrm{Re}_{m,p}\,\mathrm{Pr}_{m,p}\right]$
Present work	Serpentine channel: $Nu_{m,p} = 0.06\left(De_{m,p}\,\mathrm{Pr}_{m,p}\right)^{0.8459}$; where $20.01 \le De_{m,p} \le 118.38$; $5.90 \le \mathrm{Pr}_{m,p} \le 5.92$ Straight channel: $Nu_{m,p} = 0.016\left(\mathrm{Re}_{m,p}\,\mathrm{Pr}_{m,p}\right)^{0.8283}$; where $139.35 \le \mathrm{Re}_{m,p} \le 454$; $5.90 \le \mathrm{Pr}_{m,p} \le 5.95$

The previous works of literature reveal the fact that most of the pressure drop studies are performed within a cylindrical packed column in the vertical orientation with the structured packing. The columns are also large in dimensions. A few studies were reported on the pressure drop (frictional) of the liquid-liquid two-component multiphase flow in the packed straight (Su et al., 2010) and

unpacked serpentine rectangular narrow channels (Wu and Sundén, 2019). The studies of the multiphase flow through the rectangular serpentine channel in packed condition are scarce. The serpentine channel may provide a greater extent of mixing between the phases compared to the same dimension straight channel. Few literature are available about the influence of the flow parameters on the local entropy generation (Deinirel and Kahraman, 1999; Nazari et al., 2017) (entropy generated per unit volume, one of the determining factors for the performances of the thermal machines), other than the temperature gradient for the flow through the straight and the serpentine packed channels. The present context aims at the comparative study of pressure drop (frictional) and local entropy generation rate between two separate packed channels with the straight and serpentine geometries. The Nusselt number correlations were developed for the liquid-liquid two-phase flows through the straight and serpentine packed channels. The impact of pressure drops on the local entropy generation rates was explained for both the channels, as mentioned earlier. The effect of the actual flow velocities of the phases (in case of the two-phase flows) on the pressure drops and local entropy generation rates, as well as the degree of heat transfer, were discussed in the present context. The effect of effective particle diameters of the packing material and the different aqueous-organic phases (water-toluene, water-benzene, and water-p-xylene) on the entropy generation were also studied as well.

4.2. Materials and methods

Two packed channels (the serpentine channel with three semicircles of curvature radius (R_c) = 0.0255 m and the straight channel) of the same cross-sectional area and length were used for the present experimentation as shown in Fig. 4.1. The diameter (d), height (h) and length (L) of the channels are 0.002 ± 0.0001 m, 0.010 ± 0.0001 m and 0.2403 ± 0.0001 m respectively. The length of the serpentine channel is the same as the actual length of the straight channel, 0.02403 m. Both the channels were packed with the same type of sand particles of different effective particle diameters of 4.6×10^{-4} m, 5.5×10^{-4} m, and 6.5×10^{-4} m. A water-bath was used to maintain the temperature outside the channels. The water-bath temperature was maintained at 323 K temperature. Two syringe pumps (supplied by Amar Equipments Pvt. Ltd.) were used to pump the fluids (water-toluene, water-benzene, and water-p-xylene), which can control the flow rate as well. Water was used as the aqueous phase, and toluene, benzene, and p-xylene were used as the organic

phases, passed through the channel. The syringe speed ratios (water/organic) varied from 0.3 to 3.0 for the straight channel and 0.7 to 1.6 for the serpentine channel.

(a)

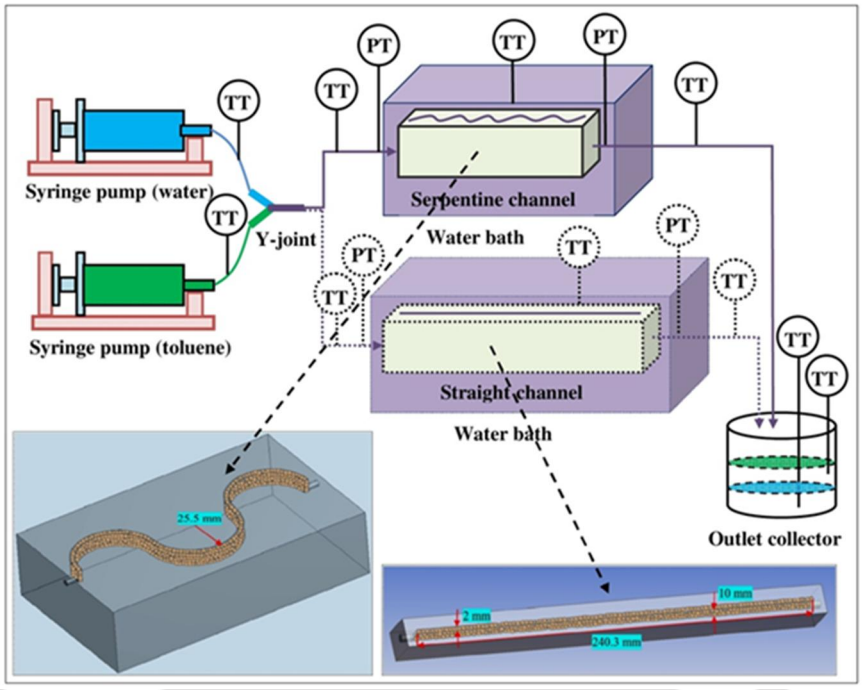

(b)

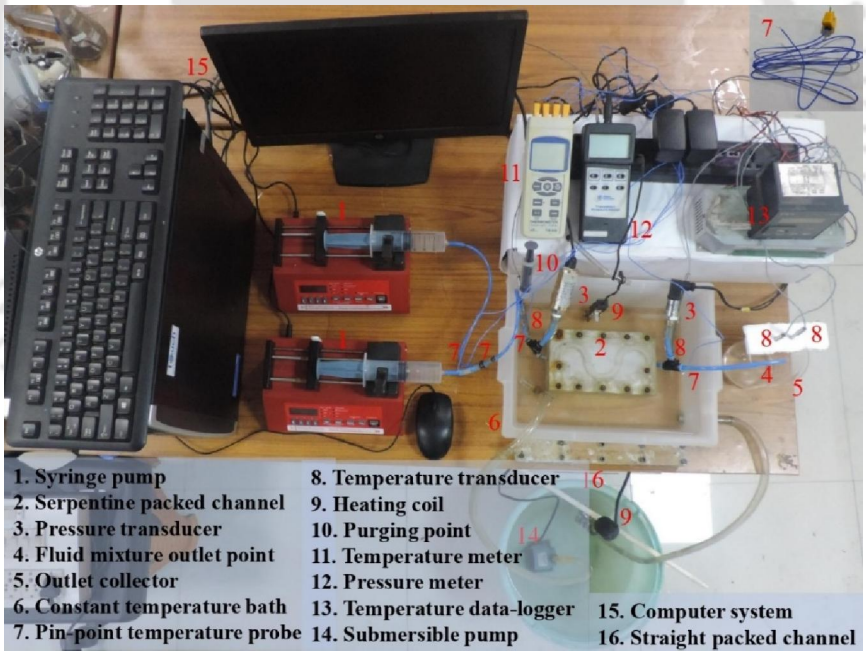

Fig. 4.1. (a) Schematic illustration of the experimental setup (PT – Pressure Transducer and TT – Temperature Transducer), and (b) typical snapshot of the experimental setup.

Two pressure transducers (PS100-5bar, Lutron Electronics) were attached to the inlet and outlet flow lines of the experimental channel to measure the pressure gradient. The pressure transducers were connected to the two pressure meters (Fisher Scientific Traceable^{TM}) and finally to a computer to record the data. The data recording software was taken the average of 100 data and recorded the result as the pressure data for a particular set of flow conditions. Temperature sensors (Fisher Scientific Traceable LIVE^{TM}) with data-logger were used to record the temperature data. One at the constant temperature water-bath and another six at the inlet and outlet respectively to measure the inlet and outlet temperatures of single, and water-organic mixed phases. The two phases were collected at the outlet collector, where the phases were separated by gravity and were recycled. The physical properties (density, viscosity, and surface tension) of the fluids were estimated by following the procedures described elsewhere (Mondal and Majumder, 2018a; Mondal and Majumder, 2018b). The water-organic mixture density (ρ_m), viscosity (μ_m), and surface tension (σ_m) inside the channels were calculated by using the two-fluid models (Eberhart, 1966) as $\rho_m = \rho_w\alpha_w + \rho_o\alpha_o$, $\mu_m = \mu_w\alpha_w + \mu_o\alpha_o$ and $\sigma_m = y_w\sigma_w + y_o\sigma_o$ respectively. The subscripts *'w'*, *'o'*, and 'm' correspond to the aqueous phase, organic phase, and the mixture of the two-phases, respectively. α and y are the holdup of the fluids and the mole fraction of the components. The holdups of the fluids inside the channel were estimated with the help of the volumetric flow rates measurement technique. In this method, the total volumetric flow rates of the mixed phases and the individual volumetric flow rates (after the phase separation by gravity) of the phases were measured with the help of a stopwatch and a measuring cylinder. The total volume of the mixture collected per unit time is the volumetric flow rate of the mixture. The volume of the individual phases can be measured after the gravity separation, and their volumetric flow rates can be determined by dividing the collected volume with the collection time. Then the holdup values of the individual phases inside the channels were calculated separately from the ratios of the volumetric flow rates of the individual phase to the total volumetric flow rates of the mixture.

In the packed bed, the flow properties depend on the properties of the packing materials and the bed. The average particle diameter (d_p) was calculated by using standard sieves set (American Standard Test Sieve Series). The average particle diameter of the sand particle determined in the

present work is 4.63×10^{-4} m, 5.52×10^{-4} m, and 6.54×10^{-4} m, which are classified as the medium sand (Zou and Yu, 1995). The effective porosity of the bed (ε_{eff}) was calculated by the ratio of total bed volume to the total pore volume. The values determined in the present experiment are 0.36, 0.38, and 0.40, respectively, which are approximately equal to the value calculated from the correlation developed by Zou and Yu (1995). In this regard, it is worthy of mentioning that Zou and Yu (1995) classified the sand particles according to their average diameter range and provided the effective porosity for the sand bed. The sphericity of the particle was determined according to the Krumbein and Sloss method (Krumbein and Sloss, 1963). It was done by analyzing an image of the particles with the help of an image analyzing software (Digimizer® 4 software). As per the present experiment, its value is 0.85, which falls within the range of 0.50 to 0.90 as per the characteristic feature of natural sand reported by Cho et al. (2006). The physical properties of the packed materials, as well as the fluids, are tabulated in Table 4.4.

Table 4.4. Physical properties of the fluids, packed materials, and the bed.

Fluid properties:					
Fluids	**Density (kg m^{-3})**	**Viscosity (N-s m^{-2})**	**Surface tension (N m^{-1})**	**Thermal conductivity (W m^{-1} K^{-1})**	**Specific heat capacity (J kg^{-1} K^{-1})**
Water (298 K)	997.05	8.90×10^{-4}	7.22×10^{-2}	0.6104	4179.0
Toluene (298 K)	864.00	5.60×10^{-4}	2.77×10^{-2}	0.1398	1745.5
Benzene (298 K)	876.50	6.12×10^{-4}	2.76×10^{-2}	0.1385	1759.0
p-xylene (298 K)	860.00	3.43×10^{-4}	2.83×10^{-2}	0.1313	1837.5
Packed material properties:			**Packed bed properties:**		
Packed material	**Sphericity (-)**	**Average particle diameter (m)**	**Type of bed**	**Packed bed density (kg m^{-3})**	**Effective porosity (-)**
Medium sand particle	0.85	4.63×10^{-4}	Medium sand packed bed	1376	0.36
	0.85	5.53×10^{-4}		1325	0.38
	0.85	6.54×10^{-4}		1274	0.40

4.2.1. Estimation of heat transfer coefficient

In the case of forced convection, the heat transfer coefficient was determined by using Eq. (4.1) (Incropera and DeWitt, 1990; Nazari et al., 2017).

$$h'_{m,p} = \frac{M'_{m,p}\, C_{p,m}(T_{outlet} - T_{inlet})}{A_S \Delta T_{lm}} \tag{4.1}$$

In Eq. (4.1), A_s is the effective surface area of the heat transfer. The specific heat capacity $C_{P,m}$ was calculated by, (Rule of Mixtures Calculator for Heat Capacity, internet sources)

$$C_{p,m} = \left(\frac{Q_W \rho_w}{Q_W \rho_w + Q_o \rho_o}\right) C_{p,w} + \left(\frac{Q_o \rho_o}{Q_W \rho_w + Q_o \rho_o}\right) C_{p,o} \tag{4.2}$$

Q, assigned as the fluid volumetric flow rate. The heat transfer coefficient and the mass flow rate of the liquid-liquid mixture through the packed bed are represented by $h'_{m,p}$, and $M'_{m,p}$ ($M'_{m,p} = \left(\frac{U_m}{\varepsilon_{eff}}\right) A_c \rho_m$ (Incropera and DeWitt, 1990); where A_c is the cross-sectional area of the channel, and U_m is the actual velocity of the mixture within the channel). The inlet and outlet temperatures of the liquids are designated as T_{inlet} and T_{outlet}. LMTD or ΔT_{lm} is the logarithmic mean temperature difference ($\Delta T_{lm} = \frac{\Delta T_{inlet} - \Delta T_{outlet}}{\ln(\Delta T_{inlet} / \Delta T_{outlet})}$; where the inlet and outlet temperature differences are represented by the terms ΔT_{inlet} and ΔT_{outlet}, respectively (McCabe et al., 2005)). The terms ΔT_{inlet}, and ΔT_{outlet} were calculated from the temperature differences between the phases at the inlet and outlet by measuring the temperatures of the fluids just before mixing, and immediately after the phase separation at the collection tank. The inlet temperatures of both the fluids (water-toluene) and their mixtures before entering the channels were maintained at 318 K. Therefore, the ΔT_{inlet} values are fixed at 278 K. The channel blocks along with the packing materials were given sufficient time before each run to attain the water-bath temperature, 323 K. The outlet temperatures of the mixtures, hold different values depending on the mass flow rate of the channels along with the channel geometries (318.5 K – 319 K for the serpentine channel and 318.3 K – 318.8 K for the straight channel). Hence, the ΔT_{lm} values varied from 4.48 – 4.75 at an average of 4.61 for the serpentine channel and 4.58 – 4.84 at an average of 4.71 for the straight channel. According to Martin (1981), 1/6th of the total number of particles relocates and eventually

interacts with the heat transfer surface. Thus the effective surface area of the particle (A_s) taking part in the convection process is the surface area of the 1/6th of the total number of particles. The total number of particles (N') in the packed bed was estimated by using the correlation (Eq. (4.3)), proposed by Jamialahmadi et al. (1995).

$$\frac{N' d_p^2}{d_H L} = (1 - \varepsilon_{eff}) \frac{3 d_H}{2 d_p} \tag{4.3}$$

where d_H is the hydraulic diameter of the channels. The surface area of one particle (A_p) is calculated by, (Jamialahmadi et al., 1995)

$$A_p = \frac{\pi^{1/3} \left(6 v_p\right)^{2/3}}{\varphi_p} \tag{4.4}$$

v_p is the volume of a single particle, φ_p is the sphericity of the particles. The volume of the single-particle can be calculated from the mass of the particle in the bed as per the following mass balance (Moffat, 1988)

$$N' v_p = M_b / \rho_b \tag{4.5}$$

where ρ_b is the density of the bed, and M_b is the mass of the bed of particles. Based on the experimental heat transfer coefficient data, the Nusselt number was defined by (McCabe et al., 2005)

$$Nu_{m,p} = \frac{h'_{m,p} d_p}{k_{m,p}} \tag{4.6}$$

where $Nu_{m,p}$ is the Nusselt number, which mainly depends on two dimensionless numbers, Reynolds number ($Re_{m,p}$) and Prandtl number ($\mathrm{Pr}_{m,p} = \frac{C_{P,m} \mu_m}{k_{m,p}}$ (McCabe et al., 2005)). In Eq. (4.6), the average particle diameter (d_p) was used instead of characteristic length as it is equivalent to the equivalent diameter of the channels in case of the empty channels and equivalent to the average particle diameters in case of packed channels. $k_{m,p}$ is the conductive heat transfer coefficient for the liquid-liquid flow through the packed bed which was calculated by (Incropera and DeWitt,1990)

$$k_{m,p} = \alpha_w k_w + \alpha_o k_o \tag{4.7}$$

4.2.2. Local entropy generation

Heat transfer in a system depends on the thermodynamic irreversibility and the local entropy generation. Entropy generation decreases the quality of the heat transfer phenomenon, as it is the measure of chaos. Hence, to optimize the thermodynamic and fluid flow irreversibility, the minimization of the entropy generation is desired. At the diabatic flow condition, the combination of the second law of thermodynamics and the energy equations resulted in the entropy generation rate per unit length ($ds'_{m,p}$), is represented by Eq. (4.8) (Revellin et al., 2009),

$$\underbrace{ds'_{m,p}}_{\text{entropy generation}} = \underbrace{\frac{q_{m,p}^2 P}{h'_{m,p}\Delta T_{lm}^2}}_{\text{heat transfer contribution}} + \underbrace{\frac{M'_{m,p}U_m/\varepsilon_{eff}}{\Delta T_{lm}}\left(-\frac{\Delta P_f}{L}\right)_{m,p}}_{\text{pressure drop contribution}} \tag{4.8}$$

where, $q_{m,p}$ is the two-phase convective heat flux in the packed bed, and P is the channel perimeter. The value of $q_{m,p}$ is calculated by using Eq. (4.9) (Revellin et al., 2009).

$$q_{m,p} = h'_{m,p}\Delta T_{lm} \tag{4.9}$$

During the whole process, the channel-wall temperature was maintained at 303 K.

4.2.3. Error analysis

The percentage of errors ($\%E$) between the experimental data and the estimated values from the correlations are calculated by the Eq. (4.10). Finally, the mean absolute percentage error ($MAPE$) between the experimental results and the results obtained from the correlations proposed by various authors and the newly developed correlations were calculated. $MAPE$ values are determined by Eq. (4.11), where the experimental and predicted values are denoted by EV and PV, respectively. N is the total number of measurements in the Eq. (4.11) (Mondal and Majumder, 2018a, and 2018b).

$$\%\mathrm{E} = \left(\frac{\mathrm{E}V - PV}{\mathrm{EV}}\right)\times 100\% \tag{4.10}$$

$$MAPE = \frac{1}{N}\sum\left(\left|\frac{(\mathrm{EV}-\mathrm{PV})}{\mathrm{EV}}\right|\right)\times 100\% \tag{4.11}$$

4.2.4. Uncertainty analysis of the experimentally measured data

The estimation of the experimental uncertainty is essential to assess the reliability of the results. The uncertainties in the measured data propagate into the results. In the present context, the average values of the six to eight experiments were taken as the final values. The detailed uncertainty analysis was done, followed by Mondal and Majumder (2018a, and 2018b), and Moffat (1988). (**Appendix - I**)

4.3. Results and discussion

4.3.1. Pressure gradient (frictional) for the liquid-liquid flow in the packed straight and serpentine channel

Pressure gradient (Frictional) for the liquid-liquid flow, considering there is no pressure drop due to acceleration, can be represented as [34]

$$\left(\frac{\Delta P_f}{L}\right)_{m,p} = \left(\frac{\Delta P_T}{L}\right)_{m,p} - \left(\frac{\Delta P_g}{L}\right)_{m,p} - \left(\frac{\Delta P_{inlet}}{L}\right)_{m,p} \tag{4.12}$$

where $\Delta P_T / L$ is the total pressure gradient obtained from the experiment, $\Delta P_g / L$ is the pressure gradient, due to the gravitational acceleration. In the subscript '*m,p*', *m* refers to the liquid-liquid mixture, and *p* refers to the packed condition. $\Delta P_{inlet} / L$ is the total inlet pressure gradient (considering the outlet pressure gradient is as zero), which can be expressed as (Mondal and Majumder, 2018a)

$$\left(\frac{\Delta P_{inlet}}{L}\right)_{m,p} = (K' + \zeta)\frac{\rho_m \left(U_m / \varepsilon_{eff}\right)^2}{2L} \tag{4.13}$$

In the Eq. (4.13), K' and ζ are the coefficients of head loss due to contraction or expansion and the entrance, which were considered as 0.5 and 1.31, respectively. Two loss coefficients were used in Eq. (4.13), due to the presence of two head losses in the experimental setup, just before the entrance where the inlet pipe diameter changed from 0.004 m to 0.002 m, and at the entrance, where the 0.002 m circular geometry is changed to the 0.010 m rectangular geometry. U_m were calculated by (Mondal and Majumder, 2018a)

$$U_m = \frac{U_o}{\varepsilon_{eff}\alpha_o} + \frac{U_w}{\varepsilon_{eff}\alpha_w} \tag{4.14}$$

where U_o and U_w are the actual velocities of the organic and water phases, respectively. By performing the dimensional analysis and the regression analysis of the dependent flow parameters, Mondal and Majumder (2018a, and 2018b) suggested the correlations of the pressure drop (frictional) for the liquid-liquid flow through the packed straight and serpentine channels which are expressed as

$$\left(\frac{d_p}{\rho_m U_m^2 / \varepsilon_{eff}^2}\right)\left(\frac{\Delta P_f}{L}\right)_{m,p} = 2\left(f_m^{'}\right)_p = 6.930\times10^{1}\left(\mathrm{Re}_{m,p}\,Ca_{m,p}\right)^{0.3089}\left(Fr_{m,p}\right)^{-2.1987} \text{ (Straight channel)} \tag{4.15}$$

$$\left(\frac{d_p}{\rho_m U_m^2 / \varepsilon_{eff}^2}\right)\left(\frac{\Delta P_f}{L}\right)_{m,p} = 2\left(f_m^{'}\right)_p = 4.419\times10^{1}\left(De_{m,p}Ca_{m,p}\right)^{0.073}\left(Fr_{m,p}\right)^{-1.694} \text{ (Serpentine channel)} \tag{4.16}$$

where $\left(f_m^{'}\right)_p$ is the Fanning friction factor for the flow of the phase mixture. $De_{m,p}$, $Ca_{m,p}$ and $Fr_{m,p}$ in the Eqs. (4.15-4.16) represent the Dean number ($De_{m,p} = \mathrm{Re}_{m,p}\sqrt{\frac{d_p}{2r_c}}$, where $\mathrm{Re}_{m,p} = \frac{d_p\rho_m(U_m/\varepsilon_{eff})}{\mu_m}$ (McCabe et al., 2005)), Capillary number ($Ca_{m,p} = \frac{\mu_m(U_m/\varepsilon_{eff})}{\sigma_m}$ (McCabe et al., 2005)), and Froude number ($Fr_{m,p} = \frac{U_m/\varepsilon_{eff}}{\sqrt{gd_p}}$ (McCabe et al., 2005), respectively

(The theory for the calculation of the correlation coefficient and standard error with ANOVA is given in **Appendix – I**).

In the present work, a correlation for the pressure drop (frictional) in the packed serpentine channel is developed incorporating the viscous and inertial terms of Ergun equation, following trial and error method, which is expressed as

$$\left(\frac{\Delta P_f}{L}\right)_{m,p} = \left[\frac{135.6\mu_m U_m\left(1-\varepsilon_{eff}\right)^2}{\phi_p^2 d_p^2 \varepsilon_{eff}^3} + \frac{0.12\rho_m U_m^2\left(1-\varepsilon_{eff}\right)}{\phi_p d_p \varepsilon_{eff}^3}\right] \text{ (for serpentine channel)} \tag{4.17}$$

where 135.6 and 0.12 are the dimensionless constants. The frictional pressure drop correlation is suggested for the rectangular straight packed channel which is represented by

$$\left(\frac{\Delta P_f}{L}\right)_{m,p} = \left[\frac{56.3\mu_m U_m \left(1-\varepsilon_{eff}\right)^2}{\phi_p^2 d_p^2 \varepsilon_{eff}^3} + \frac{0.1\rho_m U_m^2 \left(1-\varepsilon_{eff}\right)}{\phi_p d_p \varepsilon_{eff}^3}\right] \qquad \text{(for straight channel)} \qquad (4.18)$$

The dimensionless constants were found to be 56.3 and 0.10 for the straight channel, as shown in Fig. 4.2. The Eqs. (4.17–4.18) are valid within the range of operating variables: $139 \le \mathrm{Re}_{m,p} \le 454$; $0.0035 \le Ca_{m,p} \le 0.011$ and $3.40 \le Fr_{m,p} \le 11.55$. The newly developed equations based on Ergun viscous and inertial terms for the straight and serpentine packed channels closely predict the experimental data with the *MAPE* values of 2.04 and 2.46 within the specified operating variables, as shown in Fig. 4.2, and Table 4.5. In case of the serpentine channel, the pressure drop models demonstrated by Reichelt (1972), Eisfeld and Schitzlein (2001), and Singh et al. (2006) resemble the experimental data approximately with *MAPE* values of 13.03, 17.95 and 21.88 respectively (Table 4.5) whereas, for straight packed channel Nemec and Levec (2005) correlation satisfies the experimental pressure drop data with MAPE value of 77.77. In the case of the serpentine channel, the friction factor models given by Idelchik (1989), and Wu and Pruess (1996) were satisfied the experimental data with the MAPE values of 17.33 and 62.5, respectively (Table 4.5).

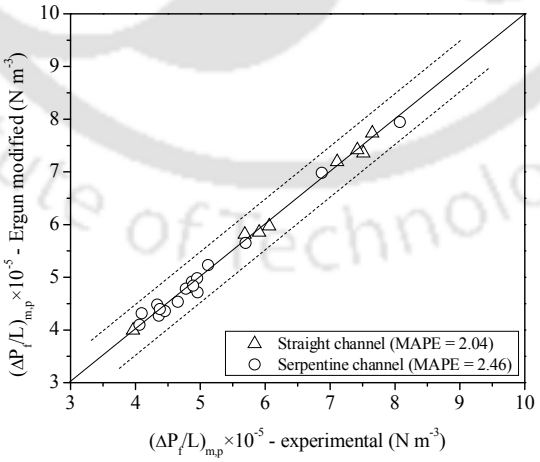

Fig. 4.2. Experimental versus predicted pressure drop values (phases: water-toluene, and d_p = 4.63×10^{-4} m).

The serpentine channel results in more pressure drop for the same actual mixture velocity as compared to the straight channel of the same dimensions, and the predicted pressure drop obtained from the correlations available in the previous literature does not express the experimental results precisely, as shown in Table 4.5, and Fig. 4.3.

Table 4.5. Deviation of the experimental pressure drop and friction factor values with the available correlations (phases: water-toluene, and $d_p = 4.63 \times 10^{-4}$ m).

Pressure drop			**Friction factor**		
Authors	**Mean absolute percentage error (MAPE)**		**Authors**	**Mean absolute percentage error (MAPE)**	
	Straight channel	**Serpentine channel**		**Straight channel**	**Serpentine channel**
Ergun, 1952; McCabe et al., 2005	406.71	43.94	Carman, 1937	311.19	23.37
Metha and Hawley, 1969	480.53	76.31	Ergun, 1952; McCabe et al., 2005	322.49	19.88
Reichelt, 1972	539.76	13.03	Rose, 1945	-	-
Macdonald et al., 1979	415.56	60.16	Rose and Rizk, 1949	-	-
Feng, 1989	99.02	99.58	Hicks, 1970	-	-
Foumeny et al., 1993	192.65	42.60	Tallmadge, 1970	-	-
Lee and Ogawa, 1994	94.24	53.04	Brauer, 1971	324.12	23.17
Liu and Masliyah, 1996	407.31	57.58	Lee and Ogawa, 1974	99.49	99.56
Raichura et al., 1999	755.21	173.41	Jones and Krier, 1983	335.94	25.34
Gibilaro, 2001	347.48	69.36	Watanabe, 1989	-	-
Eisfeld and Schitzlein, 2001	199.08	17.95	Idelchik, 1989	245.14	17.33

Nemec and Levec, 2005	77.77	88.80	Wu and Pruess, 1996	62.5	62.5
Dolejš and Machač, 2005	92.35	677.27	Nemec and Levec, 2005	427.69	32.69
Vafai et al., 2006	382.82	63.08	Singh et al., 2006	272.42	22.88
Singh et al., 2006	266.18	21.88	Montillet et al., 2007	362.52	-
Montillet et al., 2007	167.52	96.05	Ozahi et al., 2008	-	-
Çarpinlioğlu et al., 2008	95.99	93.34	Yang et al., 2012	-	-
Cheng, 2011	-	41.43	Harrison et al., 2013	-	-
Allen et al., 2013	289.02	356.57	Chen et al., 2017a	466.17	32.02
Chen et al., 2017a	497.03	47.60	Guo et al., 2017	-	-
Tian et al., 2018	91.29	96.41	Present work	2.12	2.58
Present work	2.04	2.46			

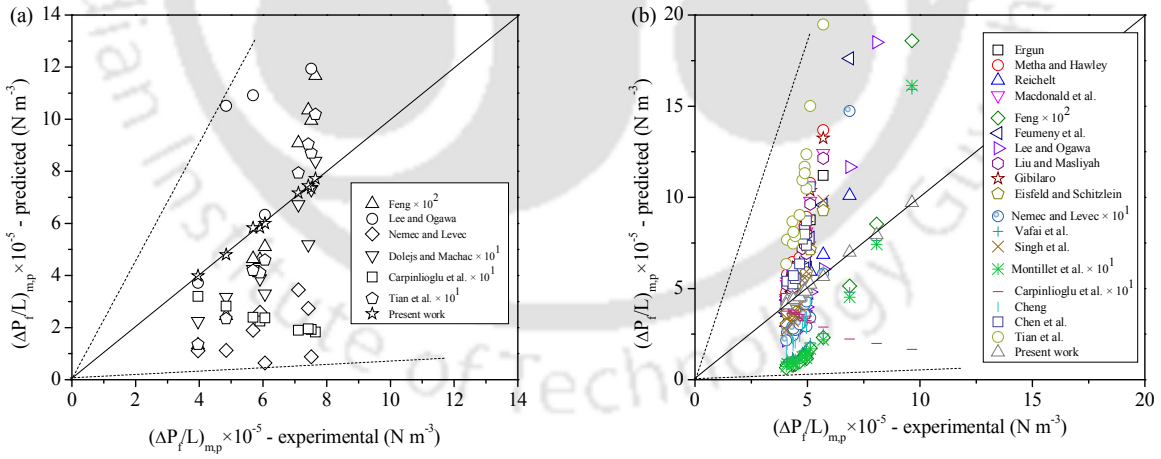

Fig. 4.3. Parity plot of the experimental pressure drops with the available correlations (a) Straight channel and (b) Serpentine channel (phases: water-toluene, and $d_p = 4.63 \times 10^{-4}$ m).

The main reasons of the deviations with the previous correlations are for the difference in geometry (large size cylindrical column in vertical orientations), as well as the variation in the physical

properties of the fluid and the packing materials, which were used by different investigators as cited in Table 4.5. The variations of experimental pressure drop with the mass flow rate for the flow-through both the channels are shown in Fig. 4.4. As expected, the pressure drop increases with the increase of mass flow rate in case of the channel flow. At a constant mass flow rate, the pressure drop (frictional) is higher for the packed serpentine channel, due to the presence of secondary flow or Dean flow.

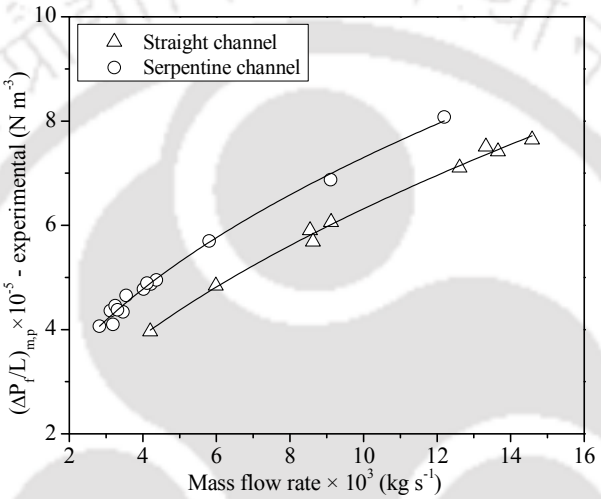

Fig. 4.4. Experimental pressure drop versus mass flow rate (phases: water-toluene, and d_p = 4.63 × 10^{-4} m).

4.3.2. Convective heat transfer

At the lower Reynolds number values, both the channels experience the same effects on the Nusselt number values. In the case of the serpentine channel due to the effect of Dean flow (curvature effect), the Nusselt number values were found to be higher than the straight channel at the higher Reynolds number values, as shown in Fig. 4.5.

In the present study correlations for the convective heat transfer coefficient incorporating Nusselt numbers were suggested by doing the dimensional and regression analysis for the two-phase flow through the packed straight and serpentine channel considering the same temperature driving force between the inlet and outlet, which are expressed respectively as

$$Nu_{m,p} = 2.41\times10^{-2}\left(\mathrm{Re}_{m,p}\right)^{0.99}\left(\mathrm{Pr}_{m,p}\right)^{0.35} \quad \text{for straight channel} \quad (4.19)$$

$$Nu'_{m,p} = 3.34\times10^{-2}\left(De_{m,p}\right)^{1.11}\left(\mathrm{Pr}_{m,p}\right)^{0.72} \quad \text{for serpentine channel} \quad (4.20)$$

Eq. (4.19) and Eq. (4.20) are valid within the ranges of $92.08 \le \mathrm{Re}_{m,p} \le 454$; $5.89 \le \mathrm{Pr}_{m,p} \le 5.95$ and $23.54 \le De_{m,p} \le 96.65$.

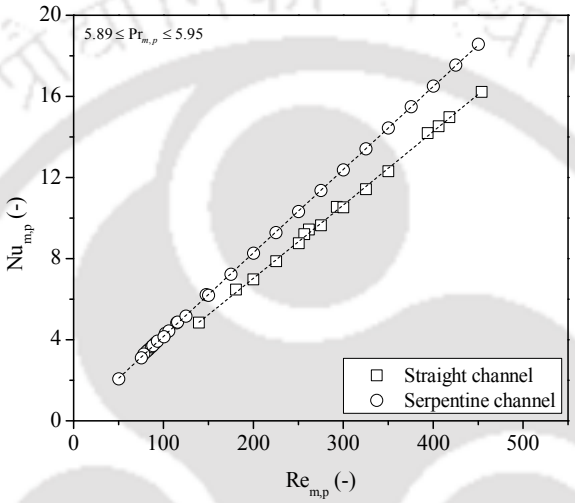

Fig. 4.5. Variation of the Nusselt number values concerning the Reynolds number values for the liquid-liquid flow through the packed straight and serpentine channel (phases: water-toluene, and $d_p = 4.63 \times 10^{-4}$ m).

As shown in Fig. 4.5, the Nusselt number increases, when the Reynolds number ($Re_{m,p}$) increases, in the case of both channels. However, the increment is more significant in the case of the serpentine channel due to the curvature effect, which implied the higher heat transfer coefficient or higher transfer rate than the straight channel according to the first law of thermodynamics. The experimental Nusselt number values were compared with the values estimated from the correlations available in the literature and tabulated in Table 4.6.

Table 4.6. Deviation of the experimental Nusselt number values with the available correlations in turbulent flow condition (phases: water-toluene, and $d_p = 4.63 \times 10^{-4}$ m).

Authors	Mean absolute percentage error (MAPE)	
	Straight channel	Serpentine channel
Dittus-Bolter, 1942	68.62	87.52
Ranz and Marshall, 1952	71.28	35.66
Bird et al., 1960	125.60	23.85
Beek, 1962	406.73	271.17
Hsu, 1965	216.79	110.21
Siderman, 1966	288.67	157.92
Kunii and Levenspiel, 1969	378.16	239.41
Galloway and Sage, 1970	712.72	340.58
Whitaker, 1972	216.26 and 61.28	38.02 and 233.60
Gnielinski, 1976	63.75	85.29
Wakao et al., 1979	-	525.91
KTA, 1983	556.60 and 652.33	361.47 and 422.83
Kays and London, 1984	393.83	114.79
Incropera and DeWitt, 1990	269.74	187.55
Macias – Mechin et al., 1991	210.77	97.03
Kemp et al., 1994	73.11	35.97
Kuwahara et al., 2001	151.05	133.07
Nsofor and Adebiyi, 2001	430.71	612.49
Kreith et al., 2001	306.41	197.54
Kamiuto and Yee, 2005	264.52	30.53
Melissari and Argyropoulos, 2005	17.48	28.14
Benmansour et al., 2006	712.72	340.58
Saidi et al., 2006	106.13	15.78
Frischmann et al., 2008	160.22	39.91
Nakayama et al., 2009	-	607.57
Zhou et al., 2010	224.72	137.54
Nie et al., 2011	160.58	19.27
Yang et al., 2012	39.71	50.74
Incropera et al., 2013	-	649.82
Roshan et al., 2014	-	-
Feng et al., 2016	22.32	42.10

Zanoni et al., 2017	-	67.02
Chen et al., 2017a	199.28	8.99
Tian et al., 2018	-	50.74
Present work	3.71	6.17

The correlations developed by Melissa and Argyropoulos (2005) and Feng et al. (2016) satisfied the experimental data with the *MAPE* values of 17.48 and 22.32 for the straight channel. Whereas, Chen et al. (2017a), Nie et al. (2011), and Saidi et al. (2006) correlations satisfied the present experimental data with the *MAPE* value of 8.99, 19.27, and 15.78 respectively for the serpentine channel (Table 4.6). The newly generated correlations satisfy the experimental values very closely with the *MAPE* values of 3.71 and 6.17 for the straight and serpentine channel, respectively. The deviations of the experimental values from various correlations are shown in Fig. 4.6 and tabulated in Table 4.6. As the pressure drop, the Nusselt number values also showed high deviations with the literature due to the reasons mentioned earlier. With the increase of the Reynolds number, the Nusselt number increases by 3.63% for the straight channel and 4.12% for the serpentine channel.

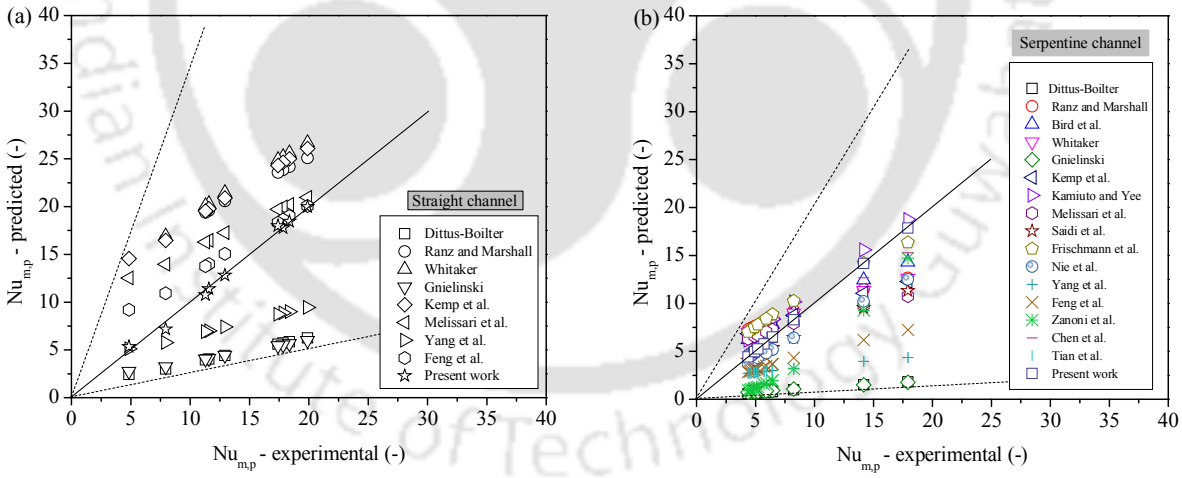

Fig. 4.6. Experimental versus predicted (from the available correlations) Nusselt number values (a) Straight channel and (b) Serpentine channel (phases: water-toluene, and d_p = 4.63 × 10^{-4} m).

Though the difference in the Nusselt number values between the two geometries is found very small in the present context, it can be enhanced by decreasing the curvature ratio (Curvature ratio = hydraulic diameter of the channel / (2 × radius of curvature) = 0.065 in the present case) of the

serpentine geometry for a particular mass flow rate (Naphon and Suwagrai, 2007). Higher Nusselt number corresponds to a higher heat transfer coefficient, which enables the packed serpentine channel more efficient than the packed straight channel for its use as a heat transfer device.

4.3.3. Relation of heat transfer coefficient in terms of friction factor

The friction factor, related to the pressure drop, is another essential factor to influence the Nusselt number as well as the heat transfer coefficient. The influence of the friction factor on the pressure drop and the Nusselt number were shown in Fig. 4.7(a) and Fig. 4.7(b), respectively. The friction factor is reduced with the increase in pressure drop, which increases with the increasing mass flow rate. The reduction rate is more significant in the case of the serpentine channel compared to the straight channel, as shown in Fig. 4.7(a). The higher friction factor corresponds to the higher Nusselt number as well as the higher heat transfer coefficient, as shown in Fig. 4.7(b), which ensures the serpentine channel more efficient to heat transfer.

Based on the present experimental results, correlations for the heat transfer coefficients were also developed by incorporating the friction factors, which are represented for the straight and serpentine packed channels respectively as

$$St_{m,p} = 0.68\times10^{-1}(\mathrm{Re}_{m,p})^{-0.044}(\mathrm{Pr}_{m,p})^{-0.981}(Fa_{m,p})^{0.048} \quad \text{for straight channel} \quad (4.21)$$

$$St'_{m,p} = 1.03\times10^{-1}(De_{m,p})^{-0.020}(\mathrm{Pr}_{m,p})^{-0.486}(Fa_{m,p})^{0.064} \quad \text{for serpentine channel} \quad (4.22)$$

where

$$Fa_{m,p} = \frac{\left(f_m^{'}\right)_p / 2}{1+5\sqrt{\left(f_m^{'}\right)_p / 2}\left(\mathrm{Pr}_{m,p}-1\right)} \quad (4.23)$$

In Eqs. (4.21-4.22), Stanton number (the ratio of heat transferred into a fluid to the thermal capacity of the fluid) is defined for the straight and serpentine channel respectively by, (Incropera and DeWitt, 1990)

$$St_{m,p} = Nu_{m,p}/(\mathrm{Re}_{m,p}\,\mathrm{Pr}_{m,p}) \quad (4.24)$$

$$St'_{m,p} = Nu_{m,p}/(De_{m,p}\,\mathrm{Pr}_{m,p}) \quad (4.25)$$

The Eqs. (4.21-4.22) are strictly satisfied with the experimental data with *MAPE* values of 3.78 and 5.63, respectively.

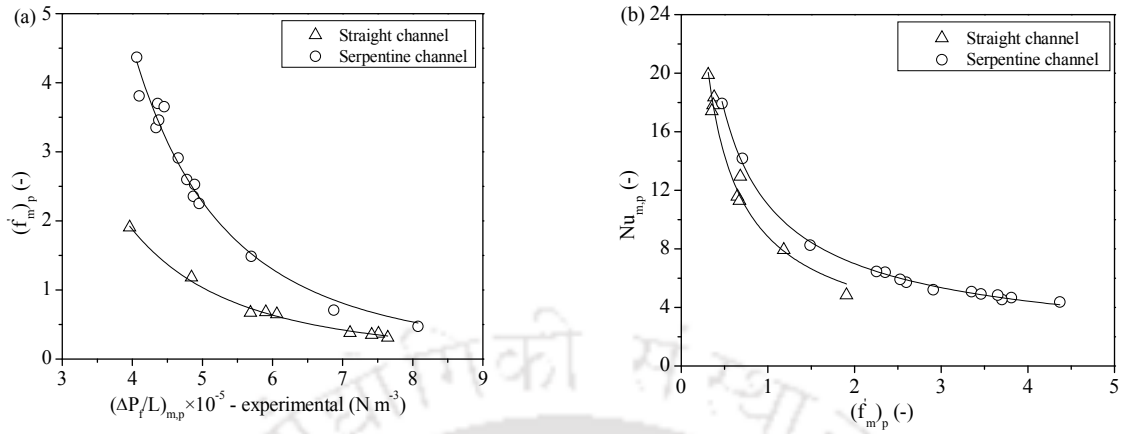

Fig. 4.7. Deviation of the friction factor with the (a) pressure drop, and (b) Nusselt number (phases: water-toluene, and d_p = 4.63 × 10^{-4} m).

4.3.4. Entropy generation rate for the liquid-liquid flow based on the separated flow model

The entropy generation rate for the liquid-liquid flow through the channel is dependent on the pressure drop (frictional) along with the other flow parameters like the actual velocity of the fluids mixture, the mass flow rate of the fluids and obviously on the Nusselt number as the heat transfer coefficient (Eq. (4.8), described in the materials and method section).

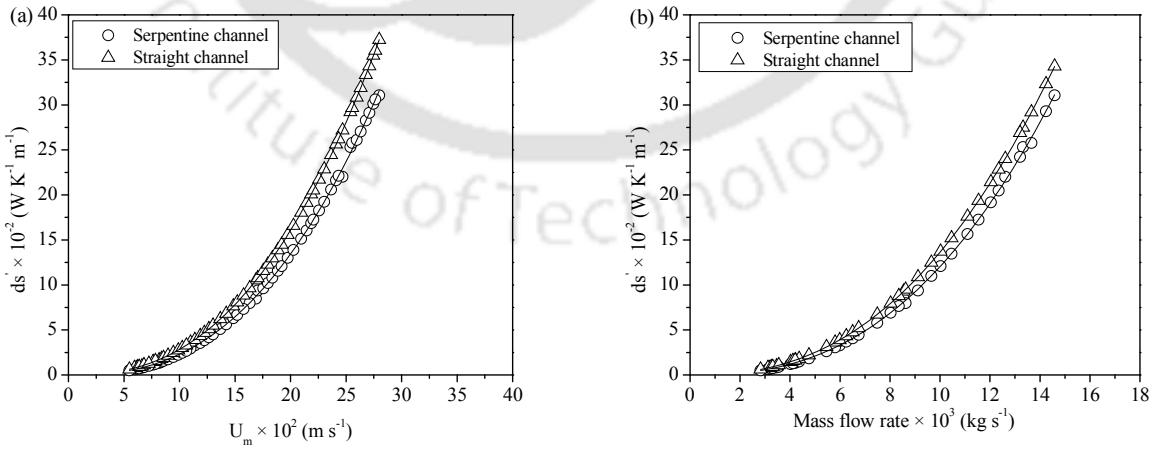

Fig. 4.8. Variation of the entropy generation concerning the (a) actual velocity of the fluid mixture, and (b) mass flow rate of the mixture (phases: water-toluene, and d_p = 4.63 × 10^{-4} m).

Packed materials, packed bed geometry, and the properties of the fluids can control the local entropy generation when the driving force for the heat transfer is the same for both the straight and serpentine packed channels. The effect of actual mixture velocity on the local entropy generation rate inside the channels is shown in Fig. 4.8. With the increase of the actual velocity of the fluid-mixture, the Reynolds number, as well as the turbulence increases, which increases the entropy generation. At a fixed actual velocity of the mixture, the local entropy generation is lower subject to the serpentine channel due to the curvature or Dean effect initiating secondary flow (Fig. 4.8(a)). The fluids mass flow rate increases with the increase of the actual velocity, which shows a similar effect on the entropy generation (Fig. 4.8(b)). As said earlier, the Nusselt number and pressure drop also influence the rate of the local entropy generation, as shown in Fig. 4.9(a), and Fig. 4.9(b). The same trends were observed in Fig. 4.9, as the effect of the actual velocity of the fluids mixture (Fig. 4.8(a)) and mass flow rate (Fig. 4.8(b)). When the mass flow rate (resulted at the increase of actual mixture velocity), Nusselt number, and the pressure drop of the mixture increases, the rate of the local entropy generation increases (Fig. 4.8 and Fig. 4.9). The entropy generation is higher for the straight channel concerning the serpentine channel for a particular value of Nusselt number and pressure drop (Fig. 4.9(a) and 4.9(b)).

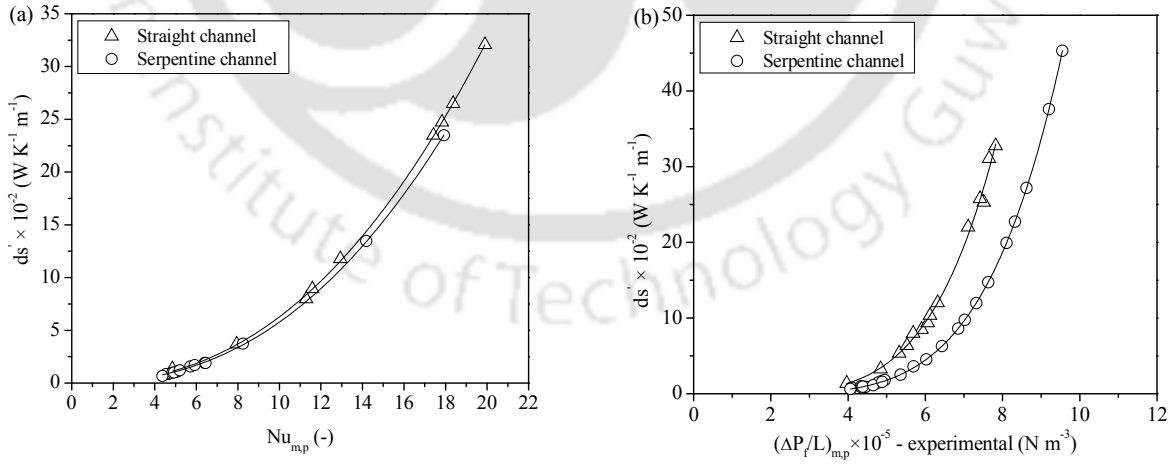

Fig. 4.9. Variation of the local entropy generation rate concerning (a) the Nusselt number, and (b) pressure drop (phases: water-toluene, and d_p = 4.63 × 10^{-4} m).

If the curvature ratio of the serpentine geometry decreases, the entropy generation due to friction decreases, and thus the deviation between the entropy generation rate in the case of the straight and serpentine geometries may be increased (Khosravi-Bizhaem and Abbassi, 2018). Bejan number ($Be = ds_{m,p\ \text{(heat transfer)}} / ds'_{m,p}$ (Incropera and DeWitt, 1990; Zhou et al., 2010)), determines the importance of heat transfer contribution to the total entropy generation. In the case of channel flow, at the lower mass flow rate (lower pressure drop), the entropy generation is mainly due to heat transfer. However, at the higher mass flow rate (higher-pressure drop), the entropy generation mainly depends on the pressure drop contribution (Revellin et al., 2009). As per present experimental result, the Bejan number within the range of experimental conditions were close to zero indicated the influence of the fluid flow irreversibility rather than the thermal irreversibility to the entropy generation. Hence, the pressure drop contribution is a prominent factor in the present experimental condition. Both types of geometries (straight and serpentine), provided the same increasing trend in entropy generation. Still, serpentine geometry acquires a lower entropy generation than the straight geometry due to the secondary flow. Hence, the serpentine channel may be appropriate at the higher mass flow rate with the higher Nusselt number and reduced entropy generation, but at the lower mass flow rate, the straight channel may be used.

The effect of the particle diameter (packing material) on the Bejan number and the entropy generation is shown in Fig. 4.10(a) and Fig. 4.10(b). The Bejan number value decreases with the increase of mass flow rate and acquires the lower values in the case of the serpentine channel for a particular mass flow rate. Hence, at the higher mass flow rate, the heat transfer contribution is lower than the pressure drop contribution to the entropy generation in the case of both the channels. Still, the effect is higher in the case of the serpentine channel due to the higher pressure drop (Fig. 4.10(a)). At a fixed mass flow rate, with the increase of particle diameter of the packing material, the Bejan number value increases for a particular channel geometry as the pressure drop value decreases. As the diameter increases, the gap between the two Bejan number curves for the two different geometries decreases as the pressure drop values come closer, diminishing the effect of Dean flow for the serpentine channel. The lower Bejan number value, in the case of the serpentine channel, promotes the contribution of the fluid flow irreversibility more than the heat transfer irreversibility, resulting from lower entropy generation, than the straight channel (Fig. 4.10(b)). At the lower mass flow rate, the entropy generations are more or less the same for both the channel

geometries and the entire particle diameter range. With the increase of mass flow rate, the entropy generation values for the channel geometries deviates, and the serpentine channel holds the lower value at the expense of higher-pressure drop.

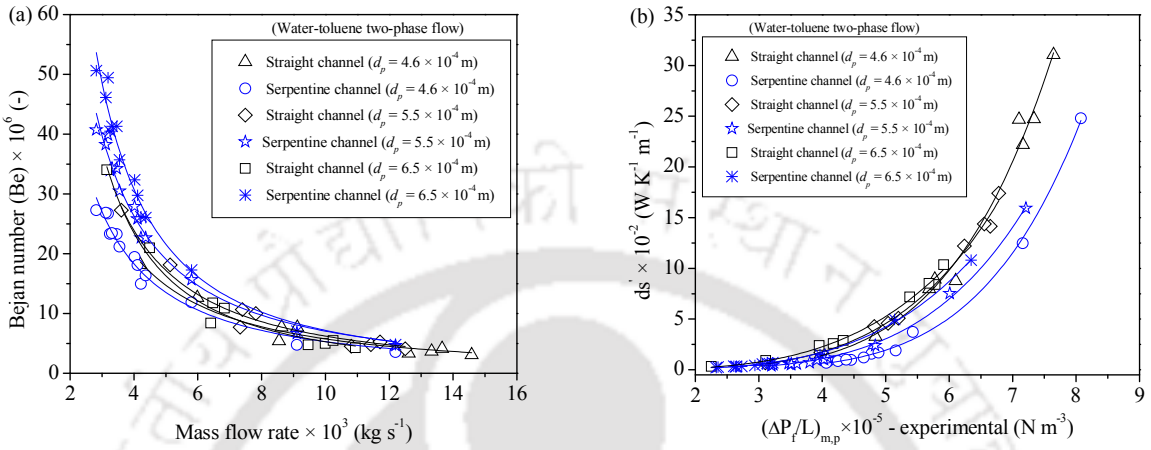

Fig. 4.10. Influence of the particle diameter (packing material) using the separated flow model, (a) Bejan number as a function of mass flow rate, and (b) local entropy generation as a function of mass flow rate.

At the higher value of mass flow rate, the entropy generation rate decreases with the decrease of particle diameter. It provides a lower value in the case of the serpentine channel, which acquires a higher pressure drop and lower Bejan number value (Fig. 4.10(a) and Fig. 4.10(b)). Hence, the packed serpentine channel geometry, with the lower particle diameter and at the higher mass flow rate, promotes heat transfer applications for its lower entropy generation.

At a particular volumetric flow rate, the variation of the fluids in the mixture may also affect the mass flow rate and the pressure drop as well as the Bejan number and the entropy generation depending on the physical properties of the fluid. In a flowing fluid system, the viscosity of the fluids has a huge impact on the pressure loses, and it increases with the increase of viscosity of the fluids. With the decrease of viscosity of the fluid mixture, the Bejan number value increases (Fig. 4.11(a)), and the heat transfer contribution increases, increasing the entropy generation (Fig. 4.11(b)) as the pressure loss value decreases. As a result, the water-benzene mixture for a given flow rate, having the higher viscosity, acquires the higher pressure loss as well as lower Bejan number (Fig. 4.11(a)) with the generation of the lower entropy (Fig. 4.11(b)). As shown in Fig.

4.10, the serpentine channel geometry experienced the lower Bejan number and lower entropy generation as compared with the straight channel at the higher mass flow rate for the water-benzene mixtures. Hence, the packed serpentine channel geometry prefers the heat transfer application provided with the higher viscosity of the fluid mixture.

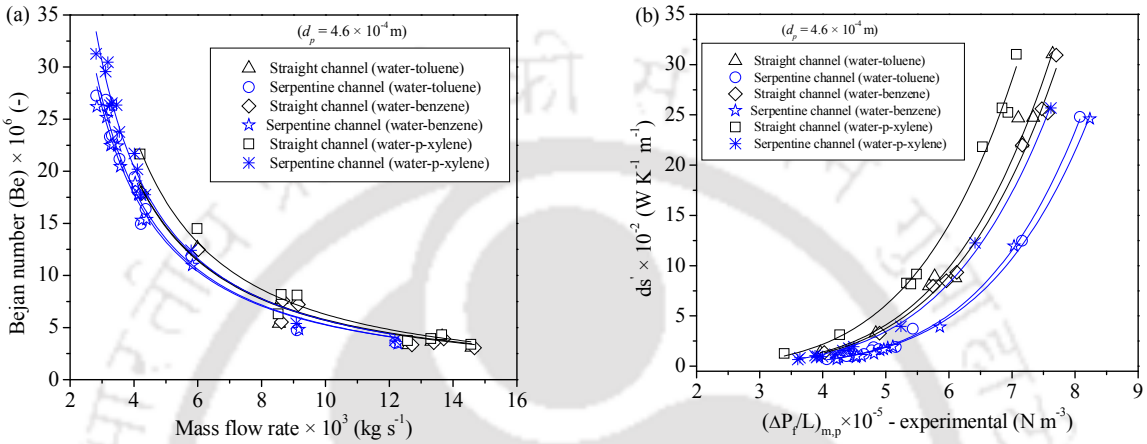

Fig. 4.11. Influence of the fluid mixtures (liquid-liquid two-phase) using the separated flow model, (a) Bejan number as a function of mass flow rate, and (b) local entropy generation as a function of mass flow rate.

However, at the lower mass flow rate, both the channel geometries acquired the same amount of entropy generation; according to the higher Nusselt number value (heat-transfer coefficient value), the serpentine channel is preferable over the straight channel (Fig. 4.5). In the case of the heat transfer applications, the straight channel packed with the smaller-size particle, and encountered the flow of higher viscous fluid mixture, may be used only in case of a lower mass flow rate. But, for the higher mass flow rate serpentine packed channel is more advantageous compared to the straight channel geometry at the same mass flow rate for its higher frictional pressure drop (better mixing), as well as the lower local entropy generation rate.

4.4. Conclusions

The new correlations for the frictional pressure drop (modifying the Ergun equation) and the Nusselt number were generated for the present channel geometry, fluid, and the packed material

based on the idea of the available correlations. Based on the current investigation, the subsequent interpretations are made:

(a) The decreasing particle diameter favors the heat transfer by the decrement of the Bejan number values, and the decrement of the entropy generation at a particular mass flow rate.

(b) Fluid mixture with the higher viscosity acquires the higher-pressure loss as well as the lower Bejan number, prefers the heat transfer contribution decreasing the entropy generation.

(c) The entropy generation rate is higher for the straight packed channel geometry when the same pressure drop, particle diameter, and the fluid mixture are encountered.

The suggested correlations for the pressure drop (frictional) and Nusselt number depending on the present experimental data can be applied for the design of packed multiphase heat and mass transfer units. In the case of the straight packed channel, the entropy generation rate is higher, when both the channels of the same dimension encountered the same pressure drop, particle diameter, mass flow rate, and the fluid mixture due to the lower mixing in the absence of Dean flow. The current research results suggested the use of rectangular serpentine packed channel geometry (provided with the smaller particle diameter and the higher viscosity of fluid mixture) at the higher mass flow rate as the transport devices for its higher heat transfer rate and lower entropy generation.

Chapter 5

Extractive Mass Transport in Rectangular Packed and Unpacked Millimetric Channel-based Devices

5.1 Introduction

Solvent extraction or liquid-liquid extraction is a tool of analytical chemistry by which every metallic component present in the periodic table are separable depending on their relative solubilities in two different immiscible liquids, generally water and an organic solvent. Solvent extraction is the second most important and attractive separation technique used in the industries for the selective separation and purification of metals from their mixtures as well as from their ores. Solvent extraction consists of the transfer of one or more number of solids from feed solutions to another immiscible liquid, called the solvent. The solvent enriched with the solute(s) is called the extract, and the feed solution, depleted in the quantity of solute(s), is called the raffinate. Depending on the selectivity and the reactivity, extraction processes are classified into two categories: the physical, and reactive extraction. In the physical extraction processes, the solute consists of a low distribution coefficient. Whereas, in the reactive extraction processes provide high mass transfer coefficient, and can provide selective separation of the constituent present in the feed by the chemical reaction with the reactive component of the solvent at the higher efficiency. The reactive extraction depends on the various parameters like aqueous and organic phase compositions, types of complexes formed, properties and types of the solvent, temperature, and pH of the feed (Kahya et al., 2001). The stripping of metal ions may be achieved by mixing the metal-organic complex with the strongly acidic solution. In the present context, the extractive separation of one of the heavy metal (copper) has been documented, which is an important engineering metal having wide industrial applications. It is also a toxic metal for living creatures and water pollutants after a specific limit. Therefore, the maximum recovery of the copper metal from the industrial effluent would be environmentally as well as economically beneficial. Presently, researchers and engineers

are also interested in miniaturization or scaling down approaches for the intensification of extraction. An increase in the surface to volume ratio increases the reaction and mass transport rate, which is significant in the case of the millimetric channels. Millimetric channels have the potential to overcome the shortcoming associated with large-scale equipment by reducing the analyte to the reagent volume. Various types of extractants were used so far in the copper extraction, mainly oximes and organophosphorus compounds from the Cyanex and Lix® group of companies, as shown in Table 5.1.

Table 5.1. Various types of extractants used in copper extraction.

(a) Cyanex group of extractants		
Extractants	**Extractant compositions**	**Diluents**
Cyanex 272	Bis (2,4,4-trimethylpentyl) phosphinic acid	Xylene (Sole and Hiskey, 1995; Gupta et al., 2003), Kerosene or Isododecane (Sahu et al., 2004; Gouvea and Morais, 2010; Biswas and Singha, 2007), 1-hexanol (Biswas and Singha, 2007), 1-heptanol (Biswas and Singha, 2007), N-heptane (Wang et al., 2012a), Shellsol D70 (Cheng et al., 2016)
Cyanex 302	Monothio-analog of Cyanex 272	Xylene (Sole and Hiskey, 1995; Gupta et al., 2003)
Cyanex 301	Dithio-analog of Cyanex 272	Xylene (Sole and Hiskey, 1995; Gupta et al., 2003), Isododecane (Fouad, 2009)
Cyanex 923	A mixture of four trialkyl-phosphine oxides	Kerosene (Tang and Steenari, 2015)
Cyanex 921	TOPO which contains trialkylphosphine oxide	Kerosene (Pradhan et al., 2014; Mishra and Devi, 2011)
(b) LIX group of chemicals		

LIX 84	2-hydroxy-5-nonylacetophenone oxime	Tetradecane (Hu et al., 2000), Kerosene (Sahu et al., 2004), Shellsol D70 (Cheng et al., 2016)
LIX 84-I	2-hydroxy-5-nonylacetophenone oxime	Kerosene (Reddy and Priya, 2005; Lu and Dreisinger, 2013), Toluene (Hu et al., 2013)
LIX 54	1-phenyldecanone-1,3-diones	Kerosene (Kyuchoukov et al., 1998; Cierpiszewski and Szymanowski, 2001)
LIX 973N	A mixture of 5-nonylsalicylaldoxime and. 2-hydroxy-5-nonylacetophenone oxime	Iberfluid (Alguacil and Cobo, 1999)
LIX 860	2-hydroxy-5-dodecylsalicylaldoxime	Mixture of n-hydrocarbons (Laxarova and Boyadzhie, 1993)
LIX 860N IC	5-nonylsalicylaldoxime	Exxsol D80 (Willner and Fornalczyk, 2014), Kerosene and a mixture of phosphine oxides (Tang and Steenari, 2015)
LIX 984N or LIX 984N-C or LIX 984	1:1 volume blend of LIX 860N-IC and LIX 84-IC or mixture of 5-nonylsalicyl aldoxime and 2-hydroxy-5-nonyl acetophenone oxime	Kerosene (Aminian and Bazin, 2000; Kul and Çetinkaya, 2009; Gouvea and Morais, 2010; Sridhar and Verma, 2011; Liqing et al., 2011; Lu and Dreisinger, 2013; Sinha et al., 2016), Isododecane (Fouad, 2009), Escaid®100 (Ochromowicz and Chmielewski, 2013)
LIX 841C	2-hydroxy-5-nonylacetophenone oxime	Kerosene (Choubey et al., 2015)
LIX 63	5,8-diethyl-7-hydroxydodecan-6-oxime	Kerosene (Gouvea and Morais, 2010),

		Shellsol D70 [100% aliphatic] (Zhu et al., 2012)
LIX 7950	Tri-alkyl guanidine	N-dodecane (Xie and Dreisinger, 2009)
LIX 7820	Quaternary amine and nonylphenol	N-octane (Xie and Dreisinger, 2009)
LIX 612N-LV	Proprietary mixture of 2-hydroxy-5-nonyl benzaldehide oxime and a high flash point hydrocarbon diluents with low viscosity	Kerosene (Gouvea and Morais, 2010; Lu and Dreisinger, 2013), Escaid®100 (Ochromowicz and Chmielewski, 2013)
LIX 664N	Mixture of 5-nonylsalicylaldoxime with a proprietary ester modifier and a high flash point hydrocarbon diluents	Kerosene (Kumar et al., 2013)
(c) Chemicals and mixtures of extractants		
2-ethylhexanal oxime	2-ethylhexanal oxime	Kerosene (Shibata et al., 1999)
N,N,N',N'-tetrahexylpyridine-3,5-dicarboxamide with 2-hydroxy-5-t-octylbenzophenone oxime or l-phenyldecane-1,3-dione	N,N,N',N'-tetrahexylpyridine-3,5-dicarboxamide with 2-hydroxy-5-t-octylbenzophenone oxime or l-phenyldecane-1,3-dione	Toluene (Resterna and Szymanowski, 2000)
Di(2-ethylhexyl)pyridine-2,4-dicarboxylate	Di(2-ethylhexyl)pyridine-2,4-dicarboxylate	Toluene (Cierpiszewski and Szymanowski, 2001)

2,4-dicarboxylate		
Acorga CLX-50	Di-isodecyl pyridine 3,5-dicarboxylate	Kerosene (Bouvier et al., 1998), Toluene (Cierpiszewski and Szymanowski, 2001)
Acorga M5640	A fatty ester 2,4,4-trimethyl-1,3-pentanediol diisobutyrate modified 5-nonylsalicylaldoxime	ShellSol D70 (Agarwal et al., 2010; Ferreira et al., 2010), Escaid®100 (Ochromowicz and Chmielewski, 2013)
H_2L	N,N'-bis(2-hydroxy-5-bromo- benzyle) 1,2 diaminopropane	Chloroform (Kara and Alkan, 2002)
N-6-(2-ethylhehylamido)-2-pyridine carboxylic acid and N-6-(t-dodecylamido)-2-pyridine carboxylic acid	N-6-(2-ethylhehylamido)-2-pyridine carboxylic acid and N-6-(t-dodecyl amido)-2-pyridinecarboxylic acid	Kerosene (Tasaki et al., 2007)
N 902	2-hydroxy-5-nonyl salicylaldoxime	Kerosene (Cui et al., 2007)
TBP	Tri-butyl Phosphate	1-octanol (Lee et al., 2008), Petroleum-based organic solvents (Chang et al., 2010), Shellsol D70 [100% aliphatic] (Zhu et al., 2012), Kerosene (Choubey et al., 2015)
TOMAS	Trioctylmethylammonium salicylate	Ethanol (Egorov et al., 2010)
4,4-dimethyl-1-(4-dodecyl	4,4-dimethyl-1-(4-dodecylphenyl)-	Kerosene (Hui-ping et al., 2010)

phenyl)-1,3-pentanedione (β-diketone)	1,3-pentanedione (β-diketone)	
LK-C2	One of the 136ydroxyl oxime, similar structure with LIX 984	Kerosene (Zhang et al., 2010b)
PC-88A	Mono-2-ethylhexyl ester	N-heptane (Wang et al., 2012a)
Lauric acid	Lauric acid	Benzene (Ghanadzadeh and Abbasnejad, 2011)
Mixture of Cyanex 301 and LIX 984N	Mixture of Cyanex 301 and LIX 984N	Isododecane (Fouad, 2009)
D2EHPA Or PIA-8	Di(2-ethylhexyl)phosphoric acid	Kerosene and 5 (volume %) TBP (Shibata and Nishimura, 1982), Kerosene (Nagaosa and Binghua, 1997; Ihm et al., 1988; Geist et al., 2000; Ren et al., 2007; Gouvea and Morais, 2010; Chang et al., 2011; Bidari et al., 2013), Heptane (Nagaosa and Binghua, 1997), Naphtezol M (Nagaosa and Binghua, 1997), Petroleum-based organic solvents (Chang et al., 2010), N-heptane (Wang et al., 2012a; Belkhouche et al., 2005)
N-(thiocarbamoyl) benzamidine and N-benzoylthiourea derivatives	N-(thiocarbamoyl) benzamidine and N-benzoylthiourea derivatives	Toluene (Aamrani et al., 1999), Kerosene (Aamrani et al., 1999), Cumene (Aamrani et al., 1999)
EHO	2-ethylhexanal oxime	Kerosene (Shibata et al., 1999)

Dithizone	Sulfur-containing organic compound	1-butyl-3-methylimidazolium hexafluorophosphate [C4mim][PF6] (Wei et al., 2003)
2-H-5-BDA	2-hydroxy-5-dodecylbenzaldehyde	Kerosene (Molinari et al., 2004)
FHA	A mixture of fatty hydroxamic acids from palm olein	Alcohol (Yeen et al., 2005)
Pyridineketoximes	Oxime of 1-(2-pyridyl)tridecan-1-one	Toluene and Exxsol D80, both with 10% (v/v) addition of decan-1-ol (Wieszczycka et al., 2012)

The extraction efficiency of D2EHPA, Cyanex 272, LIX 63, LIX 984N, LIX 612N-LV on copper (II) extraction was investigated by Gouvea and Morais, 2010. They concluded that D2EHPA is the best extractant for the Cu (II) extraction process. In the present study, D2EHPA has been used as the Cu (II) extractant diluted in benzene.

In the liquid-liquid extraction processes, the extent of mixing between the two phases is important as it enhances the mass transfer coefficient. Every researcher in this field is trying to modify the extraction devices to get a high percentage of separation utilizing less amount of mechanical and electrical energy. The different types of reactors used for the extraction process are shown in Table 5.2.

Table 5.2. The different types of reactors used for the extraction process.

Type of reactors	Findings	References
Stirred cell reactor	The mass transfer kinetics for the extraction of Cu (II), Cd (II), Ni (II), Pb (II), and Zn(II) from sulfate solution using D2EHPA in kerosene as the extracting phase was studied. They determine the mass transfer coefficients of each metal in the experimental condition.	Geist et al., 2000

Stoppard flasks in a thermostatic bath shaker	Investigated the extraction and stripping equilibrium of Cu (II). Cu(II) is extracted from the aqueous acetate buffer solution using D2EHPA dissolved in kerosene as the extractant. The results showed that acetate ions greatly improve copper extraction efficiency.	Ren et al., 2007
A constant interfacial area cell	Studied the rate of copper (II) extraction from the copper-laden aqueous solution using D2EHPA dissolved in kerosene.	Juang and Chang, 1993
A box type Eberbach shaker	The kinetics and mechanism of the extraction of copper with 2-hydroxy-5-nonylbenzophenone oxime were investigated.	Carter and Freiser, 1980
A pulse sieve plate column	Performed the copper extraction experiments for selecting the composition of the organic phase and the pH of the leach solution. Studied the hydrodynamic and mass transfer performance of the extraction column using an organic phase with 10% (v/v) Acorga M5640 and 2.5% (v/v) iso-tridecanol.	Ferreira et al., 2010
A mass transfer cell with vibrational mixing	Studied the kinetics of metal extraction by the chelate formation in 1980 and examined the rate of extraction of copper from the aqueous solution by LIX 64N dissolved in kerosene in the year 1981.	Rod, 1980, and 1981
A two-impinging-jets reactor (TIJR)	TIJR was utilized for the extraction of copper using LIX 84 as the extractant. The effects of the upper disk speed, aqueous and organic flow rates, the reactor's dimension, including the disk diameter and the distance between the disks, have been investigated.	Dehkordi, 2002
Flow-through porous media	Experimented with the applications to heap leaching of copper ores and showed that in case of packed microchannel the extraction efficiency is 81-96%.	Su et al., 2010

From the previous literature, it is clear that a few studies on extraction have been done on the serpentine rectangular millimetric channels with and without packing materials. The objective of the present study is to optimize the extraction parameters of copper after the separation of it from an aqueous phase mixture using a commercially available extractant diluted in benzene through a rectangular serpentine packed and unpacked millimetric channels. The present study also focuses on the difference between the performances of those two channels.

5.2. Experimental methods and materials

Generally, copper remains as a mixture of various metal ions in the industrial effluents. Hence, initially a lab-made mixture of copper, nickel, and cadmium of different concentrations was taken as the experimental solutions. Gravimetric analysis was done to estimate the copper separated from the other two metals as a hydroxide-precipitate by the addition of dilute sodium hydroxide (NaOH) solution into the mixture. Depending on the stability of the three metal hydroxides with pH, copper was separated from the mixture as a copper hydroxide precipitate within a pH value of 5.5 to 7.5. The copper hydroxide precipitate was separated by filtration using Whatma® 42 filter paper and dissolved in excess ammonia solution (NH_4OH). A deep blue color solution resulted in the formation of a copper amine complex $[Cu(NH_3)_4]^{2+}$ was used as the experimental copper solution. A flow chart of the whole process is shown in Fig. 5.1. The pH of the solution was measured by a digital tabletop pH meter (Equiptronics, EQ 610 model). A schematic diagram of the extraction and stripping section is shown in Fig. 5.2.

Both the extraction and stripping unit consists of two centrifugal pumps which provide the flows of aqueous and organic phases, transforming into one mixed-flow passing through a 'Y' connector before entering the test section. Inlet zone contains two rotameters, two control valves, two bypass lines along with two control valves and two sets of pressure sensors (PS100-2BAR and PS100-5BAR from Lutron Electronics, accuracy: 1% full-scale) connected with two pressure meters (Fisher Scientific Traceable™, accuracy: 1% full-scale +1 digit) just before and after the inlet and outlet points. Two pressure meters are connected to computers for data logging. The test section contains the rectangular serpentine channel block and a temperature sensor (Fisher Scientific TraceableLIVE™, accuracy: ± 0.1 °C) dipped in a constant temperature bath.

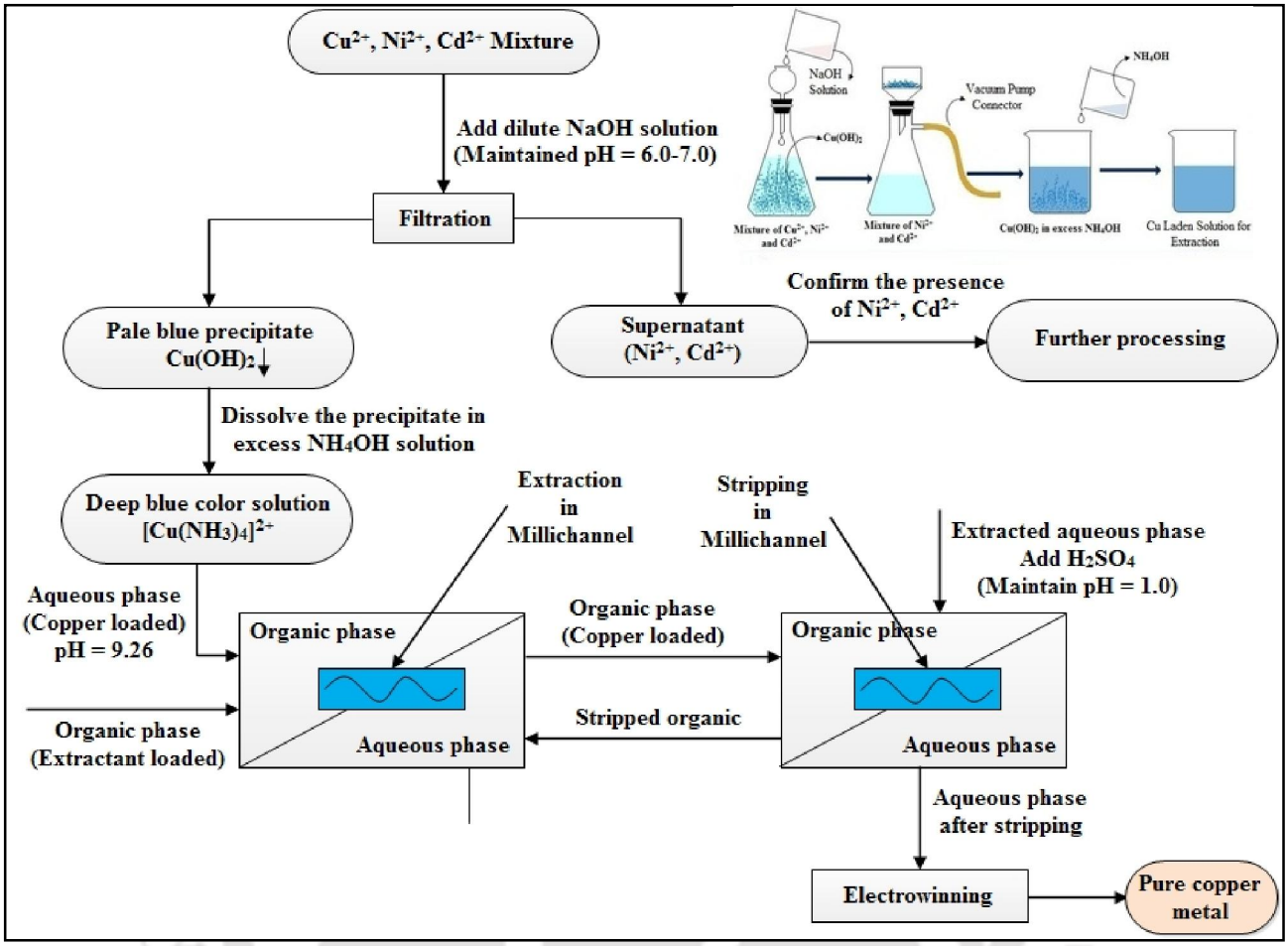

Fig. 5.1. Details of the process flow chart.

The channel was 240 ± 0.3 mm long (L), 2 ± 0.1 mm width (w), and height (h) of 10 ± 0.1 mm with the radius of curvature (R_c) 25.5 ± 0.1 mm. Medium red sand as a packing material was used for making the packed bed in the channel. The physical properties of the systems measured at 25 ± 1 °C are shown in Table 5.3. The pressure and the temperature sensors are calibrated before the main experiment with the help of a manometer and thermometer, respectively. The physical properties of the experimental fluids such as densities, viscosities and surface tensions are measured by specific gravity bottle (ATICO Medical Pvt. Ltd., AM-90024, 100 ml), rheometer (Anton Paar, Physica MCR-301) and tensiometer (Kyowa Interface Science, DY-300) respectively. Finally, the volumetric flow rate of the two-fluid mixtures is measured by measuring cylinder and a stopwatch by collecting the sample for a particular time. The volumetric flow rates are controlled and measured by the valves and the rotameters. The pressure drop for a particular

mixture flow rate is measured by the pressure sensors. The aqueous to organic volume ratio (*A/O* ratio) of each phase in the channel is calculated from the total mixed-phase volumetric flow rate and the volumetric flow rate of a single-phase for a particular set of flow condition. The initial and final concentration of copper in the aqueous phase was measured by a flame type atomic absorption spectrophotometer (Varian, AA240FS model). The concentration of copper in the organic phase was calculated by subtracting the final concentration from the initial concentration of copper in the aqueous phase.

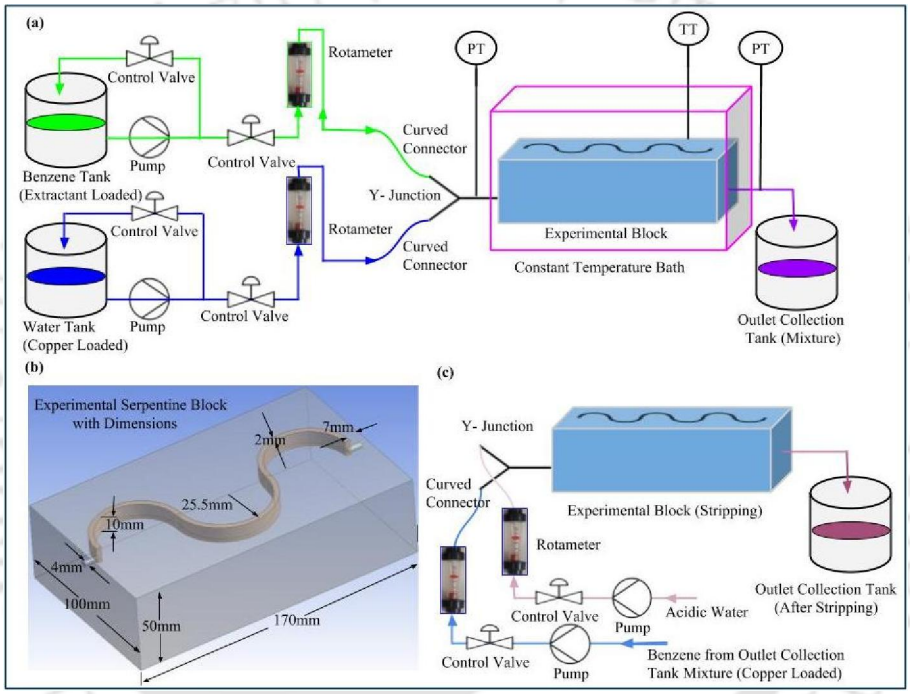

Fig. 5.2. Details of the experimental setup: (a) schematic diagram of the extraction process, (b) 3D view of serpentine channel block, and (c) schematic diagram of the stripping process.

Table 5.3. The physical properties of the fluids, measured at 25 ± 1 ˚C.

Phases	**Density (kg m^{-3})**	**Viscosity (N-s m^{-2})**
Water	997.05	8.90×10^{-4}
100 ppm CuSO4 Solution	997.35	8.91×10^{-4}
200 ppm CuSO4 Solution	997.61	8.92×10^{-4}
300 ppm CuSO4 Solution	997.86	8.93×10^{-4}
400 ppm CuSO4 Solution	998.11	8.94×10^{-4}

Benzene	873.68	6.03×10^{-4}
0.01M D2EHPA in benzene	873.99	7.03×10^{-4}
0.02M D2EHPA in benzene	874.31	7.92×10^{-4}
0.05M D2EHPA in benzene	875.25	10.81×10^{-4}

The average particle diameter ($d_{p,eff}$), effective porosity of the packed bed (ε_{eff}), and sphericity of the packing material (ϕ_p) are the three important parameters to govern the hydrodynamics as well as mass transfer in the packed bed. The average particle diameter is determined by the sieve of sizes ASTM No. 35 and 40 (U.S. Standard). The average particle size, as per the present experiment is 462 μm. The effective porosity is calculated by the ratio of the volume of the pores to the total volume of the bed. The effective porosity estimated experimentally in the present work is 0.36. The total volume of the bed is calculated by the channel dimensions. The wetted solid volume is measured by the liquid displacement method. The pore volume is obtained by subtracting the volume of the wetted solid from the total volume of the bed. The solid is taken in wetted condition to minimize the liquid absorption during the measurement. The sphericity is calculated by using the modified procedure of Krumbein and Sloss (1963). It is defined as the ratio between the diameters of the largest drawn circle possible inside the particle (r_p) to the diameter of the smallest drawn circle surrounding the particle (r_c). It is determined by analyzing a snapshot of the sand particle taken by Sony DSC-H400 Point and Shoot Camera using Digimizer® 4 software. The mathematical form of sphericity of particle is expressed as Eq. 5.1.

$$\phi_p = \frac{r_c}{r_p} \tag{5.1}$$

From the analysis, it is found that the sphericity of the particle is 0.80, which is within the range of 0.50 to 0.90 for natural sands reported by Cho et al. (2006). The holdup of each phase inside the channel was measured by the volumetric flow rate measurement process using a measuring cylinder (Borosil, 100 ml, Tolerance ±0.5 ml) and a stopwatch (Seiko digital stopwatch Cal. S056, Accuracy ±0.0012%).

5.3. Theoretical Background

The copper forms a pale blue precipitate by the addition of dilute sodium hydroxide (NaOH) or ammonium hydroxide (NH_4OH) solution at a pH range of 5.5 to 7.5. This results in a deep blue

color solution of copper ammonia complex by the addition of excess ammonia solution (NH_4OH) to the precipitate at a pH above 9.0. The reactions occurred are represented by Eqs. (5.2-5.4).

Cu^{2+}: $CuSO_4$ (aq.) + 2NaOH (aq.) = $Cu(OH)_2\downarrow$ + Na_2SO_4 (aq.) (5.2)

(Pale blue precipitate)

$CuSO_4$ (aq.) + 2NH_4OH (aq.) = $Cu(OH)_2$ + $(NH_4)_2SO_4$ (aq.) (5.3)

(Pale blue precipitate)

$Cu(OH)_2\downarrow$ + 4NH_4OH (aq.) = $[Cu(NH_3)_4](OH)_2$ (aq.) + 4H_2O (5.4)

(Pale blue precipitate) (Deep blue solution)

The presence of the other two metals cadmium and nickel in the aqueous solution was confirmed by the following Eq. (5.5) and Eq. (5.6).

Cd^{2+} : $CdSO_4$ (aq.) + Na_2S (s) + Heat = $CdS\downarrow$ + Na_2SO_4 (aq.) (5.5)

(Yellow color precipitate)

Ni2+ : $NiSO_4$ (aq.) + Na_2S (s) + Heat = $NiS\downarrow$ + Na_2SO_4 (aq.) (5.6)

(Black color precipitate)

A mixture of Cd^{2+} and Ni^{2+} solution along with Na2S, when heated, forms a yellowish black color precipitate, which confirms the mix of the two above-specified metals. The nickel can be separated from the mixture of nickel and cadmium by the formation of a Ni-DMG (nickel-dimethyl glyoxime) complex, a red color chelate, as shown in Eq. (5.7).

Ni^{2+} : $NiSO_4$ + $2C_4H_8O_2N_2$ = $Ni(C_4H_7O_2N_2)_2\downarrow$ + H_2SO_4 (5.7)

(DMG) (Ni-DMG complex)

(Red chelate)

The hydraulic diameter and actual velocity of the mixture through the channel are calculated respectively by the Eq. (5.8) and Eq. (5.9).

$$d_H = \frac{4A}{2(h+w)} = \frac{2hw}{(h+w)} \quad (5.8)$$

$$U_m = \frac{Q_a + Q_o}{A} = \frac{Q_a + Q_o}{hw} \tag{5.9}$$

where A is the cross-sectional area of the channel, h and w are the height and width of the channel, Q_a and Q_o are the volumetric flow rate of the aqueous and organic phase, respectively.

The mixture properties like density (ρ_m), viscosity (μ_m) of two fluids are calculated by the Eq. (5.10) and Eq. (5.11).

$$\rho_m = \left(\frac{\chi_a}{\rho_a} + \frac{1-\chi_a}{\rho_o}\right)^{-1} \tag{5.10}$$

$$\mu_m = \left(\frac{\chi_a}{\mu_a} + \frac{1-\chi_a}{\mu_o}\right)^{-1} \tag{5.11}$$

where

$$\chi_a = \frac{Q_a}{Q_a + Q_o} \tag{5.12}$$

The parameter χ in Eqs. (5.10-5.12) represents the volumetric flow rate fraction, *'a'* and *'o'* represent the aqueous and organic phase, respectively. The experiments have been conducted within a range of 100 – 400 ppm $CuSO_4$ solutions having pH 2-10 with 0.01 - 0.05 M extractant solution [Bis-(2-ethylhexyl)-phosphate] (H2EHPA) diluted in benzene. The extent of extraction (% E) and the extraction efficiency (% η) are expressed by Eq. (5.13) and Eq. (5.14) respectively (Darekar et al., 2016).

$$\%E = \frac{C_a^{in} - C_a^{out}}{C_a^{in}} \times 100 \tag{5.13}$$

$$\%\eta = \frac{C_a^{in} - C_a^{out}}{C_a^{in} - \frac{C_O^{out}}{K_D}} \times 100 \tag{5.14}$$

where C_a^{in} is the solute concentration in the aqueous phase at the inlet, C_a^{out} is the solute concentration in the aqueous phase at the outlet, C_o^{out} is the solute concentration of the organic phase at the outlet, K_D is the distribution coefficient. The percentage efficiency depending on the various organic to the aqueous phase flow ratios (O/A ratios), is expressed by the Eq. (5.15) (Darekar et al., 2016).

$$\%\eta = \frac{C_a^{in} - C_a^{out}}{\left\{1 - \frac{1}{K_D(O/A)}\right\}C_a^{in} + \frac{1}{K_D(O/A)}C_a^{out}} \times 100 \quad (5.15)$$

The overall volumetric mass transfer coefficient (K_La) is expressed as Eq. (5.16) (Darekar et al., 2016).

$$K_L a = \frac{C_a^{in} - C_a^{out}}{\frac{V_{Channel}}{Q_a}\Delta_{LMC}} \quad (5.16)$$

The logarithmic mean concentration difference (Δ_{LMC}) is defined as

$$\Delta_{LMC} = \frac{(C_a^{in} - C_{a,Eqb}^{in}) - (C_a^{out} - C_{a,Eqb}^{out})}{\ln\{(C_a^{in} - C_{a,Eqb}^{in})/(C_a^{out} - C_{a,Eqb}^{out})\}} \quad (5.17)$$

where $V_{Channel}$ is the total volume of the serpentine channel, Q_a is the total volumetric flow rate of the aqueous phase. The logarithmic mean concentration difference is used to calculate the overall volumetric mass transfer coefficient in Eq. (5.16). $C_{a,Eqb}^{in}$ and $C_{a,Eqb}^{out}$ are the solute concentration in the aqueous phase in equilibrium with the solute concentration of the organic phase at the inlet and outlet, respectively. Darekar et al. (2014) proposed a correlation for the overall volumetric mass transfer coefficient applicable for the flow through the serpentine microchannel, which can be expressed as the Eq. (5.18).

$$K_L a = \frac{1}{(0.850 + 0.360\frac{O}{A} + \frac{25.795}{U_m}} \quad (5.18)$$

where, U_m is the actual velocity of the mixture inside the serpentine millimetric channel.

5.4. Results and discussion

5.4.1. Extraction study in packed and unpacked channels

The main parameters for liquid-liquid extraction are pH of the metal ion solution, concentration of the extractant solution (C_E), metal ion concentration (C_m), and the temperature (T) of the extractant and metal ion solutions. The pH effect on the copper extraction process has been performed by dissolving pure copper sulfate in milli-Q water (Milli-Q®, IQ 7000).

The pH dependency on the extraction process was evaluated by taking a particular concentration of metal ion solution and the extractant solution at a constant temperature, as shown in Fig. 5.3.

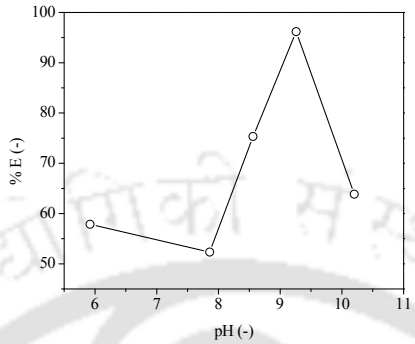

Fig. 5.3. Variations of extraction percentage (%E) with the solution pH (C_m = 0.0047 M, C_E = 0.05 M, A/O = 1 or U_m = 0.177 m s^{-1} & U_w = 0.099 m s^{-1} for packed channel, U_m = 0.76 m s^{-1} & U_w = 0.38 m s^{-1} for unpacked channel).

From Fig. 5.3, it is seen that % E decreases with increasing pH from 5.92 to 7.86, then increases with increasing pH from 7.86 to 9.26 and again decreases from pH 9.26 to 10.20, which indicates that the pH value significantly affected the % E compared with other factors. The decrease of % E at the pH range of 5.92-7.86 is due to the less solubility of the copper ion in the aqueous phase with the formation of $Cu(OH)_2$ in the presence of OH^- ion which tends to separate the Cu^{2+} as the precipitate. The extractant molecules have to break the Cu-OH bonds to extract copper, which results in the extraction percentage decrease slightly. When the excess base (NaOH or ammonium hydroxide) is added, the copper has dissolved again in the aqueous phase forming a deep blue color solution. As much as the basicity increases, the value of the distribution coefficient, which is the ratio of the concentration of copper (II) in the organic phase to the aqueous phase increases (Cortina et al., 1995). According to Ren et al. (2007) and Ihm et al. (1988), in the extraction process, H^+ enters the aqueous phase and Cu^{2+} moves towards the organic phase. Due to the release of the H^+ from the extractant into the aqueous phase, the pH of the aqueous phase decreases from the pH at equilibrium state (Ren et al., 2007). At lower pH, the concentration of the H^+ remains high, which favors the backward reaction, according to Le Chatelier's principle. With increasing pH, the alkalinity of the aqueous phase increases, favoring the forward reaction, and the metal ion expresses the tendency to move towards the organic phase, results in increasing the extraction

percentage within pH ranges of 7.86 to 9.26. The isoelectric point (the point at which a particular molecule carries no electrical charge) is 9.5 for the Cu^{2+} ion. As a consequence, at a higher pH value greater than 9.50, the extractant molecule is prone to extract a statistically neutral molecule, which results in a decrease of percentage extraction *(*% *E*). The maximum % *E* value was observed at a pH of 9.26. The maximum extraction was found 96.17% for the 300 ppm (0.0047 M) copper ion solution and 0.05 mol.lit^{-1} (0.05 M) extractant solution as shown in Fig. 5.3.

It is seen that *A/O* (aqueous to organic phase volume) ratio has an impact on the extraction percentage as well as the extraction efficiency. The variations of degree of extraction as a function of the *A/O* ratios for both packed and unpacked channels are shown in Fig. 5.4.

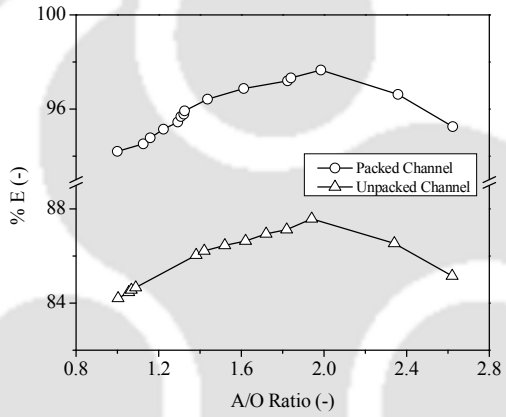

Fig. 5.4. Variations of extraction percentage with the *A/O* ratio (C_m = 0.0047 M, C_E = 0.05 M, pH = 9.26).

With an increasing A/O ratio from A/O = 1, percentage extraction increases up to a certain limit (around 1.9) and then decreases. The increase is due to the availability of the more number of metal ions in the vicinity. After that limit, the number of metal ions is more than enough for the affinity of the extractant molecules.

In a packed or unpacked channel, the *A/O* ratio depends on the actual velocities of the either of the two phases U_w (actual velocity of the aqueous phase) and U_o (actual velocity of the organic phase). When the U_m (actual velocity of the mixture, is the sum of the actual velocities of the two phases) increase from 0.055 m s^{-1} to 0.36 m s^{-1}, the *A/O* ratios increase from 0.78 to 2.62 for the packed

channel, whereas for the unpacked channel the *A/O* ratios increase from 0.496 to 1.38 with the increase of U_m values from 0.18 m s^{-1} to 0.94 m s^{-1}. At a particular pH, fixed metal ion, and extractant concentration, with the increase of the actual mixture velocity, higher mixing is achieved, which is influenced by the increased pressure inside the channel (Mondal and Majumder, 2018a). This effect is higher in the case of the packed channel due to the flow of the fluid through the tortuous paths. Instead of showing higher value for the packed channel, both the packed and unpacked channel shows the same trend. With the increase of flow velocity or *A/O* ratio, the rate of extraction reflecting the extraction percentage increases as shown in Fig. 5.4.

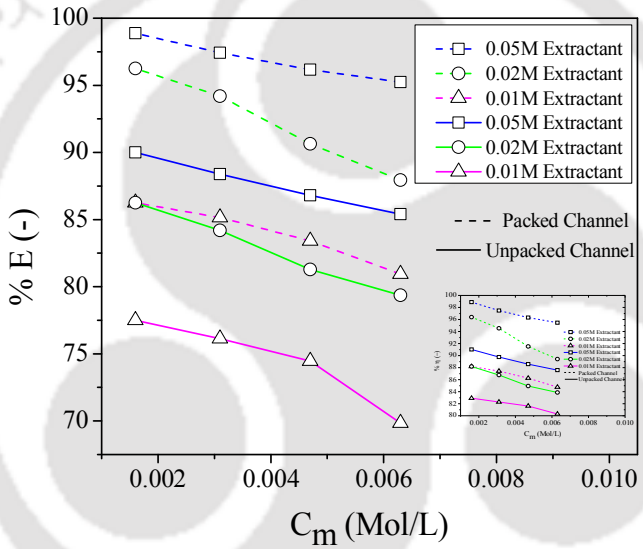

Fig. 5.5. Variations of extraction percentage (%*E*) and extraction efficiency (%η) with the Copper concentration (solution pH 9.26, *A/O* = 1, U_m = 0.177 m s^{-1}, U_w = 0.099 m s^{-1}, U_m = 0.76 m s^{-1} & U_w = 0.38 m s^{-1} for unpacked channel).

From Fig. 5.5, it is seen that for a particular extractant concentration with increasing copper concentration (C_m) in the aqueous phase, the % *E* decreases as the metal ion concentration increases at a fixed concentration of extractant. With increasing the copper concentration, the extraction rate remains initially high. Still after a while, the affinity of the extractant molecule towards the metal ion is decreased due to the occupancy of the binding sites of the extractant molecule by the metal ions. It lowers the overall extraction percentage. The % *E* value increases with increasing the extractant concentration (C_E) in the organic solvent for a fixed aqueous phase

metal ion concentration. With increasing the extractant concentration, the number of binding sites increases. Therefore, it is worth to say that the % *E* mainly depends on the availability of the vacant site percent at the extractant molecule. A maximum of 98.88% extraction was obtained at 0.05 M of extractant concentration at the metal ion concentration of 100 ppm.

The packed channel exhibits a higher extraction percentage than the unpacked channel (Fig. 5.5) for a particular extractant concentration (C_E) and metal ion concentration (C_m) since extraction is mainly the surface phenomena and the interfacial area of contact between the two phases increases with packing. According to the pressure drop concept, the packed channel experience a higher pressure drop compared to the unpacked channel for the same flow condition resulting in higher mixing as well as higher extraction percentage. High liquid-liquid dispersion is possible in the packed channel, which permits high mass transfer between the two immiscible phases. The maximum of 99.88% and 90.00% of copper extraction are obtained for packed and unpacked channel respectively for the 0.05 M extractant in benzene and the 100 ppm (0.00156 M) copper ion concentration in the aqueous phase at a pH of 9.26 (Fig. 5.5).

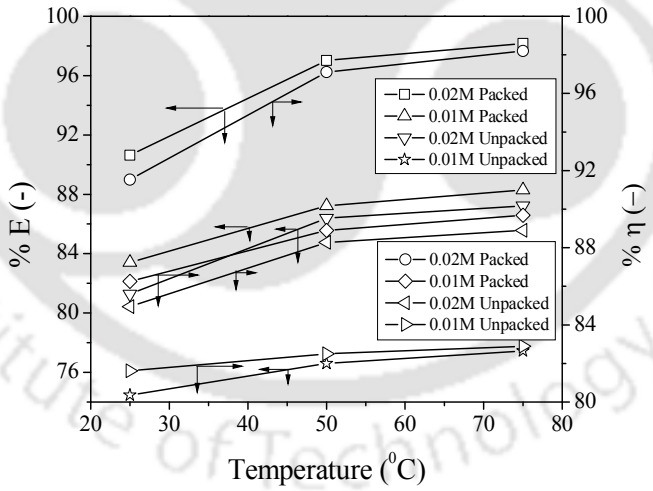

Fig. 5.6. Effect of temperature on extraction percentage and extraction efficiency in packed and unpacked channel (C_m = 300 ppm or 0.007 M, C_E = 0.002 M and 0.001 M, pH = 9.26, A/O = 1, U_m = 0.177 m s^{-1} & U_w = 0.099 m s^{-1} for packed channel).

The variation of extraction efficiency ($\%\eta$) with the copper ion concentration (C_m) follows the same trends as the percentage extraction (Fig. 5.5). The maximum extraction efficiency has been observed 98.89% for the packed channel, whereas the unpacked channel shows 91.01% (Fig. 5.5). Fig. 5.6 shows the variation of % E with the increase of temperature (T) and also with the increase of extractant concentration. The % E increases with the increase of temperature, but the rate of increase is higher for the temperature range of 25-50 $^{\circ}$C, whereas the rate decreases within the range of 50-75 $^{\circ}$C for a particular extractant concentration. The increase in temperature increases the particle movement inside the phases. Therefore, the starting region of the plot is steeper than the latter part. Thus in practice, an extraction temperature of 50 $^{\circ}$C could be used to avail the combined effects of the excellent extraction efficiency as well as a higher extraction rate. The experiments were performed up to a temperature of 75 $^{\circ}$C to avoid the evaporation of the organic phase. When the extractant concentration increases, the % E also increases for a fixed temperature, as shown in Fig. 5.5 and Fig. 5.6. In both of the extractant concentrations, the trend is the same; only the rate of the extraction rate increment is higher in case of higher extractant concentration. The extraction efficiency also increases wth the increase of temperature, due to the increased movement of the molecule (Brownian motion) inside the phases. The equilibrium time at different temperatures for a fixed value of metal ion concentration, extractant concentration, and pH is shown in Fig. 5.7.

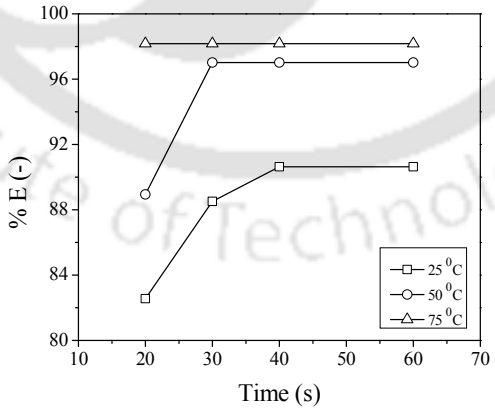

Fig. 5.7. Variations of extraction percentage with time at the different temperatures (C_m = 300 ppm, C_E = 0.02 M, pH = 9.26, A/O = 1, U_m = 0.177 m s^{-1} & U_w = 0.099 m s^{-1} for packed channel).

It is seen that the percentage extraction fixed at 90.64% on and after the 40s at 25 ˚C, which was fixed at 97.02% and 98.17% at 50 ˚C and 75 ˚C on and after 30s and 20s respectively. At the temperatures of 25 ˚C, 50 ˚C and 75 ˚C the equilibrium reaches in 30-40s, 20-30s, and 10-20s, respectively, as shown in Table 5.4.

Table 5.4. Variation of extraction percentage with respect to time and temperature at C_m = 0.0047 M i.e., 300 ppm, C_E = 0.02 M, pH = 9.26, A/O = 1.

Temp. / Time	20s	30s	40s	60s
25 ˚C	82.55	88.51	90.63	90.63
50 ˚C	88.94	97.02	97.02	97.02
75 ˚C	98.17	98.17	98.17	98.17

The time-dependent percentage extraction study was performed in the case of the unpacked channel only. Due to the higher mass transfer rate for the packed channel, the equilibrium comes before 10s. But there is required around 10-12s for the separation of the two phases.

5.4.2. Stripping in packed channel

Stripping depends on the bond strength of the extractant molecule and the metal ion. The stripping of the metal ion from the organic phase to the aqueous phase is required before the electrowinning or electroextraction process to get the pure metals on the electrodes. The physical properties of the stripping medium (H_2SO_4 solution) at different temperatures and pH values are shown in Table 5.5.

Table 5.5. Physical properties of the stripping medium (H_2SO_4 solution) at different temperatures and pH values.

Temperature (˚C)	pH (-)	Density (kg m^{-3})	Viscosity (N m^{-2})
25	0.5	1004.31	9.77×10^{-4}
	1.0	999.38	9.17×10^{-4}
	1.5	997.78	8.99×10^{-4}

	2.0	997.33	8.93×10^{-4}
50	0.5	994.78	5.96×10^{-4}
	1.0	989.94	5.67×10^{-4}
	1.5	988.41	5.57×10^{-4}
	2.0	987.92	5.54×10^{-4}
75	0.5	981.64	4.13×10^{-4}
	1.0	976.86	3.97×10^{-4}
	1.5	975.35	3.91×10^{-4}
	2.0	974.87	3.89×10^{-4}

The main parameters for the stripping process are optimized in case of the packed channel only. The effect of the parameters follows the same trends in spite of giving higher value in the case of the packed channel. This is due to the higher contact area available between the two phases and higher overall volumetric mass transfer rate, which is the multiplication of the mass transfer coefficient and the specific interfacial area. Stripping of metal ion from the organic phase is mainly done by using acidic aqueous phase. The pH of the aqueous phase is another important stripping parameter.

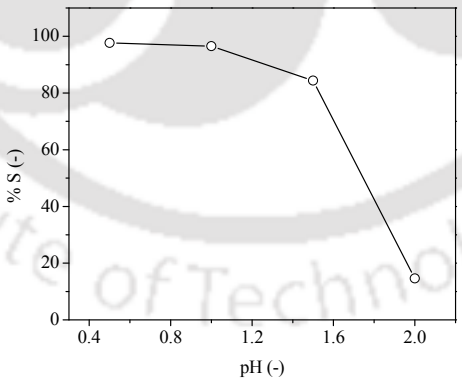

Fig. 5.8. Variations of stripping percentage (%*S*) with the pH of the acidic aqueous phase at metal ion concentration in the organic phase = 0.0022 M, $A/O = 1$, $U_m = 0.177$ m s^{-1} & $U_w = 0.099$ m s^{-1} for packed channel, Temperature = 25 ˚C.

With decreasing pH, i.e., with increasing the acidity of the acidic aqueous phase, the stripping percentage (*% S*) increases. Fig. 5.8 shows that reducing the pH from 2.0 to 0.5, the stripping percentage increases to the highest value of 97.66% at a pH of 0.5. The increased rate of stripping percentage is higher at the initial pH decrease from 2.0 to 1.5. The increase in the rate of stripping percentage decreases later on and shows the minimum value at the pH ranges from 1.0 to 0.5. At very low pH, the acidic aqueous phase can corrode the metal electrode itself. The optimum pH 1.0-1.5 is selected for the stripping study. The main reason behind the increase of stripping percentage with the decrease of pH value is that with the increase in acidity of the aqueous phase the concentration of the H^+ ion in the solution increases, which increases the solubility of the metal ion in the aqueous phase-shifting the equilibrium towards stripping (Eq. (5.19)).

$$\overline{CuR_2 2HR} + 2H^+ \xleftrightarrow{K_e} Cu^{2+} + 2\overline{H_2R_2} \qquad (5.19)$$

The fact is opposite to the extraction equilibrium (Eq. (5.20)). Temperature dependency of the stripping process is shown in Fig. 5.9.

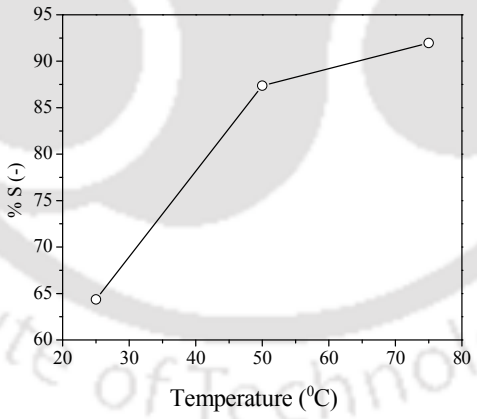

Fig. 5.9. Variations of stripping percentage (%*S*) with temperature (metal ion concentration in the organic phase = 0.0022 M, *A/O* = 1, U_m = 0.177 m s^{-1} & U_w = 0.099 m s^{-1} for packed channel, pH = 1.5).

With the increase in temperature, from 25-75 ˚C for a particular metal ion concentration in the organic phase (0.0022 M) and a pH of 1.5, the stripping percentage increases rapidly up to the

temperature of 50 ˚C. At the temperature range of 50-75 ˚C, the stripping percentage is increased, but the rate of increase is very low (Fig. 5.9). Though the viscosities of both phases decrease with temperature, the viscosity of the organic phase always remains higher than the acidic aqueous phase, as shown in Table 5.3 and Table 5.5. Hence the stripping is increased with decreasing viscosity, as the molecular diffusion is increased from high viscous to lower viscous liquid.

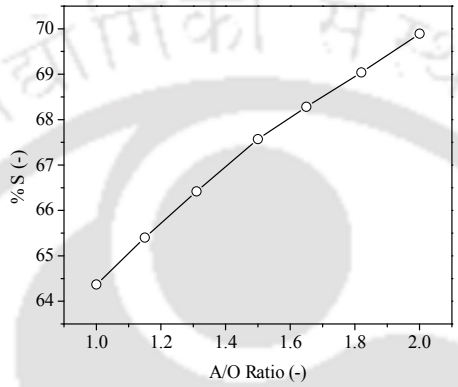

Fig. 5.10. Variations of stripping percentage with the *A/O* ratio (C_m in the organic phase = 0.0022 M, pH = 1.5, Temperature = 25 ˚C).

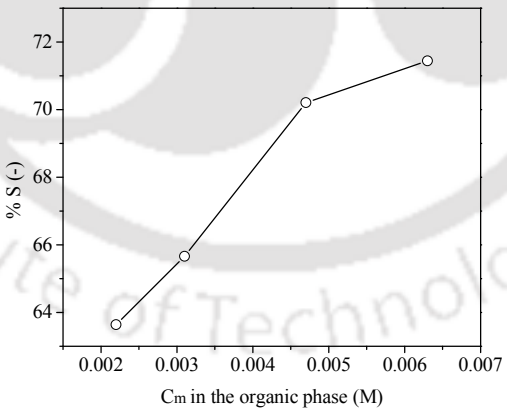

Fig. 5.11. Variations of the percentage stripping (%*S*) with metal ion concentration (*Cm*) in the organic phase (*A/O* = 1, U_m = 0.177 m s^{-1} and U_w = 0.099 m s^{-1} for packed channel, pH = 1.5, Temperature = 25 ˚C).

From the experiment, it is seen that the A/O ratio does not significantly change the stripping. With the increase of *A/O* ratio from 1-2, only a 5% increase in the stripping percentage has been observed (Fig. 5.10). It is better to operate the stripping process at an *A/O* ratio equal to one for saving pumping as well as electrical costs. According to Huang et al. (1986), the stripping process does not depend on the D2EHPA concentration in the organic phase and the *A/O* ratio. The stripping increases with increasing the metal ion concentration in the organic phase due to the concentration difference between the phases. The variation of the degree of the stripping with the changes in the metal ion concentration in the organic phase is shown in Fig. 5.11. Initially, the stripping percentage increases with the increase of metal ion concentration in the organic phase at a particular *A/O* ratio. But, after a certain value (0.0045 M), the rate of the increase of the stripping percentage becomes low due to the saturation of the aqueous phase with the metal ions. Further increase in the ion concentration in the organic phase does not result in the increase of the stripping percentage.

5.4.3. Determination of the equilibrium constant for the copper extraction process

In a nonpolar solvent like benzene, di-(2-ethylhexyl) phosphoric acid (D2EHPA) remains as a dimer by making hydrogen bonding. But, it has an affinity towards the heavy metal ions present in the aqueous phase, which remains in contact with the organic surface containing D2EHPA. It forms a complex with the heavy metal ions. It's dimer formation, and also the complex formation with the copper metal ion is shown in Fig. 5.12.

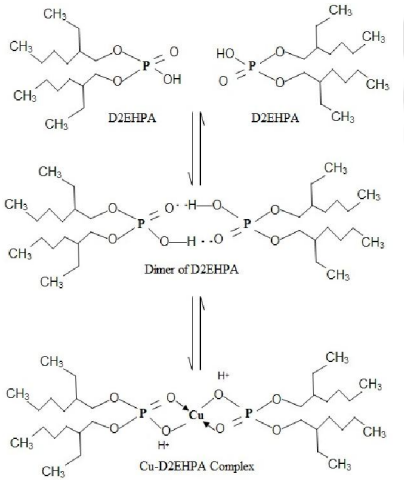

Fig. 5.12. Dimer and copper complex formation by the extractant D2EHPA.

The overall extraction reaction of the copper ion with the extractant solution D2EHPA is shown by the Eq. (5.20) (Ihm et al., 1988; Ren et al., 2007).

$$Cu^{2+} + 2\overline{H_2R_2} \xleftrightarrow{K_e} \overline{CuR_2 2HR} + 2H^+ \quad (5.20)$$

where K_e is the equilibrium constant which can be represented as

$$K_e = \frac{\left[\overline{CuR_2 2HR}\right]\left[H^+\right]^2}{\left[Cu^{2+}\right]\left[\overline{H_2R_2}\right]^2} \quad (5.21)$$

The overbar indicates the species present in the organic phase.

In Eq. (5.21), as the H^+ ion exchanges with the Cu^{2+} ion and enters into the aqueous phase, the equilibrium pH becomes lower than the initial pH. One Cu^{2+} ion goes to the organic phase releasing two H^+ ion in the aqueous phase. As the concentration of H^+ increases in the solution, the pH of the solution decreases, which leads to slow down the reaction. The values of equilibrium pH and their corresponding equilibrium constant (K_e) are shown in Table 5.6.

The K_e for packed channel varies from 1.52×10^{-6} to 1.05×10^{-5}, whereas for the unpacked channel it varies from 3.67×10^{-6} to 2.09×10^{-5} (Table 5.6). According to Le Chatelier's principle and Eq. (5.19), pH has an important role in the equilibrium constant K_e. Literature shows that the K_e value ranges from 1.8×10^{-3} to 2.02×10^{-3} for the Cu^{2+} extraction from the copper sulfate solution by D2EHPA extractant at the equilibrium pH of 3.75 to 3.81 (Ihm et al., 1988). The values of equilibrium constants at our experimental pH, are within the range reported in the literature.

Table 5.6. The equilibrium pH values and their corresponding K_e values.

Temperature (˚C)	**Initial pH (-)**	**Equilibrium Ph (-) (Unpacked Channel)**	**Equilibrium Ph (-) (Packed Channel)**	**K_e for unpacked Channel (-) [Eq. (5.21)]**	**K_e for packed Channel (-) [Eq. (5.21)]**
25	9.26	6.76	6.72	4.91×10^{-06}	1.39×10^{-05}
	9.26	7.04	7.00	2.78×10^{-06}	7.39×10^{-06}

	9.26	7.22	7.17	1.95×10^{-06}	4.91×10^{-06}
	9.26	7.34	7.29	1.52×10^{-06}	3.67×10^{-06}
50	9.26	6.75	6.70	7.39×10^{-06}	1.84×10^{-05}
	9.26	7.03	6.98	4.20×10^{-06}	9.83×10^{-06}
	9.26	7.19	7.14	2.98×10^{-06}	6.46×10^{-06}
	9.26	7.30	7.26	2.34×10^{-06}	4.85×10^{-06}
75	9.26	6.70	6.65	1.05×10^{-05}	2.09×10^{-05}
	9.26	6.98	6.93	5.93×10^{-06}	1.16×10^{-05}
	9.26	7.15	7.11	4.17×10^{-06}	7.93×10^{-06}
	9.26	7.27	7.20	3.28×10^{-06}	5.88×10^{-06}

5.4.4. Determination of the mass transfer coefficient for the copper extraction process

The mass transfer coefficients (K_La) are calculated by using the Eqs. (5.16) and (5.17). The experimental results are analyzed by Darekar et al. (2014) model, applicable for the flow-through serpentine microchannel (Eq. 5.18). Taking A/O ratio = 1, the K_La value from Darekar et al. model (2014) becomes 8.74×10^{-3} for the packed channel and 7.96×10^{-3} for the unpacked channel. In the present study, the mass transfer is the reactive mass transfer. The other parameters, like pH, initial and final concentration of the ions in the aqueous and organic phases, may also have an influence on the K_La values, similar to the K_e values. As per Eq. (5.16) the K_La value depends on the initial and final concentration of the metal ion solution and the $V_{Channel}/Q_a$ ratio, which is referred to as residence time inside the reactor (θ_r). In the present work, the samples are manually collected,

and after the phase separation, the aqueous phase is tested for the determination of copper ion concentration. As a consequence, the total time required to collect the sample for tests after the phase separation is considered as the residence time (θ_r). The K_La values for the packed and unpacked channel are shown in Table 5.7, at different variables.

Table 5.7. The K_La values for the packed and unpacked channels (A/O = 1).

Channels	**The initial concentration of copper in the aqueous phase (mol l^{-1})**	**The final concentration of copper in the aqueous phase (mol l^{-1})**	Δ_{LMC} **(mol l^{-1})**	**Residence time, θ_r (s)**	K_La **(s^{-1})**
Packed	1.60×10^{-3}	1.80×10^{-5}	1.58×10^{-3}	120	8.37×10^{-3}
Packed	1.60×10^{-3}	1.80×10^{-5}	1.58×10^{-3}	90	11.2×10^{-3}
Packed (actual reaction time)	1.60×10^{-3}	1.80×10^{-5}	1.58×10^{-3}	10	1.0×10^{-1}
Unpacked	1.60×10^{-3}	1.60×10^{-4}	1.43×10^{-3}	120	8.33×10^{-3}
Unpacked	1.60×10^{-3}	1.60×10^{-4}	1.43×10^{-3}	90	11.1×10^{-3}
Unpacked (actual reaction time)	1.60×10^{-3}	1.80×10^{-5}	1.43×10^{-3}	10	1.0×10^{-1}

As shown in Table 5.7, at a particular A/O ratio and pH value, logarithmic mean concentration difference (Δ_{LMC}), i.e., the mass transfer flux, is higher for the packed channel, which favors a higher amount of mass transfer. But the flux does not significantly change the volumetric mass transfer coefficient (K_La). The mass transfer coefficient highly depends on the residence time. Higher residence time results in lower volumetric mass transfer coefficient at constant concentration difference. Though the rate of increase of the K_La values for the packed and unpacked channels are the same, for the same flow condition, the packed channel has the low residence time due to the decrease of flow area and increase in flow velocity. Therefore, the packed channel is highly efficient than the unpacked channel under the same A/O ratio. Our experimental results satisfy the Darekar et al. (2014) model very closely.

5.5. Conclusions

The main parameters for the copper extraction and stripping process were optimized for the flow through a rectangular serpentine channel, and the effect of packing on the extraction efficiencies was explained in this present work. It is observed that pH is one of the most important parameters for the extraction process. At a pH = 9.26, C_m = 0.047 M, C_E = 0.05 M and A/O = 1, the higher percentage of extraction (96.17%) as well as higher extraction efficiency (96.32%) is obtained by the packed channel whereas the unpacked channel shows 86.81% extraction at an efficiency of 88.58%. For a particular A/O ratio, the present newly developed packed serpentine channel is more efficient than the unpacked channel. After fixing the parameters of the extraction process at a particular value other than temperature, the percentage of extraction and efficiency for both the channels increases, but at a temperature 50 ˚C, the higher extraction percentage (97.02%) and higher extraction efficiency (97.11%) for packed channel again proved its benefit over the unpacked channel which showed 86.38% copper extraction with an efficiency of 88.28%. The use of a packed channel as the stripping device has also given a fruitful result over the other one. The highest stripping percentage (97.66%) is achieved by the packed channel. It is seen that the K_e and the K_La values are quite satisfactory for the packed channel. Due to a large number of benefits like higher reaction rate, the higher mass transfer coefficient, and for the higher extraction efficiency (98.89%), the rectangular packed channel device may be used as a highly efficient extraction as well as stripping or any other reaction devices. The present work may be helpful for the motivation and innovation of the new rectangular serpentine packed channel mass transfer devices in the future.

Chapter 6

Synthesis of Graphene-based Material and Its Characterization for Adsorption in Millimetric Fixed-bed Device

Adsorption is an effective separation process by which the atoms, ions, or molecules from a gas, liquid, or dissolved solid adhere to a surface. The industries widely use adsorption for its cost-effectiveness. This process mostly depends on the interactions between the adsorbent and adsorbate molecules. In this process, a film of the adsorbate molecules is created on the surface of the adsorbent molecules. The adsorbent is usually porous, having high surface area, which can adsorb substances onto its surface with the help of intermolecular forces. The adsorbate is a substance, which is adsorbed on the surface of another substance. From the previous chapter 5, it is clear that the packed millimetric channels are more efficient in the mass transfer over the unpacked channels. The packing materials used so far were inert (medium-sized red sand), effected the mass transfer characteristics by only enhancing the interactions between the two phases. If an active material can replace it, then the mass transport process will be intensified. In the continuous mode, the residence time of the adsorbate molecules inside the small millimetric channels is very low, and the adsorption process is a slow process, which is another big challenge in front of us. Graphene-based adsorbent materials attracted the attention of the researchers due to its high surface area, presence of functional groups specific for adsorptions, and its ability to form π-bonds. In the present context, graphene-based adsorbent synthesized for the removal of one kind of universally used drug naproxen.

6.1. Introduction

Naproxen ($C_{14}H_{14}O_3$, NPX), is a widespread non-steroidal anti-inflammatory drug, widely prescribed by the medical practitioner for pain relief such as muscle aches, headache, dental pain, tendonitis, and menstrual cramps. After the intake, drugs are absorbed by the body organisms and take part in metabolic reactions. The organisms leave the unmetabolized substances comprising these drugs via urine or sludge into the sewage water. Moreover, the main sources of these drug contaminations are the inefficient effluent of the pharmaceutical industries, the improper ejection of unused or expired drugs in hospitals, which are increasing water contamination day by day due to their stability. Naproxen may affect water quality adversely. Human life and ecosystem can be directly influenced by the long-term intake of contaminated aquatic food like fish and potable water (Isidori et al., 2005; Önal et al., 2007). It may affect the regulation and functioning of the organisms present in the ecosystems by influencing the activity of enzymes as it is a biologically active substance (Górny et al., 2019). The reported ranges of their existence in the environment are 0.1–2.6 μg dm^{-3} in treated wastewater and 0.01–0.1 μg dm^{-3} in surface waters (Isidori et al., 2005; Boyd et al., 2005; Tang et al., 2014). The researchers employed various removal methods for the separation or degradation of NPX from the contaminated water. The coagulation-flocculation, sedimentation, ultrasonic-degradation processes are not effective enough (Im et al., 2013). The other important processes are photo-degradation (Jallouli et al., 2016), bio-degradation (Wojcieszynska et al., 2014; Górny et al., 2019), and the advanced oxidation processes such as chlorination (Boyd et al., 2005), degradation with UV/H_2O_2 (Kim et al., 2009; Afonso-Olivares et al., 2016), ozonation (Li et al., 2019; Patel et al., 2019)), and their combinations or others. Advanced oxidation processes may produce 1-(6-methoxy-2-naphthyl) ethanol, 1-(6-methoxynaphthalen-2-yl) ethanone, 2-ethyl-6-methoxynaphthalene, 1-(6-methoxynaphthalen-2-yl) ethyl-hydroxy-peroxide as the byproducts in the reaction medium (Jallouli et al., 2016). Although the advanced oxidation processes are highly effective in removing or degrade naproxen from the aqueous medium, it may create environmental toxicity due to the production of highly toxic intermediates than the parent compound (Straub and Stewart, 2007). However, the adsorption process is quite effective and mostly used for the removal of naproxen without the formation of any harmful byproducts. Activated carbon (Önal et al., 2007; Yu et al., 2008), activated carbon nanocomposite (Begum and Ahmaruzzaman, 2018), activated sludge (Tang et al., 2014), micelle–

clay complex (Qurie et al., 2013), nanoparticles decorated onto graphene oxide (Nodeh et al., 2018) are used as adsorbents, extensively.

In recent years, reduced graphene oxide (RGO) has attracted great attention from researchers for its good electrical, thermal, mechanical, and optical properties. Moreover, RGO and its nanocomposites are broadly used as excellent adsorbents and applied in water purification processes. Adsorption being a surface phenomenon not only depends on the surface area and micropores present, but it also depends on the surface characteristics of the adsorbing materials. The 2D planes of RGO film with the attachment of fewer amounts of functional groups provide high surface area and bonding sites susceptible to adsorption. The delocalized π-electrons present in RGO film have strong binding efficiency towards the harmful pollutants, which makes it a rapid adsorbent for the removal of contaminants (Apul et al., 2013). Otherwise, nanoparticles have efficient disinfectant or degradation or complex formation ability depending on the surface charge under optimized pH conditions. Hence, the nanoparticles decorated RGO film may provide excellent removal efficiency towards the various water pollutants, like, harmful organic dyes (Sun et al., 2014; Song et al., 2016; Nafiey et al., 2017), heavy metals (Nafiey et al., 2017; Sang et al., 2017; Padhi et al., 2017; Zhang et al., 2018), phenol and phenolic compounds (Nafiey et al., 2017; Padhi et al., 2017) as well as pharmaceuticals (Lin et al., 2017; Fang et al., 2018).

Previously, RGO and its composites, have been produced using a variety of reducing agents like acids, such as alanine (Wang et al., 2017a) and ascorbic acid (Zhang et al., 2010c), metal or metal oxides (Pei and Cheng, 2012; Chua and Pumera, 2014), reducing sugars (Liu et al., 2016), reducing salts (Bo et al., 2014), hydrazine (Gao et al., 2010; Park et al., 2011), organic compounds like indole (Liu et al., 2013b) and plant extracts (Lee and Kim, 2014; Suresh et al., 2015). These RGO were utilized in versatile purposes other than the removal of naproxen. A very few studies have been performed for the adsorption of NPX on RGO or RGO nanocomposites produced by chemical reduction using sodium borohydride (Park et al., 2018) and Sodium ascorbate (Umbreen et al., 2018). Moreover, the silver-decorated reduced graphene oxide nanocomposites have been attracted the attention of the researchers for its huge application like heterogeneous nanocatalysis (Navalon et al., 2016; Wang and Astruc, 2018), hydrogen peroxide detection (Tajabadi et al., 2015), photocatalysis (Qustia et al., 2014; Wang et al., 2017b), temperature (Neella et al., 2017),

ammonia gas (Kavinkumar and Manivannan, 2016) and H_2S gas sensing (Ovsianytskyi et al., 2018) and also in water purification (Deng et al., 2017; Mangalam et al., 2019).

Recently, the use of bio-extracts as the reducing agents are gaining importance to the scientific community for the green synthesis of nanoparticles that are useful for their various kinds of applications, as said earlier. In this regard, turnip (Brassica rapa subsp. Rapa) leaves-extract is remarkable (Vilchis-Nestor et al., 2008; Martinez et al., 2010; Salam et al., 2012). The phenolic and nitrogen compounds, vitamins, reducing sugars, terpenoids, and other metabolites present in the turnip leaves may act as the reducing agents in green synthesis of nanoparticles (Salam et al., 2012). The presence of polyols, hydroxyl, and carboxylic groups may act as reducing as well as a capping agent in the nanoparticle synthesis (Vilchis-Nestor et al., 2008). Turnip leaves-extract contains a sufficient amount of ascorbic acid or vitamin C (95.28 ± 0.98 to 143.38 ± 7.31 mg per 100 g) and total phenolics (218.54 ± 48.77 to 240.01 ± 6.08 mg per 100 g) may signify it as an active reducing medium (Martinez et al., 2010). The practical application of the Ag-RGO nanocomposite in the water purification fields should be advantageous for its higher adsorptive removal capacity and efficiency towards the water contaminants. The Conductive Ag-nanoparticles in the synthesized material may have antimicrobial activity (Moghayedi et al., 2017) based on the charge generated on it depending on the experimental pH values (Abbaszadegan et al., 2014) as well as it can show the catalytic activity towards naproxen degradation/complex formation (Bastus et al., 2014). The Ag-nanoparticles degraded byproducts formed, if any, may also be adsorbed/removed by the RGO surfaces with the higher π-π interactions. Ag-nanoparticles may also increase the hydrophilicity of the graphene film. Higher hydrophobicity can provide a higher adsorption capacity by expanding the adsorbate and adsorbent interactions. Hence, the prepared Ag-RGO film may be utilized by the industries for the adsorptive removal of naproxen without any harmful byproducts generation.

As per literature, the use of the silver (Ag) nanoparticles decorated RGO (Ag-RGO) film synthesized by the green method using turnip leaves-extract is the initiation for the adsorptive removal of naproxen, which is considered in the present study. The main objectives of the present study are to synthesize the Ag-RGO film using turnip leaves-extract and its utilization as an efficient remediation of naproxen by adsorption from the naproxen-contaminated water without

the formation of harmful byproducts. Besides, the adsorption parameters were optimized to obtain the maximum adsorption capacity. The adsorption kinetics and equilibrium isotherms were also enunciated based on the present experimental conditions.

6.2. Experimental

6.2.1. Reagents and Materials

Natural graphite flakes (atomic weight = 12.01, assay ≥ 99.5%) and caustic soda pellets (NaOH, MW = 40.00, assay = 98.0%) were bought from Himedia Laboratories Private Limited. Potassium permanganate ($KMnO_4$, MW = 158.03, assay = 99.0%) was purchased from Central Drug House (P) Limited. The other required chemicals, 98.0% sulfuric acid (H_2SO_4, MW = 98.08 g mol^{-1}, assay = 95.0 – 98.0%), 88.0% phosphoric acid (H_3PO_4, MW = 98.0 g mol^{-1}, assay ≥ 85.0%), 37.0% hydrochloric acid (HCl, MW = 36.46 g mol^{-1}, assay = 36.5 – 38.0%), 30.0% hydrogen peroxide (H_2O_2, MW = 34.01 g mol^{-1}, assay = 29.0 – 32.0%) and silver nitrate ($AgNO_3$, MW = 169.87 g mol^{-1}, assay ≥ 99.5%) of ACS reagent grade were supplied by Merck Life Science Private Limited. Hayman Group Limited supplied ethyl alcohol AR (C_2H_6O, MW = 46.07 g mol^{-1}, assay = 99.9%). Anhydrous naproxen ($C_{14}H_{13}O_3$, MW = 230.26 g mol^{-1}, assay = 98.5 – 101.5%) meets USP testing specifications supplied by Sigma-Aldrich (USA), was used in the present experiments without any further purification.

6.2.2. Preparation of graphene oxide (GO)

GO was prepared following the improved Hummers method without using $NaNO_3$, which restricts the release of NO_X. The GO produced by this method constitutes a more regular structure with less disrupted basal plane, making the process advantageous for mass production (Marcano et al., 2010). Improved Hummers method is further modified herewith (modified improved Hummers method), to produce high quality GO in a more economical way of consuming lesser time and chemicals than the improved Hummers method. 90 cm^3 concentrated H_2SO_4 and 10 cm^3 concentrated H_3PO_4 acids (9:1 ratio) were mixed and stirred for 30 min using a magnetic stirrer. Then 2 g of natural graphite flakes (GF) were added to the acid mixture and stirred for one hour. The mixture temperature was maintained at 273 – 278 K with the help of an ice bath, and 12 g of $KMnO_4$ was added slowly with continuous stirring. The mixture was stirred for 90 min, followed

by sonication for one hour at 208 K and 20 min at 358 – 363 K, respectively. A deep green color solution was obtained, indicating the completion of the oxidizing reaction (Fig. 6.1). Then 150 cm^3 and 350 cm^3 of milli-Q water were added successively and sonicated the solutions for one hour, respectively, at 298 – 308 K to complete the hydrolysis.

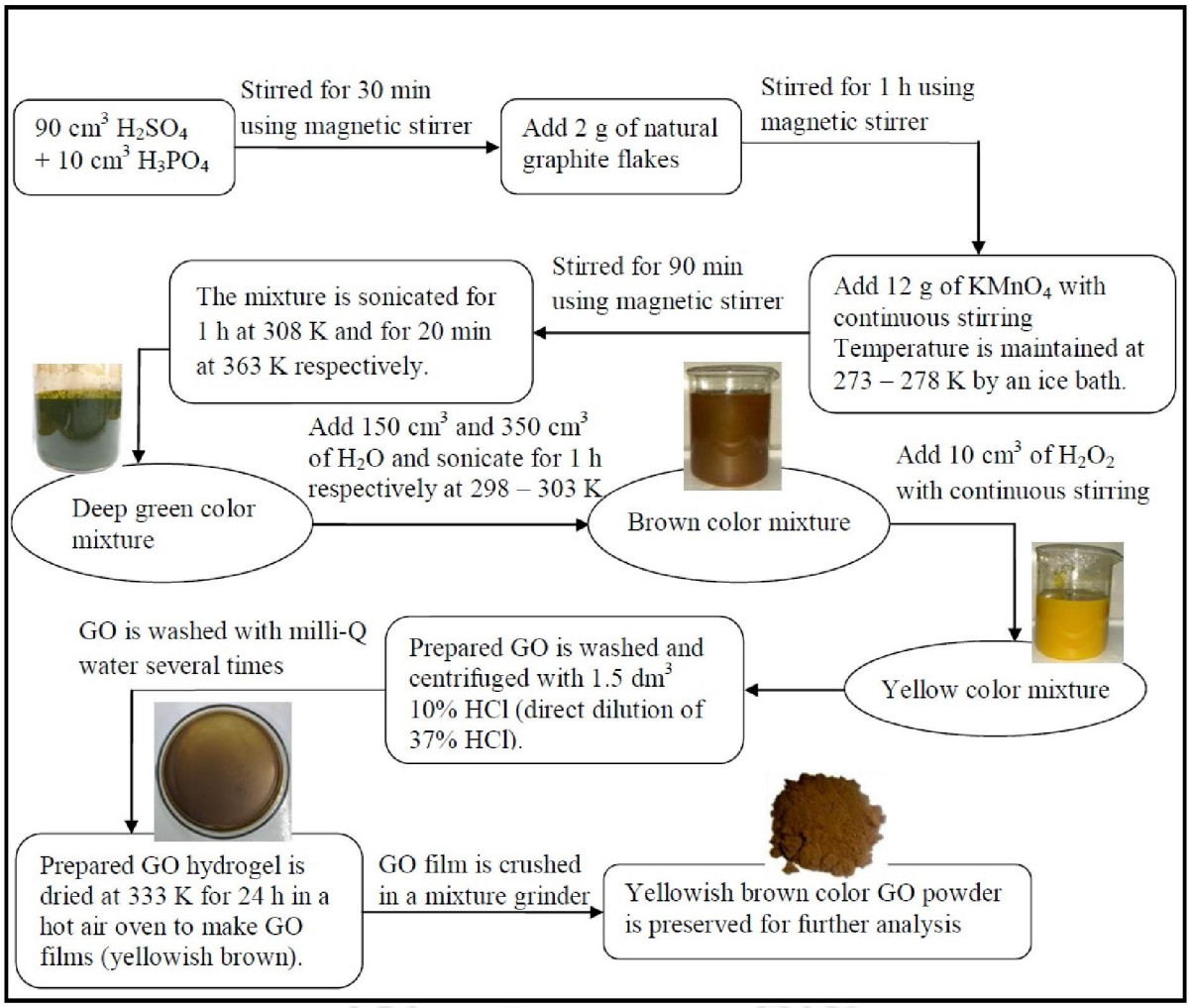

Fig. 6.1. GO preparation scheme (modified improved Hummers method).

A brown color mixture was obtained, and 10 cm^3 30.0% H_2O_2 was added to the brown color solution with 10 min continuous stirring to remove the unreacted $KMnO_4$ from the solution mixture then the brown color solution turns into yellow color. The prepared GO was washed with 1.5 dm^3 of 1:10 aqueous HCl solution (direct dilution of 37.0% concentrated HCl) to remove metal ions. Then the prepared GO was washed and centrifuged (12000 rpm for 20 min) with the milli-Q

water several times (minimum seven times) and got the GO hydrogel of final pH 3.02. The prepared GO hydrogel was then dried in a hot air oven for 24 h at 333 K. The dried GO film was crushed by a mixture grinder to get GO powder of yellowish-brown color, which was preserved for the further analysis. A detailed flow diagram for the GO synthesis has been shown in Fig. 6.1.

6.2.3. Green synthesis of silver-reduced graphene oxide (Ag-RGO) nanocomposite

100 g of fresh green turnip leaves collected from the local market were cut into pieces and taken into 400 cm^3 milli-Q water in a one dm^3 glass beaker. It was heated at 353 K for two hours with continuous stirring and filtered to get the leaves-extract. The leaves-extract was then concentrated to 100 cm^3 by boiling (yellowish-green in color) and preserved for further use (pH 5.30). After that, 100 mg of GO powder was dispersed into 50 cm^3 milli-Q water by one hour sonication at room temperature 298 K (pH 2.96). Then 20 cm^3 0.1 M $AgNO_3$ (pH 9.86) solution and 70 cm^3 concentrated turnip leaves-extract were added into the GO suspension. The mixture was then heated for 24 h at 353- 363 K temperature with continuous stirring (pH 5.92). The color of the solution turns black with the simultaneous reduction of GO to RGO and Ag^+ to Ag-nanoparticles. The prepared RGO film decorated with Ag-nanoparticles (Ag-RGO nanocomposite film) was filtered and centrifuged with milli-Q water (13400 rpm for 20 min), dried at 363 K for 24 hours in an oven and conserved for the additional experimentations.

6.2.4. Characterization methods

The physical properties and structure of the nanocomposite material were analyzed by the X-ray powder diffraction (XRD) (Model: D8 Advance, Make: Bruker, Netherlands) with Cu-Kα radiation of wavelength 1.5406 Å (40 kV, 40 mA) over the range of 2θ = 10–80° at a rate of 3° min^{-1}. The surface functional groups of the synthesized material were recognized by Fourier-transform infrared spectroscopy (FTIR) (Model: IR Affinity-1, Make: Shimadzu, Japan) using finely ground KBr with 0.5% of the sample to form pellets with the average of 30 scans ranges from 400–4000 cm^{-1}. The graphene layer formed in the prepared sample was analyzed by a Raman system (Make: Horiba Jobin Vyon, Model: LabRam HR, Japan) with the help of the band shift by dispersion of monochromatic light (wavelength 488 nm). Field Emission Transmission Electron

Microscope (FETEM) (Make: JEOL, Model: 2100F, Japan) and Field Emission Scanning Electron Microscope (FESEM) (Make: Zeiss, Model: Sigma, Germany) were used to inspect the surface morphology of the prepared sample. The composition of the prepared material was analyzed by Energy-dispersive X-ray spectroscopy (EDS). NPX concentrations before and after the adsorption experiments were measured by High-Performance Liquid Chromatography (HPLC) (Model: Prominence HPLC System; Make: Shimadzu, Singapore). The other necessary instruments, like the digital balance (Model: ME 204, Make: Mettler Toledo, Switzerland), pH meter (Model: pH 700, Make: Eutech Instruments, Singapore), magnetic stirrer with a hot plate (Make: Antech, Model: AN-MSH-680), ice flaker machine (Make: NTF, Model: SLF 225, Italy), sonicator (Model: 3.5 L/00H/DTC, Make: PCI, India), centrifuge (Model: 2-16P, Make: Sigma, Germany), hot air oven (Model: Digital, Make: SoNuu, India) and mixture grinder (Model: LLMG20 500 W, Make: Lifelong, India) were used for the desired material synthesis purpose.

6.2.5. Adsorption experiments

Naproxen adsorption was conducted in a batch mode with continuous stirring with the help of magnetic stirrer using 20.2 mg of Ag-RGO composite (suspended by one hour sonication in 2 cm^3 milli-Q water) and 50 cm^3 NPX solutions in each case. Continuous mixing was achieved by moving a glass rod in the opposite direction of magnetic stirring. The effective parameters like pH (2.50, 4.50, 6.50 and 8.50 at room temperature 298 K), adsorption time (0.33–3.0 min) and naproxen concentration (25–100 mg dm^3) on the adsorption capacity were investigated. The naproxen removal percentages (*R%*), the adsorption capacities (mg g^{-1}) at equilibrium and at time *t* were calculated based on the naproxen concentrations before and after the adsorption studies following Eq. (6.1), Eq. (6.2) and Eq. (6.3) respectively.

$$\%R = \frac{C_0 - C_e}{C_0} \times 100 \tag{6.1}$$

$$q_e = \frac{V}{m}(C_0 - C_e) \tag{6.2}$$

$$q_t = \frac{V}{m}(C_0 - C_t) \tag{6.3}$$

where C_0 (mg dm^{-3}) and C_e (mg dm^{-3}) are the initial and equilibrium concentrations of naproxen in solution, q_e (mg g^{-1}) is the equilibrium adsorption capacity, C_t (mg dm^{-3}) and q_t (mg g^{-1}) are the

concentration of NPX in the solution and adsorption capacity of the adsorbent at time *t*. *V* (dm^3) is the volume of naproxen solution taken for each batch adsorption study, and *m* (g) is the adsorbent (Ag-RGO) dosage.

The concentration of NPX was measured by HPLC, provided with a UV detector and a C18 column (Eclipse XDB, Agilent, USA) having dimensions of 250 mm × 4.6 mm, and packed with the particles of 5 µm diameter. The mobile phase was a mixture of acetonitrile (50%) and 1% aqueous solution of acetic acid (50%) with an isocratic flow rate of 1.0 cm^3 min^{-1}. The detection wavelength and temperature were set at 260 nm and 298 K, respectively.

6.2.6. Adsorbent regeneration experiments

Regeneration study is necessary, as it is a crucial factor for the industrial use of adsorbents. The used adsorbent was regenerated at room temperature by mixing with 100 cm^3 pure ethyl alcohol. The mixture was stirred for one hour using a magnetic stirrer, sonicated for 30 min, filtered, washed with ethyl alcohol, and finally dried in a hot air oven for further use. A similar process was repeated for regeneration purposes up to the fifth recycle.

6.3. Results and discussion

6.3.1. Material characterization results

Fig. 6.2(a) shows the X-ray diffraction patterns for GF, GO, and Ag-RGO. GF shows the sharp peak at 2θ = 26.6°, which corresponds to interlaying spacing value (d_s) of 3.36 Å for (002) plane. GO has a much higher *d* spacing value (28.0 Å) for 2θ = 10.45° due to the involvement of oxide bonds, which confirms the extensive oxidation of GF. The pattern for Ag-RGO shows the four peaks 38.1°, 44.2°, 64.4°, and 77.4° and assigned planes were found to be (111), (200), (220), and (311) (Dutta et al., 2013; Bhunia and Jana, 2014; Shao et al., 2015; Jiao et al., 2015; Maryami et al., 2016; Neella et al., 2017). This approves a face-centered cubic (FCC) lattice in Ag-RGO [JCPDS no. 01-087-0597].

Raman spectroscopy is one of the widely used and most sensitive techniques to characterize disorder in sp^2 hybridized carbon materials. A comparison of Raman spectra of GF, GO, and Ag-RGO is shown in Fig. 6.2(b). The plane stretching vibrations between sp^2 carbon atoms are

responsible for G band (graphitic peak) is due to the E_{2g} vibrational mode resulted from the C-C bond stretching inside all the sp^2 carbon samples whereas the D band (disorder peak) is important for the A_{1g} vibrational mode arisen from the disordered shape of sp^2-hybridized carbon systems. GF shows the G band characteristic peak at 1540 cm^{-1}, as well as a weaker D band at 1330 cm^{-1}.

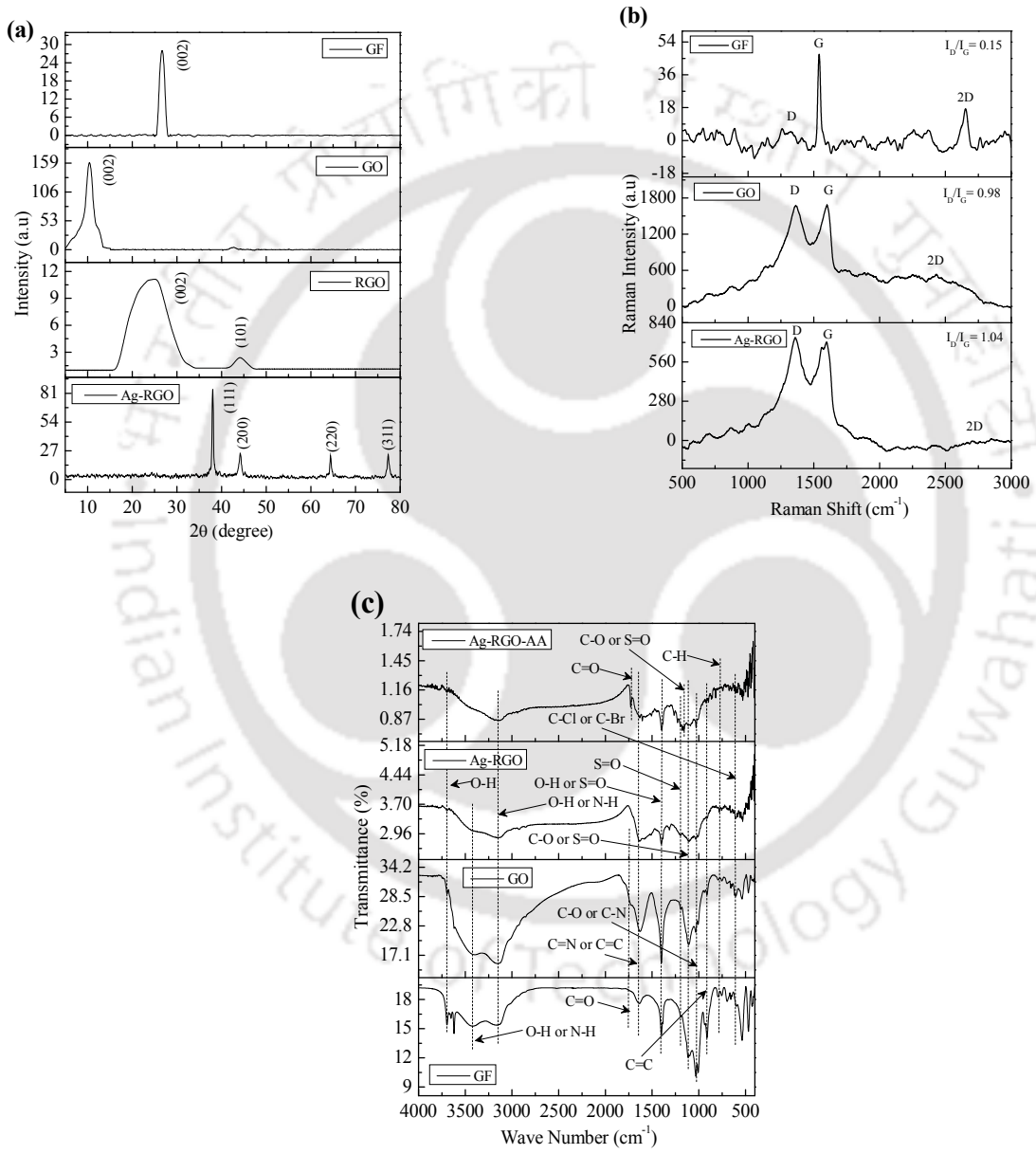

Fig. 6.2. (a) X-ray diffraction pattern (b) Raman spectroscopy of GF, GO, Ag-RGO nanocomposite, and (c) FTIR spectrum of GF, GO, Ag-RGO nanocomposite and Ag-RGO-AA (Ag-RGO nanocomposite after adsorption).

In GO, the G band widened and shifted towards 1600 cm^{-1} to 1540 cm^{-1} due to amorphization in the lattice (Dutta et al., 2013; Bhunia and Jana, 2014; Jiao et al., 2015). Higher I_D/I_G of GO (0.98) than GF (0.15) indicates the oxidation. In Ag-RGO, the I_D/I_G increased from 0.98 to 1.04, which may correspond to a higher degree of disorder, new and isolated smaller graphitic domains, or multilayer formation due to chemical bonding between GO and Ag-nanoparticles (Dutta et al., 2013; Shao et al., 2015).

Fig. 6.2(c) shows the FTIR spectrum of GF, GO, Ag-RGO, and Ag-RGO-AA (Ag-RGO after adsorption study), which determines the functional groups present in the materials. Peaks at 3695 cm^{-1}, 3422 cm^{-1}, and 3151 cm^{-1} correspond to the O-H bond stretching of free or intra-molecularly bonded alcohol. The peak at 1394 cm^{-1} represented O-H bending of alcohol or carboxylic acid groups. Peaks exhibited at 3422 cm^{-1}, and 3151 cm^{-1} demonstrate the presence of N-H bonds stretching of primary amines or amine salts. The peak at 1646 cm^{-1} represented medium or strong C=C stretching of mono-substituted, di-substituted, or conjugated alkene groups, whereas the peak at 914 cm^{-1} corresponds to the C=C bending of alkene groups. The wavelength 1646 cm^{-1} represented the common C=N bond stretching of imine or oxime groups. The peaks at 1394 cm^{-1} and 1198 cm^{-1} are the evidence of S=O bonds stretching of sulfate or sulfonyl chloride. The evidence of strong bond stretching of C-O secondary alcohol, tertiary alcohol, aliphatic ether, vinyl ether, or alkyl aryl ether was confirmed by the presence of peaks at 1198 cm^{-1}, 1109 cm^{-1}, and 1023 cm^{-1}. The peak at 1023 cm^{-1} also corresponds to the presence of common C-N bond stretching of amine groups. The peak identified at 773 cm^{-1} is the evidence of the C-H bending of the mono-substituted and 1-2-disubstituted benzene derivative. The peak at 609 cm^{-1} represented the bond stretching of the halo compounds (C-Cl or C-Br). The peak present in the Ag-RGO-AA compound at the wavelength 1721 cm^{-1} corresponds to the C-H bending of aromatic compounds or C=O stretching of aldehydes, conjugated anhydrides, aliphatic ketones, carboxylic acids or α,β-unsaturated esters. Strong C-O bond stretching of tertiary alcohol or the S=O bond stretching of sulfonamides, sulfones or sulfonic acids were represented by the peak at 1155 cm^{-1} (Blázquez et al., 2011; Dutta et al., 2013; Shao et al., 2015; Jiao et al., 2015; Infrared spectroscopy adsorption table, LibreTexts™). The FTIR spectrum of Ag-RGO (before adsorption) and Ag-RGO-AA (after adsorption) indicates a decrease in the intensity of the peaks for the latter one along with some shifts or changes in some of the characteristic bands. In case of Ag-RGO-AA, the peaks

disappeared at 1307 cm^{-1} and appeared at 1721 cm^{-1}, 1264 cm^{-1}, 859 cm^{-1}, 816 cm^{-1}. The peak of C-O shifted from 1109 cm^{-1} to 1155 cm^{-1}. These results implied the possibility that adsorption may take place through an ion-exchange process rather than complexation (Kiran et al., 2005; Blázquez et al., 2011). Figs. 6.3(a) and 6.3(d) show the FETEM micrographs of GO and Ag-RGO. The images illustrate the sheet-like structures and homogeneous dispersion of GO and Ag-nanoparticles on the RGO sheets, respectively. Ag-nanoparticles are found more or less uniform in shape and sizes (diameter: 34.49 nm to 61.70 nm) with an average particle diameter of 48.46 nm (inset figure of Fig. 6.3(d)). According to Meng et al. (Meng et al., 2015), the Ag-RGO nano-crystals with the Ag-particle (diameter of 40-45 nm), showed an efficient catalytic activity in 8 min. and according to Bastus et al. (2014), the Ag-nanoparticles of diameter 53.2 nm functionalized easily than 19.7 nm and 103.1 nm particles (53.2 nm > 103.1 nm > 19.7 nm) and also stable enough against aggregation. Hence, high functionalization efficiency and catalytic activity, as well as naproxen degradation efficiency, may be provided by the newly synthesized Ag-RGO material without Ag-nanoparticles aggregation. Moreover, the larger size of the Ag-particles may be due to some aggregation bound by the bio-organic capping molecules present in the leaves-extract (Maryami et al., 2016). Figs. 6.3(c) and 6.3(f) demonstrate the FESEM images of GO and Ag-RGO, which illustrate the even distribution of Ag-nanoparticles on RGO sites, which associates with presence of oxygen-containing polar functional groups on RGO surface (Bhunia and Jana, 2014; Li et al., 2017).

Figs. 6.3(b) and 6.3(e) represent the SEAD pattern for GO and Ag-RGO. The four rings assigned to a face-centered cubic lattice plane of Ag-nanoparticles, which are (111), (200), (220), and (311). Meanwhile, the ring-shaped pattern of diffraction recommends the crystalline structure of Ag-nanoparticles (Li et al., 2017).

Figs. 6.4(a) and 6.4(b) represent the EDS spectrum of GO and Ag-RGO, respectively, which confirm the introduction of Ag-nanoparticles on the RGO sheet. Fig. 6.4(a) validates the presence of carbon and oxygen in GO. It is evident in Fig. 6.4(b) that the relative intensity of C decreased in Ag-RGO and Ag-nanoparticles are present in a significant amount (32.3 wt%). According to Divya et al. (2018), 30 wt% Ag-nanoparticles showed catalytic degradation/complex formation activity towards organic compounds (Rhodamine B), which may be the evidence of catalytic

degradation/complex formation efficiency towards naproxen (organic compound) in the present case. In the case of 30 wt% at an average diameter of 48.46 nm, the release rate of Ag-nanoparticles in the form of Ag^+ depending on the pH value from the RGO surface to the solution is quite low. With increasing concentration (wt%) and decreasing size, the release rate increases (Molleman and Hiemstra, 2017). Hence, the presence of Ag^+ in the acidic pH stacked on the RGO surface may increase the removal efficiency of the naproxen molecules by adsorption/complex formation. Images of multi-elemental EDS mapping of Ag-RGO is shown in Fig. 6.4(c), which indicates that the Ag-RGO composite is mainly composed of C, O, and Ag elements.

6.3.2. Parametric effects on naproxen adsorption capacity

6.3.2.1. Effect of pH on the naproxen adsorption capacity

The adsorbate and adsorbent interaction depends on the following interactive forces (a) electrostatic attraction or repulsion between the charged adsorbent and naproxen molecules, (b) $\pi-\pi$ interaction (between reduced graphene oxide and the benzene ring present in the naproxen molecules) and (c) H-bonding. The electrostatic interactive force depends on the isoelectric point (the pH at which a particular molecule behaves as electrically neutral in the statistical mean), which may shift towards the higher pH values with the increasing amount of doped materials (Zuccaro et al., 2015). In the case of the currently synthesized material, the doping percentage of the silver nanoparticles is 32.3 or higher, according to the EDS spectrum (Fig. 6.4(b)). Hence the pH of the solutions plays a vital role in the adsorption mechanism. The effect of pH on the NPX removal using Ag-RGO was studied at the pH values of 2.50, 4.50, 6.50, and 8.50. The acidic and basic pHs were maintained with the addition of 1 M HCl and NaOH solutions, respectively. The removal efficiency was higher at pH 4.50 than the highly acidic (pH 2.50) and highly basic (pH 8.50) conditions (Fig. 6.5(a)). Such adsorption nature could result in depending on the point of zero charges (PZCs) of the graphene-based materials (pH_{pzc} ~ 6.0, the pH value when the surface has a net zero charge) (Zuccaro et al., 2015), and the ionization form of naproxen (pKa ~ 4.2). Hence, at pH > 4.2, ionization of NPX led to form anions. Additionally, at pH < 4.2, the adsorbent surface behaves as positively charged, and at pH > 6, the adsorbent surface behaves as negatively charged (Nodeh et al., 2018).

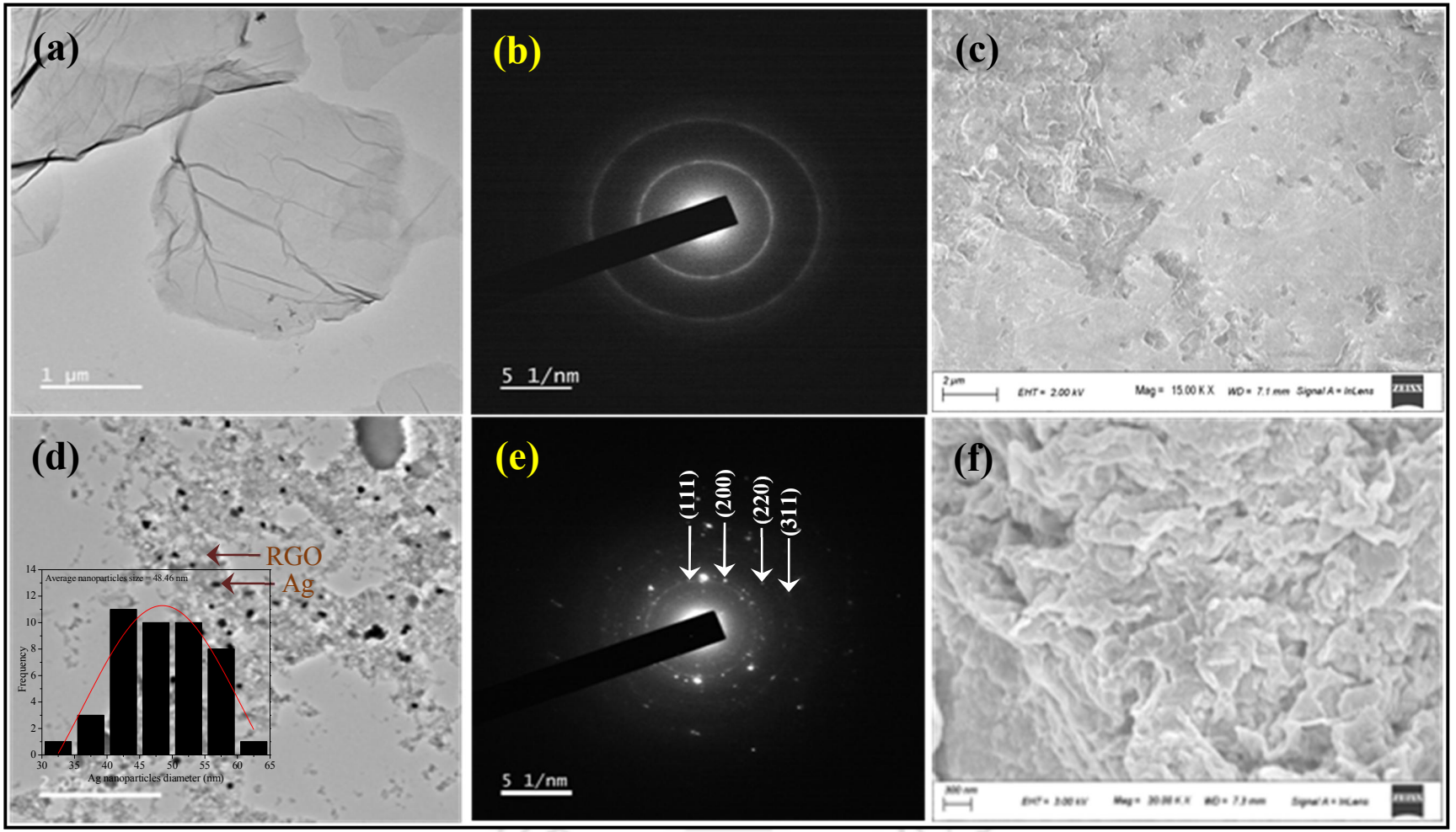

Fig. 6.3. (a) FETEM micrograph of GO, (b) SEAD pattern of GO, (c) FESEM image of GO, (d) FETEM micrograph of Ag-RGO, and size distribution of Ag-nanoparticles (inset figure), (e) SEAD pattern of Ag-RGO and (f) FESEM image of Ag-RGO.

Thus, the high electrostatic interactions between the oppositely charged adsorbent surfaces and the naproxen anions ensured the high adsorption capacity and efficiency of Ag-RGO toward NPX at pH 4.50. At pH < 4.2, the ionic interaction is not possible, and at pH> 6, the electrostatic repulsive force between the naproxen anions and negatively charged surfaces of the adsorbent diminishes the adsorption capacity and efficiency. Moreover, when the pH value decreased, the detachment of Ag^{+} from the RGO surface increased (Molleman and Hiemstra, 2017). At pH 2.50, the number of Ag^{+} releases into the solution decreasing the adsorption on the adsorbent surface, whereas, at pH 4.50, most of the Ag^{+} ions remain on the RGO surface, increasing the adsorption capacity towards negatively charged naproxen anions. The maximum adsorption capacity and efficiency were obtained at pH 4.50, considered as the optimum pH value.

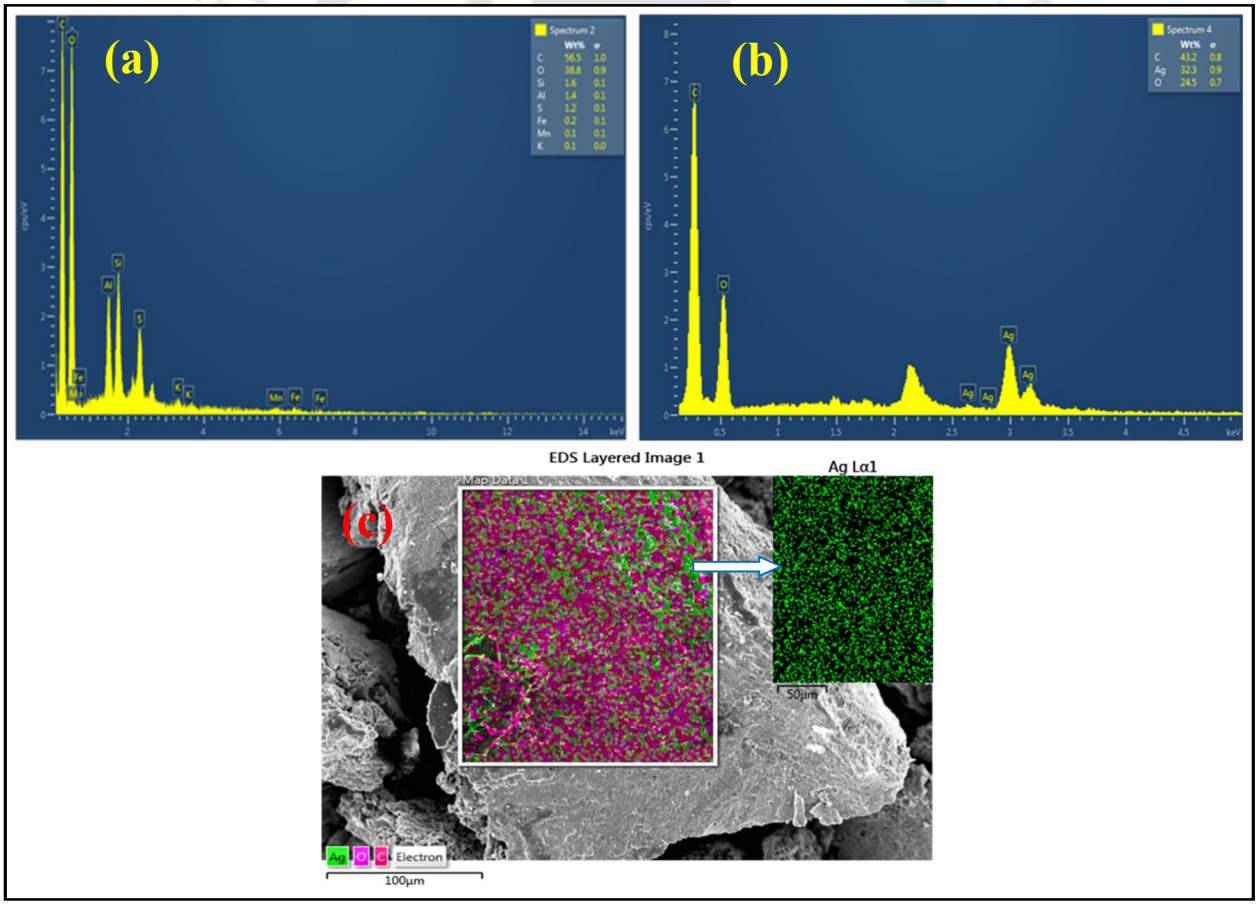

Fig. 6.4. (a) EDS spectrum of GO, (b) EDS spectrum of Ag-RGO, and (c) EDS mapping of Ag-RGO nanocomposite.

6.3.2.2. Effect of the initial naproxen concentration on the adsorption capacity

The effect of initial concentration on the adsorption capacities was studied using 100 mg dm^{-3}, 50 mg dm^{-3}, and 25 mg dm^{-3} NPX solutions at room temperature (298 K) for a fixed value of adsorbent dose (20.2 mg per 50 cm^3). It was observed that for particular pH value, the adsorption capacity increases with the increase of initial NPX concentration in the solution, probably due to the availability of more NPX anions for adsorption before the surface vacant site saturation point reached (Fig. 6.5(b)). Beyond the saturation point, the adsorption capacity will remain constant, or some desorption will occur even if the initial concentration increases. At the present experimental condition, 100 mg dm^{-3} showed a higher adsorption capacity of 229.25 mg g^{-1} (92.62%) at pH 4.50.

6.3.2.3. Effect of the contact time on the naproxen adsorption capacity

Generally, the physical adsorption capacity of the adsorbent material increases with the increase of contact time. However, when ionic interactions present between surfaces of the adsorbent and the adsorbate ions, the adsorption process becomes faster. The effect of contact time on the adsorption capacities was examined by mixing 20.2 mg of Ag-RGO into 50 cm^3 aqueous solution of NPX (for the optimum pH value of 4.5 at different NPX concentrations of 25-100 mg dm^{-3}) and collecting the samples at different time intervals (Fig. 6.5(c)). The removal efficiency reached to 75.13% within 0.33 min and increased to 92.46% in 2.0-3.0 min for 100 mg dm^{-3} concentration at a pH value of 4.50. Which demonstrated the rapid adsorption of NPX on the adsorbent surface before reaching the equilibrium due to the possible interactions between the positively charged external surface and the negative NPX anions. The adsorption of NPX using Ag-RGO attained the equilibrium within 2.0 min to 3.0 min as the removal capacities were not changed significantly (Fig. 6.5(c)). Therefore, 3.0 min can be considered as the equilibrium time for further adsorption studies.

6.3.3. Adsorption kinetics

Pseudo-first-order, pseudo-second-order, intra-particle diffusion, and Elovich models were used to estimate the kinetic parameters of the NPX adsorption at the pH 2.50-8.50, contact time 3 min, adsorbent dose 20.2 mg and initial NPX concentration of 100 mg dm^{-3} obtained from the previous optimization results (Fig. 6.5).

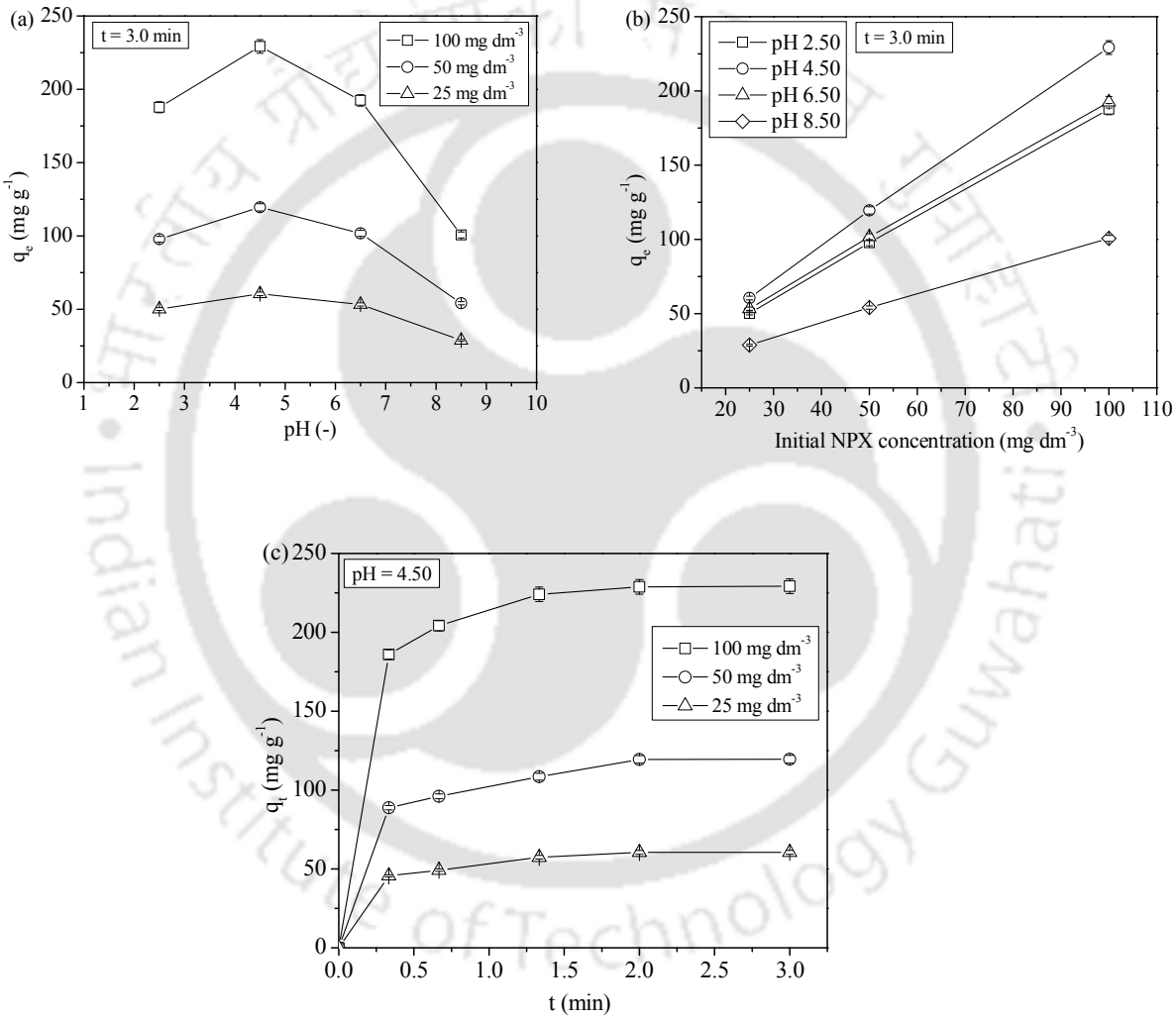

Fig. 6.5. Variations of the adsorption capacities depending on the (a) pH, (b) initial NPX concentration, and (c) contact time.

The linearized form of the Pseudo-first-order model can be expressed as (Aydin et al., 2008; Bouhamed et al., 2012; Bouhamed et al., 2016)

$$\log(q_e - q_t) = \log q_e - \frac{k_1 t}{2.303} \quad (6.4)$$

The amount of NPX adsorbed (mg g^{-1}) on the Ag-RGO nanocomposite at equilibrium and at time t are represented by q_e and q_t, respectively. The parameter, k_1 is the first-order rate constant. The values of k_1 were obtained from the *log* $(q_e - q_t)$ versus t (min) plot for the variant concentration of NPX anions (Fig. 6.6(a)). The pseudo-second-order kinetic model can be represented by (Ozcan et al., 2005; Sandy et al., 2012; Demiral and Gungor, 2016)

$$\frac{t}{q_t} = \frac{1}{k_2 q_e^2} + \frac{t}{q_e} \quad (6.5)$$

Where k_2 is the second-order rate constant (g mg^{-1} min^{-1}). The values of k_2 and q_e can be calculated from the intercept and slope of the plot of t/q_t against t (Fig. 6.6(b)).

The intraparticle diffusion equation is represented by (Ozcan et al., 2005; Bouhamed et al., 2012; Bouhamed et al., 2016)

$$q_t = k_p t^{1/2} + C_1 \quad (6.6)$$

where C_1 is the intercept and k_p is the rate constant (mg g^{-1} $min^{-1/2}$) of the intra-particle kinetic model, which is obtained from the slope of q_t versus $t^{1/2}$ plot (Fig. 6.6(c)). This model is used to understand the steps of diffusion. The Elovich kinetic model is used to examine the presence of chemical adsorption processes, which is applicable to the heterogeneous absorbing surfaces. The linearized form of the Elovich equation is represented as (Homagai et al., 2010)

$$q_t = \frac{\ln(a_e b_e)}{b_e} + \frac{1}{b_e} \ln t \quad (6.7)$$

where a_e and b_e are the initial sorption rate (mg g^{-1} min^{-1}) and the scope of surface coverage for the chemisorption (g mg^{-1}), which are obtained from the intercept and slope of the q_t versus ln$t$ plot (Fig. 6.6(d)). The average relative errors (*ARE%*) were calculated by using Eq. (6.8) to find out the suitable match of the experimental data with the kinetic and isotherm models.

$$ARE(\%) = \frac{100}{N} \sum_{1}^{N} \left| \frac{q_{cal} - q_{\exp}}{q_{\exp}} \right| \quad (6.8)$$

Where N represents the number of data points. q_{exp} and q_{cal} (mg g^{-1}) are the equilibrium values obtained from the experiment and the isotherm model, respectively.

The average relative errors (*ARE%*) were estimated to ascertain the deviation between the experimental data and the data obtained from the kinetic and isotherm models by using the Eq. (6.8). The parameters, calculated from the kinetic models, are tabulated in Table 6.1.

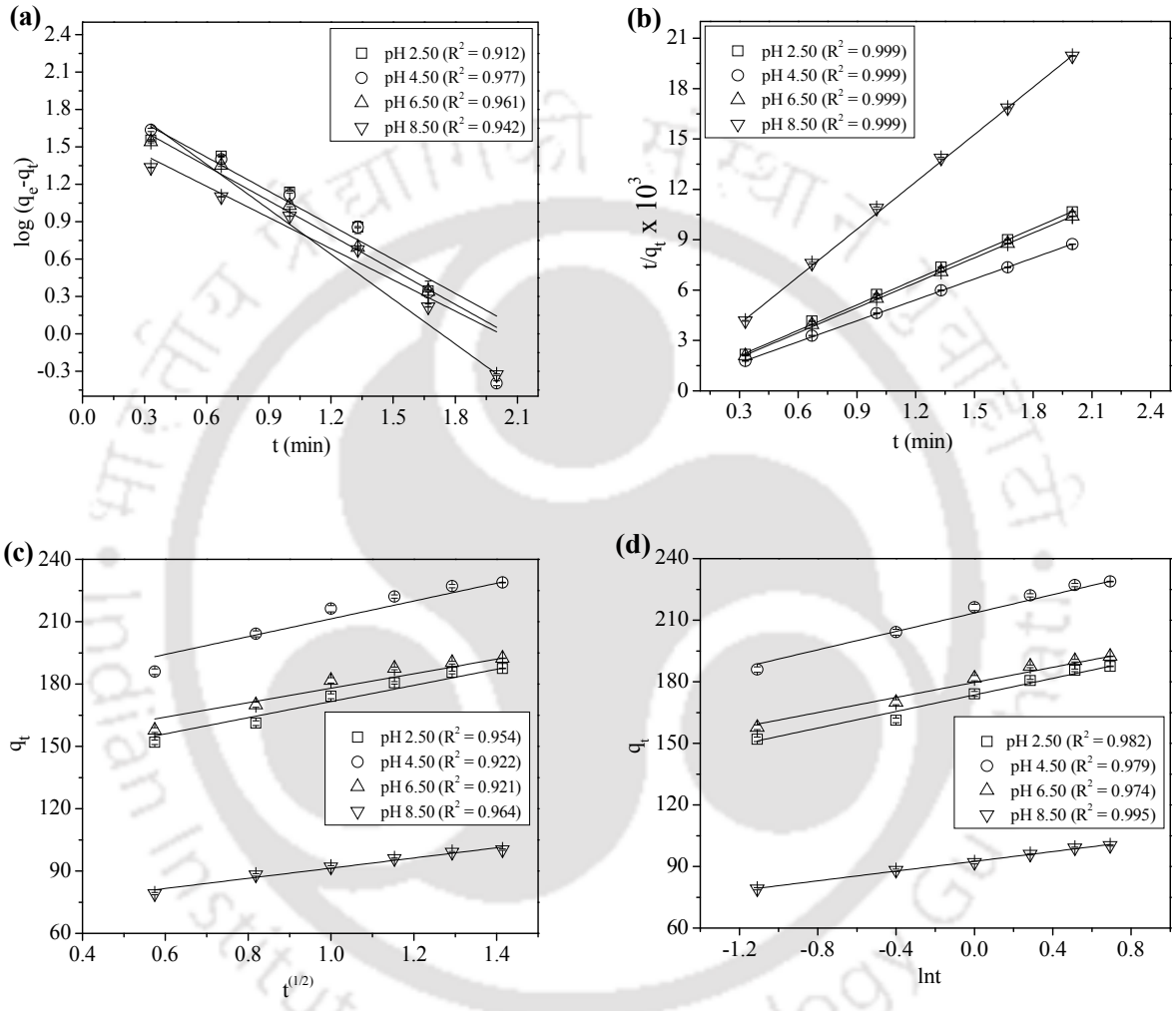

Fig. 6.6. NPX adsorption kinetics: (a) pseudo-first-order model, (b) pseudo-second-order model, (c) intra-particle diffusion model and (d) Elovich model.

The experimental data fitted with the pseudo-second-order kinetic model with the higher correlation coefficient value of R^2 = 0.99 and lower *ARE%* compared with the pseudo-first-order kinetic model at all pH values. The minimum value of k_2 (k_2 = 0.044) at pH 4.50 corresponds to the relatively high driving force of the concentration gradient sustained for more extended time for the adsorption of the NPX anions (NPX dissociation occurs at that pH value to form NPX anions)

towards positively charged binding sites of Ag-RGO surface giving higher adsorption capacity (Demirbas et al., 2009; Maryami et al., 2016).

Table 6.1. Kinetic parameters for the NPX adsorption onto the Ag-RGO nanocomposite film (NPX concentration, 100 mg dm^{-3}; the volume of NPX solution, 50 cm^3; Ag-RGO dose, 20.2 mg; temperature, 298 K and contact time, 0.33 - 3 min).

Kinetic models	pH	Kinetic parameters		R^2	*ARE%*
Pseudo-first -order	2.50	$k_1 = 2.096$	$q_e = 91.80$	0.912	56.12
	4.50	$k_1 = 2.764$	$q_e = 120.00$	0.977	50.44
	6.50	$k_1 = 2.126$	$q_e = 79.24$	0.961	63.35
	8.50	$k_1 = 1.920$	$q_e = 48.24$	0.942	57.80
Pseudo-second -order	2.50	$k_2 = 0.056$	$q_e = 197.98$	0.999	3.02
	4.50	$k_2 = 0.044$	$q_e = 237.58$	0.999	3.28
	6.50	$k_2 = 0.051$	$q_e = 200.60$	0.999	3.55
	8.50	$k_2 = 0.086$	$q_e = 104.54$	0.999	3.10
Intra-particle diffusion	2.50	$k_p = 38.90$	$C_1 = 132.68$	0.954	1.45
	4.50	$k_p = 42.83$	$C_1 = 168.55$	0.922	1.63
	6.50	$k_p = 34.88$	$C_1 = 143.12$	0.921	1.64
	8.50	$k_p = 24.48$	$C_1 = 66.90$	0.964	1.14
Elovich	2.50	$a_e = 1.09\times10^5$	$b_e = 0.050$	0.982	0.85
	4.50	$a_e = 3.08\times10^5$	$b_e = 0.045$	0.979	0.82
	6.50	$a_e = 3.29\times10^5$	$b_e = 0.054$	0.974	0.93
	8.50	$a_e = 0.29\times10^5$	$b_e = 0.084$	0.995	0.41

The q_e value at that pH (237.58 mg g^{-1}) was only 3.63% higher than the experimental equilibrium value (229.25 mg g^{-1}), and the q_t values deviate with the low *ARE%* of 3.28. This tendency provides the evidence of an indication that the rate-limiting step for the adsorption of NPX on the Ag-RGO surface followed the chemisorption process involving valence forces by sharing the electrons between the adsorbent surface and the adsorbate molecules. The increasing pH value causes the negatively charged surface, and the k_2 values also increased from 0.044 to 0.086. In the

case of intra-particle diffusion model, the non- zero value of intercept C_1 shown in Table 6.1 explains the fact that the adsorption process follows a complex mechanism not only the intra-particle diffusion as the rate-limiting step (Sohni et al., 2017; Umbreen et al., 2018). The higher value of k_p (k_p = 42.83) at pH 4.50 validates the existence of intra-particle distribution at that pH. According to the results shown in Table 6.1, the a_e values of the Elovich model were high enough to satisfy the kinetic data, as demonstrated in Fig. 6.6, exhibiting fast adsorption kinetics where the equilibrium attained within 3 min. Moreover, the much lower values of b_e were also (smallest b_e =0.045, for pH 4.50) the evidence of excellent adsorption and effective π–π interaction between the Ag-RGO and NPX molecular surfaces (Zhao et al., 2011; Umbreen et al., 2018). At the pH value of 4.50, the Elovich model held a higher correlation coefficient value of R^2 = 0.98, and the q_t values deviate with the very low *ARE%* of 0.82, which was the authentication of the chemisorption process.

6.3.4. Adsorption isotherms

Adsorption isotherms experimented at the pH range of 2.50-8.50 with the 50 cm^3 NPX solutions of different concentrations (25-100 mg dm^{-3}) for the contact time of 3 min and the adsorbent dose of 20.2 mg in each case. Langmuir, Freundlich, Temkin, and Dubinine-Radushkevich (D-R) adsorption isotherm models were studied. The Langmuir adsorption model, applicable mainly for the monolayer adsorption processes where the surfaces of the adsorbent are uniform, can be represented as (Demirbas et al., 2009; Homagai et al., 2010)

$$\frac{C_e}{q_e} = \frac{1}{bq_o} + \frac{C_e}{q_o} \tag{6.9}$$

where C_e and q_e are the solution concentration of NPX at equilibrium (mg L^{-1}) and the amount of NPX adsorbed on the AC (mg g^{-1}), respectively. The adsorption equilibrium constant is represented by b (L mg^{-1}), and q_o is the maximum adsorption capacity (mg g^{-1}). The adsorption coefficients were determined from the intercept and slope of a plot of C_e/q_e versus C_e (Fig. 6.7(a)). The heterogeneous systems are described by an empirical equation called Freundlich isotherm, is expressed as (Feng et al., 2009; Demiral and Gungor, 2016)

$$\log q_e = \log k_f + \frac{1}{n}\log C_e \tag{6.10}$$

The adsorption capacity and its intensity are represented by the terms k_f and n, which were determined from the intercept and slope of *log* q_e versus *log* C_e plot (Fig. 6.7(b)).

The Temkin isotherm model accounts for the adsorbate and adsorbent interaction. The heat of adsorption decreasing linearly with the coverage and the uniform distribution of binding energy are the main assumptions of this model. The Temkin adsorption isotherm model can be represented as (Cheng et al., 2015)

$$q_e = B \ln k_t + B \ln C_e \tag{6.11}$$

The Temkin adsorption isotherm constants k_t (equilibrium binding energy, L mg^{-1}) and B (related to the heat of sorption) were calculated from the q_e versus lnC_e plot (Fig. 6.7(c)). D-R model is generally used to analyze the sorption processes where the surface is heterogeneous, and the sorption potentials of the sorption sites are variable. The linear form of the D-R model is expressed as (Ghaedi et al., 2014)

$$\ln q_e = \ln q_s - B'\varepsilon^2 \tag{6.12}$$

where ε is the Polanyi potential, related to the equilibrium as follows

$$\varepsilon = RT \ln\left(1 + \frac{1}{C_e}\right) \tag{6.13}$$

In Eq. (6.12), q_s and q_e are the adsorption capacity (mol g^{-1}) and the concentration of NPX in equilibrium on the adsorbent surface (mol g^{-1}), respectively. The model constants q_s and B' (mol^2 kJ^{-2}) are obtained from the lnq_e versus ε^2 plot (Fig. 6.7(d)). C_e is the solution concentration of NPX at equilibrium (mol L^{-1}), R is the universal gas constant (8.314 $\times 10^{-3}$ kJ mol^{-1} K), and T (K) is the absolute temperature (Eq. (6.13)). The mean free energy of adsorption (E) is obtained by the Eq. (6.14), which is calculated with the aforementioned B' value (Gonzalez and Pliego-Cuervo, 2014).

$$E = 1/\sqrt{2B'} \tag{6.14}$$

Fig. 6.7, represents the isotherm models, and the model constants are described in Table 6.2, which indicate that the adsorption pathways or the isotherm followed changed with the change in pH values. Through the correlation coefficient, values were high enough; the experimental data were not satisfied by the Langmuir monolayer adsorption capacity as it showed a very high deviation from the experimental data at all the pH values. Hence, the experimental data may be satisfied by the Freundlich isotherm model.

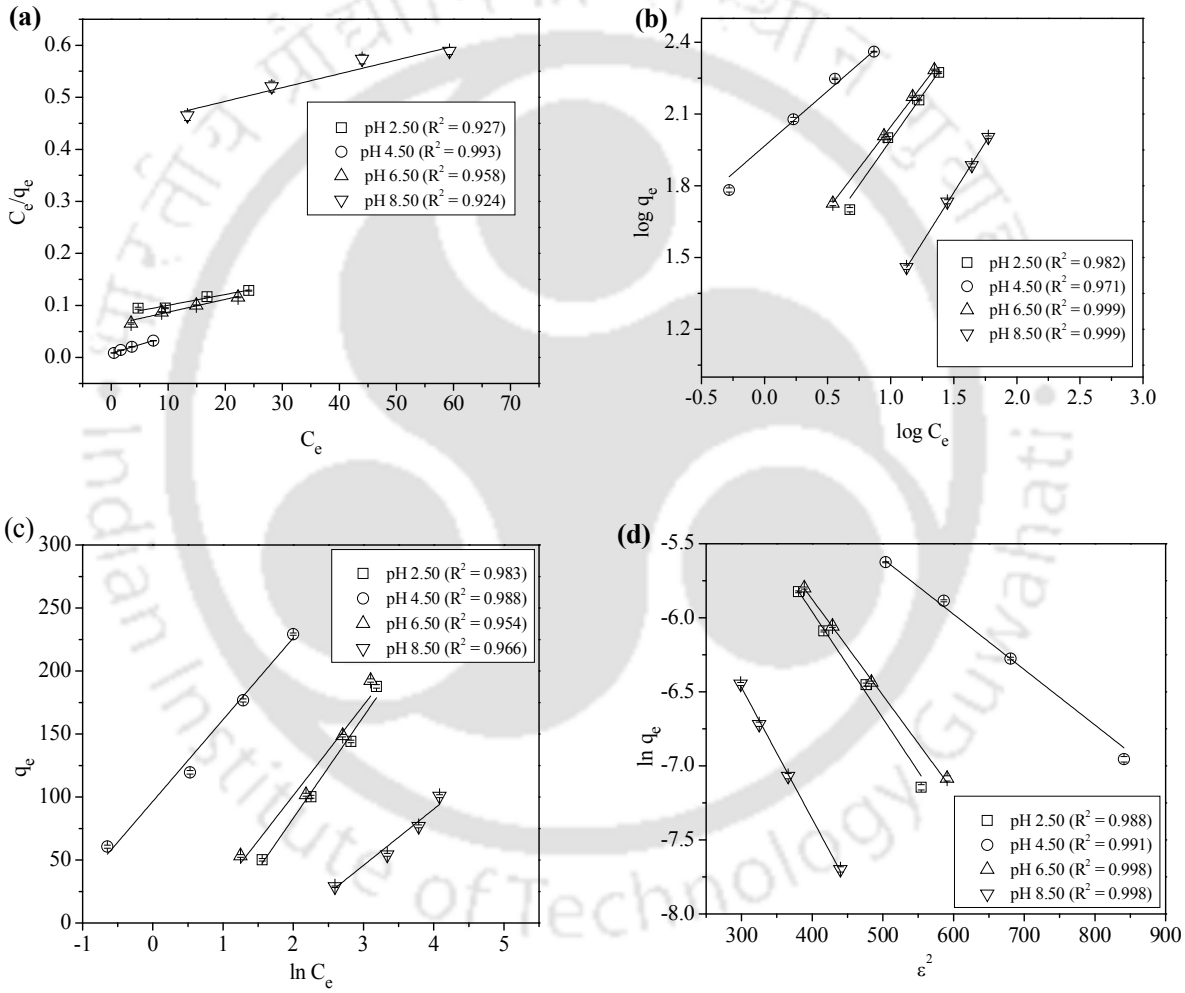

Fig. 6.7. Adsorption isotherms: (a) Langmuir, (b) Freundlich, (c) Temkin, and (d) Dubinine-Radushkevich (D-R).

Table 6.2. Adsorption isotherm constants for the sorption of NPX onto the Ag-RGO (NPX concentrations, 25, 50, 75, and 100 mg dm^{-3}; the volume of NPX solution, 50 cm^3; Ag-RGO dose, 20.2 mg; temperature, 298 K and contact time, 3 min).

Isotherms	pH	Constants			R^2	*ARE%*
Langmuir	2.50	q_o = 483.09	b = 0.026		0.927	2.61
	4.50	q_o = 302.11	b = 0.414		0.993	3.74
	6.50	q_o = 406.50	b = 0.039		0.958	2.77
	8.50	q_o = 378.79	b = 0.006		0.924	1.57
Freundlich	2.50	k_f = 17.44	n = 1.33		0.982	1.09
	4.50	k_f = 92.61	n = 2.18		0.971	1.16
	6.50	k_f = 22.63	n = 1.44		0.999	0.17
	8.50	k_f = 3.27	n = 1.19		0.999	0.18
Temkin	2.50	B = 80.67	K_t = 0.38		0.983	4.30
	4.50	B = 64.84	K_t = 4.43		0.988	5.63
	6.50	B = 71.62	K_t = 0.56		0.954	7.92
	8.50	B = 44.61	K_t = 0.14		0.966	7.08
D-R	2.50	q_s = 0.046	B' = 0.0071	E = 8.39	0.988	5.74
	4.50	q_s = 0.025	B' = 0.0037	E = 11.62	0.991	4.68
	6.50	q_s = 0.036	B' = 0.0064	E = 8.84	0.998	3.68
	8.50	q_s = 0.022	B' = 0.0088	E = 7.54	0.998	2.97

The constant k_f, which shows the tendency of the adsorbent to adsorb ranges from 3.27 to 92.71 mg g^{-1} and n represents the potentiality of the adsorbate to be adsorbed, hold the values greater than 1 in all the cases. The highest values of k_f and n were obtained at pH 4.50, with the low *ARE%* of 1.16. The q_e value calculated at that pH was 231.69 mg g^{-1}, 1.06% higher than the experimental q_e value (229.25 mg g^{-1}). Therefore, the Freundlich isotherm model indicates the favorable multilayered adsorption of NPX on the heterogeneous surface of the Ag-RGO nanocomposite film. The positive values of the Temkin constant B obtained in the present context designate the endothermic nature of the process, which provides evidence of chemical or ionic interaction rather than the physical adsorption (Inam et al., 2017). The D–R isotherm model analyzed the mean free

energy (E) required for the adsorption process along with the type of adsorption. According to Kose et al. (2011), the free energy, $E > 8$ kJ mol^{-1} is responsible for the chemical adsorption process, but according to Argunet et al. (2007), when 8 kJ mol^{-1} < E < 16 kJ mol^{-1}, ion-exchange is the governing factor. In the case of $E > 16$ kJ mol^{-1}, the diffusion processes mainly govern the adsorption. As shown in Table 6.2, the E values varied from 7.54 (at pH 8.50) to 11.62, indicates that the nature of adsorption changes from physical to chemical or ion-exchange type with the change in pH values. A good agreement with the chemical or ion-exchange route of adsorption was observed at the optimum pH value (pH = 4.50), having a maximum E value of 11.62 kJ mol^{-1} and minimum B' value (activation energy required for the adsorption process) of 0.0037 mol^2 kJ^{-2}. The Langmuir isotherm and the pseudo-second-order kinetic model showed a higher correlation coefficient and fixed values for NPX adsorption, which could have a close similarity with the bond formation between the NPX anions and the positively charged groups; however, the higher correlation coefficients of Freundlich isotherm recommends more than one mechanism and a degree of heterogeneity for the ionic species present in the solution and on the substrate surface. Therefore, the results obtained from the experimental data make it difficult to suggest a specific mechanism for the adsorption of NPX anions on the surfaces of Ag-RGO nanocomposite film. Naproxen adsorption capacities of various kinds of adsorbents, along with their fitted kinetic and isotherm models were shown in Table 6.3.

Table 6.3. Naproxen adsorption capacities of various kinds of adsorbents along with their fitted kinetic and isotherm models.

Adsorbent used	**Kinetic model**	**Isotherm model**	**pH (-) for maximum adsorption**	**Initial NPX concentration (mg dm^{-3})**	**Maximum adsorption capacity (mg g^{-1})**	**Reference**
Activated carbon from waste apricot	Pseudo-second-order	Langmuir	5.82	100-500	106.38	Önal et al., 2007
Activated coal	-	Freundlich	6.4	1×10^{-5}-8×10^{-4}	3.5	Yu et al., 2008

Fe_3O_4-SiO_2 nanoparticles decorated GO	-	Freundlich	5.0	10-400	31.25	Nodeh et al., 2018
RGO-hydrogel	Pseudo-second-order	Langmuir	2.0	100-1000	360	Umbreen et al., 2018
Activated carbon from agricultural byproduct	Pseudo-second-order	Langmuir	2.01	20	39.5	Baccar et al., 2012
Natural clay	Pseudo-second-order	Freundlich	6.0	50	37.0	Khazri et al., 2016
Activated biochar	-	Freundlich	6.5	3.30	64.5	Jung et al., 2015
Metal–organic framework MIL-101	Pseudo-second-order	Langmuir	5.0	1-20	154.0	Hasan et al., 2013
Bone char	Pseudo-first-order	Sips model (includes the features of both Langmuir and Freundlich)	7.0	50-200	3.2	Avila et al., 2015
Carbon-based magnetic adsorbents	Pseudo-second-order	Langmuir	3.0	1-30	20.75 (carbon nanotubes) 87.79 (activated carbon)	Ilbay et al., 2015
Ag-RGO	Pseudo-second-order, Elovich	Freundlich, D-R	4.50	25-100	229.25	Present study

6.3.5. Statistical analysis

The user-defined discrete design and reduced quadratic model of RSM were used to optimize the following three parameters: pH (*A*), initial NPX concentration (*B*, mg dm^{-3}), and the contact time (*C*, min) to maximize the NPX adsorption capacity on the surface of Ag-RGO film. A statistical regression model equation was developed to optimize the parametric conditions of the adsorption process. The employment of the experimental process data and the variables, overall interactive effects on it make the methodology practicable. The average equilibrium adsorption data, q_e (mg g^{-1}) were used to acquire the predicted responses. The statistical analysis utilizes experimental data, and their interactions on the process which was accomplished by placing the experimental process data to a model equation expressed as (Eq. (6.15)) (Zhang et al., 2011a; Inam et al., 2017),

$$Y = \beta_o + \sum_{j=1}^{k} \beta_j x_j + \sum_{j=1}^{k} \beta_{jj} x_j^2 + \sum\sum_{i>j} \beta_{ij} x_i x_j + e_i \qquad (6.15)$$

where Y and β_o represent the response and a coefficient (constant); β_j, β_{jj} and β_{ij} are the linear, quadratic and second-order interaction coefficients, x_i and x_j are the independent variables; k and e_i are assigned for the number of designed factors and the error terms, respectively. The parameters are shown in Eq. (6.15) can be estimated by using the formula

$$X_i = \frac{x_i - x_o}{\Delta x_i} \qquad (6.16)$$

where x_i and x_o represent the coded and uncoded values (at the center point) of the i^{th} independent variable, and Δx_i is the step change values between the low (-1) and high level (+1). The $\log_{10}$ transformed and reduced quadratic model equation represented in terms of the coded factors is expressed by Eq. (6.17).

$$log_{10}(q_t) = +2.16 + 0.0099A + 0.2963B + 0.0597C - 0.0141BC - 0.0833A^2 - 0.0912B^2 - 0.0466C^2 \qquad (6.17)$$

Predictions about the response can be made using Eq. (6.17) in terms of coded factors. A large *F*-value (5257.40) and a low *p*-value (< 0.05) validate the significance of the model and model terms. The predicted values were kind enough to estimate a precise response having the standard deviation (std. dev.), the coefficient of variance (*CV*, %), the adjusted and predicted R^2 values of 0.0069, 0.3437, 0.9993 and 0.9989, respectively. The *CV* value (is the ratio of the stand. dev. to the mean value of response) determines the reproducibility of the model. A model is considered as

sensitive if its *CV* value is less than 15%. The process optimization results, achieved from the design expert software, were quite similar to the experimental optimization results (Fig. 6.8).

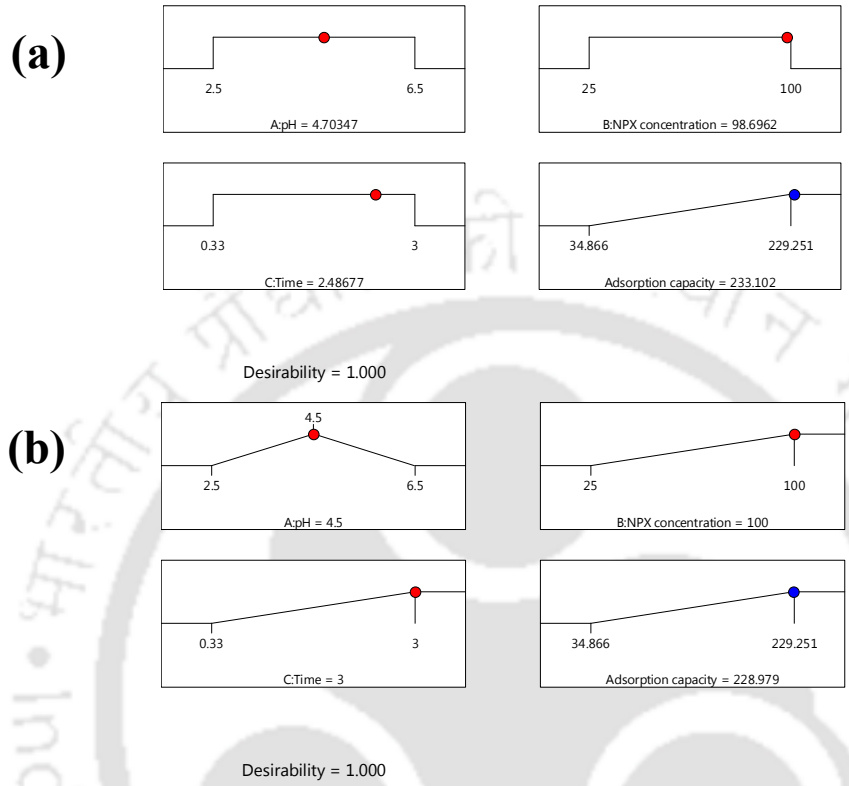

Fig. 6.8. Numerical optimization for the (a) independent factors varied within the range (pH, initial concentration, time) to get the maximum response (adsorption capacity) and (b) user-defined factors (pH targeted to 4.50, NPX concentration and time focused to maximum) to get maximum response.

The adsorption capacity obtained at the numerically optimized conditions (pH: 4.70, NPX concentration: 98.70 mg dm^{-3} and time: 2.49 min) is 233.10 mg g^{-1} (Fig. 6.8(a)), 1.68% higher than the value estimated at experimentally optimized conditions (229.25 mg g^{-1} at pH: 4.50, NPX concentration: 100 mg dm^{-3} and time: 3 min). When the pH was targeted to 4.50, and the other two parameters were maximized, the adsorption capacity achieved from the design expert software was 228.98 mg dm^{-3}, which was only 0.12% lower than the experimental value of 229.25 mg g^{-1} as shown in Fig. 6.8(b). The 3D plot for the surface response of NPX adsorption onto the Ag-RGO nanocomposite film concerning the actual pH factor is represented in Fig. 6.9, where at the pH

4.50 and NPX concentration 100 mg dm^{-3}, the maximum adsorption capacity was obtained. Hence, the experimental observations were satisfied by the numerical analysis data.

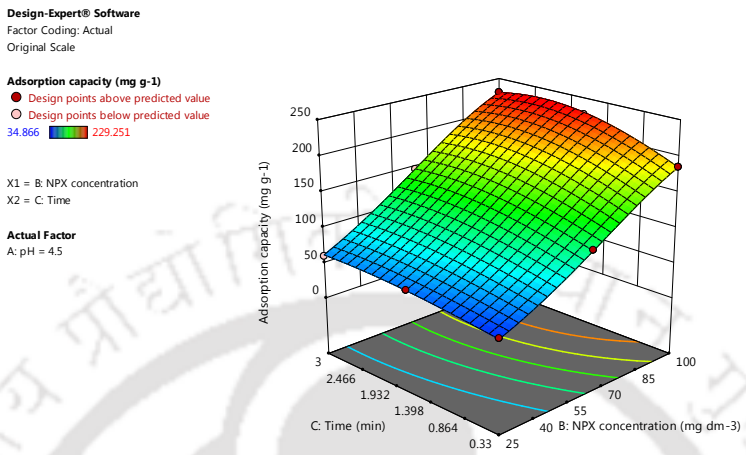

Fig. 6.9. 3D plot for the surface response of NPX adsorption onto Ag-RGO nanocomposite film concerning actual factor: pH = 4.50.

6.3.6. Regeneration of the adsorbent

The samples used in the highest adsorption conditions (pH 4.50, initial NPX concentration 100 mg dm^{-3} and adsorption time 3 min) were regenerated by washing with a conventional solvent ethyl alcohol and reused again for the adsorptive removal of NPX.

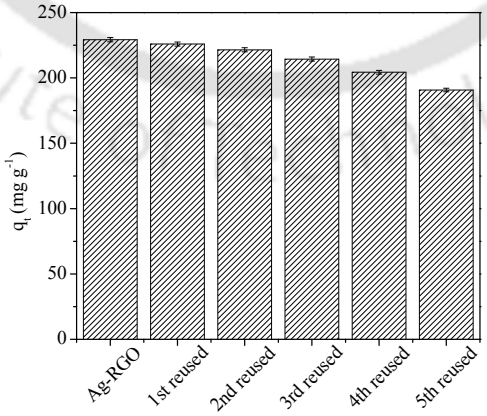

Fig. 6.10. Effect of recycling numbers on the adsorbed amount of NPX over Ag-RGO composite (pH: 4.50, adsorption time: 3 min and initial concentration of NPX: 100 mg dm^{-3}).

As shown in Fig. 6.10, the adsorption capacities of Ag-RGO towards NPX (100 mg dm^{-3}) decreased slightly with the increasing number of recycles. However, the adsorption capacity decreased only 16.78% (38.47 mg dm^{-3}) after the fifth cycle. The regeneration data demonstrated its possible application as a suitable adsorbent in commercial plants.

6.4. Conclusion

This study demonstrated that the newly synthesized Ag-RGO nanocomposite film (following a newly developed green route) provides significant removal efficiency of 92.62% for the NPX anions from their contaminated solutions. The adsorption process was highly dependent on the pH of the initial solution, and the maximum removal capacity of 229.25 mg g^{-1} was obtained at pH 4.50 for the initial NPX concentration of 100 mg dm^{-3} in less than 3 min. Pseudo-second-order kinetic model and Elovich model were best fitted with the experimental data indicating chemical/ion-exchange type of adsorption at the optimum pH value (pH 4.50). The innovative adsorption capacities were well explained by the Freundlich isotherm rather than the Langmuir isotherm, suggesting the multilayer adsorption on the heterogeneous surfaces for the naproxen removal process. The free energy (E) and the required activation energy (B') for the D-R adsorption isotherm holds the highest (E = 11.62 kJ mol^{-1}) and lowest (B' = 0.0037) values at pH 4.50, also confirm the chemical or ion-exchange type of adsorption. The reduced quadratic model under the user-defined discrete design of RSM well explained the parametric optimization results from the experiments. Although the NPX adsorption by Ag-RGO film is encouraging, its mechanism is very complex and not precisely defined. Further studies are required to decide the exact mechanism of the adsorption process that occurred in the reaction medium. Lastly, the Ag-RGO nanocomposite film, having a high NPX adsorption capacity with fast kinetics, suggested a newly synthesized highly efficient adsorbent in the wastewater treatment industries with excellent recyclability.

Chapter 7

Adsorptive Mass Transport in Millimetric Multichannel Device Packed with the Graphene-based Material

The previous study, described in chapter three, revealed the fact that with the increase of flow rate or the introduction of air or the lowering of the cross-section of the channel, the mixing or mass transfer efficiency increases, and the column exhausted faster. However, due to the decrement of the residence time, the total adsorption capacity of the column decreases. Therefore, the lower flow rate and higher cross-sectional area without the introduction of air facilitates the higher adsorption capacity at the expense of some lower efficiency. This chapter seven reports the copper (II) adsorption behavior along with the parametric optimization for the multichannel-based packed adsorption device having a higher cross-sectional area without the introduction of air.

7.1. Introduction

Freshwater is one of the essential natural resources on our planet, and it is in a limited amount. With the ever-increasing population and demand, we need to be more judicious in our usage of fresh water and make sure we leave more than a sufficient amount for our future generations. The quality of water has also deteriorated over the years. Large-scale industries dump their wastewater into the water bodies. Industries like electroplating, battery manufacturing, chemical manufacturing, and metal finishing generate large-amount of wastewater, which have a high concentration of heavy metals. The presence of heavy metals is hazardous to the environment due to their toxicity and bioaccumulation tendency. Heavy metals such as copper can be harmful to human health if it is consumed in moderate to high concentrations. The World Health Organization (WHO) has recommended that the maximum allowable concentration of Cu (II) in drinking water

is 1.5 mg dm^{-3} (Anirudhan et al., 2013). Therefore, the remediation of copper contamination is environmentally and economically advantageous. Adsorption is one of the most important and widely used separation process approved by the industries.

The researchers have studied the adsorption capacities and efficiencies of the various types of adsorbents like activated carbon (Mondal and Majumder, 2019a and 2019b), chitosan (Li and Bai, 2005; Ngah and Fatinathan, 2008), kaolinite (Hizal and Apak, 2006), zeolite (Elwakeel et al., 2018), and silica gel (Wang et al., 2009), etc. for years. Reduced graphene oxide (Zhang et al., 2014; Fu and Huang, 2018) or graphene oxide composite (Kong et al., 2017; Huang et al., 2018) might be a suitable adsorbent due to its high surface area, high adsorption capacity, and affinity towards the metal contaminants. In the present context, amine-functionalized reduced graphene oxide was tested for the adsorptive removal of copper (II), as the functional group amine can form covalent bonds with most of the metals ions, which can increase the adsorption capacity of the adsorbent. As per previous literature, most of the copper (II) adsorption studies were performed in batch mode (Kong et al., 2017; Elwakeel et al., 2018; Huang et al., 2018; Mondal and Majumder, 2019a and 2019b). Though the batch processes are safe and easy to manage, it requires more energy, more cost, and longer time. However, Continuous processes are efficient and cost-effective. With the revolution of the industries, the amount of contaminated effluents increases. Therefore, the continuous mode of operation is essential to attend the recent increasing demand of the industries, which is signified by the application of fixed bed adsorption devices packed with the adsorbent materials (Hessel et al., 2005). The packing materials in a fixed bed intensified the interaction properties, increasing the mass transport or adsorption rate. The continuous operation in a fixed bed device provides higher adsorption capacity than that in the batch adsorption (Barquilha et al., 2017). The design of a particular fixed-bed adsorption device operating in the continuous mode, with its higher removal capacity as well as efficiency using an efficient packing material, for the removal of the metal contaminant is required. The copper (II) (heavy metal contaminant) adsorption studies performed by the various investigators in the fixed bed devices of higher dimensions are shown in Table 7.1. The details about all the models stated in Table 7.1 have been described in Table 7.2. As described in Table 7.1, though the adsorption studies were performed in the continuous mode using different kinds of adsorbent materials, these studies were carried out in the columns of larger dimensions.

Table 7.1. Details of copper adsorption studies performed in the fixed beds.

Adsorbent used	Operational parameters	Influent copper (II) concentration (mg dm^{-3})	Influent volumetric flow rate (ml min^{-1})	Model investigated	Operating pH (-)	Thomas maximum adsorption capacity (mg g^{-1})	Reference
Functionalized SBA-15 mesoporous silica	Flow rate and bed height	31.8 – 317.8	0.4 – 0.8	Thomas and Bed depth service time models	4.5 – 4.8	101.67	Shahbazi et al., 2013
Polyamidoamine							
Chitosan–zeolite composite	Bed height	15.0 – 40.0	0.17	Bed depth service time and Clark model	1.0 – 6.0	25.96	Ngah et al., 2012
Kenaf (Hibiscus cannabinus, L) fibers	Flow rate and bed height	100.0	4.0 – 9.0	Thomas and Bed depth service time models	5.0	47.27	Hasfalina et al., 2012
Surface-modified Eucalyptus globulus seeds	Initial concentration, flow rate and bed height	25.0 – 150.0	5.0 – 25.0	Thomas, Bed depth service time and Yoon-Nelson models	-	300.5	Kumar et al., 2015
Magnetized sawdust (Fe_3O_4–SD)	Initial concentration, flow rate	10.0 – 30.0	15.0 – 25.0	Thomas, Adam-Bohart and Yoon-Nelson models	5.0	31.89	Kapur and Mondal, 2016

	and bed height						
Amino-functionalized ramie stalk	Initial concentration flow rate and bed height	19.1 – 44.5	3.0 -5.0	Thomas, Adam-Bohart, Yoon-Nelson, and Bed depth service time models	5.0	33.55	Wang et al., 2018b
Sugarcane bagasse	Initial concentration, flow rate and bed height	76.95	1.4	Thomas and Adam-Bohart models	6.0	66.85	Xavier et al., 2018
Yersiniabactin, immobilized to XAD16 resin	Flow rate and pH	2.0 – 6.2	10.0 – 30.0	Thomas and Modified dose response models	5.0 – 7.0	7.63	Moscatello et al., 2018
Tetraethylene pentamine-modified sugarcane bagasse	Initial concentration, flow rate and bed height	20.0	6.25	Thomas and Yoon-Nelson Models	5.1	16.52	Chen et al., 2017
Natural and immobilized marine algae Sargassum sp.	Initial concentration, flow rate and bed height	49.25 – 49.63	6.0	Thomas model	5.0	130.90	Barquilha et al., 2017

Sodium hydroxide-modified oil palm frond	Flow rate and bed height	100.0	8.2 – 24.7	Adams-Bohart, Thomas and Yoon-Nelson Models	4.5	13.87	Salamatinia et al., 2008
Dried activated sludge and dried activated nano-sludge	Flow rate and bed height	25.0	2.0 – 6.0	Thomas model	3.0	5.5	Ahmari et al., 2015
Activated charcoal and bone charcoal in 1: 1 ratio	Flow rate and bed height	100.0	10.0 – 30.0	Thomas model, Yoon-Nelson model	-	54.31	Tadepalli et al., 2016
Cedrus deodara sawdust	Flow rate and bed height	93.0	1.8 – 5.3	Bohardt-Adams, Wolborska, Modified dose-response, and Thomas model	-	55.63	Mishra et al., 2013
Modified chitosan hydrogel	Initial concentration, flow rate and bed height	50 - 100	0.2 – 0.4	Adams-Bohart, Thomas and Yoon-Nelson Models	6.0	45.0	Kavianinia et al., 2012
Lignocellulosic wastes	Initial concentration, flow rate	50 - 100	1.0 – 3.0	Adams-Bohart, Thomas and Yoon-Nelson Models	5.5	60.21	Chowdhury et al., 2015

	and bed height						
Sugarcane Bagasse	Initial concentration, flow rate and bed height	18.0	100 - 200	Thomas, Adams-Bohart and Yoon-Nelson models	5.0	3.98	Duga et al., 2016
Activated carbon prepared from nipa palm nut	Initial concentration, flow rate and bed height	50 - 150	5.0 – 10.0	Thomas, and Yoon-Nelson models	7.0	17.22	Nwabanne and Igbokwe, 2012

Table 7.2. Details about all the models investigated previously for the adsorption in the fixed bed.

Model	Equation	Parameters (unit)
Adams-Borhart	$\ln\left(\frac{C_0}{C_t}-1\right)=\frac{K_{AB}N_0 l}{U}-K_{AB}C_0 t$	K_{AB} = Adams-Borhart rate constant (ml mg^{-1} min^{-1}), N_0 = The sorption capacity of the adsorbent per unit volume of the bed (mg ml^{-1}), l = bed length for horizontal channel (m), and U = Actual velocity inside the bed (m min^{-1}).
Thomas	$\frac{C_t}{C_0}=\frac{1}{1+\exp\left[\frac{K_T}{Q}\left(q_0 M-C_0 V_t\right)\right]}$	K_T = Thomas rate constant (ml min^{-1} mg^{-1}), and q_0 = Adsorption capacity of the adsorbent (mg g^{-1}).
	Linearized form:	

	$\ln\left(\frac{C_0}{C_t}-1\right)=\frac{K_T q_0 M}{Q}-\frac{K_T C_0}{Q}V_t$	
Yoon-Nelson	$\ln\left(\frac{C_t}{C_0-C_t}\right)=K_{YN}\left(t-t'\right)$	K_{YN} = Yoon-Nelson model-constant (min^{-1}), and t' = The required time for 50% adsorbate breakthrough (min).
Bed depth service time (BDST)	$t=\frac{N_0}{C_0 U}l-\frac{1}{C_0 K_{BDST}}\ln\left(\frac{C_0}{C_t}-1\right)$	K_{BDST} = Rate constant for Bed depth service time model (ml mg^{-1} min^{-1}), N_0 = The sorption capacity of the adsorbent per unit volume of the bed (mg ml^{-1}), l = bed length for a horizontal channel (m), and U = Actual velocity inside the bed (m min^{-1}).
Dose-Response	$\frac{C_t}{C_0}=1-\frac{1}{1+\left(\frac{C_0 Q}{q_0 M}\right)^a}$	a = Constant (-), and q_0 = Adsorption capacity of the adsorbent (mg g^{-1}).
Clark	$\frac{C_t}{C_0}=\left(\frac{1}{1+Ae^{-rt}}\right)^{\frac{1}{n-1}}$	A & r = The Clark model constants (-), and n = The Freundlich parameter (-).

Moreover, nowadays, the milli- and microchannel-based devices are gaining importance as a simple and inexpensive means of achieving high process efficiency. Due to their reduced sizes, milli- and micro-channels can minimize the imperfections associated with the larger-scale equipment. The transport phenomena can be enhanced by packing the channel with any solid materials efficient for the phase interactions. Though the Micro- and milli-channels have the limitations of high throughput, they are used to enhance the applications which involve surface phenomena (for example, adsorption) as they include the usage of high surface areas for the small amount of volume, treated based on their hydrodynamics and phase mixing. Strong capillary forces differentiate the hydrodynamics between giant- and miniature-packed beds. In the case of the miniature packed beds, the mass transfer resistance is negligible, and the overall mass transfer is mostly coupled with the kinetic studies, provides the additional advantages of the miniature devices. The throughput of the small channel can be increased by increasing the numbers of the parallel channels in a single device. The hydrodynamics and mixing properties, as well as the separation efficiencies, depends on the dimensional variation of the devices. The hydrodynamic behaviors of the larger dimensional devices are different from the devices of the smaller dimensions. Hence, for designing an efficient adsorption device of a smaller dimension, the study of the hydrodynamics and the mixing characteristics inside the device are essential as the mixing efficiency highly affects the other parameters like transport rate, product yield, and selectivity. Moreover, the parallel multichannel devices are more efficient than the series of channels of the same dimension (Kockmann, 2007). The multi-millimetric channels provide the fast mixing effect and the compact transport properties. As a result, it can be used for multiple purposes like heat and mass exchange, mixing, and chemical reactions (Guo et al., 2018).

From the previous literature, few studies on hydrodynamics and RTD are available for the flow-through millimetric packed single channel of cylindrical geometry (Tidonaet al., 2012; Knoblochet al., 2013; Faridkhou and Larachi, 2014), square geometry (Faridkhou and Larachi, 2014; Serres et al., 2018), and the rectangular millimetric multichannel, especially with packing (Losey et al., 2001; Faridkhou et al., 2016), without packing (Guo et al., 2018). However, these studies were not sufficient in the field of hydrodynamics for the flow through the packed miniature devices. As per our knowledge, the packed multichannel-based millimetric devices are used for the chemical reactions that occurred under high pressure, and temperature like the Fischer–Tropsch synthesis

(Knobloch et al., 2013), and hydrogenation reaction (Losey et al., 2001), no adsorption study was executed in such channel geometries. In spite of that, the copper (II) adsorption behavior of the amine-functionalized RGO is also unavailable in the previous studies. There is no particular relationship between the hydrodynamic parameters and the contaminant removal efficiency of the adsorbent materials. In the present study, the hydrodynamics and mixing characteristics for the flow through the packed multichannel bed were studied by the pulse tracer input method. The mixing characteristics depending on the operating variables were addressed based on the available correlations. A new correlation is proposed based on the experimental results to predict the mixing intensity. Secondly, the copper adsorption studies were carried out in the aforementioned packed multichannel-based device. The coated glass beads of diameter $3.0 \times 10^{-4} – 4.0 \times 10^{-4}$ m were used as the packing materials, where RGO-NH_2 acted as the adsorbent. The kinetic mass transfer rate or adsorption rate is also correlated with the hydrodynamic parameters. The present study will provide the readers with an overall idea about the impact of hydrodynamics and mixing on the adsorption phenomena or any kind of transport, which will be helpful for designing the multichannel-based millimetric transport devices.

7.2. Experimentation

7.2.1. Reagents and instrumentation

Hydrogen peroxide (H_2O_2, 30%, M.W. = 34.01 g mol^{-1}), Sulfuric acid (H_2SO_4, 98%, M.W. = 98.08 g mol^{-1}), Nafion® 117 binders (5% in a mixture of lower aliphatic alcohol and water), and Amine functionalized reduced graphene oxide (RGO-NH_2) were purchased from Sigma-Aldrich. Hydrochloric acid (HCl, 37.0%, M.W. = 36.46 g mol^{-1}) and potassium chloride (KCl, 99.5%, M.W.= 74.55 g mol^{-1}) of ACS reagent grade were supplied by Merck Life Science Private Limited. Glass beads of an average diameter (d_p) of 350 µm was purchased from Apex Abrasives Industries, and copper (II) sulfate pentahydrate ($CuSO_4.5H_2O$, 98.5%, M.W. = 249.69 g mol^{-1}) was supplied by HiMedia Laboratories. Field Emission Scanning Electron Microscope (FESEM) (Make: Zeiss, Model: Sigma, Germany) was used to examine the surface morphology of the Piranha cleaned, and RGO-NH_2 coated glass beads. Deionized water from the Milli-Q water purification system (Millipore, MA, USA) was used in the experiment.

The main experimental section consists of a rectangular multichannel (11 channels) block packed with the glass beads. The dimensions of each channel were 2×10^{-3} m width (w) and 1.2×10^{-3} m height (h). The total length (l) of all the channels was 9.7×10^{-1} m, and the average of the total length was considered as the length (l_i) of each channel (8.82×10^{-2}) of the multichannel block. The particle diameter (d_p) is considered as the characteristic length in the case of the packed bed. It was assumed that the flow was equally divided among the channels. A schematic diagram of the experimental setup is shown in Fig. 7.1.

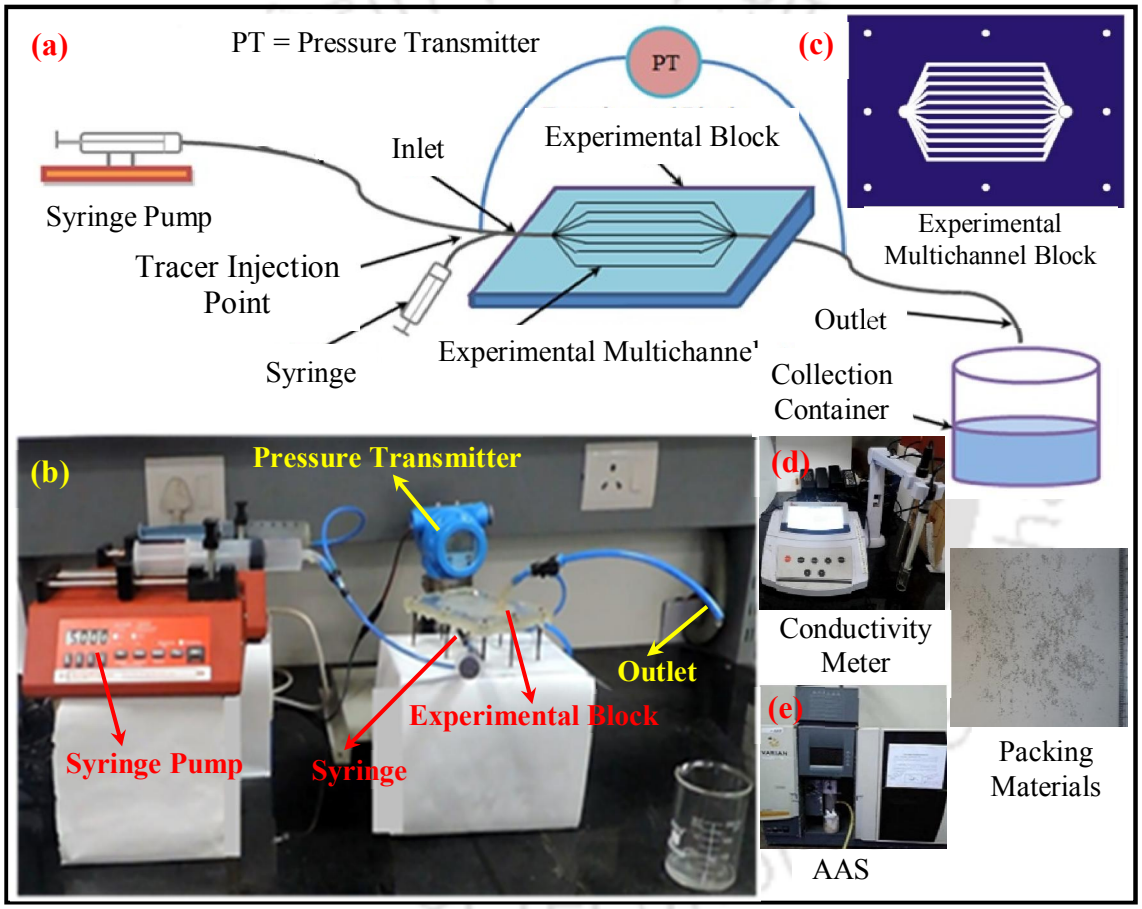

Fig. 7.1. (a) Schematic diagram of the experimental setup (b) Snapshot of the experimental setup, (c) Top view of the experimental multichannel block, (d) Conductivity meter, and (e) AAS instrument.

A syringe pump (supplied by Amar Equipments Pvt. Ltd.) was used to regulate the aqueous volumetric flow rate (with or without copper contaminations) through the channels, and the tracer solution was inserted (pulse input) into the system just before the inlet point through an injection

port. A pre-calibrated differential pressure transmitter (Make: Electronet Equipments Pvt. Ltd., Model: ELPRT100SDP, Accuracy: ± 0.075% of URL for turndown ratio ≤ 10:1) was connected at the inlet and outlet points to measure the pressure drop with respect to the volumetric flow rates of the fluid. An electrical conductivity meter (Model: VSI-04 ATC Deluxe, VSI Electronics Pvt. Ltd., India) was used to measure the conductivities of the collected samples to determine the tracer concentrations. A hot air oven (Model: Digital, Make: SoNuu, India) was used for the drying of the coated glass beads. Atomic Absorption Spectrophotometer (AAS) (Model: Spectra AA 220FS, Make: Varian) was used to measure the copper concentration (with the help of concentration versus absorbance calibration) during the experimentation. All the experiments were performed at room temperature (298 K).

7.2.2. Experimental methods

7.2.2.1. Piranha Cleaning

The glass beads were cleaned by the Piranha solution so that the coating can be stabilized on the etched beads for a longer time. The Piranha solution was made by mixing 30% H_2O_2 and 98% H_2SO_4 in a 1:3 ratio. The glass beads were dipped into the Piranha solution and were kept for an hour. Thereafter, the glass beads rinsed with deionized water several times to wash away all the acid. Then the glass beads were dried in the oven at 333 K for a day. The FESEM images of the Piranha cleaned, and the RGO-NH_2 coated glass beads are shown in Fig. 7.2. Piranha solution, a mixture of sulfuric acid (H_2SO_4) and hydrogen peroxide (H_2O_2), is a strong oxidizing agent. Therefore, it can remove most of the organic matters by etching, increasing the surface roughness (Jradi et al., 2011), and it can also hydroxylate most of the surfaces (adding -OH groups) (Ismail, 2016), making them highly hydrophilic in nature. Due to the increase of roughness (rough surface is visible in Fig. 7.2(b)), functionality, and the hydrophilicity, the stability of the coated materials on the Piranha cleaned surface increases (Jradi et al., 2011).

7.2.2.2. Mixing studies (Residence Time Distribution, RTD)

Firstly, the packed channel (packed with uncoated glass beads) was filled with the fresh Milli-Q water so that the air inside the channel is removed. Then the syringe pump was started, and the 0.5 ml of 1 M KCl solution as a tracer was injected just before the inlet of the packed bed by the pulse input method. The stopwatch was started immediately with the pulse input, and the samples were

collected at the outlet with the same time intervals. The conductivities (S m^{-1}) of the collected samples were measured to estimate the concentrations of the tracer solution at the outlet point with respect to time. At the same time, the differential pressures (minimum 20 readings) were noted down, and the average of the readings was considered as the actual pressure difference between the inlet and outlet points. The same processes were repeated by varying the flow rates of the fluid.

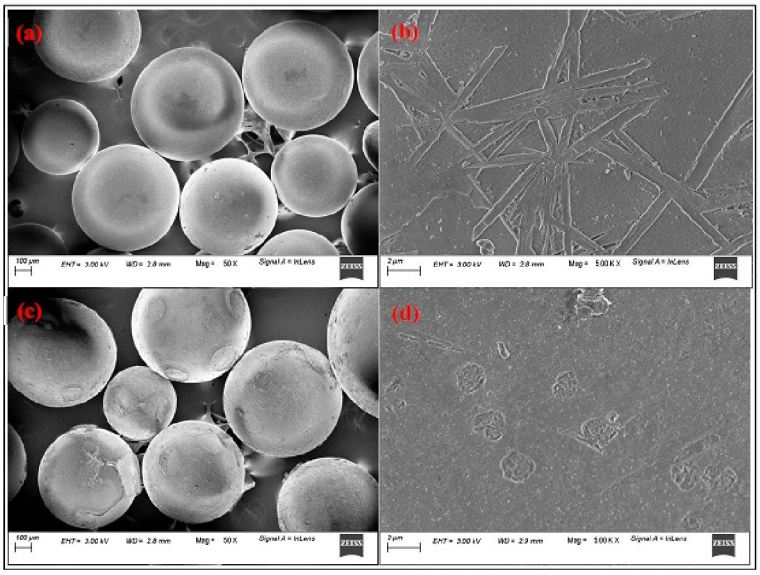

Fig. 7.2. FESEM image of the glass beads, (a-b) Piranha cleaned, and (c-d) RGO-NH_2 coated.

7.2.2.3. Coating of glass beads

The glass beads were coated with RGO-NH_2 with the help of the Nafion binder. A mixture of 50 mg RGO- NH_2 and 10 ml Nafion (5%) was sonicated for an hour. After the sonication, the glass beads were added into the prepared colloidal solution and kept in the hot oven (at 313 K) to dry for 24 hours. When the glass beads were completely dried, it was packed inside the bed, and the device becomes ready for the adsorption study. After each individual adsorption study, the exhausted packing materials were removed, and the device was packed by the new live one.

7.2.2.4. Procedure to perform the adsorption studies

Copper solutions of different concentrations (2.5 mg dm^{-3}, 5 mg dm^{-3} and 10 mg dm^{-3}) were passed through the packed bed (packed with the coated glass beads) at different flow rates (2 ml min^{-1}, 5 ml min^{-1}, 10 ml min^{-1} and 15 ml min^{-1}) using a syringe pump. The bed was packed with a constant

amount of adsorbent, 4.231 mg (estimated by subtracting the weight of uncoated glass beads from the coated one used for the packing). The pressure differences at different flow rates were recorded by a differential pressure transmitter, fitted with its two terminals at the two ends of the bed. After switched on the syringe pump, the samples were collected from the outlet at an equal interval of time. The concentration of the Cu(II) ions in the outlet samples (C_t) were determined by the calibrated AAS instrument. All the adsorption experiments were performed at a normal pH range of 5.40 - 5.45, which held after the preparation of the copper solutions.

7.3. Theoretical background

7.3.1. Pressure drop analysis

The pressure drop analysis was done according to section 3.3.1. The properties of the multichannel device, packing materials, and the flowing fluid through the channel of higher cross-sectional area (multichannel block – 2) as shown in Table 3.1.

7.3.2. Residence Time Distribution (RTD) analysis

7.3.2.1. Moment analysis and the axial dispersion model

The moment analysis and the axial dispersion model were demonstrated according to section 3.3.2.1 in Chapter 3.

7.3.2.2. Velocity distribution model

The analysis of the velocity distribution model was analyzed in section 3.3.2.2 in Chapter 3.

7.3.3. Specific energy dissipation and the mixing performance in the multichannel packed bed

The specific energy dissipation (E_d) and the mixing performance in the multichannel packed bed device were estimated in a similar way, as shown in section 3.3.3 in Chapter 3.

7.3.4. Adsorption study

The total treated volume of the fluid (V_{eff}, ml) for the adsorption is calculated by using the Eq. (7.1) (Kapur and Mondal, 2016; Tsai et al., 2016).

$$V_{eff} = Qt_t \tag{7.1}$$

where t_t (min) is the total time of flow. The quantity of the total contaminant adsorbed ($q_t^{'}$, mg) is calculated by

$$q_t^{'} = \frac{Q}{1000}\int_{t=0}^{t=t_t} C_{ad}\,dt = \frac{Q}{1000}\sum_{t=0}^{t=t_t}(C_0 - C_t)dt \tag{7.2}$$

where C_0 and C_t are the inlet solute concentration (mg dm^{-3}) and the solute concentration in the effluent (mg dm^{-3}), respectively. C_{ad} (mg dm^{-3}) is the quantity adsorbed at time t_t. Q is the volumetric flow rate of the fluid (ml min^{-1}). The total quantity of copper (II) fed to the packed bed (m_t, mg) can be estimated by following Eq. (7.3) (Kapur and Mondal, 2016; Tsai et al., 2016).

$$m_t = \frac{C_0 Q t_t}{1000} \tag{7.3}$$

The total removal percentage ($\%R$) of the soluble contaminant is calculated as

$$\%R = \left(\frac{q_t}{m_t}\right)\times 100 \tag{7.4}$$

The error percentages ($\%E$) between the experimental (q_{exp}) and the calculated (q_{cal}) values are determined by

$$\%E = \frac{\left|q_{\exp} - q_{cal}\right|}{q_{\exp}}\times 100 \tag{7.5}$$

where q_{exp} and q_{cal} are the adsorption capacities obtained from the experiment, and from the model equation, respectively.

7.3.4.1. Modeling of adsorption in channels

Thomas and Yoon-Nelson models are extensively used to investigate the adsorption kinetics in the packed bed (Salamatinia et al., 2008; Kumar et al., 2015; Wang et al., 2018b). The present study was concentrated to find out the best-suited model for the adsorption occurred, which can explain the adsorption kinetics, the characteristics of the breakthrough curves, and finally can estimate the adsorption capacity of the channel-based packed bed device for the removal of Cu (II).

7.3.4.1.1. Thomas model

The Thomas Model is very effective in the estimation of the adsorption capacity and the parameters of the kinetic model for continuous flow through the packed bed. The expression given by Thomas for the analysis of the performance of a packed bed is (Thomas, 1944; Baek et al., 2007)

$$\frac{C_t}{C_0} = \frac{1}{1+\exp\left[\frac{K_T}{Q}\left(q_0 M_a - C_0 V_t\right)\right]} \tag{7.6}$$

The linearized form of the Thomas model is as follows

$$\ln\left(\frac{C_0}{C_t}-1\right) = \frac{K_T q_0 M_a}{Q} - \frac{K_T C_0}{Q} V_t \tag{7.7}$$

where M_a is the total mass of the adsorbent (g), V_t is the volume of fluid passed at time t. q_0 is the total adsorption capacity of the adsorbent (mg g^{-1}), and K_T is the Thomas rate constant (dm^3 min^{-1} mg^{-1}).

7.3.4.1.2. Yoon-Nelson model

This model does not control by the physical properties of the adsorption bed, characteristics of the adsorbate, and the nature of the adsorbent materials. The linearized form of the Yoon-Nelson model is represented by (Yoon and Nelson, 1984)

$$\ln\left(\frac{C_t}{C_0 - C_t}\right) = K_{YN}\left(t - t'\right) \tag{7.8}$$

where the Yoon-Nelson model-constant, the sampling time, and the required time for 50% adsorbate breakthrough are denoted by K_{YN} (min^{-1}), t (min), and t' (min), respectively. The values of K_{YN} and t' are estimated from the intercept and slope of the $\ln[C_t/(C_0 - C_t)]$ versus time (t) plot.

7.4. Results and discussion

7.4.1. Mixing characteristics

7.4.1.1. Effect of volumetric flow rate on RTD curves and axial dispersion model (ADM)

At the lower flow rate, the RTD curves become broader, which corresponds to the higher mean residence time (t_m) (Fig. 7.3). The Peclet number, one of the most important axial dispersion model

parameters, which generally reflects the degree of mixing, increases with the increase in flow rate or Reynolds number (Fig. 7.4(a)). The Peclet number is significant to measure the relative extent of the advection versus diffusion, where a larger number indicates an advection dominated distribution, and a smaller number indicates a diffusive flow. Almost in all the cases of the packed bed, the same trend of increasing Peclet number with the increasing flow rate was obtained (Chung and Wen, 1968; Yuan et al., 2004; Zhang et al., 2016; Rastegar and Gu, 2017; Sharma et al., 2017). At the low velocities, when the Peclet number holds the lower value, the diffusive process dominates. In that case, the dispersion coefficient is proportional to the ratio of the diffusion coefficient and the tortuosity (τ). At the higher velocities of the fluid, when the Peclet number is higher ($Pe_a > 10$), the dispersion by the advection will dominate (Zhang et al., 2016). The inversion of the Peclet number (Pe_a) is called the channel dispersion number. The RTD curves become broader with the higher values of the channel dispersion number, as shown in Fig. 7.3 (Rossi et al., 2017). As per the present experiment, the lowest flow rate (1.0 ml min^{-1}) corresponds to the highest dispersion number (1.11 (-)) for the single channel, and the values varied from 0.51 (23.0 ml min^{-1}) to 1.11. The axial dispersion coefficients were calculated from the RTD curves.

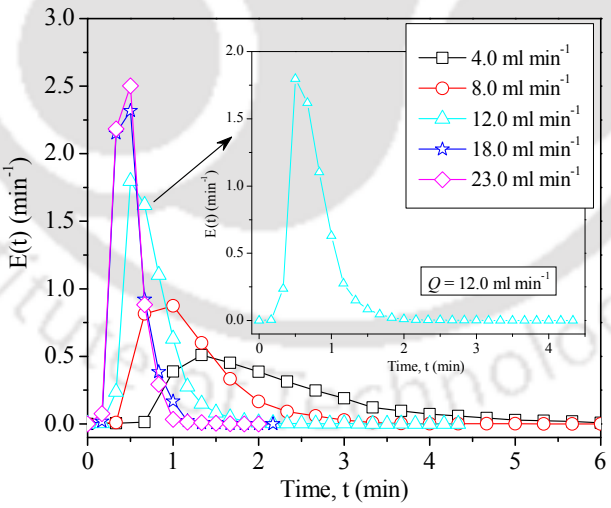

Fig. 7.3. The RTD curves at different flow rates (the inset figure is the broad view of the RTD curve at the flow rate of 12.0 ml min^{-1}).

A higher liquid flow rate resulted in the higher axial dispersion coefficient, as shown in Fig. 7.4(b), where the Peclet number and the axial dispersion coefficient have been calculated by using the Eq.

(3.11) and Eq. (3.10), respectively. With the increasing volumetric flow rate, the rate of specific energy dissipation increases, which results in higher axial dispersion, as shown in Fig. 7.5(a). In the present case, the specific energy dissipation (E_d) values were $<10^2$ W kg^{-1} ($10^{-2} < E_d < 10^{-1}$); hence, the mixing processes were affected by the molecular diffusion with the various flow rates of fluid (Su et al., 2016).

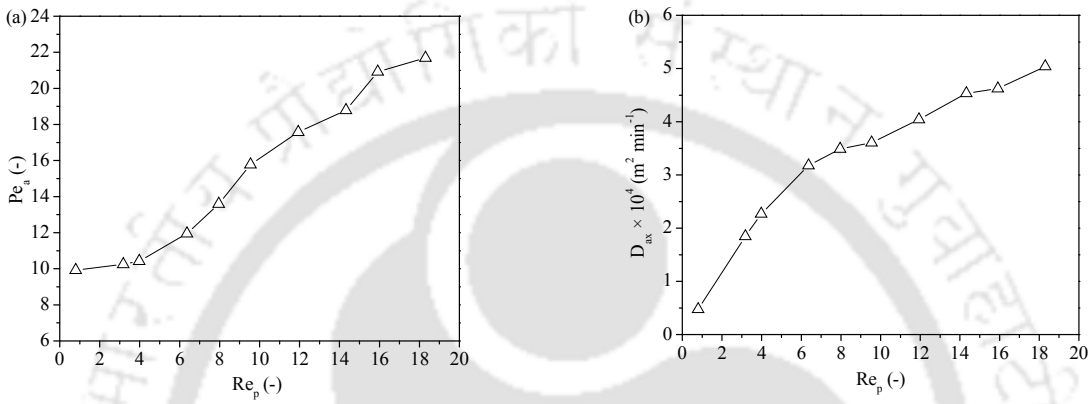

Fig. 7.4. Variation of the (a) Peclet number, and (b) axial dispersion coefficient with respect to the Reynolds number.

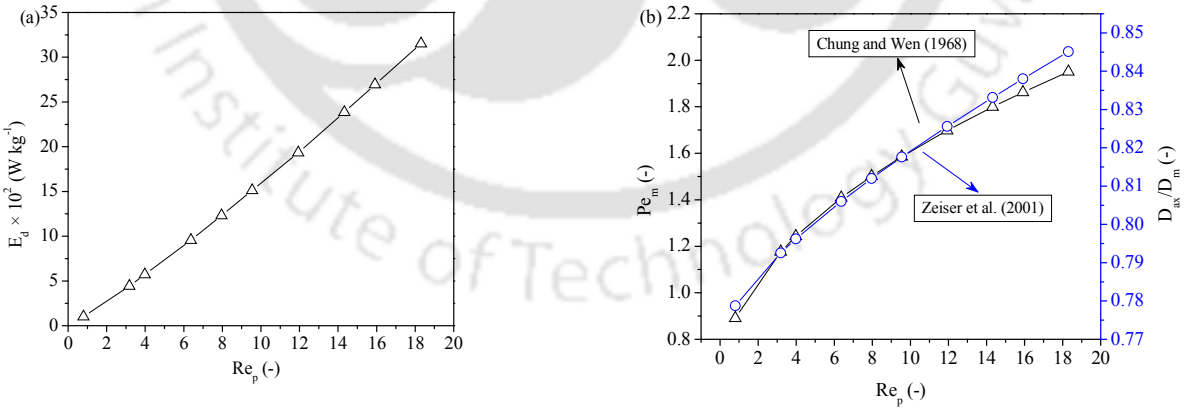

Fig. 7.5. Variation of the (a) Rate of specific energy dissipation, and (b) the D_{ax}/D_m ratio with respect to the Reynolds number.

D_{ax}/D_m ratio increases with the increasing Reynolds number indicates the fact that the axial dispersion coefficient dominates over the diffusion coefficient at higher velocities (Fig. 7.5(b)).

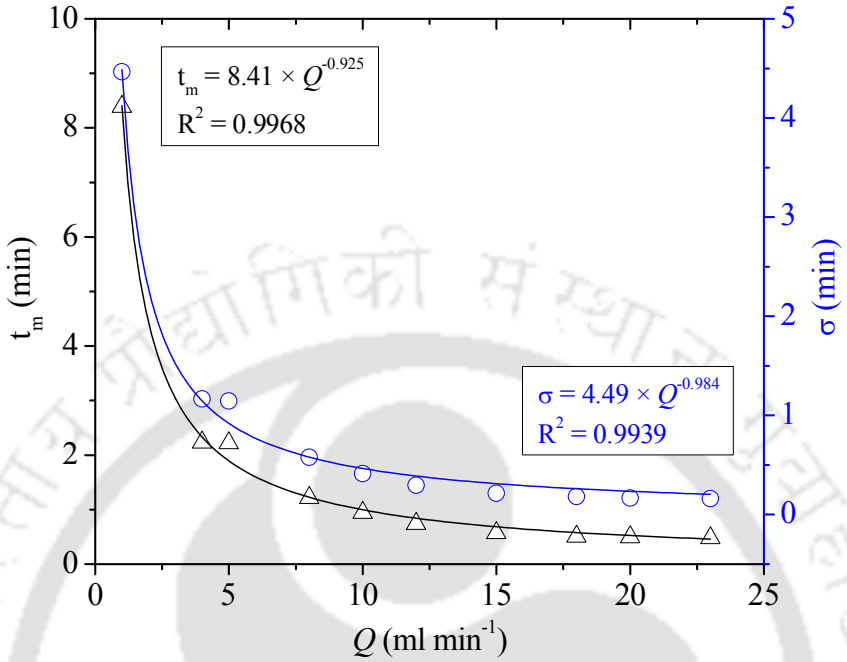

Fig. 7.6. Variation of the mean residence time (t_m), and the variance (σ) of RTD with respect to the volumetric flow rate.

When the flow rate increases, the Reynolds number increases, giving the tracer molecules less time to pass the device (Fig. 7.6). With the increasing liquid flow rate, the retention time in the device decreases, which decreases the overall mass transport. The RTD parameters, Reynolds number, pressure drop, and the specific energy dissipation for the individual channel are shown in Table 7.3.

7.4.1.2. Effect of pressure drop on mixing characteristics

Pressure drop is one of the most important factors to estimate the performance of a millichannel-based packed bed. Pressure drop is depleted into the energy input required for the process of mixing. Pressure drop for the continuous flows through the packed systems depends on the particle Reynolds number (Re_p) and increases with the increase of the aforementioned dimensionless number. The Reynolds number increases with the increasing flow velocity and the decrease of the Fanning friction factor (f'). The pressure drop is dependent on the Reynolds number, which increases with the increase of the volumetric flow rate, is shown in Fig. 7.7.

In the present context, the mixing efficiencies of the multichannel-based device are explained in terms of breakthrough curves in the context of their volumetric flow rate as well as pressure drops.

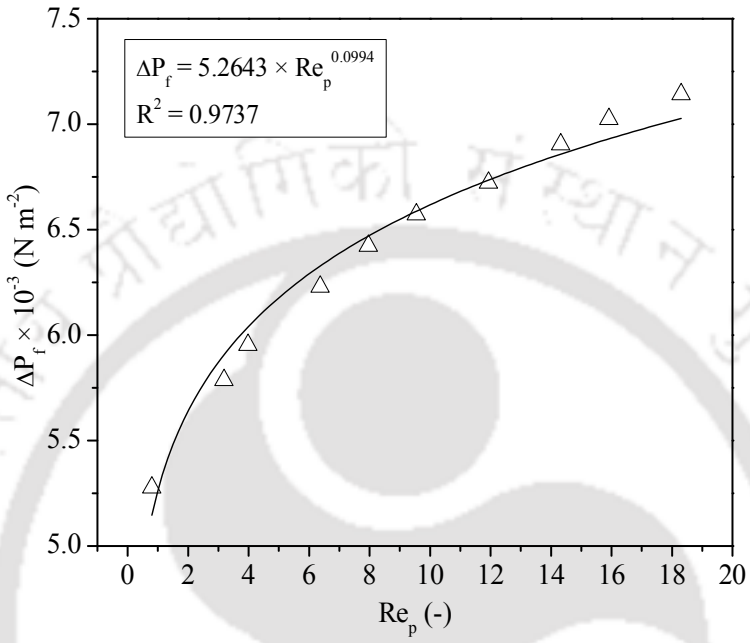

Fig. 7.7. Pressure drop variation with respect to the Reynolds number.

Table 7.3. Mean residence time, Particle Reynolds number, and the coefficient of axial dispersion D_{ax} in the multichannel based packed bed device for different flow rates with a KCl of 1 mole dm^{-3} solution (T = 298 K).

Total volumetric flow rate, Q (ml min^{-1})	**Velocity through an individual channel, U_i (m min^{-1})**	**Mean residence time, t_m (min)**	**Total pressure drop, ΔP_f (N m^{-2})**	**Particle Reynolds number for an individual channel, Re_p (-)**	**σ_θ^2 (-)**	**Axial Peclet number of the multichannel packed bed, Pe_a (-)**	**Axial dispersion coefficient for an individual channel, D_{ax} (m^2 min^{-1})**	**Specific energy dissipation for the individual channel, E_d (W kg^{-1})**
1.0	3.79×10^{-2}	8.4	5.28×10^{3}	0.80	2.83×10^{-1}	9.91	4.77×10^{-5}	1.01×10^{-2}
4.0	1.52×10^{-1}	2.23	5.79×10^{3}	3.18	2.72×10^{-1}	10.23	1.85×10^{-4}	4.44×10^{-2}
5.0	1.90×10^{-1}	2.22	5.95×10^{3}	3.98	2.66×10^{-1}	10.41	2.27×10^{-4}	5.71×10^{-2}
8.0	3.03×10^{-1}	1.22	6.23×10^{3}	6.37	2.24×10^{-1}	11.90	3.18×10^{-4}	9.56×10^{-2}
10.0	3.79×10^{-1}	0.95	6.42×10^{3}	7.96	1.91×10^{-1}	13.54	3.49×10^{-4}	1.23×10^{-1}
12.0	4.55×10^{-1}	0.74	6.57×10^{3}	9.55	1.60×10^{-1}	15.72	3.61×10^{-4}	1.51×10^{-1}
15.0	5.68×10^{-1}	0.57	6.72×10^{3}	11.94	1.40×10^{-1}	17.53	4.04×10^{-4}	1.93×10^{-1}
18.0	6.84×10^{-1}	0.51	6.91×10^{3}	14.32	1.29×10^{-1}	18.76	4.53×10^{-4}	2.38×10^{-1}
20.0	7.56×10^{-1}	0.50	7.03×10^{3}	15.91	1.14×10^{-1}	10.90	4.62×10^{-4}	2.70×10^{-1}
23.0	8.70×10^{-1}	0.48	7.14×10^{3}	18.30	1.10×10^{-1}	21.56	5.04×10^{-4}	3.15×10^{-1}

7.4.1.3. Generation of correlation between the axial dispersion coefficient and the molecular diffusion coefficient

The axial dispersion coefficient is a function of different operating variables such as the actual velocity (U), density (ρ), viscosity (μ) of the fluid, the hydraulic diameter (d_H) of the individual channel, and the particle diameter (d_p) of the packing material, etc. The dimensional analysis yields the following relation

$$\frac{D_{ax}}{d_p\left(U/\varepsilon_{eff}\right)} = f\left(\frac{d_H}{d_p}, \frac{1}{\mathrm{Re}_p}, \frac{1}{We_p}, \frac{D_m}{d_p\left(U/\varepsilon_{eff}\right)}\right) \tag{7.9}$$

Multiple regression analysis was done to generate the correlation of the axial dispersion coefficient with the molecular diffusion coefficient, which can be expressed as

$$D_{ax}/D_m = 1.18(\mathrm{Re}_p \times Ca_p)^{0.064} = 1.18 \times We_p^{0.064} \tag{7.10}$$

The correlation coefficient and the standard error of the Eq. (7.10) was found to be 0.97, and 0.05, respectively (The theory for the calculation of the correlation coefficient and standard error with ANOVA is given in Appendix – I). The proposed correlation is valid within the range of operating variables: $0.80 < Re_p < 18.30$, $1.85 \times 10^{-5} < We_p < 9.77 \times 10^{-3}$.

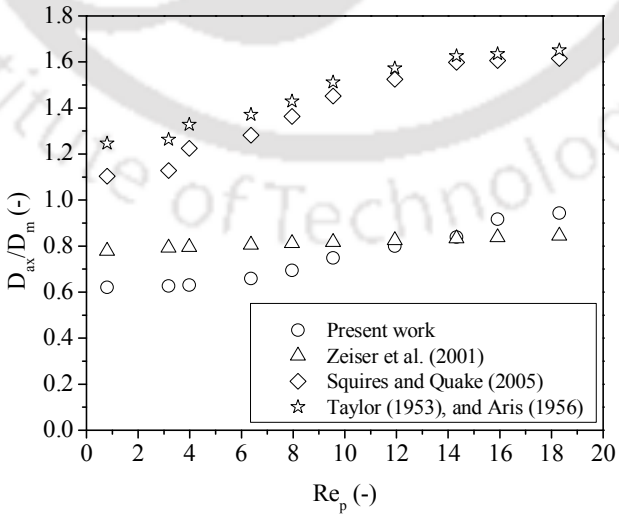

Fig. 7.8. Variation of the (D_{ax}/D_m) ratios with respect to the Reynolds number.

The D_{ax}/D_m values obtained in the present context are compared with the values obtained from the various correlations of Taylor (1953), and Aris (1956) (Eq. (3.14)); Squires and Quake (2005), and Ajdari et al. (2006) (Eq. (3.15)); and Zeiser et al. 2001 (Eq. (3.20)), and shown in Fig. 7.8. The present proposed correlation satisfied the experimental data with a maximum error of 5.0%. When the experimental results were compared with the available correlations, the correlation suggested by Zeiser et al. (2001), closely resembled the experimental data with the maximum error of 25% (Fig. 7.8).

7.4.2. Results of the adsorption studies

7.4.2.1. Breakthrough curves (BTCs)

The variation of concentration of Cu (II) ions with respect to time for different flow rates and initial levels of concentrations is called the breakthrough curve. The breakthrough curves are essential for determining the adsorption capacity and efficiency of the adsorbent material in the packed bed at the breakthrough point, as well as at the exhaustion point (the point where the vacant sites of the adsorbent saturated by the adsorbate molecules). At first, during the startup, the effluent remains free from the contaminant, which becomes available in the effluent after the breakthrough point. At the exhaustion point, the concentration of the contaminant in the influent and effluent becomes same. The points where the ratios of the effluent to influent concentrations of the contaminant reached 0.1 were considered as the breakthrough points, and when it reached to 0.95, those were considered as the exhaustion points in the present experiment. Longer the breakthrough time (t_b) indicates higher efficiency of the adsorbent material packed in the channel in removing the desired contaminant. That is, the removal capacity of the packed material is high, and it will function for a longer time without regeneration/replacement. Such materials, device geometry, and operating conditions are always convenient in surface adsorption technology, especially for water treatment technology.

7.4.2.2. Effect of flow rate on the breakthrough curve

Influent flow rate is one of the most important factors for the determination of the effectiveness of the adsorbents in the continuous flow fixed-bed adsorption device. The effect of the influent flow rate for the adsorptive removal of Cu (II) on the RGO-NH_2 coated glass beads was studied by changing the influent flow rates (2, 5, 10, and 15 ml min^{-1}) for a fixed initial concentration of the

contaminant. Fig. 7.9 shows the plot of normalized Cu (II) concentration (C_t/C_0) and time (t) at the varying flow rates. The similar types of variations were observed for the different influent concentrations (2.5 mg dm^{-3} (Fig. 7.9(a)), 5.0 mg dm^{-3} (Fig. 7.9(b)), and 10.0 mg dm^{-3} (Fig. 7.9(c))). At the higher flow rate, the breakthrough point appeared readily, and for a fixed concentration, the saturation point of bed reached faster for the flow rate of 15.0 ml min^{-1} and reached slower for the flow rate of 2.0 ml min^{-1}. As the velocity increased for 2.0 ml min^{-1} to 15.0 ml min^{-1} at the copper concentration of 2.50 mg dm^{-3}, the Cu (II) molecules eluted faster, and the time of breakthrough decreased from 48 to 5 min (Table 7.4). The essential BTC parameters are tabulated in Table 7.4. The speed of the adsorption zone increased at the higher flow rates, and the time required to achieve the breakthrough concentration was lower as compared to that at the lower flow rate (Fig. 7.9).

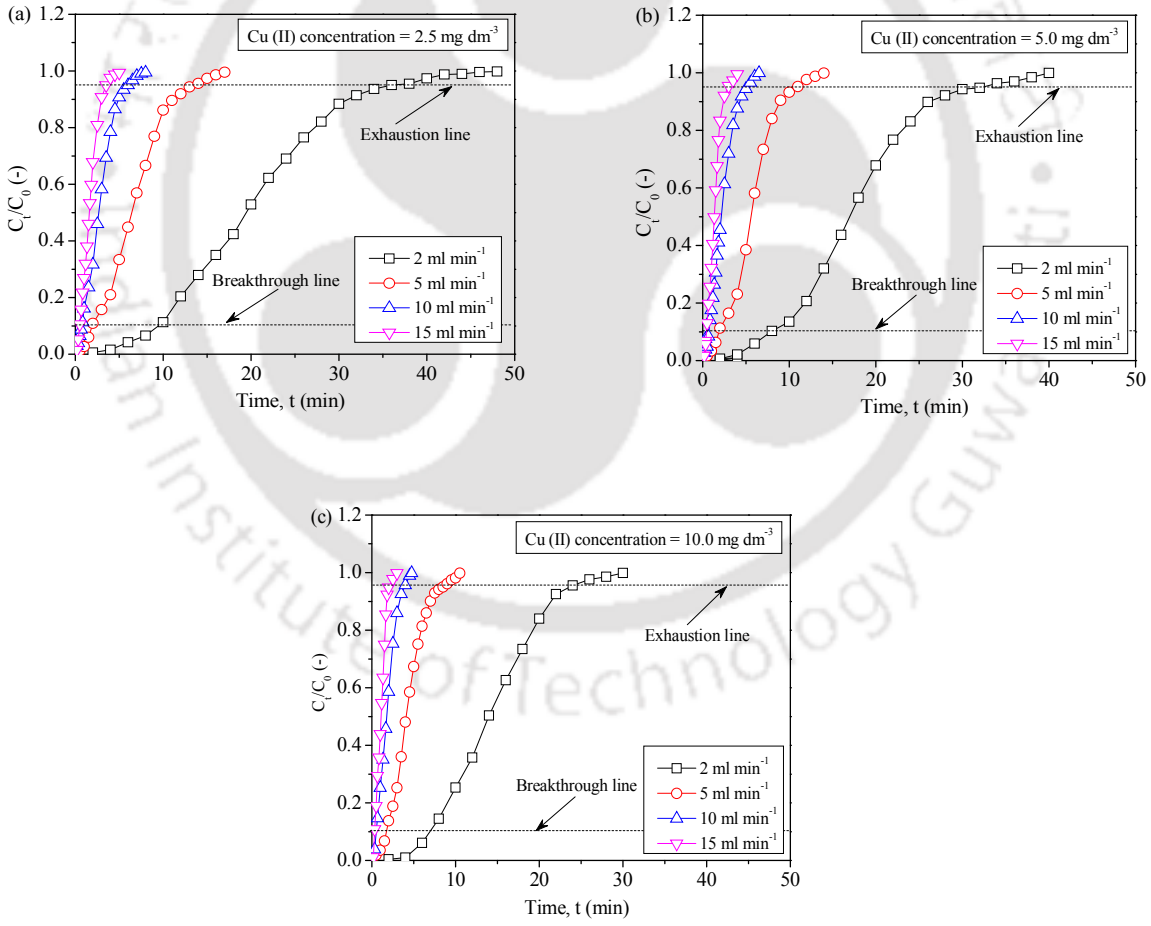

Fig. 7.9. Breakthrough curves for the Cu(II) solution at the different flow rates of (a) 2.5 mg dm^{-3}, (b) 5.0 mg dm^{-3} and, (c) 10.0 mg dm^{-3}.

From Table 7.4, it is clear that the Cu(II) removal percentage, as well as the adsorption capacity, decreased with the increasing flow rate. The mass transfer rate increased with the increasing velocity, which magnified the rate of adsorption. Hence, at the higher flow rate, the early breakthrough point was observed. At the higher flow rates, the residence time or the contact time of the adsorbate molecules in the packed bed was lower, so the intra-particle diffusion phenomena between the adsorbate and the adsorbent molecules did not accomplish properly. Therefore, the total adsorption capacity decreased, and the equilibrium was not achieved.

Table 7.4. Estimated parameters from the breakthrough curves for the adsorption of Cu (II) on the RGO-NH_2 coated glass beads at different influent flow rates and concentrations.

Q (ml min^{-1})	Concentration (mg dm^{-3})	t_b (min)	V_{eff} (ml)	t_t (min)	m_t (mg)	q_t (mg)	% R
2.0	2.5	9.53	96.0	48.00	0.240	0.095	39.58
2.0	5.0	7.93	80.0	40.00	0.404	0.166	41.04
2.0	10.0	7.00	60.0	30.00	0.606	0.268	44.15
5.0	2.5	1.98	85.0	17.00	0.212	0.078	36.54
5.0	5.0	1.86	70.0	14.00	0.354	0.131	37.15
5.0	10.0	1.73	52.5	10.50	0.530	0.205	38.75
10.0	2.5	0.78	80.0	8.00	0.200	0.065	32.31
10.0	5.0	0.72	65.0	6.50	0.328	0.109	33.18
10.0	10.0	0.53	47.5	4.75	0.478	0.166	34.67
15.0	2.5	0.48	75.0	5.00	0.187	0.058	31.15
15.0	5.0	0.43	60.0	4.00	0.303	0.098	32.19
15.0	10.0	0.33	45.0	3.00	0.454	0.152	33.43

It was the evidence of the fact that the saturation time increases with the decrease in flow rate. It is due to the combined effect of the higher residence time, along with the availability of the higher number of contaminant molecules for a particular concentration. When the bed acquired a higher value of exhaustion point, longer time required to saturate the adsorbent inside the bed, eventually larger volume of inflow passed, increasing the availability of a higher number of adsorbate molecules though the concentration was fixed. Hence, lower flow rates, as well as the lower

concentrations of the contaminant, are desirable for the feasible operation of packed bed adsorption devices for its better efficiency, capacity, and durability.

From Table 7.4, it was clear that compared to the other flow rate intervals, %R differs significantly when the flow rate was increased from 2.0 – 5.0 ml min^{-1}. It is probably due to the disappearance of the dead zones. According to Guo et al. (2018), it was assumed that the flow is equally divided into the individual channels. However, practically it did not happen. According to Menon et al. (2019), in the case of the packed bed, when the flow rate increases, the dead zone decreases, increasing the active region. From the experimental results, it is evident that in the present case of the millimetric multichannel system, most of the dead zones are converted to the active zone for the changes of flow rate from 2.0 – 5.0 ml min^{-1}. Therefore, the deviation in %R was maximum in that case.

7.4.2.3. Effect of initial concentration on the breakthrough curve

The adsorption experiment was conducted with different concentrations of Cu (II) ions: 2.5 mg dm^{-3}, 5.0 mg dm^{-3}, and 10.0 mg dm^{-3}. The typical variations of the breakthrough curves depending on the initial concentrations of the contaminant are shown in Fig. 7.10.

For a fixed flow rate (2.0 ml min^{-1} (Fig. 7.10(a)), 5.0 ml min^{-1} (Fig. 7.10(b)), 10.0 ml min^{-1} (Fig. 7.10(c)), and 15.0 ml min^{-1} (Fig. 7.10(d))), it was observed that the saturation point of the bed was reached earliest for the 10.0 mg dm^{-3} solution, and reached latest for the 2.5 mg dm^{-3} solution. Therefore, the saturation time decreases with an increase in initial concentration as with the increasing concentration, the number of contaminant molecules increases in a particular volume. The higher number of contaminant molecules occupied the vacant sites of the adsorbent readily. However, with the increment of influent concentration, due to the higher concentration gradient, the mass transfer rate and the adsorption capacity increases for a particular flow rate. As shown in Table 7.4, the highest adsorption capacity was obtained at a lower flow rate (2.0 ml min^{-1}), and higher influent concentration (10.0 mg dm^{-3}). Therefore, though the lower concentration is suitable for longer operation times, a higher concentration is preferable to achieve an elevated adsorption capacity.

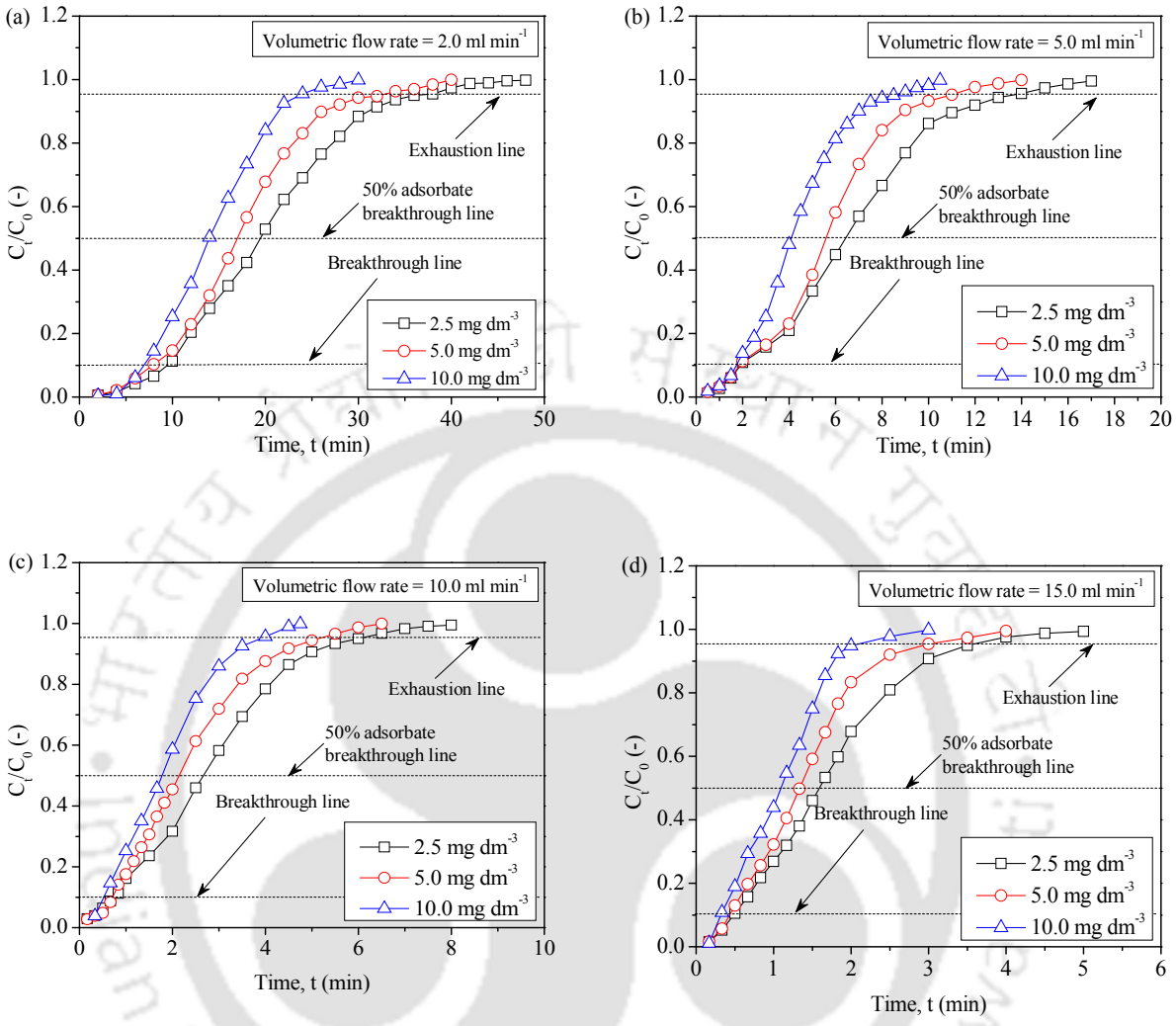

Fig. 7.10. Breakthrough curves for the Cu(II) solution at the different influent concentration of: (a) 2.0 ml min^{-1}, (b) 5.0 ml min^{-1}, (c) 10.0 ml min^{-1}, and (d) 15.0 ml min^{-1} Cu (II) solution at different influent concentrations.

7.4.3. Dynamic modeling of adsorption in channel-based packed bed device

7.4.3.1. Thomas model for the adsorption study

According to the Thomas model, the effect of influent concentration on the adsorption capacity is shown in Fig. 7.11. The stiffness of the straight line increases with the increase of concentration at a particular flow rate, which signifies the decrease of the K_T values with the increase of the adsorption capacity due to the availability of the more number of adsorbate molecules. The lowest K_T value (Thomas model parameter) and highest adsorption capacity (q_0) were obtained for the

influent concentration of 10.0 mg dm^{-3} at a 2 ml min^{-1} flow rate are 0.035 dm^3 min^{-1} mg^{-1}, and 61.91 mg g^{-1}, respectively. The Thomas model parameters are shown in Table 7.5.

From Table 7.5, it is clear that when the influent concentration is increased, the K_T values were found to decrease, and the adsorption capacity increased for a particular flow rate due to the presence of a sufficient concentration gradient. The opposite trend was followed for the increasing flow rate at a particular concentration due to the shorter residence time. The calculated adsorption capacity values from the Thomas model satisfied the experimental data with higher correlation coefficients of 0.96 to 0.99, and the percentage errors of 12 – 15%. From the analysis, it is obvious that the adsorption process does not follow the second-order rate equation properly, as per one of the assumptions of the Thomas model.

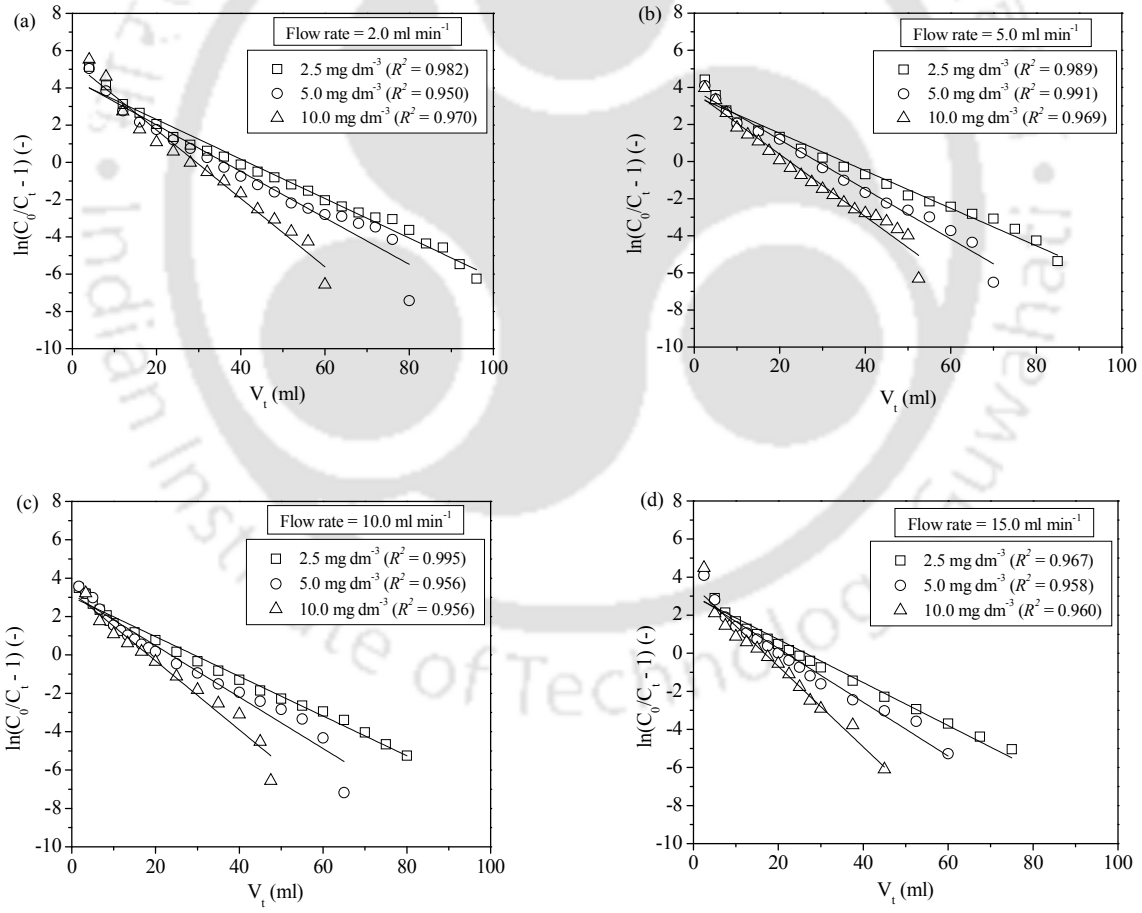

Fig. 7.11. Thomas model plot for the concentration variation at the constant flow rate, (a) 2 ml min^{-1}, (b) 5.0 ml min^{-1}, (c) 10.0 ml min^{-1}, and (d) 15.0 ml min^{-1}.

Table 7.5. Thomas kinetic model constants at the different experimental conditions.

Flow rates of fluid (ml min^{-1})	Initial Cu (II) concentrations (mg dm^{-3})	K_T (dm^3 mg^{-1} min^{-1})	q_0 (mg g^{-1}) - experimental	q_0 (mg g^{-1}) - calculated	R^2	%E
2.0	2.5	0.085	21.94	24.64	0.98	12.30
2.0	5.0	0.049	38.39	43.19	0.95	12.48
2.0	10.0	0.035	61.91	71.19	0.97	15.00
5.0	2.5	0.202	17.96	20.73	0.99	15.42
5.0	5.0	0.132	30.41	34.42	0.99	13.19
5.0	10.0	0.083	47.54	53.30	0.97	12.11
10.0	2.5	0.414	14.95	17.25	0.99	15.41
10.0	5.0	0.265	25.22	28.20	0.96	11.82
10.0	10.0	0.178	38.48	43.65	0.96	13.43
15.0	2.5	0.679	13.51	15.59	0.97	15.40
15.0	5.0	0.420	22.59	26.02	0.96	15.22
15.0	10.0	0.314	35.16	39.97	0.96	13.68

The efficiency of the millimetric multichannel device compared to the conventional copper adsorption columns available in the literature, in terms of the Thomas rate constant values, are tabulated in Table 7.6.

Table 7.6. Copper (II) adsorption efficiencies of the columns in terms of Thomas rate constant (K_T).

Column dimensions	Largest K_T value (dm^3 min^{-1} mg^{-1})	Reference
Borosilicate glass column (I.D. = 1.8 cm, and length = 76 cm)	2.57×10^{-4}	Tsai et al., 2016
Circular column (length = 75.5 cm)	1.28×10^{-2}	Mishra et al., 2013
Cylindrical column (I.D. = 4cm, and total height of the column =100 cm)	2.68×10^{-5}	Tadepalli et al., 2016

A glass column (I.D. = 1 cm, and height = 30 cm)	1.30×10^{-7}	Kavianinia et al., 2012
Pyrex glass column (I.D. = 4.5 cm, and height = 30 cm)	4.30×10^{-7}	Chowdhury et al., 2015
Cylindrical column (I.D. = 5 cm, and height = 30 cm)	3.61×10^{-5}	Duga et al., 2016
A glass adsorption column (I.D. = 30 mm, and length = 300 mm)	1.67×10^{-4}	Nwabanne and Igbokwe, 2012
Jacketed stainless steel column (I.D. = 2.8 cm, and height = 50 cm)	3.00×10^{-2}	Barquilha et al., 2017
Laboratory-scale glass column (I.D. = 0.6 cm, and length 12 cm)	2.50×10^{-5}	Shahbazi et al., 2013
PVC column (I.D. = 10 cm, and height = 70 cm)	7.38×10^{-5}	Hasfalina et al., 2012
A glass column (I.D. = 3 cm, and height = 40 cm)	2.96×10^{-3}	Kumar et al., 2015
A glass column (I.D. = 1.1 cm, and height = 15 cm)	9.62×10^{-6}	Wang et al., 2018b
Bio-Rad chromatography columns (2.5 × 10, 5 × 30, and 5 × 50 cm)	8.01×10^{-3}	Moscatello et al., 2018
Perspex up-flow column (I.D. = 45.0 mm, and height = 110.0 mm)	3.58×10^{-3}	Salamatinia et al., 2008
A glass tube (I.D. = 2/5 cm, and length = 50 cm)	7.05×10^{-6}	Ahmari et al., 2015
A jacket glass column (I.D. = 1.0 cm, and length = 10.0 cm)	1.29×10^{-3}	Xavier et al., 2018
A glass column (I.D. = 2.54 cm, and length = 30 cm)	2.60×10^{-3}	Kapur and Mondal, 2016
Rectangular millimetric multichannel device	6.79×10^{-1}	Present work

*N.B.: I.D. = Internal diameter.

In the present case, the most significant rate constant value is quite higher (6.79×10^{-1} dm^3 min^{-1} mg^{-1}), than the conventional columns, where the values laid within the range of 4.30×10^{-7} to 1.28×10^{-2} dm^3 min^{-1} mg^{-1}, represented the higher efficiency of the experimental multichannel device (Mishra et al., 2013; Chowdhury et al., 2015).

7.4.3.2. Yoon-Nelson model

Yoon-Nelson model is a simple theoretical model to examine the behavior of the breakthrough curves of the adsorption processes. Yoon –Nelson model constants (K_{YN}) for the various flow rates and concentrations are obtained from the slope of the straight line of $ln[C_t/(C_0 - C_t)]$ vs. t, which are shown in Fig. 7.12 and tabulated in Table 7.7.

Table 7.7. Yoon-Nelson kinetic model constants at different experimental conditions.

Flow rates of fluid (ml min^{-1})	**Initial Cu (II) concentrations (mg dm^{-3})**	***K_{YN}* (min^{-1})**	***t'* (min) - experimental**	***t'* (min) - calculated**	***R^2***	***%E***
2.0	2.5	0.212	19.33	20.85	0.98	7.83
2.0	5.0	0.233	16.93	18.42	0.97	8.78
2.0	10.0	0.352	13.87	14.91	0.97	7.53
5.0	2.5	0.505	6.46	7.02	0.98	8.60
5.0	5.0	0.669	5.59	5.76	0.98	3.09
5.0	10.0	0.839	4.10	4.47	0.97	9.04
10.0	2.5	1.034	2.68	2.92	0.99	9.15
10.0	5.0	1.341	2.15	2.36	0.96	10.00
10.0	10.0	1.799	1.77	1.83	0.96	3.14
15.0	2.5	1.696	1.60	1.76	0.97	10.21
15.0	5.0	2.120	1.33	1.45	0.96	9.42
15.0	10.0	3.174	1.08	1.12	0.96	3.01

It can be noticed that the model equation fulfilled the experimental data satisfactorily with the higher regression coefficient of > 0.96. The percentage errors between the experimental and predicted *t′* (the time required for the 50% breakthrough) values lie within the range of 3.0 – 10.0%, which proves the better match of the model compared to the Thomas model.

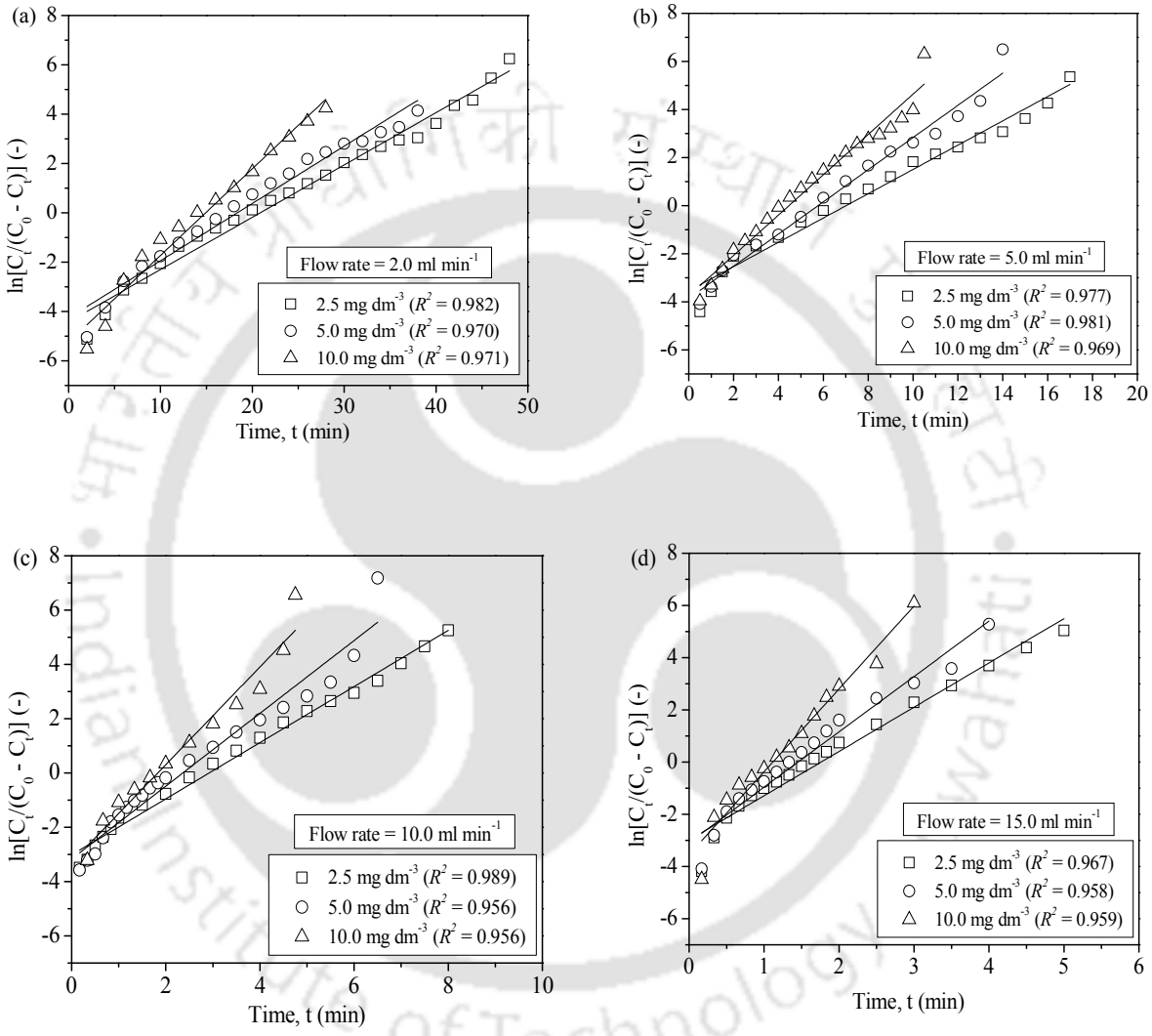

Fig. 7.12. Yoon-Nelson model plot at the flow rate: (a) 2 ml min^{-1}, (b) 5.0 ml min^{-1}, (c) 10.0 ml min^{-1}, and (d) 15.0 ml min^{-1}.

From Table 7.7, it is clear that with the increase of both the flow rate and Cu(II) concentration, the K_{YN} value increased, whereas the *t′* value decreased. At the higher concentration, the Cu(II)

molecules raised competition to occupy the vacant sites on the surface of the adsorbent, which resulted in a higher adsorption rate.

7.4.3.3. The effect of the Peclet number and the Damköhler number on the kinetic mass transfer rate (adsorption rate)

The recovery percentages by adsorption as a function of the Peclet number and the Damköhler number can be expressed as (Levenspiel, 1999)

$$\%R = \frac{4a_e \exp\left(Pe_a/2\right)}{(1+a_e)^2 \exp(Pe_a a_e/2) - (1-a_e)^2 \exp(-Pe_a a_e/2)} \times 100 \qquad (7.11)$$

where

$$a_e = \sqrt{1+4(Da/Pe_a)} \qquad (7.12)$$

where Da is the Damköhler number, a dimensionless number, which is expressed as the ratio of the adsorption rate to the diffusive mass transfer rate, and thus quantifies the effect of convection-diffusion on the overall adsorption process. The Damköhler number (Da) for the n^{th}-order reaction can be represented as

$$Da = K_r C_0^{n-1} t_t \qquad (7.13)$$

where K_r is the kinetic mass transfer rate (rate of adsorption). As the Thomas model satisfied the experimental adsorption data with 12-15% error, the adsorption process was not recommended to follow the second-order kinetic model properly, and the axial dispersion was also encountered effectively. In general, adsorption is a complex multistep process, and the kinetic studies provide valuable insights into the sorption mechanisms, which include mass transfer, diffusion, and surface phenomenon. However, in reality, the kinetic models are not enough to describe the complex adsorption processes. Putting the values of n = 1 (for the first-order reaction), and the other experimental data in the above Eq. (7.13), the K_r (min^{-1}) values for different flow conditions are calculated and tabulated in Table 7.8. According to Tadepalli1 and Murthy (2017), during the column adsorption studies of copper (II), the mass transfer coefficients hold the values in the order of 10^{-12} for the variable flow rate and bed height. However, Losey et al. (2001) reported the average reaction rate in the range of 10^{-4} – 10^{-3} for the cyclohexane hydrogenation reaction in the microfabricated multiphase packed-bed reactors. In that point of view, the experimental

millimetric multichannel packed-bed device was efficient enough, having the kinetic mass transfer rate in the range of 10^{-2} – 10^{-1}, as shown in Table 7.8.

Table 7.8. Calculated K_r values at various flow conditions.

Flow rates of fluid (ml min^{-1})	Initial Cu (II) concentrations (mg dm^{-3})	$a_{e\,(-)}$	Pe_a (-)	$\%R$ (-) - calculated	Da (-)	K_r (min^{-1})
2.0	2.5	1.183	10.08	39.52	1.007	2.10×10^{-2}
2.0	5.0	1.180	10.08	40.14	0.989	2.47×10^{-2}
2.0	10.0	1.164	10.08	41.01	0.894	2.98×10^{-2}
5.0	2.5	1.192	10.41	36.54	1.095	6.44×10^{-2}
5.0	5.0	1.189	10.41	37.15	1.077	7.69×10^{-2}
5.0	10.0	1.181	10.41	38.75	1.027	9.78×10^{-2}
10.0	2.5	1.166	13.54	32.31	1.217	1.52×10^{-1}
10.0	5.0	1.162	13.54	33.18	1.186	1.82×10^{-1}
10.0	10.0	1.155	13.54	34.67	1.131	2.38×10^{-1}
15.0	2.5	1.132	17.53	31.15	1.233	2.47×10^{-1}
15.0	5.0	1.129	17.53	32.19	1.204	3.01×10^{-1}
15.0	10.0	1.124	17.53	33.43	1.154	3.85×10^{-1}

when $Da < 1$, the diffusion rate is higher than the adsorption rate and reaches equilibrium earlier as in case of influent flow rate 2 ml min^{-1}. The adsorption rate is greater than the diffusion rate for $Da > 1$, and the distribution is diffusion-limited as like the situation encountered by the influent flow rate of 5 ml min^{-1} to 15 ml min^{-1} (Table 7.8). Therefore, the limiting phenomena change with the changes in the volumetric flow rate of the influent. If the Peclet number is considered constant for a particular flow rate, then with the increase of concentration total operation time of the device and the Damköhler number decreases, but the kinetic adsorption rate increases due to the presence of higher concentration gradient as shown in Table 7.8. The adsorption rate also increases with the increase of flow rate as well as the Peclet number due to the availability of the greater number of adsorbate molecules within less time interval, but the total adsorption capacity decreases due to the less operation time of the device. A multistage regression analysis was done to predict the

correlation of *%R* as a function of Peclet number (Pe_a) and the Damköhler number (Da), which is expressed as

$$\%R = 4.95\times10^{01}\left(Pe_a\right)^{-0.096}\left(Da\right)^{-0.858} \qquad (7.14)$$

The values estimated by the Eq. (7.14) satisfied the experimental data within 0.68% deviation. The correlation coefficient and the standard error were 0.99 and 0.006, respectively, within the operating ranges of $10.08 < Pe < 17.53$, and $0.89 < Da < 1.23$.

7.4.4. Regeneration of the adsorptive multichannel based fixed-bed device

The multichannel-based packed bed device was regenerated by passing 0.05 M hydrochloric acid (HCl) solution at the flow rate of 5.0 ml min^{-1} for 60 min. It is known that with the increase of HCl concentration in the solution, the regeneration efficiency increases, but the higher acidic condition may peel off the coating from the surface of the glass beads. Hence, such a lower acidic medium was used in the present case. The recycling process was repeated for at least five times, and it was reused again for the adsorption study at a flow rate of 2.0 ml min^{-1} with the influent concentration of 10.0 mg dm^{-3}. It was observed that the adsorption capacities of the regenerated adsorbent were decreased by only 5.45% after five times regeneration, as shown in Fig. 7.13.

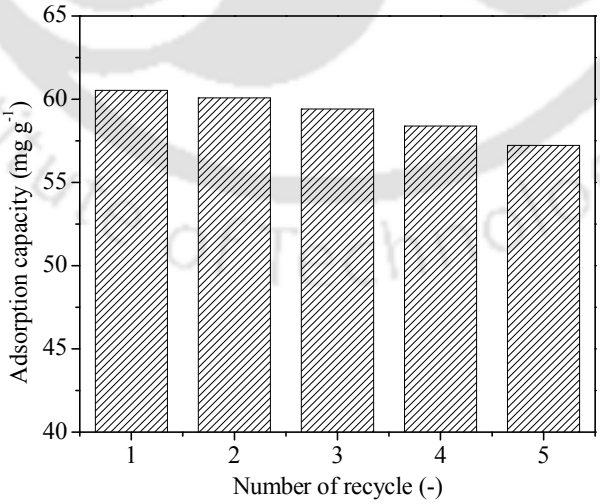

Fig. 7.13. Recycling of the adsorbent material.

Therefore, the multichannel-based packed bed device (packed by the RGO-NH_2 coated glass beads) showed excellent adsorption efficiency as well as the regeneration efficiency.

7.5. Conclusion

With the variation of volumetric flow rates from 1.0 to 23.0 ml min^{-1}, the Peclet number varies from 9.91 to 21.56. The increase in the volumetric flow rate increases the frictional pressure drop. As the Reynolds number increases, the specific energy dissipation rate and the D_{ax}/D_m ratio increases, which indicates that at the higher velocity, the axial dispersion coefficient is dominating over the diffusion coefficient. The higher-pressure drop corresponds to the higher mixing efficiency for the packed bed, providing the required energy input to the mixing process. The proposed correlation for the ratio of axial dispersion and molecular diffusion coefficient satisfied the experimental data within a $\pm$ 5.0% error. From the adsorption studies, it can be concluded that with the increase of velocity, the mass transfer coefficient increases, but due to the less residence time, the adsorption capacity decreases. Both the mass transfer coefficient and the adsorption capacity increases with the increase in influent concentration due to the increase of the concentration gradient. However, from the perspective of the bed, the operational view, higher concentration saturates the device earlier, and the regeneration requires in a short time. Hence, the packed bed should be operated at a lower flow rate and lower concentration to get the performance for a longer time. In the present case, the optimum condition was 2.0 ml min^{-1} flow rate and 10.0 mg dm^{-3} concentration with respect to operational time and capacity. The RGO-NH_2 showed sufficient adsorption capacity towards the copper ions concerning the other RGO composites available in the literature. Both the Thomas and Yoon-Nelson models satisfied the experimental data within a 15.0% error. The newly developed correlation for the *%R* met the experimental data within 0.68% deviation. The packed bed was regenerated well with the decrement of the adsorption capacity of 5.45% after five recycle. From the overall analysis, it can be concluded that the millimetric multichannel packed bed device, as well as the RGO-NH_2 may be used for the adsorptive removal of copper (II) contaminant to fulfill the increasing demand of the society.

Chapter 8

Overall Conclusions and Recommendations

This chapter summarizes the overall conclusions drawn from the previously discussed chapters and provides the recommendations for further work.

8.1. Overall conclusions

- The present work has been tried to fabricate a millichannel-based transport device, provided with a higher efficiency towards the transport processes. In this concern, the different millimetric geometries were considered. The hydrodynamics inside the devices were studied, as the transport processes depend on the flow behavior inside the geometries. The geometries are used in the heat transfer and extractive mass transfer applications. The millimetric geometry was then packed with the synthesized graphene-based material, and utilized as an effective and efficient adsorptive mass transport device. Hence, this study contains a vast field from material synthesis to its applications in the separation or water purification processes in millichannel-based devices.
- In the case of the multiphase flows through the packed geometries of identical dimensions, the serpentine packed channels provide better mixing characteristics over the straight channels at the expense of higher frictional pressure loss, due to the initiation of the Dean flow creating greater turbulence. The pressure drop values increases from 5.86×10^5 N m^{-3} to the 9.64×10^5 N m^{-3}, for the multiphase flow through the serpentine geometry at the same volumetric flow rates of the fluids.
- At the higher Reynolds number value ($Re_{m,p} = 455$), due to the effect of Dean flow (curvature effect), the Nusselt number value was found to be higher for the packed serpentine channel ($Nu_{m,p}$ = 18.73) compared to the straight channel geometry ($Nu_{m,p}$ = 16.18). Moreover, at a particular Nusselt number value ($Nu_{m,p}$ = 18), the

local entropy generation rate was lower in case of the serpentine channel ($ds' = 23.66 \times 10^2$ W K^{-1} m^{-1}) over the straight channel ($ds' = 25.15 \times 10^2$ W K^{-1} m^{-1}). The serpentine packed channel geometry is more efficient than the straight channel with respect to the heat transfer between the phases providing higher Nusselt number and the lower entropy generation.

- The performance study of the packed and unpacked serpentine channel reveals that the extraction efficiency of the packed channel is higher (85-99%) than the unpacked channel (80-91%). The overall volumetric mass transfer coefficient values (K_La) were 8.33×10^{-3} s^{-1}, and 8.37×10^{-3} s^{-1} for the unpacked and packed serpentine millichannels, respectively, at the same residence time of 120 s.
- The graphene-based nanocomposite materials are efficient enough with respect to the adsorption capacity associated with their faster kinetics. The Ag-RGO nanocomposite showed the maximum naproxen removal capacity of 229.25 mg g^{-1} at pH 4.50 for the initial NPX concentration of 100 mg dm^{-3} in less than 3 min (NPX removal efficiency was 92.62%).
- From the copper (II) adsorption studies, performed in a millimetric multichannel-based packed bed device under the continuous mode, it is clear that with the increase of velocity, the mass transfer coefficient increases, but the overall adsorption capacity decreases due to the decrease in residence time. Both the mass transfer coefficient and the adsorption capacity increases for the higher influent concentration because of an increased concentration gradient. However, the higher concentration saturates the device earlier, and the regeneration requires in a short time. Hence, the packed bed devices should be operated at a lower flow rate and lower concentration to get the performance for a longer time.
- The millichannel-based packed bed devices may be used in heat and mass transport applications, where high efficiency and precession are required. The millchannel-based fixed-bed devices may also be applicable in a highly reactive environment where high heat and pressure are generated.

8.2. Recommendations for further work

The probable recommendations for future research in the prescribed field can be summarized as

- All the contaminated samples were synthetic (laboratory-made); hence the synthesized materials and the device can be used for the real industrial effluents where the interferences are present, which will cause the changes of the results.
- The mass or heat transport performances for the serpentine channels were higher than the straight channel geometries. However, the differences between their performances were negligible. The acceptable differences may be achieved by changing the curvature ratios and the number of bending in the near future.
- The experimental data obtained from the fluid flow operations can be compared with the results of the CFD simulations.
- The metal ion extractants are mainly the LIX and Cyanex group of chemicals, which are costly. The new cheap extractant with better extraction efficiency and better recovery during stripping can be synthesized by applying the retrosynthetic analysis techniques.
- The synthesized adsorbent material was not selective for a particular contaminant. The selective nature can be provided, either by changing the surface properties or by making the surface functionality with the specific groups.
- In the continuous mode of operation, RGO-NH_2 was used as the adsorbent material, which is a costlier one. The synthesis of cheap adsorbent provided with the highly charged surfaces may solve this economic issue.
- The multichannel-based packed bed device was operable for a very short period. Hence, the new design is required so that it can be operated for a longer time.

References

Aamrani, F.Z.E., Kumar, A., Cortina, J.L., Sastre, A.M., 1999. Solvent extraction of copper(II) from chloride media using N-(thiocarbamoyl)-benzamidine and N-benzoylthiourea derivatives. Anal. Chim. Acta 382, 205-213.

Abbaszadegan, A., Ghahramani, Y., Gholami, A., Hemmateenejad, B., Dorostkar, S., Nabavizadeh, M., Sharghi, H., 2014. The effect of charge at the surface of silver nanoparticles on antimicrobial activity against gram-positive and gram-negative bacteria: A preliminary study. J. Nanomater. 2015, 1-8.

Abdelall, F.F., Hahn, G., Ghiaasiaan, S.M., Abdel-Khalik, S.I., Jeter, S.S., Yoda, M., Sadowski, D.L., 2005. Pressure drop caused by abrupt flow area changes in small channels. Exp. Therm. Fluid Sci. 29, 425-434.

Afonso-Olivares, C., Fernández-Rodríguez, C., Ojeda-González, R.J., Sosa-Ferrera, Z., Santana-Rodríguez, J.J., Doña Rodríguez, J.M., 2016. Estimation of kinetic parameters and UV doses necessary to remove twenty-three pharmaceuticals from pre-treated urban wastewater by UV/H_2O_2. J. Photochem. Photobiol. A 329, 130-138.

Agarwal, S., Ferreira, A.E., Santos, S.M.C., Reis, M.T.A., Ismael, M.R.C., Correia, M.J.N., Carvalho, J.M.R., 2010. Separation and recovery of copper from zinc leach liquor by solvent extraction using Acorga M5640. Int. J. Miner. Process. 97, 85-91.

Ahmari, Z., Khosravi, M., Niazi, A., 2015. Removal of Cu(II) from aqueous solutions using dried activated sludge and dried activated nano-sludge: adsorption on a fixed-bed column. Orient. J. Chem. 31, 933-938.

Ajdari, A., Bontoux, N., Stone, H.A., 2006. Hydrodynamic dispersion in shallow microchannels: the effect of cross-sectional shape. Anal. Chem. 78, 387-392.

Alguacil, F.J., Cobo, A., 1999. Solvent extraction with LIX 973N for the selective separation of copper and nickel. J. Chem. Technol. Biotechnol. 74 (5), 467-471.

Allen, K.G., Backström, T.W.V., Kröger, D.G., 2013. Packed bed pressure drop dependence on particle shape, size distribution, packing arrangement and roughness. Powder Technol. 246, 590–600.

Aminian, H., Bazin, C., 2000. Technical note solvent extraction equilibria in copper(II)-iron(III)-LIX984 system. Miner. Eng. 13 (6), 667-672.

Anirudhan, T.S., Jalajamony, S., Sreeku-mari, S.S., 2013. Adsorptive removal of Cu(II) ions from aqueous media onto 4-ethyl thiosemicarbazide intercalated organophilic calcined hydrotalcite. J. Chem. Eng. Data 58, 24-31.

Apul, O.G., Wang, Q., Zhou, Y., Karanfil, T., 2013. Adsorption of aromatic organic contaminants by graphene nanosheets: comparison with carbon nanotubes and activated carbon. Water Res. 47, 1648-1654.

Aris, R., 1956. On the dispersion of a solute in a fluid flowing through a tube. Proc. Roy. Soc. A: Math. Phys. Eng. Sci. 235, 67–77.

Atmakidis, T., Kenig, E.Y., 2015. Numerical analysis of residence time distribution in packed bed reactors with irregular particle arrangements. Chem. Prod. Process Model 10, 17–26.

Avila, H.E.R., Castillo, D.I.M., Petriciolet, A.B., Albero, J.S., 2015. Assessment of naproxen adsorption on bone char in aqueous solutions using batch and fixed-bed processes. J. Mol. Liq. 209, 187-195.

Aydin, H., Bulut, Y., Yerlikaya, C., 2008. Removal of Copper (II) from aqueous solution by adsorption onto low-cost adsorbents. J. Environ. Manage. 87, 37-45.

Baccar, R., Sarra, M., Bouzid, J., Feki, M., Blanquez, P., 2012. Removal of pharmaceutical compounds by activated carbon prepared from agricultural by-product. Chem. Eng. J. 211-212, 310-317.

Baek, K., Song, S., Kang, S., Rhee, Y., Lee, C., Lee, B., Hudson, S., Hwang, T., 2007. Adsorption kinetics of boron by anion exchange resin in packed column bed. J. Ind. Eng. Chem. 13, 452-456.

Bakker, G., 1928. Handbuch d. Experimentalphysik. Vol. 6, Akademisohe Verlags-Gesellschaft, Leipzig.

Barquilha, C.E.R., Cossich, E.S., Tavares, C.R.G., Silva, E.A., 2017. Bio-sorption of nickel(II) and copper(II) ions in batch and fixed-bed columns by free and immobilized marine algae Sargassum sp. J. Clean. Prod. 150, 58–64.

Bastus, N.G., Merkoci, **F.,** Piella, J., Puntes, V., 2014. Synthesis of highly monodisperse citrate stabilized silver nanoparticles of up to 200 nm: kinetic control and catalytic properties. Chem. Mater. 26, 2836-2846.

Beek, J., 1962. Design of packed catalytic reactors. Adv. Chem. Eng. 3, 203–271.

Begum, S., Ahmaruzzaman, M., 2018. Biogenic synthesis of SnO2/activated carbon nanocomposite and its application as photocatalyst in the degradation of naproxen. Appl. Surf. Sci. 449, 780–789.

Bejan, A., 2001. Thermodynamic optimization of geometry in engineering flow systems. Energy Int. J. 4, 269–77.

Belkhouche, N.-E., Didi, M.A., Villemin, D., 2005. Separation of Nickel and Copper by Solvent extraction using di-2 ethylhexylphosphoric acid-based synergistic mixture. Solvent Extr. Ion Exch. 23, 677-693.

Benmansour, A., Hamdan, M.A., Bengeuddach, A., 2006. Experimental and numerical investigation of solid particles thermal energy storage unit. Appl. Therm. Eng. 26, 513–518.

Bhatti, M.S., Shah, K., 1987. Handbook of Single-Phase Convective Heat Transfer. John Wiley and Sons, New York.

Bhunia, S.K., Jana, N.R., 2014. Reduced graphene oxide-silver nanoparticle composite as visible light photocatalyst for degradation of colorless endocrine disruptors. ACS Appl. Mater. Interfaces 6, 20085-20092.

Bidari, E., Irannejad, M., Gharabaghi, M., 2013. Solvent extraction recovery and separation of cadmium and copper from sulphate solution. J. Environ. Chem. Eng. 1, 1269-1274.

Bigui, W., Jianlin, L., Gang, W., Qing, C., 2018. Filtration of oil from oily wastewater via hydrophobic modified quartz sand filter medium. J. Water Reuse Desal. 8, 544-552.

Bird, R.B., Stewart, W.E., Lightfoot, E.N., 1960. Transport Phenomena. 1st Ed., John Wiley and Sons Inc., New York.

Biswas, R.K., Singha, H.P., 2007. Solvent extraction of Cu (II) by purified cyanex 272. Indian J. Chem. 14, 269-275.

Blasius, P.R.H., 1913. The similarity law in the case of reimbursement in fluids. Research Issue 131, pp. 1- 41.

Blázquez, G., Martín-Lara, M.A., Tenorio, G., Calero, M., 2011. Batch biosorption of lead(II) from aqueous solutions by olive tree pruning waste: Equilibrium, kinetics and thermodynamic study. Chem. Eng. J. 168, 170–177.

Bo, Z., Shua, X., Mao, S., Yang, H., Qian, J., Chen, J., et al. 2014. Green preparation of reduced graphene oxide for sensing and energy storage applications. Sci. Rep. 4, 4684.

Bouhamed, F., Elouear, Z., Bouzid, J., 2012. Adsorptive removal of Copper(II) from aqueous solutions on activated carbon prepared from tunisian date stones: equilibrium, kinetics and thermodynamics. J. Taiwan Inst. Chem. E. 43, 741-749.

Bouhamed, F., Elouear, Z., Bouzid, J., Ouddane, B., 2016. Multi-component adsorption of copper, nickel and zinc from aqueous solutions onto activated carbon prepared from date stones. Environ. Sci. Pollut. Res. 23, 15801-15806.

Bouvier, C., Cote, G., Sobczynska, A., Bogacki, M.B., Szymanowski, J., 1998. Interfacial behavior of Acorga CLX-50 and surface kinetics of copper extraction. J. Radioanal. Nucl. Chem. 228 (1-2), 63-69.

Boyd, G., Zhang, S., Grim, D., 2005. Naproxen removal from water by chlorination and biofilm processes. Water Res. 39, 668–676.

Brauer, H., 1971. Grundlagen der Einphasen –und Mehrphasenströmungen. Sauerländer AG, Aarau.

Carman, P.C., 1937. Fluid flow through granular beds. Trans. Am. Inst. Chem. E. 15, 150–166.

Çarpinlioğlu, M.Ö., Özahi, E., 2008. A simplified correlation for fixed bed pressure drop. Powder Technol. 187, 94–101.

Carter, S.P., Freiser, H., 1980. Kinetics and mechanism of the extraction of copper with 2-hydroxy-5-nonylbenzophenone oxime. Anal. Chem. 52, 511-514.

Cavallini, D.D., Col, L., Doretti, M., Matkovic, L., Rossetto, C.Z., 2005. Two-phasefrictional pressure gradient of R236ea, R134a and R410A inside multi-portmini-channels. Exp. Therm. Fluid Sci. 29, 861–870.

Cense, A.W., Berg, S. 2009. The viscous-capillary paradox in 2-phase flow in porous media. International Symposium of the Society of Core Analysts, Noordwijk, Netherlands, Sept. 27-30.

Chang, S.H., Teng, T.T., Ismail, N., 2010. Extraction of Cu(II) from aqueous solutions by vegetable oil-based organic solvents. J. Hazard. Mater. 181, 868-872.

Chang, S.H., Teng, T.T., Ismail, N., 2011. Efficiency, stoichiometry and structural studies of Cu(II) removal from aqueous solutions using di-2-ethylhexylphosphoric acid and tributylphosphate diluted in soybean oil. Chem. Eng. J. 166, 249-255.

Chaoqun, Y., Yuchao, Z., Chunbo, Y., Minhui, D., Zhengya, D., Guangwen, C., 2013. Characteristics of slug flow with inertial effects in a rectangular microchannel. Chem. Eng. Sci. 95, 246-256.

Chen, I.Y., Chen, Y.M., Liaw, J.S., Wang, C.C., 2007. Two-phase frictional pressure drop in small rectangular channels. Exp. Therm Fluid Sci. 32, 60–66.

Chen, J.D., Yu, J.X., Wang, F., Tang, J.Q., Zhang, Y.F., Xu, Y.L., Chi, R.A., 2017. Selective adsorption and recycle of Cu^{2+} from aqueous solution by modified sugarcane bagasse under dynamic condition. Environ. Sci. Pollut. Res. 24, 1–8.

Chen, L., Lee, W., Lee, J., 2017a. Analysis of the thermal field and heat transfer characteristics of pebble beds packed in a face-centered cubic structure. Appl. Therm. Eng. 121, 473–483.

Cheng, C.Y., Barnard, K.R., Zhang, W., Zhu, Z., Pranolo, Y., 2016. Recovery of nickel, cobalt, copper and zinc in sulphate and chloride solutions using synergistic solvent extraction. Chin. J. Chem. Eng. 24, 237-248.

Cheng, N.-S., 2011. Wall effect on pressure drop in packed beds. Powder Technol. 210, 261–266.

Cheng, Z., Zhang, L., Guo, X., Jiang, X., Li, T., 2015. Adsorption behavior of direct red 80 and congo red onto activated carbon/surfactant: Process optimization, kinetics and equilibrium. Spectrochim. Acta A Mol. Biomol. Spectroscopy 137, 1126-1143.

Cherlo, S.K.R., Kariveti, S., Pushpavanam, S., 2010. Experimental and numerical investigations of two-phase (liquid-liquid) flow behavior in rectangular microchannels. Ind. Eng. Chem. Res. 49, 893–899.

Chisholm, D., 1967. A theoretical basis for the Lockhart-Martinelli correlation for two-phase flow. Int. J. Heat Mass Transfer 10, 1767–1778.

Cho, G.C., Dodds, J., Santamarina, J.C., 2006. Particle shape effects on packing density, stiffness and strength: natural and crushed sands. J. Geotech. Geoenviron. 132, 591-602.

Choi, C., Kim, M., 2011. Flow pattern based correlations of two-phase pressure drop in rectangular Microchannels. Int. J. Heat Fluid Flow 32, 1199-1207.

Choubey, P.K., Panda, R., Jha, M.K., Lee, J-c., Pathak, D.D., 2015. Recovery of copper and recycling of acid from the leach liquor of discarded Printed Circuit Boards (PCBs). Sep. Purif. Technol. 156, 269-275.

Chow, V.T., 1959. Open Channel Hydraulics. McGraw-Hill Book Company, New York.

Chowdhury, Z.Z., Hamid, S.B.A., Zain, S.M., 2015. Evaluating design parameters for breakthrough curve analysis and kinetics of fixed bed columns for Cu(II) cations using lignocellulosic wastes. BioResources 10, 732-749.

Chua, C.K., Pumera, M., 2014. Chemical reduction of graphene oxide: a synthetic chemistry viewpoint. Chem. Soc. Rev. 43, 291-312.

Chung, S.F., Wen, C.Y., 1968. Longitudinal dispersion of liquid flowing through fixed and fluidized beds. AIChE J. 14, 857-866.

Churchill, S.W., 1977. Friction-factor equation spans all fluid-flow regimes. Chem. Eng. Prog. 84, 91–92.

Cierpiszewski, R., Szymanowski, J., 2001. Copper extraction from chloride solution by solvating and chelating extractants. Solvent Extr. Ion Exch. 19 (3), 441-456.

Cortina, J.L., Miralles, N., Sastre, A.M., Aguilar, M., 1995. Solid-liquid extraction studies of Zn (II) , Cu (II) and Cd (II) from chloride media with impregnated resins containing mixtures of organophosphorus compounds immobilized on to Amberlite XAD2. Hydrometallurgy 37, 301-322.

Crowe, C.T., 2005. Multiphase Flow Handbook. CRC Press, Florida, United States.

Cui, P., G-cai, Z., R-an, C., Y-qian, Z., Y-na, Z., 2007. Recovery of copper from leaching solution of copper smelting ash. CJPE 7 (2), 273-277.

Darekar, M., Sen, N., Singh, K.K., Mukhopadhyay, S., Shenoy, K.T., Ghosh, S.K., 2014. Liquid–liquid extraction in microchannels with Zinc–D2EHPA system. Hydrometallurgy 144-145, 54-62.

Darekar, M., Singh, K.K., Mukhopadhyay, S., Shenoy, K.T., 2016. Single-stage micro-scale extraction: Studies with single microbore tubes and scale-up. Sep. Sci. Technol. 158, 160-170.

Dehkordi, A.M., 2002. A novel two-impinging-jets reactor for copper extraction and stripping processes. Chem. Eng. J. 87, 227-238.

Demirel, Y., Kahraman, R., 1999. Entropy generation in a rectangular packed duct with wall heat flux. Int. J. Heat Mass Transf. 42, 2337-2344.

Delgado, J.M.P.Q., 2006. A critical review of dispersion in packed beds. Heat Mass Transf. 42, 279–310.

Demiral, H., Gungor, C., 2016. Adsorption of copper(II) from aqueous solutions on activated carbon prepared from grape bagasse. J. Clean. Prod. 124, 103-113.

Demirbas, E., Dizge, N., Sulak, M.T., Kobya, M., 2009. Adsorption kinetics and equilibrium of copper from aqueous solutions using hazelnut shell activated carbon. Chem. Eng. J. 148, 480-487.

Deng, C.–H., Gong, J.–L., Zhang, P., Zeng, G.–M., Song, B., Liu, H.–Y., 2017. Preparation of melamine sponge decorated with silver nanoparticles-modified graphene for water disinfection. J. Colloid Interface Sci. 488, 26–38.

Dey, S., 2014. Fluvial Hydrodynamics: Hydrodynamic and Sediment Transport Phenomena. Springer-Verlag, Berlin, Heidelberg.

Divya, K.S., Chandran, A., Reethu, V.N., Mathew, S., 2018. Enhanced photocatalytic performance of RGO/Ag nanocomposites produced via a facile microwave irradiation for the degradation of Rhodamine B in aqueous solution. Appl. Surf. Sci. 444, 811–818.

Dolejš, V., Machač, I., 1995. Pressure drop during the flow of a Newtonian fluid through a fixed bed of particles. Chem. Eng. Process. 34, 1–8.

Duga, N.D.F., Imperial, P.E.A., Soriano, A.N., Nieva, A.D., 2016. Packed bed biosorption of lead and copper ions using sugarcane bagasse. AJChE 16, 23–37.

Dutta, S., Ray, C., Sarkar, S., Pradhan, M., Negishi, Y., Pal, T., 2013. Silver nanoparticle decorated reduced graphene oxide (rGO) nanosheet: A platform for SERS based low-level detection of uranyl ion. ACS Appl. Mater. Interfaces 5, 8724-8732.

Eberhart, J.G., 1966. The Surface Tension of Binary Liquid Mixtures. J. Phys. Chem. 70, 1183-1186.

Egorov, V.M., Djigailo, D.I., Momotenko, D.S., Chernyshov, D.V., Torocheshnikova, I.I., Smirnova, S.V., Pletnev, I.V., 2010. Task-specific ionic liquid trioctylmethyl-ammonium salicylate as extraction solvent for transition metal ions. Talanta 80, 1177-1182.

Eisfeld, B., Schitzlein, K., 2001. The influence of confining walls on the pressure drop in packed Beds. Chem. Eng. Sci. 56, 4321-4329.

Elwakeel, K., El-Bindary, A., Kouta, E., Guibal, E., 2018. Functionalization of polyacrylonitrile/Na-Y zeolite composite with amidoxime groups for the sorption of Cu (II), Cd (II) and Pb (II) metal ions. Chem. Eng. J. 332, 727–736.

Ergun, S., 1952. Fluid flow through packed columns. Chem. Eng. Prog. 89, 89-94.

Esmaeilzadeh, F., Lashkarboluki, R., Lashkarbolooki, M., Hezave, A.Z., 2014. Modeling of spearmint oil extraction in a packed bed using SC-CO_2. Chem. Eng. Commun. 201, 300-322.

Fang, S., Zhou, Z., Xue, J., He, G., Chen, H., 2018. Improved ciprofloxacin removal by a Fe(VI)-Fe_3O_4/graphene system under visible light irradiation. Water Sci. Technol. 2017, 527-533.

Faridkhou, A., Larachi, F., 2014. Two-phase flow hydrodynamic study in micro-packed beds – Effect of bed geometry and particle size. Chem. Eng. Process. 78, 27-36.

Faridkhou, A., Tourvieille, J.-N., Larachi, F., 2016. Reactions, hydrodynamics and mass transfer in micro-packed beds — Overview and new mass transfer data. Chem. Eng. Process. 110, 80-96.

Feng, B.H., 1989. Handbook of Chemical Engineering. vol. 3, Chemical Industry Press, Beijing.

Feng, J., Dong, H., Gao, J., Liu, J., Liang, K., 2016. Experimental study of gas–solid overall heat transfer coefficient in vertical tank for sinter waste heat recovery. Appl. Therm. Eng. 95, 136–142.

Feng, N., Guo, X., Liang, S., 2009. Adsorption study of Copper (II) by chemically modified orange Peel. J. Hazard. Mater. 164, 1286-1292.

Ferreira, A.E., Agarwal, S., Machado, R.M., Gameiro, M.L.F., Santos, S.M.C., Reis, M.T.A., Ismael, M.R.C., Correia, M.J.N., Carvalho, J.M.R., 2010. Extraction of copper from acidic leach solution with Acorga M5640 using a pulsed sieve plate column. Hydrometallurgy 104, 66-75.

Field, B.S., Hrnjak, P., 2007. Adiabatic two-phase pressure drop of refrigerants in smallchannels. Heat Transfer Eng. 28, 704–712.

Fouad, E.A., 2009. Separation of copper from aqueous sulfate solutions by mixtures of Cyanex 301and LIX® 984N. J. Hazard. Mater. 166, 720-727.

Foumeny, E.A., Benyahia, J.A., Castro, J.A., Moallem, H.A., Rashani, S., 1993. Correlations of pressure drop in packed beds taking into account the effect of the confirming wall. Int. J. Heat Mass Transfer 36, 536-540.

Fries, D.M., Trachsel, F., Rohr, P.R.V., 2008. Segmented gas–liquid flow characterization in rectangular microchannels. Int. J. Multiphase Flow 34, 1108-1118.

Frischmann, M., Engelbrecht, K., Nellis, G., Klein, S., 2008. Heat transfer coefficient in a packed sphere regenerator for use in active magnetic regenerative refrigeration. International refrigeration and air conditioning conference at Purdue, July 14-17.

Fu, W., Huang, Z., 2018. Magnetic Dithiocarbamate Functionalized Reduced Graphene Oxide for the Removal of Cu(II), Cd(II), Pb(II), and Hg(II) Ions from Aqueous Solution: Synthesis, Adsorption, and Regeneration. Chemosphere 209, 449-456.

Galloway, T.R., Sage, B.H., 1970. A model of the mechanism of transport in packed distended and fluidized beds. Chem. Eng. Sci. 25, 252-495.

Gao, X., Jang, J., Nagase, S., 2010. Hydrazine and thermal reduction of graphene oxide: reaction mechanisms, product structures, and reaction design. J. Phys. Chem. C 114, 832-842.

Garba, Z.N., Soib, S.F.B., Rahim, A.A., 2015. Valuation of activated carbon from waste tea for the removal of a basic dye from aqueous solution. J. Chem. Eng. Chem. Res. 2, 623-633.

Geist, A., Plucinski, P., Nitsch, W., 2000. Mass transfer kinetics of reactive multication co extraction into bis(2-ethylhexyl)phosphoric acid. Solvent Extr. Ion Exch. 18 (3), 493-515.

Ghaedi, M., Ansari, A., Habibi, M.H., Asghari, A.R., 2014. Removal of malachite green from aqueous solution by zinc oxide nanoparticle loaded on activated carbon: Kinetics and isotherm study. J. Ind. Eng. Chem. 20, 17-28.

Ghanadzadeh, H., Abbasnejad, S., 2011. Separation of Copper (II) with solvent extraction using lauric acid diluted in benzene. J Thermodyn Catal. 2 (2), 1-6.

Gibilaro, L.G., 2001. Fluidization Dynamics. Butterworth-Heinemann, Oxford.

Gnielinski, V., 1975. Neue Gleichungenfür den Wärme- und den Stoffübergang in turbulent durchströmten Rohren und Kanälen. Forsch. Ing.-Wes. 41, 8–16.

Gnielinski, V., 1976. New equations for heat and mass-transfer in turbulent pipe and channel flow. Int. Chem. Eng. 16, 359–368.

Gonzalez, P.G., Pliego-Cuervo, Y.B., 2014. Adsorption of Cd(II), Hg(II), and Zn(II) from aqueous solution using mesoporous activated carbon produced from Bambusa vulgaris striata. Chem. Eng. Res. Des. 92, 2715-2724.

Górny, D., Guzik, U., Hupert-Kocurek, K., Wojcieszynska, D., 2019. Naproxen ecotoxicity and biodegradation by Bacillus thuringiensis B1(2015b) strain. Ecotoxicol. Environ. Safety 167, 505-512.

Gouvea, L.R., Morais, C.A., 2010. Development of a process for the separation of zinc and copper from sulphuric liquor obtained from the leaching of an industrial residue by solvent extraction. Miner. Eng. 23, 492-497.

Gudina, E.J., Pereira, J.F.B., Costa, R., Coutinho, J.A.P., Teixeira, J.A., Rodrigues, L.R., 2013. Biosurfactant-producing and oil-degrading Bacillus subtilis strains enhance oil recovery in laboratory sand-pack columns. J. Hazard. Mater. 261, 106-113.

Guggenheim, E.A., 1957. Thermodynamics. North-Holland Publishing Co., Amsterdam.

Guo, X., Fan, Y., Luo, L., 2018. Residence time distribution on flow characterization of multichannel systems: Modelling and experimentation. Exp. Therm. Fluid Sci. 99, 407-419.

Guo, Z., Sun, Z., Zhang, N., Ding, M., Liu, J., 2017. Pressure drop in slender packed beds with novel packing arrangement. Powder Technol. 321, 286–292.

Gupta, B., Deep, A., Singh, V., Tandon, S.N., 2003. Recovery of cobalt, nickel and copper from sea nodules by their extraction with alkylphosphines. Hydrometallurgy 70, 121-129.

Gupta, N.K., Prakash, P., Kalaichelvi, P., Sheeba, K.N., 2016. The effect of temperature and hemicellulose-lignin, cellulose-lignin, and cellulose-hemicellulose on char yield from the slow pyrolysis of rice husk. Energ. Source. Part A. 38, 1428-1434.

Harnett, J.P., Kostic, M., 1989. Heat transfer to Newtonian and non-Newtonian fluids in rectangular Ducts. Adv. Heat Transf. 19, 247–356.

Harrison, L.D., Brunner, K.M., Hecker, W.C., 2013. A combined packed-bed friction factor equation: extension to higher Reynolds number with wall effects. AIChE J. 59, 703–706.

Hasan, Z., Choi, E.J., Jhung, S.H., 2013. Adsorption of naproxen and clofibric acid over a metal-organic framework MIL-101 functionalized with acidic and basic groups. Chem. Eng. J. 219, 537-544.

Hasfalina, C.M., Maryam, R.Z., Luqman, C.A., Rashid, M., 2012. Adsorption of copper(II) from aqueous medium in fixed-bed column by Kenaf fibres. APCBEE Procedia 3, 255–263.

Hessel, V., Angeli, P., Gavriilidis, A., Lowe, H., 2005. Gas-Liquid and Gas-Liquid-Solid Microstructured Reactors: Contacting Principles and Applications. Ind. Eng. Chem. Res. 44, 9750-9769.

Hicks, R.E., 1970. Pressure drop in packed beds of spheres. Ind. Eng. Chem. Fund. 9, 500–502.

Hizal, J., Apak, R., 2006. Modeling of copper(II) and lead(II) adsorption on kaolinite-based clay minerals individually and in the presence of humic acid. J. Colloid Interface Sci. 295, 1-13.

Homagai, P.L., Ghimire, K.N., Inoue, K., 2010. Adsorption behavior of heavy metals onto chemically modified sugarcane bagasse. Bioresour. Technol. 101, 2067-2069.

Hrnjak, P., Tu, X., 2007. Single phase pressure drop in microchannels. Int. J. Heat Fluid Flow 28, 2-14.

Hsu, C., 1965. Heat transfer to liquid metals flowing past spheres and elliptical rod bundles. Int. J. Heat Mass Transf. 8, 303–315.

Hu, J., Wang, S, Hu, H., Li, H., Peng, K., Liu, D., Liu, Q., Chen, Q., 2013. Improvement of separation efficiency of Cu (II) and Ni (II) in ammoniacal solutions by antagonistic effect of Aliquat336 on LIX84I. Sep. Purif. Technol. 118, 828-834.

Hu, S.-Y.B., Wiencek, J.M., 2000. Copper—LIX 84 Extraction Equilibrium. Sep. Sci. Technol. 35 (4), 469-481.

Hua, S.Z., Yang, X.N., 1985. Actual Fluid Friction Manual. National Defense Industry Press, Beijing, pp. 269.

Huang, Q., Chen, Y., Yu, H., Yan, L., Zhang, J., Wang, B., Du, B., Xing, L., 2018. Magnetic graphene oxide/MgAl-layered double hydroxide nanocomposite: one-pot solvothermal synthesis, adsorption performance and mechanisms for Pb^{2+}, Cd^{2+}, and Cu^{2+}. Chem. Eng. J. 341, 1–9.

Huang, T.-C., Juang, R.-S., 1986. Kinetics and mechanism of zinc extraction from sulphate medium with di(2-ethylhexyl)phosphoric acid. J. Chem. Eng. Jpn. 5 (19), 379-386.

Hui-ping, H., Chun-xuan, L., Xue-tao, H., Qi-wen, L., Qi-yuan, C., 2010. Solvent extraction of copper and ammonia from ammoniacal solutions using sterically hindered β-diketone. Trans. Nonferrous Met. Soc. China 20, 2026-2031.

Hwang, Y.W., Kim, M.S., 2006. The pressure drop in microtubes and the correlation development. Int. J. Heat Mass Transfer 49, 1804-1812.

Ide, H., Kariyasaki, A., Fukano, T., 2007. Fundamental data on the gas–liquid two-phase flow in Minichannels. Int. J. Therm. Sci. 46, 519-530.

Ide, H., Matsumura, H., 1990. Frictional pressure drops of two-phase gas-liquid flow in rectangular Channels. Exp. Therm Fluid Sci. 3, 362-372.

Idelchik, I.E., 1989. Flow Resistance: A Design Guide for Engineers. (English translation from Russian 2nd Ed.) Hemisphere Publishing Corporation, New York.

Ihm, S-k., Lee, H-y., Lee, D-h., 1988. Kinetic study of the extraction of copper (II) by di(2-ethylhexyl)phosphoric acid in a lewis-type cell. J. Membr. Sci. 37, 181-191.

Ilbay, Z., Sahin, S., Kerkez, O., Bayazit, S.S., 2015. Isolation of naproxen from wastewater using carbon-based magnetic adsorbents. Int. J. Environ. Sci. Technol. 12, 3541-3550.

Iliuta, I., Thyriom, F.C., Muntean, O., 1996a. Residence time distribution of the liquid in two-phase cocurrent downflow in packed beds: Air/Newtonian and non-Newtonian liquid systems. Can. J. Chem. Eng. 74, 783-796.

Iliuta, I., Thyriom, F.C., Muntean, O., Giot, M., 1996b. Residence time distribution of the liquid in gas-liquid cocurrent upflow fixed-bed reactors. Chem. Eng. Sci. 51, 4579-4593.

Im, J.K., Heo, J., Boateng, L.K., Her, N., Flora, J.R., Yoon, J., Zoh, K.D., Yoon, Y., 2013. Ultrasonic degradation of acetaminophen and naproxen in the presence of single-walled carbon nanotubes. J. Hazard. Mater. 254–255, 284-292.

Inam, E., Etim, U.J., Akpabio, E.G., Umoren, S.A., 2017. Process optimization for the application of carbon from plantain peels in dye abstraction. J. Taibah Univ. Sci. 11, 173-185.

Incropera, F.P., DeWitt, D.P., 1990. Introduction to Heat Transfer. 2nd Ed., John Wiley and Sons Inc., New York.

Incropera, F.P., Dewitt, D.P., Bergman, T.L., Lavine, A.S., 2013. Principles of Heat and Mass Transfer. 7th Ed., John Wiley & Sons, United States.

Incropera, F.P., DeWitt, David P., 2007. Fundamentals of Heat and Mass Transfer. 6th Edition, Wiley, New York, pp. 514.

Isidori, M., Lavorgna, M., Nardelli, A., Parrella, A., Previtera, L., Rubino, M., 2005. Ecotoxicity of naproxen and its photo-transformation products. Sci. Total Environ. 348, 93–101.

Ismail, M.B., Pastor, N.C., Soler, E.P., Soltani, A., Othmane, A., 2016. A comparative study on surface treatments in the immobilization improvement of hexahistidine-tagged protein on the indium tin oxide surface. J. Nanomed. Nanotechnol. 7, 1000372.

Jallouli, N., Elghniji, K., Hentati, O., Ribeiro, A.R., Silva, A.M.T., Ksibi, M., 2016. UV and solar photo-degradation of naproxen: TiO_2 catalyst effect, reaction kinetics, products identification and toxicity assessment. J. Hazard. Mater. 304, 329-336.

Jamialahmadi, M., Malayeri, M.R., Muller-Steinhagen, H., 1995. Prediction of heat transfer to liquid-solid fluidized beds. Can. J. Chem. Eng. 73, 444-455.

Jiao, T., Guo, H., Zhang, Q., Peng, Q., Tang, Y., Yan, X., Li, B., 2015. Reduced graphene oxide-based silver nanoparticle-containing composite hydrogel as highly efficient dye catalysts for wastewater treatment. Sci. Rep. 5, 11873.

Jones, D.P., Krier, H., 1983. Gas flow resistance measurements through packed beds at high Reynolds numbers. ASME J. *Fluids* Eng. 105, 168–173.

Jradi, K., Daneault, C., Chabot, B., 2011. Chemical surface modification of glass beads for the treatment of paper machine process waters. Thin Solid Films 519, 4239–4245.

Juang, R.-S., Chang, Y.-T., 1993. Kinetics and mechanism for copper (I1) extraction from sulphate solutions with bis(2-ethylhexyl)phosphoric acid. Ind. Eng. Chem. Res. 32, 207-213.

Jung, C., Boateng, L.K., Flora, J.R.V., Oh, J., Braswell, M.C., Son, A., Yoon, Y., 2015. Competitive adsorption of selected non-steroidal anti-inflammatory drugs on activated biochars: experimental and molecular modeling study. Chem. Eng. J. 264, 1–9.

Jung, C., Oh, J., Yoon, Y., 2015. Removal of acetaminophen and naproxen by combined coagulation and adsorption using biochar: influence of combined sewer overflow components. Environ. Sci. Pollut. Res. 22, 10058-10069.

Kahya, E., Bayraktar, E., Mehmeto, U., 2001. Optimization of process parameters for reactive lactic acid extraction. Turk. J. Chem. 25, 223–230.

Kamiuto, K., Yee, S.S., 2005. Heat transfer correlations for open-cellular porous materials. Int. Commun. Heat Mass Transfer 32, 947–953.

Kapur, M., Mondal, M.K., 2016. Design and model parameters estimation for fixed-bed column adsorption of Cu(II) and Ni(II) ions using magnetized sawdust. Desalination Water Treat. 57, 12192–12203.

Kara, D., Alkan, M., 2002. Preconcentration and separation of copper (II) with solvent extraction using N,N'-bis (2-hydroxy-5-bromo-benzyl) 1,2 diaminopropane. Microchem. J. 71, 29-39.

Kashid, M.N., Gerlach, I., Goetz, S., Franzke, J., Acker, J.F., Platte, F., Agar, D.W., Turek, S., 2005. Internal circulation within the liquid slugs of a liquid-liquid slug-flow capillary microreactor. Ind. Eng. Chem. Res. 44, 5003-5010.

Kavianinia, I., Plieger, P.G., Kandile, N.G., Harding, D.R.K., 2012. Fixed-bed column studies on a modified chitosan hydrogel for detoxification of aqueous solutions from copper (II). Carbohydr. Polym. 90, 875–886.

Kavinkumar, T., Manivannan, S., 2016. Uniform decoration of silver nanoparticle on exfoliated graphene oxide sheets and its ammonia gas detection. Ceram. Int. 42, 1769–1776.

Kawahara, A., Sadatomi, M., Nei, K., Matsuo, H., 2011. Characteristics of two-phase flows in a rectangular microchannel with a T-junction type gas–liquid mixer. Heat Transfer Eng. 32, 585–594.

Kays, W.M., London, A.L., 1984. Compact Heat Exchangers. 3rd Ed., McGrow-Hill, New York.

Kemp, I.C., Bahu, R.E., Pasley, H.S., 1994. Model development and experimental studies of vertical pneumatic conveying dryers. Drying Techn. 12, 1323-1340.

Khazri, H., Ghorbel-Abid, I., Kalfat, R., Trabelsi-Ayadi, M., 2017. Removal of ibuprofen, naproxen and carbamazepine in aqueous solution onto natural clay: equilibrium, kinetics, and thermodynamic study. Appl. Water Sci. 7, 3031-3040.

Khosravi-Bizhaem, H., Abbassi, A., 2018. Effects of curvature ratio on forced convection and entropy generation of nanofluid in helical coil using two-phase approach. Adv. Powder Technol. 29, 890–903.

Kim, I., Yamashita, N., Tanaka, H., 2009. Performance of UV and UV/H_2O_2 processes for the removal of pharmaceuticals detected in secondary effluent of a sewage treatment plant in Japan. J. Hazard. Mater. 166, 1134-1140.

Kim, N., Evans, E.T., Park, D.S., Soper, S.A., Murphy, M.C., Nikitopoulos, D.E., 2011. Gas–liquid two-phase flows in rectangular polymer micro-channels. Exp. Fluids. 51, 373-393.

Kiran, I., Akar, T., Tunali, S., 2005. Biosorption of Pb(II) and Cu(II) from aqueous solutions by pretreated biomass of Neurospora crassa. Process Biochem. 40, 3550–3558.

Klerk, A., 2003. Voidage variation in packed beds at small column to particle diameter ratio. AIChE J. 49, 2022-2029.

Knobloch, C., Güttel, R., Turek, T., 2013. Holdup and pressure drop in micro packed-bed reactors for Fischer-Tropsch synthesis. Chem. Ing. Tech. 85, 455-460.

Kockmann, N., 2007. Transport Phenomena in Micro Process Engineering. Springer, New York.

Kong, D., Qiao, N., Liu, H., Du, J., Wang, N., Zhou, Z., Ren, Z., 2017. Fast and efficient removal of copper using sandwich-like graphene oxide composite imprinted materials. Chem. Eng. J. 326, 141–150.

Kose, T.E., Demiral, H., Oztürk, N., 2011. Adsorption of boron from aqueous solutions using activated carbon prepared from olive bagasse. Desalin. Water Treat. 29, 110-118.

Kouidri, A., Madani, B., Roubi, B., 2015. Experimental investigation of flow boiling in narrow channel. Int. J. Therm. Sci. 98, 90-98.

Kreith, F., Manglik, R.M., Bohn, M.S., 2001. Principles of heat transfer. 6th Ed., Brooks Cole, USA.

Kreutzer, M.T., Kapteijn, F., Moulijn, J.A., Kleijn, C.R., Heiszwolf, J.J., 2005. Inertial and interfacial effects on pressure drop of Taylor flow in capillaries. AIChE J. 51, 2428-2440.

Kriel, F.H., Holzner, G., Grant, R.A., Woollam, S., Ralston, J., Priest, C., 2015. Microfluidic solvent extraction, stripping, and phase disengagement for high-value platinum chloride solutions. Chem. Eng. Sci. 138, 827–833.

Krumbein, W.C., Sloss, L.L., 1963. Stratigraphy and Sedimentation. 2nd Edition, W.H. Freeman and Company, San Francisco.

KTA3102.2., 1983. Reactor core design of high-temperature gas-cooled reactors. Part 2: Heat transfer in spherical fuel elements.

Kul, M., Çetinkaya, Ü., 2009. Recovery of copper by LIX 984N-C from electroplating rinse bath solution. Hydrometallurgy 98, 86-91.

Kulkarni, A.A., Kalyani, V.S., 2009. Two-phase flow in minichannels: Hydrodynamics, pressure drop, and residence time distribution. Ind. Eng. Chem. Res. 48, 8193–8204.

Kumar, P.S., Deepthi, A.S.L.S., Bharani, R., Rakkesh, G., 2015. Study of adsorption of Cu(II) ions from aqueous solution by surface-modified Eucalyptus globulus seeds in a fixed-bed column: experimental optimization and mathematical modeling. Res. Chem. Intermed. 41, 8681–8698.

Kumar, R., Shah, D.J., Tiwari, K.K., 2013. Separation of copper and nickel by solvent extraction using LIX 664N. J. Environ. Prot. 4, 315-318.

Kunii, D., Levenspeil, O., 1969. Fluidization Engineering. Wiley, New York, NY, pp-534.

Kuntoro, H.Y., Hudaya, A.Z., Dinaryanto, O., Deendarlianto, Indarto, 2015. Experimental study of the interfacial waves in horizontal stratified gas-liquid two-phase flows by using the developed image processing technique. 10th Int. Forum on Strategic Technology, Indonesia, June 3 - 5.

Kürten, H., Raasch, J., Rumpf, H., 1966. Beschleunigung eines kugelförmigen Feststoffteilchens im Strömungsfall konstanter Geschwindigkeit,Chem. Ing. Tech. 38, 941–948.

Kuwahara, F., Shirota, M., Nakayama, A., 2001. A numerical study of interfacial convective heat transfer coefficient in two-energy equation model for convection in porous media. Int. J. Heat Mass Transf. 44, 1153–1159.

Kyuchoukov, G., Bogacki, M.B., Szymanowski, J., 1998. Copper Extraction from ammoniacal Solutions with LIX 84 and LIX 54. Ind. Eng. Chem. Res. 37. 4084-4089.

Lanfrey, P.Y., Kuzeljevic, Z.V., Dudukovic, M.P., 2010. Tortuosity model for fixed beds randomly packed with identical particles. Chem. Eng. Sci. 65, 1891-1896.

Laxarova, Z., Boyadzhie, L., 1993. Kinetic aspects of copper (II) transport across liquid membrane containing LIX-860 as a carrier. J. Membr. Sci. 78, 239-245.

Lee, H.J., Lee, S.Y., 2001. Pressure drop correlations for two-phase flow within horizontal rectangular channels with small heights. Int. J. Multiphase Flow 27, 783–796.

Lee, J., Mudawar, I., 2005. Two-phase flow in high-heat-flux micro-channel heat sink for refrigeration cooling applications. Part I—pressure drop characteristics. Int. J. Heat Mass Transf. 48, 928-940.

Lee, J., Ogawa, K., 1974. Pressure drop through packed bed. J. Chem. Eng. Jpn. 27, 691-693.

Lee, J.S., Ogawa, K., 1994. Pressure drop through packed bed. J. Chem. Eng. Jpn. 27, 691–693.

Lee, J-c., Zhu, T., Jha, M.K., Kim, S-k., Yoo, K-k., Jeong, J., 2008. Solvent extraction of Cu(I) from waste etch chloride solution using tri-butyl phosphate (TBP) diluted in 1-octanol. Sep. Purif. Technol. 62, 596-601.

Lee, G., Kim, B.S., 2014. Biological reduction of graphene oxide using plant leaf extracts. Biotechnol. Progr. 30, 463-469.

Leon, T., Roman, U., 1984. Two-phase gas–liquid flow in rectangular channels. Chem. Eng. Sci. 39, 751–765.

Levenspiel, O., 1999. Chemical Reaction Engineering. Wiley, New York.

Li, M., Chen, Z., Wang, Z., Wen, Q., 2019. Investigation on degradation behavior of dissolved effluent organic matter, organic micro-pollutants and bio-toxicity reduction from secondary effluent treated by ozonation. Chemosphere 217, 223-231.

Li, N., Bai, R., 2005. Copper adsorption on chitosan–cellulose hydrogel beads: behaviors and mechanisms. Sep. Purif. Technol. 42, 237-247.

Li, W., Wu, Z., 2010. A general correlation for adiabatic two-phase pressure drop in micro/mini-Channels. Int. J. Heat Mass Transf. 53, 2732–2739.

Li, X., Hibiki, T., 2017a. Frictional pressure drop correlation for two-phase flows in mini and micro multi-channels. Appl. Therm. Eng. 116, 316–328.

Li, X., Hibiki, T., 2017b. Frictional pressure drop correlation for two-phase flows in mini and micro single-channels. Int. J. Multiphase Flow 90, 29-45.

Li, Y., Zhang, H., Wu, B., Guo, Z., 2017. Improving the oxidation resistance and stability of Ag nanoparticles by coating with multilayered reduced graphene oxide. Appl. Surf. Sci. 425, 194–200.

Lin, L., Wang, H., Xu, P., 2017. Immobilized TiO2-reduced graphene oxide nanocomposites on optical fibers as high performance photocatalysts for degradation of pharmaceuticals. Chem. Eng. J. 310, 389-398.

Liqing, L., Hong, Z., Zhanfang, C., Lu, Y., 2011. Recovery of copper(II) and nickel(II) from plating wastewater by solvent extraction. Sep. Sci. Eng. 19 (6), 926-930.

Liu, H., Li, T., Liu, Y., Qin, G., Wang, X., Chen, T., 2016. Glucose-reduced graphene oxide with excellent biocompatibility and photothermal efficiency as well as drug loading. Nanoscale Res. Lett. 11:211, 1-10.

Liu, P., Huang, Y., Wang, L., 2013b. Synthesis of reduced graphene oxide using indole as a reducing agent and preparation of reduced graphene oxide-Ag nanocomposites. Synth. Met. 167, 25–30.

Liu, S., Masliyah, J.H., 1996. Single fluid flow in porous media. Chem. Eng. Commun. 148–150, 653–732.

Lockhart, R.W., Martinelli, R.C., 1949. Proposed correlation of data for isothermal two-phase, two-component flow in pipes. Chem. Eng. Prog. 45, 39–48.

Losey, M.W., Schmidt, M.A., Jensen, K.F., 2001. Microfabricated multiphase packed-bed reactors: Characterization of mass transfer and reactions. Ind. Eng. Chem. Res. 40, 2555-2562.

Lu, J., Dreisinger, D., 2013. Solvent extraction of copper from chloride solution I: Extraction isotherms. Hydrometallurgy 137, 13-17.

Macdonald, I.F., El-Sayed, M.S., Mow, K., Dullien, F.A.L., 1979. Flow through porous media – the Ergun equation revisited. Ind. Eng. Chem. Fund. 18, 199–208.

Macias-Machin, A., Oufer, L., Wannenmacher, N., 1991. Heat Transfer between an Immersed Wire and a Liquid Fluidized Bed. Powder Technol. 66, 281-284.

Mangalam, J., Kumar, M., Sharma, M., Joshi, M., 2019. High adsorptivity and visible light assisted photocatalytic activity of silver/reduced graphene oxide (Ag/rGO) nanocomposite for wastewater treatment. Nano-Structures & Nano-Objects 17, 58–66.

Mansour, M.H., Kawahara, A., Sadatomi, M., 2015. Experimental investigation of gas–non Newtonian liquid two-phase flows from T-junction mixer in rectangular microchannel. Int. J. Multiphase Flow 72, 263-274.

Marcano, D.C., Kosynkin, D.V., Berlin, J.M., Sinitskii, A., Sun, Z., Slesarev, A., et al. 2010. Improved synthesis of graphene oxide. ACS Nano 4, 4806−4814.

Martin, H., 1981. Fluid Bed Heat Exchangers - A New Model for Particle Convective Energy Transfer. Chem. Eng. Commun. 13, 1-16.

Martin, J.J., 1974. An example of engineering analysis. Michigan, pp. 138-140.

Martinez, S., Olmos, I., Carballo, J., Franco, I., 2010. Quality parameters of Brassica spp. grown in northwest Spain. J. Food Sci. Technol. 45, 773-783.

Mary, P., Studer, V., Tabeling, P., 2008. Microfluidic droplet-based liquid-liquid extraction. Anal. Chem. 80, 2680-2687.

Maryami, M., Nasrollahzadeh, M., Mehdipour, E., Sajadi, S.M., 2016. Preparation of the Ag/RGO nanocomposite by use of Abutilon hirtum leaf extract: A recoverable catalyst for the reduction of organic dyes in aqueous medium at room temperature. Int. J. Hydrogen Energy 41, 21236-21245.

McAdams, W.H., 1942. Heat Transmission. 2nd Ed., McGraw-Hill, New York.

McCabe, W.L., Smith, J.C., Harriott, P., 2005. Unit operations of Chemical Engineering. 7th Edition, The McGraw-Hill Companies, Inc., New York.

Melissari, B., Argyropoulos, A.A., 2005. Development of a heat transfer dimensionless correlation for spheres immersed in a wide range of Prandtl number fluids. Int. J. Heat Mass Transf. 48, 4333–4341.

Meng, N., Zhang, S., Zhou, Y., Nie, W., Chen, P., 2015. Novel synthesis of Silver/Reduced Graphene Oxide nanocomposite and its high catalytic activity towards hydrogenation of 4-nitrophenol. RSC Adv. 5, 70968-70971.

Menon, S.H., Madhu, G., Mathew, J., 2019. Modeling residence time distribution (RTD) behavior in a packed-bed electrochemical reactor (PBER). Int. J. Chem. Eng. 2019, 856340.

Metha, D., Hawley, M.C., 1969. Wall effect in packed columns. IE Process. Des. Dev. 8, 280–282.

Mishima, K., Hibiki, T., 1996. Some characteristics of air-water two-phase flow in small diameter vertical tubes. Int. J. Multiphase Flow 22, 703-712.

Mishima, K., Hibiki, T., Nishihara, H., 1993. Some characteristics of gas–liquid flow in narrow rectangular ducts. Int. J. Multiphase Flow 19, 115–124.

Mishra, S., Devi, N., 2011. Extraction of copper (II) from hydrochloric acid solution by Cyanex 921. Hydrometallurgy 107, 29-33.

Mishra, V., Balomajumder, C., Agarwal, V.K., 2013. Adsorption of Cu (II) on the surface of nonconventional biomass: A study on forced convective mass transfer in packed bed column. J. Waste Manag. 2013, 632163.

Moffat, R.J., 1988. Describing the uncertainties in experimental results. Exp. Therm. Fluid Sci. 1, 3-17.

Moghayedi, M., Goharshadi, E.K., Ghazvini, K., Ahmadzadeh, H., Ranjbaran, L., Masoudi, R., Ludwig, R., 2017. Kinetics and mechanism of antibacterial activity and cytotoxicity of Ag-RGO nanocomposite. Colloids Surf.: B 159, 366–374.

Molinari, R., Poerio, T., Cassano, R., Picci, **N.,** Argurio, P., 2004. Copper(II) removal from wastewaters by a new synthesized selective extractant and SLM viability. Ind. Eng. Chem. Res. 43, 623-628.

Molleman, B., Hiemstra, T., 2017. Time, pH, and size dependency of silver nanoparticle dissolution: the road to equilibrium. Environ. Sci.: Nano 4, 1314-1327.

Mondal, S., Majumder, S.K., 2018a. Frictional pressure drop of aqueous-organic two-phase flow through packed and unpacked rectangular serpentine Millichannel. Exp. Therm. Fluid Sci. 94, 215-230.

Mondal, S., Majumder, S.K., 2018b. Single and aqueous-organic two-phase frictional pressure drop and local entropy generation in rectangular millichannel: Experiment and its analysis. Chem. Eng. Process. 134, 72-85.

Mondal, S., Majumder, S.K., 2018c. Studies on the copper extraction in a channel-based packed extraction device. Miner. Eng. 126, 194-206.

Mondal, S., Majumder, S.K., 2019a. Synthesis of phosphate functionalized highly porous activated carbon and its utilization as an efficient copper (II) adsorbent. Korean J. Chem. Eng. 36, 701-712.

Mondal, S., Majumder, S.K., 2019b. Honeycomb-like porous activated carbon for efficient copper (II) adsorption synthesized from natural source: Kinetic study and equilibrium isotherm analysis. J. Environ. Chem. Eng. 7, 103236.

Mondal, S., Majumder, S.K., 2020. Heat transport based on hydrodynamics and the local entropy generation rate in straight and serpentine rectangular packed narrow channels. Appl. Therm. Eng. 171, 115057.

Montillet, A., Akkari, E., Comiti, J., 2007. About a correlating equation for predicting pressure drops through packed beds of spheres in a large range of Raynolds numbers. Chem. Eng. Proc. 46, 329-333.

Moorhead, D.H., Himmelblau, D.M., 1962. Optimization of operating conditions in a packed liquid-liquid extraction column. Ind. Eng. Chem. Fundam. 1, 68-72.

Moriyama, K., Inoue, A., Ohira, H., 1992. The thermohydraulic characteristics of two-phase flow in extremely narrow channels (the frictional pressure drop and void fraction of adiabatic two component two-phase flow). Trans. JSME (Ser. B), 58, 401–407.

Morris, D.A., Johnson, A.I., 1967. Summary of hydrologic and physical properties of rock and soil materials as analyzed by the Hydrologic Laboratory of the U.S. Geological Survey. U.S. Geological Survey, Water-Supply Paper, 1839-D, pp. 42.

Moscatello, N., Swayambhu, G., Jones, C.H., Xu, J., Dai, N., Pfeifer, B.A., 2018. Continuous removal of copper, magnesium, and nickel from industrial wastewater utilizing the natural product yersiniabactin immobilized within a packed-bed column. Chem. Eng. J. 343, 173–179.

Nafiey, A.A., Addad, A., Sieber, B., Chastanet, G., Barras, A., Szunerits, S., et al. 2017. Reduced graphene oxide decorated with Co_3O_4 nanoparticles (rGO-Co_3O_4) nanocomposite: A reusable catalyst for highly efficient reduction of 4-nitrophenol, and Cr(VI) and dye removal from aqueous solutions. Chem. Eng. J. 322, 375-384.

Nagaosa, Y., Binghua, Y., 1997. Extraction equilibria of some transition metal ions by bis(2-ethylhexyl)phosphinic acid. Talanta 44, 327-337.

Nakayama, A., Ando, K., Yang, C., Sano, Y., Kuwahara, F., Liu, J., 2009. A study on interstitial heat transfer in consolidated and unconsolidated porous media. Heat Mass Transf. 45, 1365–1372.

Namasivayam, C., Kadirvelu, K., 1997. Agricultural solid wastes for the removal of heavy metals: Adsorption of Cu(II) by coirpith carbon. Chemosphere 34, 377-399.

Naphon, P., Suwagrai, J., 2007. Effect of curvature ratios on the heat transfer and flow developments in the horizontal spirally coiled tubes. Int. J. Heat Mass Transf. 50, 444–451.

Navalon, S., Dhakshinamoorthy, A., Alvaro, M., Garcia, H., 2016. Metal nanoparticles supported on two-dimensional graphenes as heterogeneous catalysts. Coordin. Chem. Rev. 312, 99–148.

Nazari, M., Vahid, D.J., Saray, R.K., Mahmoudi, Y., 2017. Experimental investigation of heat transfer and second law analysis in a pebble bed channel with internal heat generation. Int. J. Heat Mass Transf. 114, 688-702.

Neella, N., Gaddam, V., Nayak, M.M., Dinesh, N.S., Rajanna, K., 2017. Scalable fabrication of highly sensitive flexible temperature sensors based on silver nanoparticles coated reduced graphene oxide nanocomposite thin films. Sensor Actuat. A 268, 173–182.

Nemec, D., Levec, J., 2005. Flow through packed bed reactors: 1. Single-phase flow. Chem. Eng. Sci. 60, 6947–6957.

Ngah, W.S.W., Fatinathan, S., 2008. Adsorption of Cu(II) ions in aqueous solution using chitosan beads, chitosan–GLA beads and chitosan–alginate beads. Chem. Eng. J. 143, 62–72.

Ngah, W.S.W., Teong, L.C., Toh, R.H., Hanafah, M.A.K.M., 2012. Utilization of chitosan–zeolite composite in the removal of Cu(II) from aqueous solution: adsorption, desorption and fixed bed column studies. Chem. Eng. J. 209, 46–53.

Nie, X., Besant, R., Evitts, R., Bolster, J., 2011. A new technique to determine convection coefficients with flow through particle beds. Trans. ASME J. Heat Transfer 133, 041-601.

Nodeh, M.K.M., Radfard, M., Ali Zardari, L., Nodeh, H.R., 2018. Enhanced removal of naproxen from wastewater using silica magnetic nanoparticles decorated onto graphene oxide; parametric and equilibrium study. Sep. Sci. Technol. 53, 2476-2485.

Norouzi, M., Biglari, N., 2013. An analytical solution for dean flow in curved ducts with rectangular cross section. Phys. Fluids 25, 1-15.

Nsofor, E.C., Adebiyi, G.A., 2001. Measurements of the gas-particle convective heat transfer coefficient in a packed bed for high-temperature energy storage. Exp. Therm. Fluid Sci. 24, 1–9.

Nwabanne, J.T., Igbokwe, P.K., 2012. Kinetic modeling of heavy metals adsorption on fixed bed column. Int. J. Environ. Res. 6, 945-952.

Ochromowicz, K., Chmielewski, T., 2013. Solvent extraction of copper (II) from concentrated leach liquors. Physicochem. Probl. Miner. Process. 49 (1), 357-367.

Olimans, R., 1976. Two phase flow in fast-transmission pipelines. ASME paper 76-Pet-25, Petroleum Division, ASME meeting, Mexico, September 19-24.

Önal, Y., Akmil-Basar¸ C., Sarıcı-Özdemir, C., 2007. Elucidation of the naproxen sodium adsorption onto activated carbon prepared from waste apricot: kinetic, equilibrium and thermodynamic characterization. J. Hazard. Mater. 148, 727–734.

Ovsianytskyi, O., Nam, Y.–S., Tsymbalenko, O., Lan, P.–T., Moon, M.–W., Lee, K.–B., 2018. Highly sensitive chemiresistive H_2S gas sensor based on graphene decorated with Ag nanoparticles and charged impurities. Sensor Actuat. B 257, 278–285.

Ozahi, E., Gundogdu, M.Y., Carpinlioglu, M.O., 2008. A modification on Ergun's correlation for use in cylindrical packed beds with non-spherical particles. Adv. Powder Technol.19, 369–381.

Ozcan, A., Ozcan, A.S., Tunali, S., Akar, T., Kiran, I., 2005. Determination of the equilibrium, kinetic and thermodynamic parameters of adsorption of copper(II) ions onto seeds of Capsicum annuum. J. Hazard. Mater. B124, 200-208.

Padhi, D.K., Panigrahi, T.K., Parida, K., Singh, S.K., Mishra, P.M., 2017. Green Synthesis of Fe_3O_4/RGO Nanocomposite with Enhanced Photocatalytic Performance for Cr(VI) Reduction, Phenol Degradation and Antibacterial Activity. ACS Sustain. Chem. Eng. 5, 10551-10562.

Park, C.M., Heo, J., Wang, D., Yoon, Y., 2018. Heterogeneous activation of persulfate by reduced graphene oxide–elemental silver/magnetite nanohybrids for the oxidative degradation of pharmaceuticals and endocrine disrupting compounds in water. Appl. Catal. B. 225, 91-99.

Park, S., An, J., Potts, J.R., Velamakanni, A., Murali, S., Ruoff, R.S., 2011. Hydrazine-reduction of graphite- and graphene oxide. Carbon 49, 3019-3023.

Patel, S., Majumder, S.K., Das, P., Ghosh, P., 2019. Ozone microbubble-aided intensification of degradation of pharmaceuticals in a plant prototype. J. Environ. Chem. Eng. 7, 103102.

Pei, S., Cheng, H.-M., 2012. The reduction of graphene oxide. Carbon 50, 3210-3228.

Phillips, R.J., 1990. Microchannel heat sinks, Advances in Thermal Modeling of Electronic Components and Systems. Chapter 3, NY: Hemisphere Publishing Corporation, New York.

Pradhan, S., Devi, N., Mishra, S., 2014. Separation of copper and iron from chloride media using Cyanex 921 in kerosene. J. Cent. South Univ. 21, 1752-1755.

Priest, C., Zhou, J., Sedev, R., Ralston, J., Aota, A., Mawatari, K., Kitamori, T., 2011. Microfluidic extraction of copper from particle-laden solutions. Int. J. Miner. Process. 98, 168–173.

Qin, S.J., Chen, B.D., Yan, X., Xiao, Z.J., Huang, Y.P., 2012. Experimental investigation on frictional pressure drop of water in vertical rectangular channel. Nucl. Eng. Des. 250, 567–572.

Qu, W., Mudawar, I., 2003. Measurement and prediction of pressure drop in two-phase micro channel heat sinks. Int. J. Heat Mass Transfer 46, 2737-2753.

Qurie, M., Khamis, M., Malek, F., Nir, S., Bufo, S.A., Abbadi, J., et al. 2013. Stability and removal of naproxen and its metabolite by advanced membrane wastewater treatment plant and micelle–clay complex. CLEAN-Soil, Air, Water 42, 594-600.

Qustia, A.H., Mohamed, R.M., Salam, M.A., 2014. Photocatalytic synthesis of aniline from nitrobenzene using Ag-reduced graphene oxide nanocomposite. Ceram. Int. 40, 5539–5546.

Raichura, R.C., Mary, Q., College, W., 1999. Pressure drop and heat transfer in packed beds with small tube-to-particle diameter ratio. Exp. Heat Transf. 12, 309–327.

Ranz, W.E., Marshall, W.R., 1952. Evaporation from drops. Chem. Eng. Pro. 48, 141.

Rastegar, S.O., Gu, T., 2017. Empirical correlations for axial dispersion coefficient and Peclet number in fixed-bed columns. J. Chromatogr. A 1490, 133–137.

Rautenbach, R., Katz, T., 2010. Common fundamentals and unit operations in thermal desalination systems. vol I, *Eolss Publishers* Co., United Kingdom.

Reddy, B.R., Priya, D.N., 2005. Process development for the separation of copper (II), nickel(II) and zinc(II) from sulphate solutions by solvent extraction using LIX 84 I. Sep. Purif. Technol. 45, 163-167.

Reichelt, W., 1972. Berechnung des Druckverlustes einphasig durchströmter Kugel- und Zylinderschüttungen. Chem. Ing. Techn. 44, 1068–1071.

Ren, Z., Zhang, W., Meng, H., Liu, Y., Dai, Y., 2007. Extraction Equilibria of Copper(II) with D2EHPA in Kerosene from Aqueous Solutions in Acetate Buffer Media. J. Chem. Eng. Data 52, 438-441.

Resterna, A.B., Szymanowski, J., 2000. Copper extraction from chloride solutions with mixtures of solvating and chelating reagents. Solvent Extr. Ion Exch. 18 (1), 77-91.

Revellin, R., Lips, S., Khandekar, S., Bonjour, J., 2009. Local entropy generation for saturated two-phase flow. Energy 34, 1113–1121.

Ribeiro, A.M., Neto, P., Pinho, C., 2010. Mean porosity and pressure drop measurements in packed beds of monosized spheres: sidewall effects. Int. Rev. Chem. Eng. 2, 40-46.

Rod, V., 1980. Kinetics of metal extraction by chelate formation part-I: mass transfer with a fast reversible chemical reaction and product extraction. Chem. Eng. J. 20, 131-137.

Rod, V., Strnadova, L., Hancil, V., Sir, Z., 1981. Kinetics of metal extraction by chelate formation part-II: extraction of Cu(II) by hydroxyoximes. Chem. Eng. J. 21, 187-193.

Rose, H.E., 1945. On the resistance coefficient–Reynolds number relationship for fluid flow through beds of granular materials. Proc. Inst. Mech. Eng. 153, 154–161.

Rose, H.E., Rizk, A.M.A., 1949. Further researches in fluid flow through beds of granular material. Proc. Inst. Mech. Eng. 160, 493–503.

Roshan, H., Cuthbert, M.O., Andersen, M.S., Acworth, R.I., 2014. Local thermal non-equilibrium in sediments: implications for temperature dynamics and the use of heat as a tracer. Adv. Water Resour. 73, 176–184.

Rossi, D., Gargiulo, L., Valitov, G., Gavriilidis, A., Mazzei, L., 2017. Experimental characterization of axial dispersion in coiled flow inverters. Chem. Eng. Res. Des. 120, 159-170.

Saber, M., Commenge, J.M., Falk, L., 2010. Microreactor numbering-up in multi-scale networks for industrial-scale applications: impact of flow maldistribution on the reactor performances. Chem. Eng. Sci. 65, 372-379.

Sahu, A., Vir, A.B., Molleti, L.N.S., Ramji, S., Pushpavanam, S., 2016. Comparison of liquid-liquid extraction in batch systems and micro-channels. Chem. Eng. Process. 104, 190-200.

Sahu, S.K., Agrawal, A., Pandey, B.D., Kumar, V., 2004. Recovery of copper, nickel and cobalt from the leach liquor of a sulphide concentrate by solvent extraction. Miner. Eng. 17, 949-951.

Saidi, M.S., Rasouli, F., Hajaligol, M.R., 2006. Heat transfer coefficient for a packed bed of shredded materials at low peclet numbers. Heat Transfer Eng. 27, 41–49.

Salam, H.A., Rajiv, P., Kamaraj, M., Jagadeeswaran, P., Gunalan, S., Sivaraj, R., 2012. Plants: Green route for nanoparticle synthesis. Int. Res. J. Biol. Sci. 1, 85-90.

Salamatinia, B., Kamaruddin, A.H., Abdullah, A.Z., 2008. Modeling of the continuous copper and zinc removal by sorption onto sodium hydroxide-modified oil palm frond in a fixed-bed column. Chem. Eng. J. 145, 259–266.

Sandy, Maramis, V., Kurniawan, A., Ayucitra, A., Sunarso, J., Ismadji, S., 2012. Removal of copper ions from aqueous solution by adsorption using Laboratories-modified bentonite (organo-bentonite). Front. Chem. Sci. Eng. 6, 58-66.

Sang, S., Li, D., Zhang, H., Sun, Y., Jian, A., Zhang, Q., 2017. Facile synthesis of AgNPs on reduced graphene oxide for highly sensitive simultaneous detection of heavy metal ions. RSC Adv. 7, 21618-21624.

Santoso, A., Nagai, R., Mori, A., Kawahara, A., Sadatomi, M., 2006. Experimental study on two-phase flow in horizontal rectangular minichannel with Y-junction. Int. J. Eng. Res. Appl. 6, 39-48.

Seibert, A.F., Fair, J.R., 1988. Hydrodynamics and mass transfer in spray and packed liquid-liquid extraction columns. Ind. Eng. Chem. Res. 27, 470–481.

Serres, M., Schweich, D., Vidal, V., Philippe, R., 2018. Liquid residence time distribution of multiphase horizontal flow in packed bed milli-channel: Spherical beads versus open cell solid foams. Chem. Eng. Sci. 190, 149-163.

Shah, R.K., London, A.L., 1978. Laminar flow forced convection in ducts. Advances in heat transfer supplement, Academic Press, New York.

Shahbazi, A., Younesi, H., Badiei, A., 2013. Batch, and fixed-bed column adsorption of Cu(II), Pb(II), and Cd(II) from aqueous solution onto functionalized SBA-15 mesoporous silica. Can. J. Chem. Eng. 91, 739–750.

Shao, W., Liu, X., Min, H., Dong, G., Feng, Q., Zuo, S., 2015. Preparation, characterization, and antibacterial activity of silver nanoparticle-decorated graphene oxide nanocomposite. ACS Appl. Mater. Interfaces 7, 6966-6973.

Sharma, L., Nigam, K.D.P., Roy, S., 2017. Single phase mixing in coiled tubes and coiled flow inverters in different flow regimes. Chem. Eng. Sci. 160, 227-235.

Shibata, J., Mamiya, S., Matsumoto, S., Yamamoto, H., 1999. Solvent extraction of copper from chloride solution with 2-ethylhexanal oxime. Shigen-to-sozai 115 (9), 695-699.

Shibata, J., Nishimura, S., 1982. Extraction of Cu, Ni and Co with sodium salt of di-2-ethylhexylphosphoric acid. J. Japan Inst. Metals 23 (10), 614-619.

Siderman, S., 1966. The equivalence of the penetration theory and potential flow theories. Ind. Eng. Chem. Res. 58, 54–58.

Singh, R., Saini, R.S., Saini, J.P., 2006. Nusselt number and friction factor correlations for packed bed solar energy storage systems having large sized elements of different shapes. Solar Energy 80, 760–771.

Sinha, M.K., Sahu, S.K., Pramanik, S., Prasad, L.B., Pandey, B.D., 2016. Recovery of high value copper and zinc oxide powder from waste brass pickle liquor by solvent extraction. Hydrometallurgy 165, 182-190.

Sohni, S., Gul, K., Ahmad, F., Ahmad, I., Khan, A., Khan, N., Khan, S.B., 2017. Highly efficient removal of acid red-17 and bromophenol blue dyes from industrial wastewater using graphene oxide functionalized magnetic chitosan composite. Poly. Compos. 39, 3317-3328.

Sole, K.C., Hiskey, J.B., 1995. Solvent extraction of copper by Cyanex 272, Cyanex 302 and Cyanex 301. Hydrometallurgy 37, 129-147.

Song, Z.J., Ran, W., Wei, F.Y., 2016. One-step approach for the synthesis of $CoFe_2O_4$@rGO core-shell nanocomposites as efficient adsorbent for removal of organic pollutants. Water Sci. Technol. 75, 397-405.

Squires, T.M., Quake, S.R., 2005. Microfluidics: fluid physics at the nanoliter scale. Rev. Mod. Phys. 77, 977.

Sridhar, V., Verma, J.K., 2011. Recovery of copper, nickel and zinc from sulfate solutions by solvent extraction using LIX 984N. E-J. Chem. 8 (S1), S434-S438.

Stegeman, D., Rooijen, F.E.V., Kamperman, A.A., Weijer, S., Westerterp, K.R., 1996. Residence time distribution in the liquid phase in a concurrent gas-liquid trickle bed reactor. Ind. Eng. Chem. Res. 35, 378-385.

Straub, J.O., Stewart, K.M., 2007. Deterministic and probabilistic acute-based environmental risk assessment for naproxen for Western Europe. Environ. Toxicol. Chem. 26, 795-806.

Su, Y., Chen, G., Kenig, E.Y., 2015. An experimental study on the numbering-up of microchannels for liquid mixing. Lab Chip 15, 178-187.

Su, Y., Chen, G., Zhao, Y., Yuan, Q., 2009. Intensification of liquid–liquid two-phase mass transfer by gas agitation in a microchannel. AIChE J. 55, 1948–1958.

Su, Y., Zhao, Y., Chen, G., Yuan, Q., 2010. Liquid–liquid two-phase flow and mass transfer characteristics in packed microchannels. Chem. Eng. Sci. 65, 3947-3956.

Sun, J.Y., Jepson, W.P., Ohio, U., 1992. Slug flow characteristics and their effect on corrosion rates in horizontal oil and gas pipelines. SPE 24787, 215-228.

Sun, J.–Z., Liao, Z.–H., Si, R.–W., Kingori, G. P., Chang, F.–X., Gao, L., et al. 2014. Adsorption and removal of triphenylmethane dyes from water by magnetic reduced graphene oxide. Water Sci. Technol. 70.10, 1663-1669.

Sun, L., Mishima, K., 2009. Evaluation analysis of prediction methods for two-phase flow pressure drop in mini-channels. Int. J. Multiphase Flow 35, 47–54.

Suresh, D., Nethravathi, P.C., Nagabhushana, H.U., Sharma, S.C., 2015. Spinach assisted green reduction of graphene oxide and its antioxidant and dye absorption properties. Ceram. Int. 41, 4810-4813.

Tadepalli, S., Murthy, K.S.R., 2017. Column performance evaluation and hydrodynamic modeling studies for the removal of copper and cadmium using mixed adsorbent in continuous packed bed reactor. Int. J. Chemtech Res. 10, 664-6673.

Tadepalli, S., Murthy, K.S.R., Vijay, P., 2016. Removal of copper and cadmium from industrial effluents using the mixed adsorbent in the continuous flow operations. J. chem. pharm. 8, 29-40.

Tajabadi, M.T., Basirun, W.J., Lorestani, F., Zakaria, R., Baradaran, S., Amin, Y.M., 2015. Nitrogen-doped graphene-silver nanodendrites for the non-enzymatic detection of hydrogen peroxide. Electrochim. Acta 151, 126–133.

Tallmadge, J.A., 1970. Packed bed pressure drop - an extension to higher Reynolds numbers. AIChE J. 16, 1092–1093.

Tang, J., Steenari, B.-M., 2015. Solvent extraction separation of copper and zinc from MSWI fly ash leachates. Waste Manage. 44, 147-154.

Tang, L., Yu, J., Pang, Y., Zeng, G., Deng, Y., Wang, J., et al. 2018. Sustainable efficient adsorbent: Alkali-acid modified magnetic biochar derived from sewage sludge for aqueous organic contaminant removal. Chem. Eng. J. 336, 160-169.

Tang, Y., Li, X.-M. Xu, Z.-C. Guo, Q.-W. Hong, C.-Y. Bing, Y.-X. 2014. Removal of naproxen and bezafibrate by activated sludge under aerobic conditions: Kinetics and effect of substrates. Biotechnol. Appl. Biochem. 61, 333-341.

Tasaki, T., Oshima, T., Baba, Y., 2007. Selective extraction and transport of copper(II) with new alkylated pyridinecarboxylic acid derivatives. Talanta 73, 387-393.

Taylor, G., 1953. Dispersion of soluble matter in solvent flowing slowly through a tube. Proc. Roy. Soc. A: Math. Phys. Eng. Sci. 219, 186–203.

Thomas, H.C., 1944. Heterogeneous ion exchange in a flowing system. J. Am. Chem. Soc. 66, 1664-1666.

Tian, X.W., Xu, S.M., Sun, Z.H., Wang, P., Xu, L., Zhang, Z., 2018. Experimental study on flow and heat transfer of power law fluid in structured packed porous media of particles. Exp. Therm. Fluid Sci. 90, 37-47.

Tidona, B., Desportes, S., Altheimer, M., Ninck, K., Rohr, P.R.V., 2012. Liquid-to-particle mass transfer in a micro packed bed reactor. Int. J. Heat Mass Transf. 55, 522–530.

Tonomura, O., Tominari, T., Kano, M., Hasebe, S., 2007. Operation policy for micro chemical plants with external numbering-up structure. Chem. Eng. J. 135, S131-S137.

Tran, T.N., Chyu, M.C., Wambsganss, M.W., France, D.M., 2000. Two-phase pressure drop of refrigerant during flow boiling in small channels: an experimental investigation and correlation development. Int. J. Multiphase Flow 26, 1739–1754.

Tsai, W.-C., Luna, M.D.G., Bermillo-Arriesgado, H.L.P., Futalan, C.M., Colades, J.I., Wan, M.-W., 2016. Competitive fixed-bed adsorption of Pb(II), Cu(II), and Ni(II) from aqueous solution using chitosan-coated bentonite. Int. J. Polym. Sci. 2016, 1608939.

Tsaoulidis, D., Angeli, P., 2015. Effect of channel size on mass transfer during liquid–liquid plug flow in small scale extractors. Chem. Eng. J. 262, 785-793.

Tsaoulidis, D., Dore, V., Angeli, P., Plechkova, N.V., Seddon, K.R., 2013. Flow patterns and pressure drop of ionic liquid–water two-phase flows in microchannels. Int. J. Multiphase Flow 54, 1-10.

Umbreen, N., Sohni, S., Ahmad, I., Khattak, N.U., Gul, K., 2018. Self-assembled three-dimensional reduced graphene oxide-based hydrogel for highly efficient and facile removal of pharmaceutical compounds from aqueous solution. J. Colloid Interface Sci. 527, 356-367.

Vafai, K., Bejan, A., Minkowycz, W.J., Khanafer, K., 2006. A critical synthesis of pertinent models for turbulent transport through porous media. Advances in Numerical Heat Transfer, Vol. 2, Chapter 12, John Wiley & Sons Inc., Hoboken, New Jersey, pp. 389–416.

Vafai, K., Sofen, M., 1990. Analysis of energy and momentum transport for fluid flow through a porous bed. ASME J. Heat Transfer. 112, 690–699.

Varteressian, K.A., Fenske, M.R., 1936. Liquid-liquid extraction performance of a packed extraction column, using continuous countercurrent operation. Ind. Eng. Chem. 28, 928-933.

Verschaffelt, J.E., 1936. Bull. Classe Sei. Acad., Roy. Belg. 22, 373, 390, 402.

Vilchis-Nestor, A.R., Sanchez-Mendieta, V., Camacho-López, M.A., Gómez-Espinosa, R.M., Camacho-López, M.A., Arenas-Alatorre, J.A., 2008. Solvent less synthesis and optical properties of Au and Ag nanoparticles using Camellia sinensis extract. Mat. Lett. 62, 3103-3105.

Vollmari, K., Oschmann, T., Wirtz, S., Kruggel-Emden, H., 2015. Pressure drop investigations in packings of arbitrary shaped particles. Powder Technol. 271, 109–124.

Wakao, N., Kaguei, S., Funazkri, T., 1979. Effect of fluid dispersion coefficients on particle-to-fluid heat transfer coefficients in packed beds: correlation of nusselt numbers. Chem. Eng. Sci. 34, 325–336.

Wammes, W.J.A., Middelkamp, J., Huisman, W.J., deBaas, C.M., Westerterp, K.R., 1991. Hydrodynamics in a cocurrent gas-liquid trickle bed at elevated pressure, Part 2: Liquid holdup, pressure drop, flow regimes. AIChE J. 37, 1854–1863.

Wang, C., Astruc, D., 2018. Recent developments of metallic nanoparticle-graphene nanocatalysts. Prog. Mater. Sci. 94, 306–383.

Wang, F., He, F., Zhao, J., Sui, N., Xu, L., Liu, H., 2012a. Extraction and separation of cobalt (II), copper (II) and manganese (II) by Cyanex272, PC-88A and their mixtures. Sep. Purif. Technol. 93, 8-14.

Wang, F., Yu, J., Zhang, Z., Xu, Y., Chi, R., 2018b. An amino-functionalized Ramie stalk-based adsorbent for highly effective Cu^{2+} removal from water: adsorption performance and mechanism. Process Saf. Environ. Prot. 117, 511–522.

Wang, G., Gao, P., Tan, S., Wang, Z., 2013. Forced convection heat transfer and flow characteristics in laminar to turbulent transition region in rectangular channel. Exp. Therm. Fluid Sci. 44, 490-497.

Wang, H., Kang, J., Liu, H., Qu, J., 2009. Preparation of organically functionalized silica gel as adsorbent for copper ion adsorption. Int. J. Environ. Sci. 21, 1473-1479.

Wang, L., Liu, F., 2007. Forced convection in slightly curved microchannels. Int. J. Heat Mass Transfer 50, 881- 897.

Wang, L., Shi, Y., Wang, T., Zhang, L., 2017b. Silver chloride enwrapped silver grafted on nitrogen-doped reduced graphene oxide as a highly efficient visible-light-driven photocatalyst. J. Colloid Interface Sci. 505, 421–429.

Wang, Z., Nie, E., Li, J., Yang, M., Zhao, Y., Luo, X., et al. 2012b. Equilibrium and kinetics of adsorption of phosphate onto iron-doped activated carbon. Environ. Sci. Pollut. Res. 19, 2908-2917.

Wang, J., Salihi, E.C., Šiller, L., 2017a. Green reduction of graphene oxide using alanine. Mater. Sci. Eng. C 72, 1-6.

Warnier, M.J.F., de Croon, M.H.J.M., Rebrov, E.V., Schouten, J.C., 2010. Pressure drop of gas liquid Taylor flow in round micro-capillaries for low to intermediate Reynolds numbers. Microfluidics and Nanofluidics 8, 33-45.

Warrier, G.R., Dhir, V.K., Momoda, L.A., 2002. Heat transfer and pressure drop in narrow rectangular channels. Exp. Therm Fluid Sci. 26, 53-64.

Watanabe, H., 1989. Drag coefficient and voidage function on fluid flow through granular packed beds. Int. J. Eng. Fluid Mech. 2, 93–108.

Wei, G.T., Yang, Z., Chen, C.J., 2003. Room temperature ionic liquid as a novel medium for liquid/liquid extraction of metal ions. Anal. Chim. Acta 488, 183-192.

Whitaker, S., 1972. Forced convection heat transfer correlations for flow in pipes, past flat plates, single cylinders, single spheres, and for flow in packed beds and tube bundles. AIChE J. 18, 361–371.

Wieszczycka, K., Kaczerewska, M., Krupa, M., Parus, A., Olszanowski, A., 2012. Solvent extraction of copper(II) from ammonium chloride and hydrochloric acid solutions with hydrophobic pyridineketoximes. Sep. Purif. Technol. 95, 157-164.

Willner, J., Fornalczyk, A., 2014. Extraction of copper from solution after bioleaching of printed circuit boards (PCBs). METABK 53 (2), 228-230.

Wojcieszynska, D., Domaradzka, D., Hupert-Kocurek, K., Guzik, U., 2014. Bacterial degradation of naproxen – Undisclosed pollutant in the environment. J. Environ. Manage. 145, 157-161.

Woods, B.D., Hanratty, T.J., 1999. Influence of Froude number on physical processes determining frequency of slugging in horizontal gas–liquid flows. Int. J. Multiph. Flow 25, 1195–1223.

Wu, Y.S., Pruess, K., 1996. Flow of non-Newtonian fluids in porous media. Adv. Porous Media **3**, 87–184.

Wu, Z., Sundén, B., 2019. Liquid-liquid two-phase flow patterns in ultra-shallow straight and serpentine microchannels. Heat Mass Transf. 55, 1095-1108.

Xavier, A.L.P., Adarme, O.F.H., Furtado, L.M., Ferreira, G.M.D., Silva, L.H.M., Gil, L.F., Gurgel, L.V.A., 2018. Modeling adsorption of copper(II), cobalt(II) and nickel(II) metal ions from aqueous solution onto new carboxylated sugarcane bagasse. Part II: Optimization of mono-component fixed-bed column adsorption. J. Colloid Interface Sci. 516, 431–445.

Xie, F., Dreisinger, D., 2009. Studies on solvent extraction of copper and cyanide from waste cyanide solution. J. Hazard. Mater. 169, 333-338.

Xing, D., Yan, C., Wang, C., Sun, L., 2013. A theoretical analysis about the effect of aspect ratio on single-phase laminar flow in rectangular ducts. Prog. Nucl. Energy 65, 1-7.

Yang, C.Y., Webb, R.L., 1996. Friction pressure drop of R-12 in small hydraulic diameter extruded aluminium tubes with and without micro-fins. Int. J. Heat Mass Transfer 39, 801–809.

Yang, J., Wang, J., Bu, S.S., Zeng, M., Wang, Q.W., 2012. Experimental study of forced convective heat transfer in structured packed porous media of particles. Nucl. Power Eng. 33, 851–855.

Yeen, K.P., Haron, M.J., Silong, S., Basri, M., Yunus, W.M.Z.W., 2005. Copper ion extraction by a mixture of fatty hydroxamic acids synthesized from commercial palm olein. Solvent Extr. Ion Exch. 23, 713-723.

Yoon, Y.H., Nelson, J.H., 1984. Application of gas adsorption kinetics. 1. A theoretical model for respirator cartridge service life. Am. Ind. Hyg. Assoc. J. 45, 509-516.

Yu, J., Tang, L., Pang, Y., Zeng, G., Wang, J., Deng, Y., et al. 2019. Magnetic nitrogen-doped sludge-derived biochar catalysts for persulfate activation: Internal electron transfer mechanism. Chem. Eng. J. 364, 146-159.

Yu, Z., Peldszus, S., Huck, P.M., 2008. Adsorption characteristics of selected pharmaceuticals and an endocrine disrupting compound—Naproxen, carbamazepine and nonylphenol—on activated carbon. Water Res. 42, 2873-2882.

Yuan, Y., Han, M., Wang, D., Jin, Y., 2004. Liquid phase residence time distribution for a two-phase countercurrent flow in a packed column with a novel internal. Chem. Eng. Process. 43, 1469–1474.

Yue, J., Boichot, R., Luo, L., Gonthier, Y., Chen, G., Yuan, Q., 2010. Flow distribution and mass transfer in a parallel microchannel contactor integrated with constructal distributors. AIChE J. 56, 298-317.

Yue, J., Chen, G., Yuan, Q., 2004. Pressure drops of single and two-phase flows through T-type microchannel mixers. Chem. Eng. J. 102, 11-24.

Yue, J., Chen, G., Yuan, Q., Luo, L., Gonthier, Y., 2008. Hydrodynamics and mass transfer characteristics in gas–liquid flow through a rectangular microchannel. Chem. Eng. Sci. 62, 2096-2108.

Zanoni, M.A.B., Torero, J.L., Gerhard, J.I., 2017. Determination of the interfacial heat transfer coefficient between forced air and sand at Reynold's numbers relevant to smouldering combustion. Int. J. Heat Mass Transf. 114, 90-104.

Zeiser, T., Lammers, P., Klemm, E., Li, Y.W., Bernsdorf, J., Brenner, G., 2001. CFD-calculation of flow, dispersion and reaction in a catalyst filled tube by the lattice Boltzmann method. Chem. Eng. Sci. 56, 1697-1704.

Zhang, H., Ran, X., Wu, X., Zhang, D., 2011a. Evaluation of electro-oxidation of biologically treated landfill leachate using response surface methodology. J. Hazard. Mater. 188, 261–268.

Zhang, H., Tang, S., Liang, B., 2011b. Residence time distribution in two-phase flow mini-channel reactor. Chem. Eng. J. 174, 652–659.

Zhang, K., Li, H., Xu, X., Yu, H., 2018. Synthesis of reduced graphene oxide/NiO nanocomposites for the removal of Cr(VI) from aqueous water by adsorption. Micropor. Mesopor. Mat. 255, 7-14.

Zhang, W., Hibiki, T., Mishima, K., 2010a. Correlations of two-phase frictional pressure drop and void fraction in mini-channel. Int. J. Heat Mass Transf. 53, 453–465.

Zhang, X., Li, X., Cao, H., Zhang, Y., 2010b. Separation of copper, iron (III), zinc and nickel from nitrate solution by solvent extraction using LK-C2. Sep. Purif. Technol. 70, 306-313.

Zhang, Y., Chi, H., Zhang, W., Sun, Y., Liang, Q., Gu, Y., Jing, R., 2014. Highly efficient adsorption of copper ions by a PVP-reduced graphene oxide based on a new adsorption mechanism. Nano-Micro Lett. 6, 80-87.

Zhang, Y., Liu, S., Wang, L., Song, Y., Yang, M., Zhao, J., Zhao, Y., Chi, Y., 2016. In situ measurement of the dispersion coefficient of liquid/supercritical CO_2–CH_4 in a sand pack using CT. RSC Adv. 6, 42367.

Zhang, J., Yang, H., Shen, G., Cheng, P., Zhang, J., Guo, S., 2010c. Reduction of graphene oxide via l-ascorbic acid. Chem. Comm. 46, 1112-1114.

Zhao, G., Li, J., Wang, X., 2011. Kinetic and thermodynamic study of 1-naphthol adsorption from aqueous solution to sulfonated graphene nanosheets. Chem. Eng. J. 173, 185-190.

Zhao, Y., Chem, G., Yuan, Q., 2006. Liquid-liquid two-phase flow patterns in a rectangular Microchannel. AIChE J. 52, 4052-4060.

Zhou, Z.Y., Yu, A.B., Zulli, P., 2010. A new computational method for studying heat transfer in fluid bed reactors. Powder Technol. 197, 102–110.

Zhu, Z., Zhang, W., Pranolo, Y., Cheng, C.Y., 2012. Separation and recovery of copper, nickel, cobalt and zinc in chloride solutions by synergistic solvent extraction. Hydrometallurgy 127-128, 1-7.

Zou, R.P., Yu, A.B., 1995. The packing of spheres in a cylindrical container: the thickness effect. Chem. Eng. Sci. 50, 1504-1507.

Zuccaro, L., Krieg, J., Desideri, A., Kern, K., Balasubramanian, K., 2015. Tuning the isoelectric point of graphene by electrochemical functionalization. Sci. Rep. 5, 11794.

Web References

Dimensionless numbers in fluid mechanics,

https://en.wikipedia.org/wiki/Dimensionless_numbers_in_fluid_mechanics

Estimation of Flow Patterns,

http://14.139.172.204/nptel/CSE/Web/103105058/mod2lec5.html

Gas pockets and hydraulic jumps in pressurized pipelines,

https://www.google.co.in/url?sa=t&rct=j&q=&esrc=s&source=web&cd=14&ved=0ahUKEwitpara7tDYAhVJu48KHZUzBXEQFghgMA0&url=https%3A%2F%2Fpublicwiki.deltares.nl%2Fdownload%2Fattachments%2F4521988%2FUSM_WSUD_paper_0129.pdf%3Fversion%3D1%26modificationDate%3D1277126408000&usg=AOvVaw37ZnUyiPkV3t5xmAJvztag

Infrared spectroscopy adsorption table, chemistry, LibreTexts™

https://chem.libretexts.org/Reference/Reference_Tables/Spectroscopic_Parameters/Infrared_Spectroscopy_Absorption_Table

Pressure Loss Calculations,

http://fekete.com/SAN/TheoryAndEquations/HarmonyTheoryEquations/Content/HTML_Files/Reference_Material/Calculations_and_Correlations/Pressure_Loss_Calculations.htm#Multi-Phase_Flow

Rule of Mixtures Calculator for Heat Capacity, internet sources,

https://thermtest.com/thermal-resources/rule-of-mixtures

Total Porosity and Effective Porosity,

http://www.informit.com/articles/article.aspx?p=1626870&seqNum=2

USGS Wentworth Grain Size Chart,

https://www.scribd.com/doc/35548819/USGS-Wentworth-Grain-Size-Chart#download

List of Publications

A. Research papers in journals

1) **Mondal, S.**, Majumder, S.K., 2020. Fabrication of the polysulfone-based composite ultrafiltration membranes for the adsorptive removal of heavy metal ions from their contaminated aqueous solutions. ***Chemical Engineering Journal***, 401, 126036. **(Impact factor 10.652)**
2) **Mondal, S.**, Majumder, S.K., 2020. Copper adsorption based on hydrodynamics and mixing characteristics on the amine-functionalized reduced graphene oxide coated glass beads in a multichannel packed bed device. ***Industrial & Engineering Chemistry Research***, 59, 11864-11879. **(Impact factor 3.573)**
3) **Mondal, S.**, Majumder, S.K., 2020. Heat transport based on hydrodynamics and the local entropy generation rate in straight and serpentine rectangular packed narrow channels. ***Applied Thermal Engineering***, 171, 115057. **(Impact factor 4.725)**
4) **Mondal, S.**, Patel, S., Majumder, S.K., 2020. Naproxen Removal Capacity Enhancement by Transforming the Activated Carbon into a Blended Composite Material. ***Water, Air, & Soil Pollution***, 231, 37. **(Impact factor 1.900)**
5) **Mondal, S.**, Patel, S., Majumder, S.K., 2020. Bio-extract assisted in-situ green synthesis of Ag-RGO nanocomposite film for enhanced naproxen removal. ***Korean Journal of Chemical Engineering***, 37, 274-289. **(Impact factor 2.690)**
6) **Mondal, S.**, Majumder, S.K., 2019. Honeycomb-like porous activated carbon for efficient copper (II) adsorption synthesized from natural source: Kinetic study and equilibrium isotherm analysis. ***Journal of Environmental Chemical Engineering***, 7, 103236. **(Impact factor 4.300)**
7) **Mondal, S.**, Majumder, S.K., 2019. Synthesis of phosphate functionalized highly porous activated carbon and its utilization as an efficient copper (II) adsorbent. ***Korean Journal of Chemical Engineering***, 36, 701-712. **(Impact factor 2.690)**
8) **Mondal, S.**, Majumder, S.K., 2018. Single and aqueous-organic two-phase frictional pressure drop and local entropy generation in rectangular millichannel: Experiment and its analysis. ***Chemical Engineering and Processing: Process Intensification***, 134, 72-85. **(Impact factor 3.731)**
9) **Mondal, S.**, Majumder, S.K., 2018. Studies on the copper extraction in a channel-based packed extraction device. ***Minerals Engineering***, 126, 194-206. **(Impact factor 3.795)**
10) **Mondal, S.**, Majumder, S.K., 2018. Frictional pressure drop of aqueous-organic two-phase flow through packed and unpacked rectangular serpentine millichannel. ***Experimental Thermal and Fluid Science***, 94, 215-230. **(Impact factor 3.444)**

B. Research papers in conferences

1) **Mondal, S.**, Majumder, S.K., 2017. Extraction of copper from particle laden solutions in millichannel by solvent extraction. Mineral Processing Technology (MPT), Radison Blu Resort, Temple Bay, Mahabalipuram, Tamil Nadu, Chennai, India, 1th-3rd February.
2) **Mondal, S.**, Majumder, S.K., 2018. Optimization of the extraction parameters in a millichannel-based packed and unpacked rectangular serpentine extraction device. AIChE Annual Meeting, Pittsburgh, Pennsylvania, USA, 28th October - 2nd November. (Presented by Majumder, S.K.).
3) **Mondal, S.**, Majumder, S.K., 2018. Optimization of the extraction parameters in a channel-based packed extraction device. Research Conclave (RC), Indian Institute of Technology Guwahati, Assam, India, 8th-15th March.
4) **Mondal, S.**, Majumder, S.K., 2018. Utilization of chemically activated carbon synthesized from tea-waste as an efficient copper (II) adsorbent. International Conference on Water: From Pollution to Purification (ICW), Kottayam, Kerala, India, 7th-10th December.
5) **Mondal**, S., Majumder, S.K., 2019. Tea-waste based activated carbon for efficient copper (II) adsorption. Research Conclave (RC), Indian Institute of Technology Guwahati, Assam, India, 14th-17th March.
6) **Mondal**, S., Majumder, S.K., 2019. Bio-based phosphate functionalized activated carbon from Indian gooseberry seed shells for the efficient copper (II) adsorption. 16th International Conference on Environmental Science and Technology (CEST), Rodos Palace, Rhodes, Greece, 4th-7th September. (**Funded by Science & Engineering Research Board**, **SERB-DST,** International Travel Support, File No.: ITS/2019/003911)
7) **Mondal**, S., Majumder, S.K., 2019. Adsorption capacity enhancement by the surface-modification of the activated carbon-based materials. Reflux 7.0, Indian Institute of Technology Guwahati, Assam, India, 28th-29th September.
8) **Mondal**, S., Majumder, S.K., 2019. Synthesis of Ag-RGO nanocomposite using green method and its application as an efficient naproxen adsorbent. The International Conference on Sustainable Energy and Green Technology (SEGT), Millennium Hilton, Bangkok, Thailand, 11th-14th December. (**Funded by Council of Scientific and Industrial Research, CSIR - HRDG,** Travel Grant, File No.: TG/11112/19-HRD, and the Department of Chemical Engineering, IIT Guwahati)
9) **Mondal**, S., Majumder, S.K., 2019. Green synthesis of Ag-RGO nanocomposite for enhanced naproxen removal. 72nd Annual Session of Indian Institute of Chemical Engineers (CHEMCON), Indian Institute of Technology Delhi, Hauz Khas, New Delhi, India, 15th-19th December.

10) **Mondal**, S., Majumder, S.K., 2020. Utilization of the phosphate functionalized activated carbon synthesized from natural sources as the efficient copper (II) adsorbent. International Conference on Functional Materials (ICFM), Indian Institute of Technology Kharagpur, West Bengal, India, 6th-8th January.
11) **Mondal**, S., Majumder, S.K., 2020. Use of Ag-RGO nanocomposite as an efficient naproxen adsorbent. National Conference on Issues & Challenges in Water Treatment and Allied Research for Sustainable Environment (WATER), Indian Institute of Technology Guwahati, Assam, India, 23rd-25th January.
12) **Mondal**, S., Majumder, S.K., 2020. Greenly synthesized Ag-RGO nanocomposite for the efficient naproxen adsorption. 3rd International Conference on Waste Management (RECYCLE), Indian Institute of Technology Guwahati, Assam, India, 13th-14th February.

Appendix-I

A. Uncertainty analysis

Uncertainties in the measured experimental data

The average values are taken, repeating each experiment for at least five times in the present work. The standard deviation (SD) and standard uncertainties (S_U) of the experiments are expressed by the Eqs. (A1-A2). x_i is the ith component, and N is the total number of variables.

$$SD = \sqrt{\frac{\sum_{i=1}^{N}\left(x_i - \bar{x}\right)^2}{N-1}} \quad \text{(A1)}$$

$$S_U = \frac{SD}{\sqrt{N}} \quad \text{(A2)}$$

In Eq. (A1), $\bar{x}$ is the mean value, and it is represented by Eq. (A3). The relative uncertainties (R_U) in percentage are estimated by Eq. (A4) (Moffat, 1988).

$$\bar{x} = \frac{1}{N}\sum_{i=1}^{N} x_i \quad \text{(A3)}$$

$$R_U = \frac{S_U}{\bar{x}} \times 100\% \quad \text{(A4)}$$

Uncertainty analysis (Typically for Chapter 2)

Table A1. Uncertainties in the measured experimental data for the flow through unpacked and packed straight channel geometries.

Properties and measurements	Mean	No. of run	Standard Deviation × 10^2 (SD)	Standard Uncertainty × 10^2 (S_U)	% relative Uncertainties (R_U)
Total volumetric flow rate × 10^6 (m^3 s^{-1}) [without packing]	3.63 – 5.61	10	0.34 – 0.67	0. 11 – 0.21	0.030 – 0.037

Total volumetric flow rate × 10^6 (m^3 s^{-1}) [with packing]	0.72 – 1.77	10	0. 38 – 0.56	0.12 – 0.18	0.10 – 0.17
Pressure drop per unit length × 10^{-4} (N m^{-3}) [without packing]	1.40 – 3.14	10	0. 32 – 0.42	0.10 – 0.13	0.041 – 0.071
Pressure drop per unit length × 10^{-5} (N m^{-3}) [with packing]	1.54 – 5.55	10	0.30 – 0.40	0.095 – 0.13	0.023 – 0.062

Table A2. Uncertainties to the experimentally measured quantities for the flow through the unpacked and packed serpentine channel geometries.

Properties and measurements	Mean	No. of run	Standard Deviation×10^2	Standard uncertainty×10^2	% relative uncertainties
Total volumetric flow rate × 10^6 (m^3 s^{-1}) [without packing]	0.89 – 5.43	10	0.037 – 0.24	0.012 – 0.075	0.013 – 0.014
Total volumetric flow rate × 10^6 (m^3 s^{-1}) [with packing]	0.30 – 1.52	10	0.038 – 0.23	0.012 – 0.074	0.04 – 0.05
Pressure drop per unit length × 10^4 (N m^{-3}) [without packing]	3.51 – 9.28	10	0.032 – 0.038	0.010 – 0.012	0.0013 – 0.003
Pressure drop per unit length × 10^5 (N m^{-3}) [with packing]	4.09 – 9.68	10	0.033 – 0.040	0.010 – 0.013	0.0013 – 0.002

B. Calculation Procedure for Typical Multiple Regression [Chapter – 2, Equation (2.46)]

The regression equation is

$$\left(\frac{d_H}{\rho_m U_m^2}\frac{\Delta P}{L}\right) = c_1\left(\frac{R_c}{d_H}\right)^{b_1}, \mathrm{De}_p^{\,b_2}, \mathrm{Ca}_p^{\,b_3}, Fr_p^{\,b_4} \qquad \text{B1}$$

Taking logarithm on both sides of equation A1, one get

$$Log\left(\frac{d_H}{\rho_m U_m^2}\frac{\Delta P}{L}\right) = Log(c_1) + b_1 Log\left(\frac{R_c}{d_H}\right) + b_2 Log(\mathrm{De}_p) + b_3 Log(\mathrm{Ca}_p) + b_4 Log(\mathrm{Fr}_p) \qquad \text{B2}$$

The Equation B2 can be written as

$$Y = b_0 + b_1 X_1 + b_2 X_2 + b_3 X_3 + b_4 X_4 + e \qquad \text{B3}$$

where $Y = \mathrm{Log}\left(\frac{d_H}{\rho_m U_m^2}\frac{\Delta P}{L}\right)$, $X_1 = \mathrm{Log}(R_c/d_H)$, $X_2 = \mathrm{Log}(De_p)$, $X_3 = \mathrm{Log}(Ca_p)$, $X_4 = \mathrm{Log}(Fr_p)$, and $b_0 = \mathrm{Log}(c_1)$. e is the error term which has to be minimized to estimate the regression model as

$$\hat{Y} = b_0 + b_1 X_1 + b_2 X_2 + b_3 X_3 + b_4 X_4 \qquad \text{B4}$$

$\hat{Y}$ is the predicted value of Y

The intercept b_0 and coefficients b_1, b_2, b_3, and b_4 have been estimated by multiple regression analysis by "Data Analysis Tool" of Software "Microsoft Excel".

The software gives the outputs on the basis of the following calculation

The equation B3 can be written as matrix form for n (here n = 19) observations and k (here k = 4) variables as

$$\begin{bmatrix} Y_1 \\ Y_2 \\ : \\ : \\ Y_n \end{bmatrix} = \begin{bmatrix} 1 & X_{11} & X_{12} & \ldots\ldots & X_{1k} \\ 1 & X_{21} & X_{22} & \ldots\ldots & X_{2k} \\ : & : & : & \ldots\ldots & : \\ : & : & : & \ldots\ldots & : \\ 1 & X_{n1} & X_{n2} & \ldots\ldots & X_{nk} \end{bmatrix} \times \begin{bmatrix} b_0 \\ b_1 \\ : \\ : \\ b_k \end{bmatrix} + \begin{bmatrix} e_1 \\ e_2 \\ : \\ : \\ e_n \end{bmatrix} \qquad \text{B5}$$

$\Rightarrow$ **Y = X × B + e**

Regression Statistics

		Explanation
Multiple R	0.999716	R = square root of R^2
R Square	0.999433	R^2 = coefficient of determination
Adjusted R Square	0.999362	Adjusted R^2 used if more than one X variable
Standard Error	0.024346	This is the estimate of the st. dev. of the error *e*
Observations	19	Number of observations used in the regression (n)

Analysis of Variance

	Degrees Of freedom	Sum of Square	Mean Sum of Square	F-stat
Regression	2	16.702	8.351040	14089.04
Residual	16	0.009	0.000593	
Total	18	16.711		

where

$$\text{Regression Sum of Square} = B'X'Y - n\bar{Y}^2$$

$$\text{Total Sum of Square} = Y'Y - n\bar{Y}^2$$

Residual Sum of Square = Total Sum of Square – Regression Sum of Square

$$R^2 = \frac{\text{Regression Sum of Square}}{\text{Residual Sum of Square}}$$

$$F - stat = \frac{R^2/(k-1)}{(1-R^2)/(n-k)}$$

$$Adjusted\ R^2 = 1-(1-R^2)\frac{n-1}{(n-k)}$$

$$\text{Standard Error} = \sqrt{\frac{\text{Residual Sum of Square}}{n-k}}$$

$$Y' = [Y_1 \quad Y_2 \quad \ldots\ldots\ldots Y_n]$$

$$B' = [B_0 \quad B_1 \quad \ldots\ldots\ldots B_k]$$

The F-stat gives the overall F-test of null hypothesis *H0*: $b_i = 0$. The F-stat gives the associated Probability-value. Since it is greater than 0.05 at the 5% significance level we do not reject null hypothesis for the goodness of fit.